Poznan University of Technology
Faculty of Automatic Control, Robotics, and Electrical Engineering
Institute of Automatic Control and Robotics
Division of Electronic Systems and Signal Processing

Vision inspection using artificial intelligence to improve safety of aerodrome

Jakub Suder

Ph.D. dissertation

Supervisor:
Prof. Adam Dąbrowski, Ph.D., D.Sc.

Poznań 2024

First, I would like to thank my supervisor
prof. Adam Dąbrowski, Ph.D., D.Sc.,
for his guidance and invaluable advice
throughout this thesis work.

I would like to thank in particular
Tomasz Marciniak, Ph.D.,
for his continuous support, insightful comments,
patience, and inspiring cooperation with aviation experts.

I would also like to express my deepest gratitude to my family and friends,
for their understanding,
constant encouragement,
and contribution that they are.

Abstract

This thesis presents the results of research concerning vision inspection using artificial intelligence to improve safety of aerodrome. Inspection of airfields, especially runways, taxiways, and aprons, is critical from the perspective of aviation operation safety and airport operational readiness. Current standards and recommendations from the European Union Aviation Safety Agency (EASA), such as the *Artificial Intelligence Roadmap 2.0*, indicate that the inspection of manoeuvring areas in airports should employ AI-based solutions, including machine learning, deep neural networks, and logic-knowledge-based approaches, thereby supporting personnel responsible for maintaining safety.

In the doctoral dissertation, the following scientific thesis was formulated: *Proposed vision preprocessing methods, together with neural network solutions within the domain of embedded systems, substantially improve and facilitate the automated inspection process at the airports*.

There are three main research areas addressed in the dissertation, based on the recommendations aforementioned. The first area is the detection of Foreign Object Debris (FOD) in critical airport areas. Such objects can cause an aviation disaster if they come near an aircraft during the most critical phases of flight, such as take-off and landing. The dissertation presents an analysis of available databases, introduces the proprietary *PUT dataset*, and explores the use of image processing algorithms to detect such objects on aerodrome surfaces using neural network architectures, as well as image processing methods, thus aiding the airport services in this vital task. The selection of GoogLeNet and YOLOv5 significantly improved the accuracy of FOD detection, which could be investigated by using different databases and examining the influence of individual input data parameters on the final result.

The second research area, which comes from aviation regulations, is the detection of airport horizontal markings. These markings serve as guidelines for both aviation and ground personnel and have strictly defined locations. Due to stringent regulations determining the placement of aerodrome horizontal markings, it is possible to correct the alignment of the measurement platform for airport lighting inspection based on the location relative to specific lines. Conducting such inspections is critical and impacts the operational capability of the airport under reduced visibility conditions. The author prepared dataset of video recordings, *PLAVS1*, from the restricted area of the airport, and the developed line detection algorithms based on image processing methods, and their analysed their efficiency in implementation in single-board computers such as the Nvidia Jetson family.

The third research area is the classification of in-pavement airfield ground lighting. This classification involves detecting the light fixtures and assessing the wear of their prisms, evaluating the chromaticity of the light emitted by each point source, and comparing it to international standards. The proprietary dataset, *PLAVS2*, was developed for this purpose, and appropriate algorithms based on image processing methods to detect the region of interest (ROI) were selected, neural networks such as GoogLeNet, VGG-19 and ResNet, as well as performing analysis and selection of light chromaticity sensors, proposing a system to support airport services in daily inspection of manoeuvring surfaces.

The realization of the scientific research presented in the doctoral dissertation was made possible through the scientific collaboration of the Division of Signal Processing and Electronic Systems at Poznan University of Technology with Poznań–Ławica Airport.

Streszczenie

W pracy przedstawiono wyniki badań dotyczące inspekcji wizyjnej z wykorzystaniem sztucznej inteligencji w celu poprawy bezpieczeństwa portów lotniczych. Kontrola płaszczyzn lotniskowych (*ang. aerodrome*), takich jak drogi startowe, drogi kołowania oraz płyty postojowe jest krytyczna z perspektywy bezpieczeństwa wykonywanych operacji lotniczych oraz gotowości operacyjnej portu lotniczego. Współczesne standardy i zalecenia Agencji Unii Europejskiej ds. Bezpieczeństwa Lotniczego (EASA), takie jak *Artificial Intelligence Roadmap 2.0*, wskazują, aby inspekcja obszarów manewrowych w portach lotniczych wykorzystywała rozwiązana bazujące na sztucznej inteligencji, czyli uczeniu maszynowym, głębokich sieciach neuronowych oraz algorytmach decyzyjnych, wspierając tym samym osoby odpowiedzialne za utrzymanie bezpieczeństwa.

W rozprawie doktorskiej sformułowana została następująca teza naukowa: *Zmodyfikowane metody przetwarzania obrazu wraz z rozwiązaniami bazującymi na sieciach neuronowych w obszarze systemów wbudowanych znacząco usprawniają ułatwiają zautomatyzowany proces inspekcji portu lotniczego.*

Bazując na przytoczonych wcześniej zaleceniach instytucji międzynarodowych, wyodrębniono trzy główne obszary badawcze poruszane w rozprawie doktorskiej. Pierwszym z nich jest wykrywanie obiektów typu FOD (*ang. Foreign Object Debris*) na newralgicznych obszarach portu lotniczego. Obiekty takie mogą spowodować katastrofę lotniczą, jeśli znajdą się w pobliżu statku powietrznego podczas najbardziej krytycznych faz lotu, takich jak start i lądowanie. Rozprawa przedstawia analizę dostępnych baz danych, pokazuje autorską bazę danych *PUT dataset* oraz wykorzystanie algorytmów przetwarzania obrazu do wykrywania takich obiektów na płaszczyznach lotniskowych, przy zastosowaniu architektur sieci neuronowych i metod przetwarzania obrazu, wspierając tym samym służby w tym istotnym zadaniu. Dobór architektur sieci neuronowych w postaci GoogLeNet i YOLOv5 znacznie poprawił dokładność wykrywania FOD, co możliwe było do zweryfikowania przy wykorzystaniu różnych bazy danych oraz badając wpływ poszczególnych parametrów danych wejściowych na wynik końcowy.

Drugim analizowanym obszarem badawczym wynikającym z przepisów lotniczych jest wykrywanie poziomych oznaczeń lotniskowych. Oznaczenia te służą personelowi lotniczemu, ale także naziemnemu, jako wskazówki i mają swoje ściśle określone położenie. Dzięki tak rygorystycznym przepisom determinującym umiejscawianie oznaczeń poziomych, możliwe jest wykonanie poprawnego najazdu platformą pomiarową do badania nawigacyjnego oświetlenia lotniskowego nad badaną lampę w oparciu o lokalizację względem określonych linii. Przeprowadzenie takich badań jest krytyczne i wpływa na zdolność operacyjną portu lotniczego w warunkach obniżonej widzialności. W pracy przedstawiono przygotowaną bazę danych nagrań wideo *PLAVS1* z zastrzeżonego terenu portu lotniczego oraz opracowane algorytmy wykrywania linii, bazujące na metodach przetwarzania obrazu i oceniono ich efektywność w implementacji w urządzeniach wbudowanych, takich jak rodzina Nvidia Jetson.

Trzecim badanym obszarem jest klasyfikacja lamp zagłębionych oświetlenia nawigacyjnego w płaszczyzny lotniskowe. Klasyfikacja z jednej strony opiera się na wykryciu lampy i ocenie zużycia jej pryzmatu, a z drugiej, na ocenie chromatyczności barwy światła emitowanej przez dany punkt świetlny i porównanie jej z obowiązującymi normami międzynarodowymi. Opracowano w tym celu autorskie bazy danych *PLAVS2*, dobrano odpowiednie algorytmy w oparciu o metody przetwarzania obrazu w celu wykrycia obszaru zainteresowania (ROI), sieci neuronowe, takie jak GoogLeNet, VGG-19 oraz ResNet, a także dokonano analizy i doboru czujników chromatyczności światła, a następnie zaproponowano system wspierający służby lotniskowe w codziennej kontroli płaszczyzn manewrowych.

Realizacja badań naukowych przedstawionych w rozprawie doktorskiej była możliwa dzięki współpracy naukowej Zakładu Układów Elektronicznych i Przetwarzania Sygnałów Politechniki Poznańskiej z Portem Lotniczym Poznań–Ławica.

List of Abbreviations and Notations

ADAS – Advanced Driver Assistance Systems
AGL – Airfield Ground Lighting
AI – Artificial Intelligence
AUC – Area Under the Curve
B – Blue in RGB colour model
CCD – Charge-Coupled Device
CHT – Circular Hough Transform
CIE – International Commission on Illumination
CMF – Colour Matching Functions
CNN – Convolutional Neural Network
CPU – Central Processing Unit
DL – Deep Learning
DVFS – Dynamic Voltage and Frequency Switching
EASA – European Union Aviation Safety Agency
eMMC – embedded Multi-Media Card
f – focal length
FAA – Federal Aviation Administration
FN – False Negatives
FNN – Feedforward Neural Network
FOD – Foreign Object Debris
FP – False Positives
FPS – Frames Per Second
G – Green in RGB colour model
GNN – Graph Neural Network
GPU – Graphics Processing Unit
GS – Glide Slope in the ILS system
H – Hue in HSV colour space
HMI – Human-Machine Interface
ICAO – International Civil Aviation Organization
ILS – Instrument Landing System
IoT – Internet of Things
IR – Infrared
ISO – International Organization for Standardization
IVA – Intelligent Video Analysis
K_{cd} – maximum luminous efficacy
KPI – Key Performance Indicators
LED – Light-Emitting Diode
LKB – Logic - and Knowledge Based approaches
LOC – Localizer in the ILS system
$M(x, y)$ – Pixel's gradient magnitude
mAP – mean Average Precision
ML – Machine Learning
NLP – Natural Language Processing
NPV – Negative Predictive Value
PPV – Positive Predictive Value
R – Red in RGB colour model
RAM – Random Access Memory
RNN – Recurrent Neural Network
ROC – Receiver Operating Characteristic
ROI – Region Of Interest
S – Saturation in HSV colour space
SBC – Single Board Computer
SGDM – Stochastic gradient descent with momentum
SMS – Safety Management System
SoC – System-on-a-Chip
SOM – System-On-Module
SRM – Safety Risk Management
TN – True Negatives
TP – True Positives
TPC – Texture Processing Cluster
UART – Universal Asynchronous Receiver-Transmitter
UAV – Unmanned Aerial Vehicle
UV – Ultraviolet
V – Value in HSV colour space
$v(\lambda)$ – photopic luminosity function, which describes the human eye's sensitivity under well-lit conditions
VP – Vanishing point
X – Nonnegative mix of RGB in CIE 1931 colour space
x, y – coordinates in CIE 1931 colour space
(x, y) – coordinates of a point in 2D space
Y – Luminance value in the CIE 1931 colour space
YOLO – You Only Look Once
Z – Quazi blue value in the CIE 1931 colour space
$\Phi_e(\lambda)$ – spectral radiometric value
Φ_v – photometric quantity

Contents

Chapter

1. Introduction

1.1. Research area

Air operations have been growing in recent years, with an increasing number of airplanes and flights operating in many parts of the world. This trend is particularly notable in Europe, where air traffic has grown at a steady rate over the past several decades. One of the main drivers of this growth has been the liberalization of the European airline industry. Beginning in the 1990s, the European Union (EU) gradually removed restrictions on the establishment of new airlines and the routes they can operate. This has led to increased competition and lower prices, making air travel more accessible to more people. Another important factor has been the growth of the European economy, which has led to an increase in both business and leisure travel. With more people travelling for work and pleasure, the demand for air travel has increased [1], [2].

Such an intensive increase in the popularity of air transport and its availability forced the regulation of issues related to aviation safety. Every year, more and more standards and authorities are created to determine whether a given aircraft or airport is ready to perform air operations, in particular in difficult weather conditions. Various types of aviation agencies, global, European, and Polish, require inspection of individual devices located at the airport, which are part of the critical infrastructure [3], [4]. Figure 1-1 shows a view at runway 28 at the Poznań–Ławica Airport with visible airfield ground lightning (AGL).

Figure 1-1 View at runway 28 at the Poznań–Ławica Airport with visible airfield ground lightning (AGL)

Such a rapid and intense development of the civil transport aviation industry forces the development of new procedures and safety standards. For this reason, various national and multi-country aviation safety agencies are established and establish standards necessary to ensure safe aviation operations.

As part of improving security in the airport area, there are many types of vision systems implementation on which this work puts emphasis. This may include, among others, the terminal and passenger safety inspection in the event of pandemic threats (such as detecting anti-virus masks [5]), but also monitoring the flow of people, for example, using density maps [6] to improve the speed and quality of service. Another aspect may be the inspection of the safety of passengers and their luggage, as well as the detection of intrusion into the airport premises, into the restricted zone.

In this work, the operational inspection of manoeuvring areas (aerodromes) was primary focus. Aerodrome is a specifically designated area on land, which includes all associated buildings, installations, and equipment, intended for use, entirely or partially, for the arrival, departure, and movement of aircraft [3]. Such expansion was necessary due to the scope of work being carried out, but also due to scientific cooperation with the Poznań–Ławica Airport, which defined its goals and expected their implementation in a systemic manner. For this reason, detection, e.g., intrusion of people or vehicles onto the runway, is excluded, and is focused only on manoeuvring areas such as the runway, taxiways, and aprons or ramps. This division of selected issues is illustrated in Figure 1-2.

Figure 1-2 Division of selected issues of video inspection at the airport area

While working on improving aerodrome safety, the emphasis was put on the operational readiness of the airport. Then, three most important aspects were distinguished that influence the improvement of the safety of air operations and are at the same time necessary for application at the airport. These aspects are as follows:

- Airport Runway Foreign Object Debris (FOD) Detection System
- Detection of airport horizontal markings
- Quality classification of airfield ground lighting.

Each of these aspects was thoroughly analysed in terms of currently available and used methods, and then, after consultations with experts, own innovative algorithms and solutions were proposed, which significantly improve the safety of air operations. Figure 1-3 shows investigated aspects of video inspection on aerodrome.

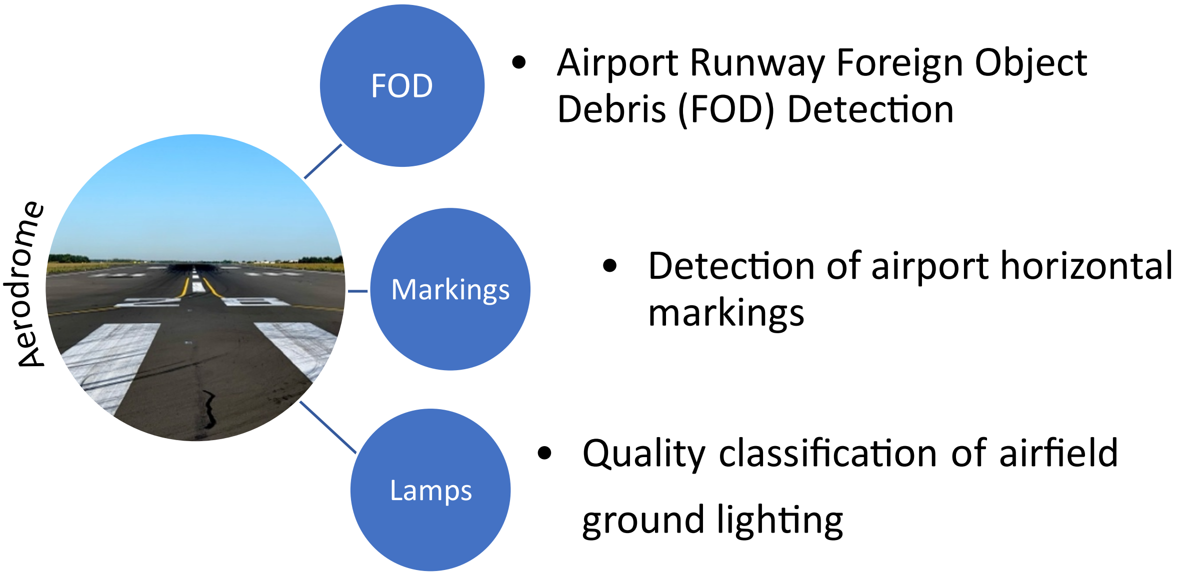

Figure 1-3 Investigated aspects of video inspection on aerodrome

Figure 1-4 shows the potential use of the algorithms developed in this doctoral thesis. Thanks to the use of a measuring platform, it is possible to inspect airport navigation lighting lamps. Their classification is carried out based on the vision system - classification of wear and based on colour and chromaticity sensors - determining the type of lamp and examining the colour of the light emitted by them. Thanks to the use of a camera at the front of the vehicle, it is possible to correctly maintain the driving track thanks to the detection of the centre line, as well as to detect dangerous FOD-type objects in the aerodrome while the vehicle is moving. In the vehicle, airport staff have a screen (HMI) informing about the proposed correction of the driving path, it also displays information about current and ongoing tests and displays appropriate warnings.

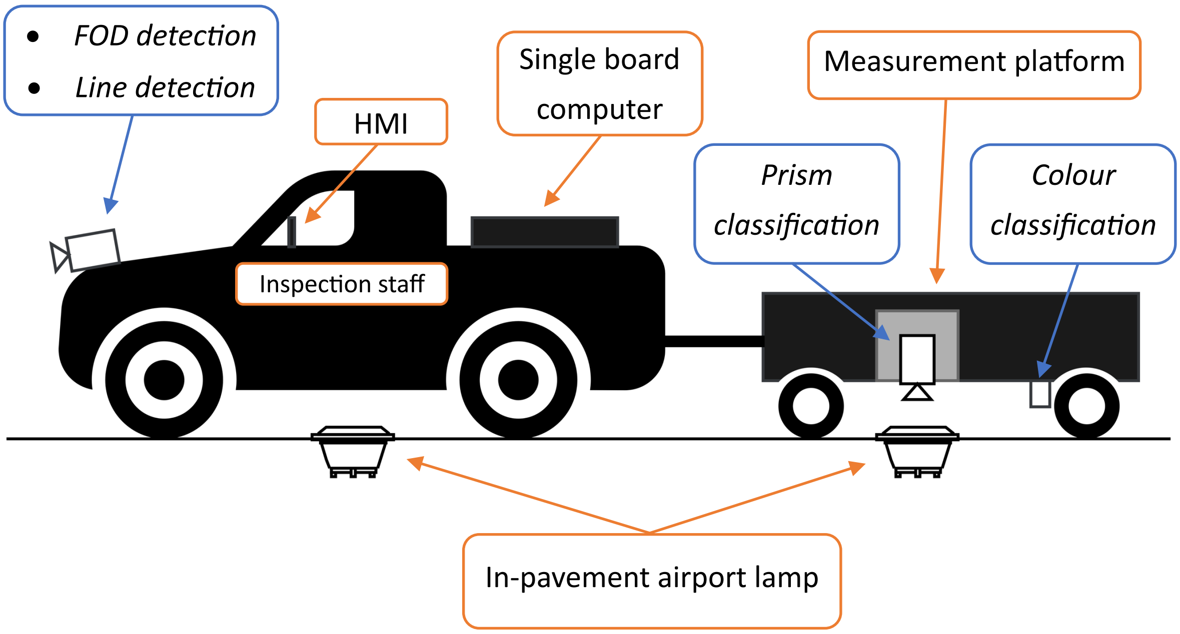

Figure 1-4 Concept of vision inspection system for aerodrome safety inspection

This thesis presents considerations and solutions that significantly improve the safety of aviation operations. For this purpose, innovative algorithms, optical sensors (such as cameras and light chromaticity sensors) and single board computers were used. It is thanks to the combination of these devices that it is possible to improve the detection of specific anomalies and inform the appropriate services about them. Additionally, the algorithms and systems created allow for the acquisition of additional data necessary for analytical research related to the consumption and inspection of lighting and navigation, as well as FOD contamination in critical areas of the airport.

All works and recommendations in this dissertation refer to the documents and regulations of three aviation security agencies. These are the European Union Aviation Safety Agency (EASA), the Federal Aviation Administration (FAA) and the International Civil Aviation Organization (ICAO). These organizations issue recommendations and necessary system certifications, ensuring world-class aviation safety. Poland, a member of the European Union, will be directly subject to the EASA regulations, which Polish airlines and airports must meet to obtain certification and maintain operational readiness.

When following procedures, the Safety Management System (SMS) for airports should be mentioned. It is a systematic approach to managing safety that integrates organizational structures, policies, procedures, and processes to identify, assess, and mitigate risks associated with aviation activities. The primary objective of an SMS is to improve safety performance by promoting a culture of proactive and continuous improvement within an airport environment.

The key components of an airport SMS typically include [7], [8], [9], [10], [11], [12]:

1. Safety Policy and Objectives: Establish a clear safety policy that reflects the airport's commitment to safety and define measurable safety objectives to guide safety performance.
2. Safety Risk Management (SRM): Identifying and analysing potential hazards and risks associated with airport operations. This involves assessing the severity and likelihood of risks and implementing measures to mitigate or eliminate them.
3. Safety Assurance: Implementing processes to monitor and evaluate the effectiveness of safety risk controls and ensure compliance with safety regulations. This involves regular safety audits, inspections, and performance monitoring.
4. Safety Promotion: Fostering a safety culture within the organization through communication, training, and awareness programs. This includes promoting the reporting of safety concerns and incidents without fear of reprisal.
5. Safety Reporting and Investigation: Establishing a reporting system for employees and stakeholders to report safety concerns, incidents, and hazards. Conducting thorough investigations to identify root causes and contributing factors.
6. Emergency Response Planning: Developing and maintaining plans and procedures to respond to emergencies and incidents promptly and effectively. This includes training personnel and conducting drills to ensure readiness.
7. Documentation and Record-Keeping: Maintaining comprehensive records of safety-related activities, incidents, and corrective actions taken. Documentation is crucial for auditing, analysis, and continuous improvement.
8. Safety Performance Monitoring and Measurement: Establishing key performance indicators (KPIs) to monitor safety performance and measuring progress toward safety objectives. This allows data-driven decision making and continuous improvement.
9. Management Review: Periodic reviews by top management to assess the overall effectiveness of the SMS, ensure compliance with safety policies, and identify opportunities for improvement.
10. Implementing an SMS is often a regulatory requirement for airports to improve safety and align with international aviation standards. It provides a structured framework for managing safety risks, learning from incidents, and continuously improving safety performance within the airport environment.

Both the International Civil Aviation Organization and the European Union Aviation Safety Agency have established guidelines and regulations regarding Safety Management

Systems for airports to ensure a standardized and effective approach to aviation safety [7], [9], [11].

ICAO's Annex 19 to the Convention on International Civil Aviation provides the international standards and recommended practices for the implementation of an SMS. Here are some key elements [7], [9]:

- ICAO requires Contracting States to establish a State Safety Program (SSP) that includes an SMS for service providers, including airports. The SSP should define the State's safety objectives, safety responsibilities, and the overall regulatory framework for safety.
- The "Safety Management Manual (SMM)" provides guidance specifically for the implementation of SMS in civil aviation, including airports. It outlines the key components such as safety policy, risk management, safety assurance, and safety promotion.
- Risk Management: ICAO emphasizes the importance of a systematic approach to risk management, including the identification of hazards, risk assessment, and the implementation of risk controls.
- Safety Assurance: This involves establishing processes to monitor and evaluate the airport safety performance and ensure that corrective actions are taken as necessary.
- Safety Promotion: ICAO encourages the promotion of a positive safety culture within the organization, emphasizing the importance of communication, training, and reporting systems.

EASA, as the European regulatory body, has its own regulations and guidelines related to SMS. The EASA regulations are applicable to European Member States and the entities falling under their jurisdiction. Key elements include [11]:

1. This regulation establishes the common rules in the field of civil aviation and creates EASA. It includes requirements for SMS implementation at the organizational level.
2. EASA has specific regulations for airports under the Aerodromes Regulation (Part-ADR), which includes requirements related to the implementation of SMS at airports.
3. Risk-Based Oversight (RBO): EASA emphasizes a risk-based approach to oversight, meaning that regulatory oversight is proportionate to the level of risk associated with the activities of the organization.

4. Performance-Based Regulation: EASA focuses on performance-based regulations, allowing organizations flexibility in achieving safety objectives while maintaining a high level of safety.
5. Airports operating within the European Union must comply with EASA regulations, including those related to SMS, to ensure a harmonized and consistent approach to safety management.

Both ICAO and EASA provide comprehensive guidelines and regulations to ensure the effective implementation of Safety Management Systems at airports, promoting a proactive and risk-based approach to aviation safety.

As mentioned earlier, the main scientific fields of this doctoral dissertation are the inspection issues of the aerodrome using optical sensors, with particular emphasis on detection of foreign object debris, detection of airport ground markings (such as taxiway and runway centre lines) and quality inspection operation and quality classification of the airfield ground navigation lighting system.

Moreover, the dissertation responds to the needs identified by EASA in relevant documents [13], which outline a human-centric approach to integrating AI in aviation. It emphasizes AI's potential to enhance safety, efficiency, and innovation in aviation while addressing challenges such as public confidence, certification, ethical integration, and staff competency. The roadmap builds on the trustworthiness of AI, guided by EU AI regulations, and sets high-level objectives and actions to ensure safe AI deployment in aviation, focusing on collaboration between stakeholders to achieve these goals.

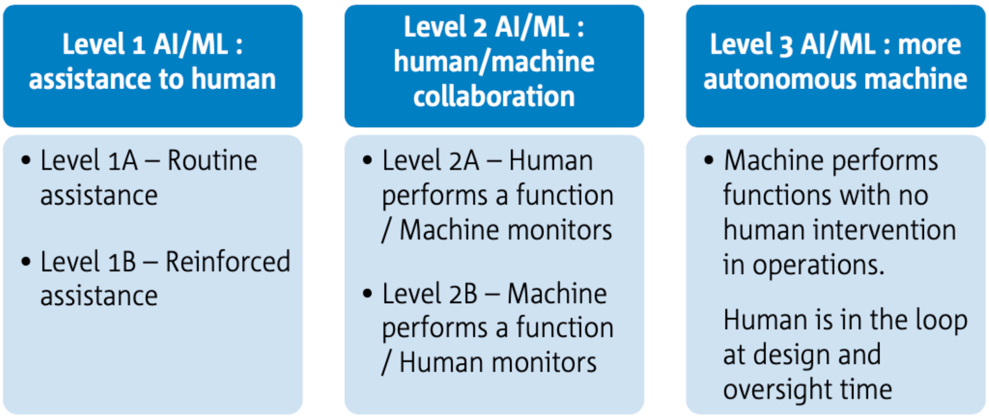

Figure 1-5 Classification of AI applications [13]

The developed algorithms particularly support Level 1 and 2 (Figure 1-5) as specified in [14]. For Level 1 AI, the end user makes all decisions with the aid of an AI-based system, and the end user is responsible for carrying out all actions. Level 2 AI-based systems can autonomously select and execute actions, yet the end user retains full oversight and the ability to override the system's functions at any time. At Level 2, decisions can be made either by the end user or automatically by the AI-based system under the user's supervision and guidance [14].

The research carried out while working on the doctoral dissertation was related to the following scientific projects:

1. Smart4All (Horizon 2020 framework under call DT-ICT-01-2019: Smart Anything Everywhere – Area 2: Customized low energy computing powering CPS and the IoT; Grant Agreement No 872614; 0211/PRKE/6428; 1.07.2020 – 31.12.2023) - The project aims to revolutionize urban living by integrating advanced technology into various aspects of daily life. Leveraging the power of IoT (Internet of Things) devices and AI (Artificial Intelligence), Smart4All seeks to create smarter, more efficient cities that enhance the quality of life for residents while promoting sustainability and resource optimization. One key aspect of the Smart4All project is the development of interconnected smart infrastructure, including smart grids, smart transportation systems, and smart buildings. These systems will enable real-time monitoring and management of energy consumption, traffic flow, and building operations, leading to reduced costs and environmental impact. Additionally, the project focuses on enhancing public services through digitalization and automation.
2. Inkubator Innowacyjności 4.0 (0614/MNSW/2948; 1.02.2021 – 31.01.2023) - The program enhances initiatives promoting scientific achievements, augments their impact on innovation development, and intensifies collaboration between the scientific community and the business environment. The need for the development of these aforementioned skills is also underscored by the European Commission within recommendations for National Reform Programs, as well as by the Committee of Scientific Policy, the Main Council for Science and Higher Education, the Conference of Rectors of Academic Schools in Poland, and organizations representing employers in Poland. Actions aimed at enhancing the skills of employees in scientific institutions and businesses in the management of scientific research, collaboration with businesses, and the commercialization of R&D results are therefore strategic from the socio-economic development perspective of the country.
3. Investigation of Algorithms Supporting Positioning of a Mobile Measuring Device for the Inspection of Airport Runway Lighting Surfaces (0211/SBAD/0522; 1.01.2022 – 31.12.2022) – Project as part of a competition for conducting scientific

research by young scientists financed in an internal competition mode at the Faculty of Control, Robotics & Electrical Engineering at Poznań University of Technology. The project enabled research such as comparative analysis of camera parameters for processing vision sequences using embedded devices, analysis of the use of single board computers, development of a module enabling fast and precise measurement of light intensity within in-pavement lamps of navigational lighting, and preparation of a concept for a supporting system for approaching and inspecting an in-pavement airfield ground lighting (AGL) lamp chromaticity, based on an embedded system.

4. Detection of Events Using Vision Monitoring and Artificial Intelligence (0211/SBAD/0920; 1.01.2020 – 31.12.2020) – Project also as part of a competition for conducting scientific research by young scientists financed in an internal competition mode at the Faculty of Control, Robotics & Electrical Engineering at Poznań University of Technology. Aimed to prepare datasets of recorded vision sequence and analyse segmentation and detection algorithms for application in embedded systems. The selection and training of neural networks was performed on previously prepared data.

1.1.1. Foreign Object Debris

The first of the security elements discussed in this work will be Foreign Object Debris (FOD) detection which is a major safety concern in the aviation industry and has the potential to cause significant damage to aircrafts and endanger the lives of passengers and crew members [15]. FOD refers to any object or debris that is present on airport runways, taxiways, or aprons, which can cause damage to aircraft components, such as engines, landing gears, or fuselages. The presence of FOD poses a significant safety risk to aircrafts and can cause delays and cancellations, as well as costly repairs and maintenance [4].

The most famous and tragic accident caused by FOD is the Concorde Air France flight 4590 plane crash. This plane accident took place on July 25, 2000 near Paris. The Concorde aircraft, accelerating on the runway of Charles de Gaulle Airport, ran at high speed (approx. 300 km/h) with its main landing gear wheel onto a strip of metal (Figure 1-6) - an engine structural element that had fallen off from the McDonnell Douglas DC-10 aircraft that had previously taken off.

Figure 1-6 Example FOD, the metal strip suspected of piercing the Concorde tyre [16]

The aviation industry is projected to suffer a financial loss of $4 billion annually, as reported in [17]. Aircraft accidents caused by FOD are a very serious threat. The main threat caused by the presence of unwanted objects on the runway is engine damage due to absorption of FOD elements, destruction of tyres or damage to the aircraft structure and reduced efficiency. Furthermore, damage to the aircraft may disrupt the proper operation of the airport, leading to loss of revenue. Airplane engines are a sensitive structural element of the aircraft, so they are susceptible to any type of objects. If they hit a running engine, they can damage rotating blades or other parts of the engine. As a consequence, this may lead to a reduction in engine efficiency, leading to a plane crash [18]. One such incident was the 2009 incident involving an Airbus A320-214 on the Hudson River. The passenger jet lost thrust in both engines due to wild geese being engulfed in the engines shortly after take-off.

Another danger is tyre damage. In some cases, FOD may result in tyre tread separation, which may cause damage to parts of the aircraft or even disruption to other aircraft scheduled to take off or land on the same route [19]. Since the Concorde disaster, FOD detection has become a priority security measure at airports.

Areas such as the fuselage, wings, and windshield can also be damaged by FOD. Damage to the aircraft structure causes aerodynamic loss. If the nose of the plane is damaged, it can damage the radar system, leading to false readings and complicated problems. Another messy effect caused by FOD may be the disruption of normal airport operations. When an aircraft is damaged on the runway, it causes delay or cancellation of the flight and financial losses.

In its reports, the FAA divides the FOD by origin as follows [20]:

- aircraft parts (fuel caps, landing gear fragments, oil dipsticks, metal sheets, nuts, bolts, washers, steel wires, doors and tyre fragments)
- airline items and catering supplies (garbage such as bottles, papers, plastic, drink cans left by passengers or ground handling staff, staff badges, pens, pencils, baggage tickets, pieces of luggage)
- natural materials (parts of plants and wild animals, stones, sand, and gravel)
- weather pollution (includes icing, snow, hail, rain and other atmospheric phenomena that may affect airport surfaces and pose a threat to aviation operations).

Figure 1-7 shows damage to aircraft caused by FOD objects. Figure 1-7a shows the damaged fan blades of the Pratt & Whitney JT8D engine after a bird collision, while Figure 1-7b shows the crash of the Concorde plane, in which a metal element on the runway punctured the tyre while gaining speed, which caused damage to the fuel tank located in wing and a fuel leak, causing the machine to burst into flames. Image Figure 1-7c shows damage to the skin of a Singapore Airlines Boeing 747-400F aircraft caused by stones on the runway.

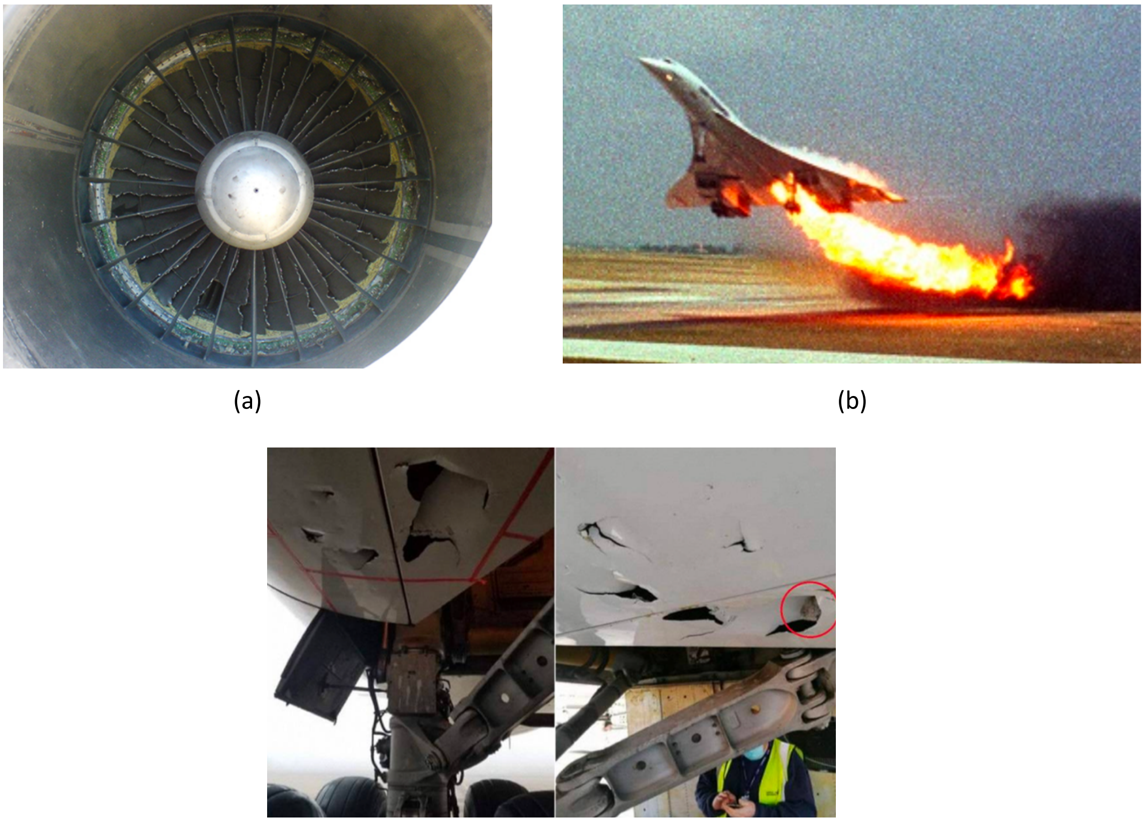

(a)

(b)

(c)

Figure 1-7 Damage caused by FOD objects [21]: (a) Pratt & Whitney JT8D engine, (b) Concorde Air France flight 4590, (c) Singapore Airlines Boeing 747-400F

In spite of the airport authorities and maintenance staff's attempts to reduce the chances of Foreign Object Debris, incidents still happen too often. This emphasizes the urgency of new and creative methods to detect and prevent FOD, all aimed at protecting both aircrafts and passengers. Worldwide airline agencies established a set of guidelines and rules to reduce the risk of FOD around airports and aircraft.

The types of FOD facilities vary greatly. They can be classified in many ways in terms of type and origin. The element can be made of any material and have any colour and size. In a study conducted at an airport over a year, more than 60% of the known FOD items collected were made of metal, and 18% of the items were made of rubber, while dark items accounted for almost 50% of the FOD collected [22].

Figure 1-8 shows objects found during a FOD walk on the runway of the Ramstein Air Base in Germany [23].

All of the debris on this page was found on the flightline of Ramstein Air Base, Germany, during FOD walks.

Figure 1-8 FOD found during a FOD walk on the runway of the Ramstein Air Base in Germany [23]

For this reason, it was so important to build a dataset, design an algorithm, and launch a system that can be used by services responsible for maintaining the operational readiness of the airport to automatically detect FOD objects on airport surfaces. The tests and verification of the necessary tools were carried out in close cooperation with the Poznań–Ławica Airport.

This dissertation introduces a novel, cost-efficient strategy for Foreign Object Debris (FOD) detection, employing a vision system operable by airport personnel. The concept of the system integrates an embedded system deployable in airport service vehicles traversing manoeuvring areas. Real-time analysis of camera-captured images is conducted utilizing sophisticated image processing algorithms, accurately discerning and pinpointing foreign objects across runways, taxiways, or aprons. By providing immediate and precise information on debris location and type, the system allows airport personnel to promptly mitigate FOD, thereby diminishing safety hazards and mitigating operational disruptions.

The dissertation delineates the design and implementation of the vision FOD detection system and evaluates its efficacy within an actual airport setting. Comparative analyses with alternative FOD detection methodologies are conducted to assess the system's effectiveness and cost-efficiency. Additionally, the potential ramifications of the system deployment on airport safety and operations are deliberated. Overall, the proposed vision FOD detection system presents a promising avenue for FOD detection and prevention, poised to significantly enhance airport safety and operational efficiency.

1.1.2. Airport horizontal markings

The next issue related to aviation safety is the detection of horizontal markings on airport manoeuvring areas. The validity of markings and lines detection can be divided into two aspects. On the one hand, detecting a line may mean improved readability and visibility. This means that the markings, especially on the runway, are in good condition and it is not necessary to remove the rubber or repaint them. The second aspect is, thanks to the precisely defined distance and location of the lines (Figure 1-9), enabling precise inspection of systems checking important operational elements of the airport.

Due to the development of a system in the form of a measurement platform for testing navigation lighting, it was necessary to develop software to support the operator/driver while moving around ground surfaces. Thanks to this, it is possible to conduct a lighting study with minimal occupation of critical points of the airport, such as the runway or taxi routes. Moreover, a correct and repeatable measurement can provide important information for research on the maintenance of lamps and their wear rate as well as reliability. Detection and inspection of the correct operation of navigation lighting may be critical in the event of an accident or unsuccessful landing, which may determine the safety of air operations and be of interest to services responsible for air transport safety. Figure 1-9 shows the view from the platform for quality testing of airport lamps during the lighting inspection. The location of the lamp over such a large area, without reference points in the form of the runway edge or other characteristic objects, is possible only based on the detection of centre lines.

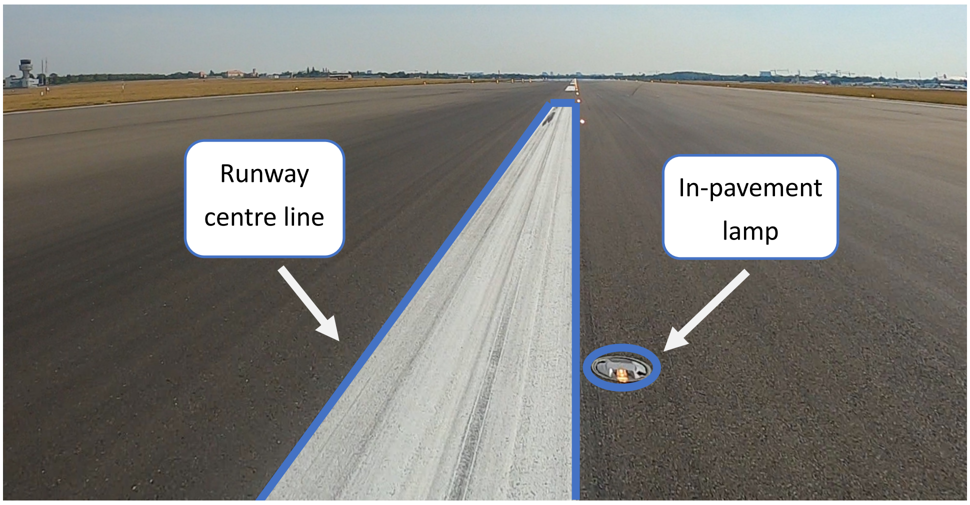

Figure 1-9 Example frame from the video sequence (runway centre line—white, runway centre line lamp—white)

The constantly growing requirements of aviation agencies regarding flight safety have for several years been determining more and more precise inspection of lighting located in various airport areas, especially on runways and taxiways [4]. The essence of investigating the operational efficiency of aviation navigation lighting, based on the Certification Specifications and Guidance Material for Aerodrome Design (CS-ADR-DSN) of the European Union Aviation Safety Agency (EASA) [4], lies in understanding the intricate interplay of factors influencing the degradation of lamps and the critical importance of their monitoring in aerodrome environments.

A medium-sized airport has about 200 central axis lamps in white and red and about 180 touchdown zone lamps. However, there are many more light points on taxiways. Importantly, each lamp must meet the standards specified in the documents on the basis of which permits are issued for the ongoing operation of the airport. Typical airport lamps are equipped with halogen bulbs, which have a limited lifetime [24]. Lamps deteriorate over time due to various mechanisms, including filament evaporation, electrode wear, and phosphor degradation (in the case of fluorescent lamps), leading to diminished luminous output and alterations in spectral characteristics. Environmental factors such as temperature fluctuations, humidity levels, and electrical irregularities can exacerbate this degradation process. Also, the sticking of rubber from tyres of landing aircraft to the heated prisms of halogen lamps significantly reduces the light efficiency of navigation lighting. Nowadays, airports are forced by demanding safety rules to gradually upgrade lighting systems to ones based on LED light sources. The light emitted by such bulbs has characteristics different from those of halogen bulbs [25], and this causes the need to prepare a measuring system that can be adapted to work with different light sources. The degradation of lamps can significantly impact the performance of navigational lighting systems, potentially compromising visibility and impeding safe air navigation within the system.

Lamp monitoring is essential to maintain the operational efficiency and safety of navigational lighting installations. Regular inspections and maintenance procedures are essential to ensure that lamps adhere to the prescribed luminance levels, colour fidelity standards, and spatial distribution requirements outlined in regulatory frameworks such as CS-ADR-DSN [4]. Deviations from these standards can pose serious risks to aviation safety, as inadequate lighting conditions can hinder pilots' ability to accurately perceive runway boundaries, approach paths, and other critical visual cues during take-off, landing, and taxiing procedures. Moreover, inconsistent or degraded lighting can impede ground personnel's ability to conduct aircraft operations safely, exacerbating the potential for accidents or incidents within the aerodrome environment.

Furthermore, comprehensive maintenance and monitoring practices are essential to optimize the lifespan and cost-effectiveness of navigational lighting systems. Proactive measures such as routine lamp replacements, cleaning, and recalibration help mitigate the effects of degradation and ensure that lighting installations remain reliable and compliant with regulatory standards over time.

Various mobile systems have been investigated to measure the technical condition of airport lamps [26], [27]. An exemplary solution is presented in Figure 1-10 [28], [29]. Such systems require precise driving of the measuring device onto the tested lamp. It is quite important because very often, incorrect hovering on the lamp or its omission misclassifies the obtained results, which increases the time and cost of the inspection process.

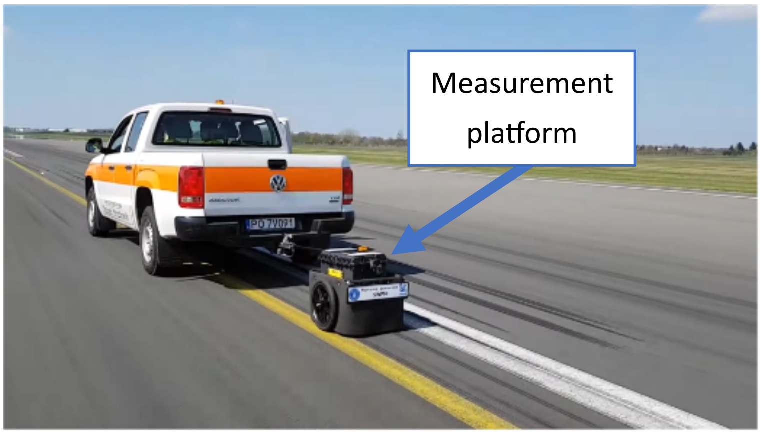

Figure 1-10 First prototype of author’s measurement platform for testing the quality of the operation of airport lamps [30]

An essential aspect of the testing process involves providing feedback to the driver or operator, allowing them to understand the adjustments needed to maintain the correct angle and trajectory on the lamps. This feedback is particularly crucial when conducting manoeuvres on extensive surfaces like runways, where significant reference points are lacking and a continuous centre line is absent, presenting a formidable challenge. The airport testing revealed that this is a highly time-consuming task that requires an individual to monitor the platform and communicate the necessary manoeuvres to the driver. Testing lamps at runway exits, where the lamps are positioned at various angles, posed particular difficulties.

Therefore, this aspect puts emphasis on the analysis of the driving path by detecting and predicting the presence of runway centre lines and taxiways. By analysing the centre lines, the algorithm aims to predict the probable location of the airport navigation lighting in-pavement lamp, allowing the operator to accurately select the optimal path for an efficient and meaningful study. When designing the platform for testing the performance of airport lighting, the author gave priority to its versatility and availability. Action cameras were used in this study due to their ability to stabilize images and capture footage of acceptable quality while withstanding various environmental conditions (such as changing weather or low light). The use of a measurement platform introduces particular challenges in maintaining the correct trajectory, especially on long straight sections where there are no fixed reference points or continuous centrelines, as well as on curves where the driver or operator cannot directly observe the exact path of the measurement platform behind the vehicle.

1.1.3. Aeronautical ground lighting

Airfield ground lighting (AGL) is an essential component of aircraft operation and play a critical role in ensuring the safety of all aircraft in the vicinity [31]. These lights are required to be operational at all times and are used to identify the location and movements of aircraft, both during the day and at night [4]. Aeronautical ground lighting systems are mandated to be operational whenever necessary for the regulation and management of air traffic and other times, depending on meteorological conditions, their activation is deemed essential for ensuring the safety of air traffic operations [32].

One of the most important uses of navigation lights (Figure 1-11) is during take-off and landing, when the aircraft are operating at low altitudes and in close proximity to each other. During these phases of flight, navigation lights are used to help pilots identify other aircraft in the vicinity, and to make informed decisions about the movements of their own aircraft [33]. For example, when approaching an airport for landing, pilots rely on the navigation lights of other aircraft to help them determine their own position and altitude relative to the runway [31].


(a) (b) (c)

Figure 1-11 In-pavement airport lamps [30], [28]: (a) factory new, (b) worn housing but prism in good condition, (c) worn housing and prism

In addition to helping pilots navigate the airspace around an airport, navigation lights also play a critical role in ensuring the safe movement of aircraft on the ground. This is particularly true for in-pavement lighting, such as runway and taxiway lights [33]. These lights are designed to help pilots navigate the airport's surface and to maintain correct alignment with the runway during take-off and landing.

Runway and taxiway lights are typically divided into several categories, including centre line lights, edge lights, and threshold lights. Centre line lights are used to help pilots maintain the correct alignment with the runway centre line, while edge lights are used to define the edges of the runway. Threshold lights, on the other hand, are used to indicate the point at which an aircraft should begin its take-off or landing roll [4].

In addition to these standard runway and taxiway lights, there are also a number of other in-pavement lighting systems that are used at airports to help pilots navigate the surface. For example, some airports use visual docking guidance systems (VDGS) to guide aircraft to their designated parking stands. These systems use a combination of lights and markers to provide pilots with precise guidance during the taxiing and parking phases of the flight [4].

Overall, navigation lights and in-pavement lighting systems are an essential component of aircraft operation and play a critical role in ensuring the safety of all aircraft at an airport. Whether helping pilots navigate the airspace around an airport or guiding them to their designated parking stands, these lights are an essential tool for ensuring the safe and efficient operation of aircraft.

In-pavement lamps in the navigation lighting system lose their properties for several reasons. The first and most devastating is the winter action taking place at the airport, i.e. the need to maintain the operational readiness of the airport even during heavy snowfall. During this period, the runway and taxiways are cleared of snow by specialized plows. Unfortunately, due to the use of metal brushes that destroy, dull and permanently damage the prisms, it is necessary to constantly check the navigation lighting lamps. Especially those located on the runway, such as the touchdown zone or the centre line [34].

The disparities in luminous intensity values between new and used lamps vary from several hundred to several thousand lux, depending upon the emitted light's colour and distance from the source. Similar variations may arise due to improper installation or inadequate testing procedures, potentially misclassifying a new lamp as worn in the results. Technical documentation outlining the airport design process specifies precise luminous intensity standards denoted in candelas. This unit serves as a benchmark against which obtained results should be compared, necessitating the conversion of sensor readings each time. Figure 1-11a depicts a new lamp, serving as a reference point, alongside its prism (Figure 1-12a), for assessing the wear of other lamps in use at the airport. The degradation of the lamp housing (Figure 1-11b) does not necessarily correlate with damage to the prisms (Figure 1-12 b, c). Notably, superficial scratches on the housing's upper surface do not impair the lamp's functionality, as its prisms remain largely unaffected, similar to those in new lamps. However, Figure 1-11c illustrates a lamp that, while appearing minimally damaged, exhibits a metal edge near the prism's apex, indicating damage incurred during operation. Such deformations compromise the prism's glass integrity (Figure 1-12d), rendering it scratched, chipped, and dim, warranting lamp replacement.

(a) (b) (c) (d)

Figure 1-12 Prisms of in-pavement lamps [30]: (a) new, (b-c) suitable for further use, (d) to be replaced

Another factor is the use of halogen bulbs or colour filters in some types of lamps, which have a limited lifespan, and, due to dynamic conditions of use, their daily inspection is necessary. The efficiency of in-pavement airport navigation lighting is also significantly limited by tyre rubber deposits left on the runway, particularly on the lamps and prisms during landing. The high temperatures of the lamps cause the rubber to adhere to the prisms, reducing their effectiveness. This rubber accumulation also impacts aviation safety and runway surface friction. The U.S. Federal Aviation Administration advises weekly inspections for rubber deposits on runways with 210 or more daily landings, while runways with fewer than 15 daily landings require annual inspections [35]. Airports must remove rubber deposits using suitable chemical or mechanical methods when necessary.

Airfield ground lighting is an essential component of critical infrastructure, playing a key role in maintaining the safety and continuity of aviation operations. As part of this critical infrastructure, any malfunction or disruption in AGL systems may result in severe operational delays and pose risks to national security by undermining air traffic management. Testing in-pavement lamps, such as runway and taxiway lights, is an important aspect of ensuring the safe operation of aircrafts at an airport. The International Civil Aviation Organization [36] and the European Aviation Safety Agency [4] have established standards and procedures for testing these lights, which vary depending on the type of lighting system and the category of instrument landing system (ILS) in use.

According to ICAO standards, in-pavement lamps must be tested at regular intervals to ensure that they are operating correctly and providing the necessary level of illumination for safe aircraft operation. The frequency of these tests is determined by the category of ILS in use at the airport [3]. ILS is a ground-based navigation aid that provides precise guidance to aircraft during the approach and landing phases, particularly in low-visibility conditions.

The ILS consists of two main components [32]:

- Localizer (LOC): The localizer provides horizontal guidance, ensuring that the aircraft is aligned with the centre line of the runway
- Glide Slope (GS): The glide slope provides vertical guidance, assisting the aircraft in maintaining the correct descent path for a safe landing.

Pilots use the ILS information displayed on cockpit instruments to make precise adjustments during their descent and approach to the runway, ensuring a safe and accurate landing [32].

For example, Category I ILS systems, which are used at airports with the highest minimum decision altitude (MDA) and the highest visibility requirements, require testing of in-pavement lamps every 90 days. Category II and III ILS systems, which are used in airports with lower MDA and visibility requirements, require testing every 30 days [36]. During testing, in-pavement lamps are checked for proper operation and alignment, and their output is measured to ensure that they are providing the required level of illumination. Any lamps that are found to be defective or out of alignment are repaired or replaced as necessary. In addition to regular testing, in-pavement lamps must also be checked before the start of each night's operation, and any defects must be corrected before aircraft can operate on the runway or taxiway.

EASA has similar regulations on the maintenance and testing of in-pavement lighting, the lighting system maintenance program must be in place and followed; this includes inspection, testing, and maintenance of all lighting systems, including in-pavement lighting [4]. The frequency of these inspections is determined by the criticality of the system, with more critical systems requiring more frequent inspections. Consequently, it is crucial to emphasize the robustness and redundancy of AGL systems to guarantee consistent performance, particularly during critical situations such as emergencies or adverse meteorological events.

It is important to note that the testing and maintenance of in-pavement lighting systems is typically performed by airport maintenance staff, who are trained to safely access the runway and taxiway areas, as well as to properly test and maintain the lighting systems.

In summary, testing of in-pavement lamps is an important aspect of ensuring the safe operation of aircraft at an airport, and it is carried out according to the standards established by ICAO and EASA. The frequency of these tests depends on the category of ILS in use, and the test includes checking for proper operation, alignment, and output to ensure that they are providing the required level of illumination.

1.2. Aim of work and scientific thesis

The research entails the design, selection, and training of deep neural networks, leveraging a highly curated dataset. This is combined with a computer vision framework to enable automated, real-time inspection of aerodrome environments for enhanced safety monitoring and assessment.

The objective of this work is an investigation and development of optimized preprocessing algorithms tailored for integration into diverse system architectures, with a specific focus on improving the quality and utility of input image data for classification-based models. The scientific task is to elaborate reliable algorithms and solutions for vision inspection using image processing and artificial intelligence to improve the safety of the aerodrome.

The detailed tasks can be formulated as:

- Development of vision algorithms for aerodrome inspection
- Preparation of video and image datasets according to new FAA standards
- Training of deep neural networks for fast runway video analysis
- Proposals of embedded systems implementations.

Particularly, the following problems were solved:

- Detection of Foreign Object Debris (FOD):
    - Preparation of new image dataset according to FAA regulations
    - Precise selection of the effective neural network architecture for FOD detection.
- Detection and evaluation of airport horizontal markings:
    - Preparation of new video dataset recorded in restricted airport area
    - Proposition of line detection algorithm using colour-based image segmentation in the HSV colour space
    - Comparison of the power requirements during real-time processing of video sequences in embedded systems
    - Energy efficiency and DVFS (Dynamic frequency scaling) analysis.
- Quality classification of airfield ground lighting:
    - Preparation of new image dataset with over 540 lamps and prisms
    - Conception of lamp and prism detection process
    - Selection of neural network for prism quality classification

  - Chromaticity inspection of airport navigation lighting lamps according to CIE 1931 and EASA standards.

Scientific thesis

On the basis of the performed research, the following scientific thesis can be formulated: *Proposed vision preprocessing methods, together with neural network solutions within the domain of embedded systems, substantially improve and facilitate the automated inspection processes at the airports*.

To experimentally check the effectiveness of the algorithms, a dataset of recordings and images recorded in restricted areas of the airport was created. This *PLAVS1* dataset consists of more than 98 GB of video recordings from airport manoeuvring areas (such as the runway, taxiways, and apron), *PLAVS2* with 1004 photos of airport navigational lighting in-pavement lamps and *PUT dataset* with 1480 FOD images. The dataset was consulted with experts from the aviation industry in order to actually present the most critical elements of the airport and their inspection.

The presented research was conducted in scientific cooperation with aviation specialist, especially from departments responsible for the airport's readiness to perform flight operations, such as the electrical power team or safety management manager. Thanks to this, it was possible to prepare datasets and check the systems in real conditions, on the runway, taxiways, and other ground surfaces. Consultations with airport representatives made it possible to adapt algorithms and solutions for efficient and reliable inspection of aerodrome, as well as to meet the requirements of national and international aviation authorities in a given area. As part of the Innovation Incubator 4.0 project, the Poznań University of Technology concluded an agreement on joint research with the airport (documents (PP)RU00021806 and 45/2022/RK), thanks to which it was possible to carry out research and tests of the proposed solutions and systems, as well as prepare datasets and consult with specialists. Figure 1-13 graphically shows the cooperation scheme between the Poznań–Ławica Airport and the Division of Signal Processing and Electronic Systems at Poznan University of Technology.

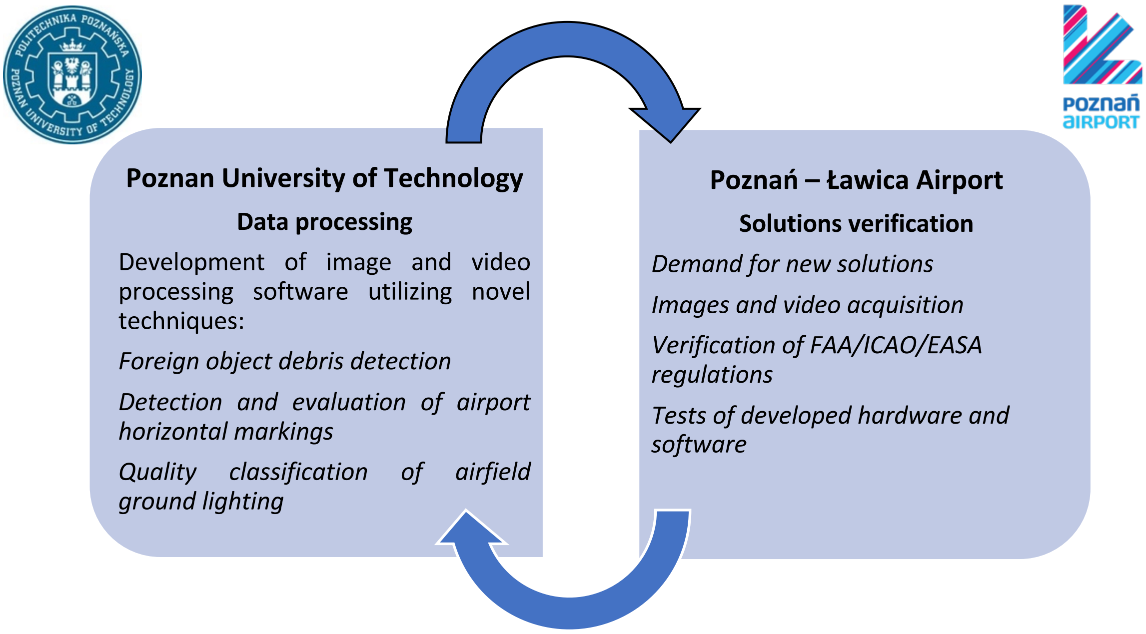

Figure 1-13 Scientific cooperation between the Poznań–Ławica Airport and the Division of Signal Processing and Electronic Systems from Poznan University of Technology

1.3. Main scientific achievements

As part of the work, the following scientific works were created, such as published papers in scientific journals, patents and reports in the subject of the dissertation:

	Foreign object debris detection
[37]	J. Suder and T. Marciniak, “Foreign Object Debris detection system using GoogLeNet,” Przegląd Elektrotechniczny, vol. 99, no. 11, pp. 251–254, Nov. 2023, doi: 10.15199/48.2023.11.47.
[38]	J. Suder and T. Marciniak, “Foreign Object Debris detection at aerodromes using YOLOv5,” in 2024 Signal Processing: Algorithms, Architectures, Arrangements, and Applications (SPA), Poznan, Poland: IEEE, Sep. 2024, pp. 66–71. doi: 10.23919/SPA61993.2024.10715612.
	Quality classification of airfield ground lighting
[28]	J. Suder, P. Maciejewski, K. Podbucki, T. Marciniak, and A. Dąbrowski, “Measuring Platform for Quality Testing of Airport Lamps,” Pomiary Autom. Robot., vol. 23, no. 2, pp. 5–13, Jun. 2019, doi: 10.14313/PAR_232/5.
[39]	J. Suder, K. Podbucki, T. Marciniak, and A. Dąbrowski, “Spectrum sensors for detecting type of airport lamps in a light photometry system,” Opto-Electron. Rev., vol. 29, no. 4, pp. 133–140, 2021, doi: 10.24425/OPELRE.2021.139383.

[40]	J. Suder, K. Podbucki, T. Marciniak, and A. Dąbrowski, “Intelligent vision system for quality classification of airport lamp prisms,” in 2022 Signal Processing: Algorithms, Architectures, Arrangements, and Applications (SPA), 2022, pp. 151–154. doi: 10.23919/SPA53010.2022.9927908.
[41]	J. Suder and T. Marciniak, “Fast Prototyping of In-Pavement Airport Navigation Lamp Prism Classification,” in 2023 Signal Processing: Algorithms, Architectures, Arrangements, and Applications (SPA), Poznan, Poland: IEEE, Sep. 2023, pp. 95–99. doi: 10.23919/SPA59660.2023.10274434.
[42]	J. Suder, K. Podbucki, and T. Marciniak, “Chromaticity measurement of airport navigation lighting using integrated colour sensor,” Opto-Electronics Review, vol. 31, no. 4. Polish Academy of Sciences (under the auspices of the Committee on Electronics and Telecommunication) and Association of Polish Electrical Engineers in cooperation with Military University of Technology, p. e147040, 2023. doi: 10.24425/opelre.2023.147040.
[43]	J. Suder, K. Podbucki, and T. Marciniak, “Raport z pomiarów fotometrycznych zagłębionych lamp oświetlenia nawigacyjnego drogi startowej Portu Lotniczego Poznań – Ławica,” Politechnika Poznańska, Poznan, Poland, r3335_2022, Aug. 2022.
Detection of airport horizontal markings	
[30]	J. Suder, K. Podbucki, T. Marciniak, and A. Dąbrowski, “Low Complexity Lane Detection Methods for Light Photometry System,” Electronics, vol. 10, no. 14, 2021, doi: 10.3390/electronics10141665.
[44]	J. Suder, K. Podbucki, and T. Marciniak, “Power Requirements Evaluation of Embedded Devices for Real-Time Video Line Detection,” Energies, vol. 16, no. 18, p. 6677, Sep. 2023, doi: 10.3390/en16186677.
[45]	Patent: A. Dąbrowski, T. Marciniak, K. Podbucki, and J. Suder, “Method for measuring the quality of operation of airport lamps and a measuring set for testing the quality of operation of recessed airport lamps,” P.442569, submitted 19.10.2022
Embedded systems for vision monitoring tasks	
[46]	J. Suder, “Parameters evaluation of cameras in embedded systems,” Przegląd Elektrotechniczny, vol. 98, no. 9, pp. 218–221, Sep. 2022, doi: 10.15199/48.2022.09.50.
[47]	J. Suder, “Possibilities of processing video sequences in embedded systems,” Przegląd Elektrotechniczny, vol. 98, no. 1, pp. 190–193, Jan. 2022, doi: 10.15199/48.2022.01.41.
[48]	K. Podbucki, J. Suder, T. Marciniak, and A. Dabrowski, “Evaluation of Embedded Devices for Real- Time Video Lane Detection,” in 2022 29th International Conference

	on Mixed Design of Integrated Circuits and System (MIXDES), Wrocław, Poland: IEEE, Jun. 2022, pp. 187–191. doi: 10.23919/MIXDES55591.2022.9838167.

Publications authored or co-authored, where the thematic focus does not have a direct correlation with the research addressed in the doctoral dissertation:

Publication details	
[49]	T. Marciniak, K. Podbucki, J. Suder, and A. Dąbrowski, “Analysis of Digital Filtering with the Use of STM32 Family Microcontrollers,” in Advanced, Contemporary Control, vol. 1196, A. Bartoszewicz, J. Kabziński, and J. Kacprzyk, Eds., in Advances in Intelligent Systems and Computing, vol. 1196., Cham: Springer International Publishing, 2020, pp. 287–295. doi: 10.1007/978-3-030-50936-1_25.
[5]	K. Podbucki, J. Suder, T. Marciniak, and A. Dabrowski, “CCTV based system for detection of anti-virus masks,” in 2020 Signal Processing: Algorithms, Architectures, Arrangements, and Applications (SPA), Poznan, Poland: IEEE, Sep. 2020, pp. 87–91. doi: 10.23919/SPA50552.2020.9241303.
[29]	K. Podbucki, J. Suder, T. Marciniak, and A. Dąbrowski, “Electronic measuring matrix for testing airport lamps,” Przegląd Elektrotechniczny, vol. 97, no. 2, pp. 49–53, Feb. 2021, doi: 10.15199/48.2021.02.12.
[6]	J. Suder, T. Marciniak, K. Podbucki, and A. Dabrowski, “Real-time density maps generation of moving objects using embedded systems,” in 2022 International Symposium ELMAR, Zadar, Croatia: IEEE, Sep. 2022, pp. 179–184. doi: 10.1109/ELMAR55880.2022.9899807.
[50]	T. Marciniak, K. Podbucki, and J. Suder, “Application of the Nucleo STM32 module in teaching microprocessor techniques in automatic control,” Przegląd Elektrotechniczny, vol. 98, no. 10, pp. 247–250, Oct. 2022, doi: 10.15199/48.2022.10.55.
[51]	K. Podbucki, J. Suder, T. Marciniak, W. Mańczak, and A. Dąbrowski, “Microprocessor-based photometric light intensity sensor for airport lamps quality testing,” Opto-Electronics Review, vol. 30, no. 4. Polish Academy of Sciences and Association of Polish Electrical Engineers in cooperation with Military University of Technology, p. e143396, 2022. doi: 10.24425/opelre.2022.143396.
[52]	K. Podbucki, J. Suder, T. Marciniak, and A. Dąrowski, “Influence of power supply on airport navigation lamps photometric test accuracy,” in 2023 Signal Processing: Algorithms, Architectures, Arrangements, and Applications (SPA), Poznan, Poland: IEEE, Sep. 2023, pp. 183–188. doi: 10.23919/SPA59660.2023.10274440.

[53]	K. Podbucki, T. Marciniak, and J. Suder, "Laboratory Assessment of In-Pavement Airport Lamp's Luminous Intensity Distribution," Appl. Sci., vol. 13, no. 24, p. 13242, Dec. 2023, doi: 10.3390/app132413242.

In the frame of scientific cooperation with Poznań–Ławica Airport, it was possible to complete an internship in the period from July 1, 2022 to September 30, 2022, during which research, calibration and implementation of a system for testing the quality of navigation lighting operation were carried out.

It is also worth mentioning the most important distinctions and awards received during scientific studies:

- Distinction of the work entitled: "Foreign Object Debris detection system using GoogLeNet" by the Scientific Committee of the 22nd National Electronics Conference as part of the "Young Scientists" competition in the thematic group Technical informatics and signal processing (15.06.2023).
- Distinction of the work entitled: "Microprocessor light intensity sensor for examining airport lamps" by the Scientific Committee of the 21st National Electronics Conference as part of the "Young science workers" competition in the thematic group Metrology (9.06.2022).
- Main Award of the Program Council of the Teleinformatics Forum and the Masovian Branch of PTI in the "Best substantive work" category for the project entitled: "Vision monitoring system for detecting wearing anti-virus masks based on learning deep neural networks" as part of the National Inter-university Young Masters Competition "Economic aspects of computerization countries, digital modernization of Poland" at the 27th Teleinformatics Forum (9.11.2021).
- Distinction of the work entitled: " Colour sensors in an application to detect the type of airport lights" by the Scientific Committee of the 20th National Electronics Conference as part of the "Young scientists" competition in the thematic group Optoelectronics and photonics (9.06.2021).
- Distinguished Graduate of Poznań University of Technology Medal. This prestigious award is granted by the Rector of Poznań University of Technology and the Medal Committee to recognize outstanding alumni of the University, 2019.
- Distinction from the Teleinformatics Forum Program Council in the category "Best Substantive Work," awarded by the Program Council of the Teleinformatics Forum in 2019, for the project titled "Platforma pomiarowa do badania jakości działania lamp lotniskowych". This award was granted in the "Best Substantive Work" category during the Young Masters Forum competition on "Economic Aspects of State Informatization"

as part of the "Digital Modernization of Poland" initiative at the XXV Teleinformatics Forum.
- The Rector's Graduation Medal of Poznań University of Technology for Outstanding Commitment to Activities Supporting the Student Community of Poznan University of Technology, 2019.
- The Dean's Award of the Poznań University of Technology Faculty of Computer Science for outstanding academic performance and exemplary conduct, 2019.
- First Prize in the IEEE 2019 "Diploma Thesis Competition," awarded by the IEEE Polish Section for the engineering thesis titled: "Platforma pomiarowa do badania jakości działania lamp lotniskowych".
- First Prize in the Competition for Outstanding Diploma Thesis in Full-time and Part-time Undergraduate or Graduate Studies in the Field of Production Technology and Organization of Services, awarded by FSNT NOT in Poznań in 2018. The award was given for the engineering thesis titled "Platforma pomiarowa do badania jakości działania lamp lotniskowych”.

As part of experimental work, many operating or currently being implemented devices were prepared. These are among others:

- A measurement platform for testing the quality of operation of in-pavement lamps in airport navigation lighting [28], [29], [30], [40], [41], [44], [45], [46], [47], [48]
- System for the chromaticity inspection of airport navigation lighting lamps [39], [42]
- Obstacle avoidance module in the autopilot of an autonomous measurement platform for continuously testing the load-bearing capacity of natural airport surfaces (BIZON) in cooperation with the Air Force Institute of Technology [54]
- System for laboratory inspection of in-pavement lamps in airport navigation lighting [51], [52], [53]
- System for checking the quality of operation of lamps in the airport navigation lighting approach system [42]
- Vision system for checking correctly worn anti-virus masks [5]
- Vision system for FOD detection [37], [38].

1.4. Organization of the thesis

The research presented in this thesis puts emphasis on vision inspection of aerodrome. As mentioned earlier, the emphasis was placed on 3 main research areas. For this reason, chapter 2. State of the art will present the most important issues in this area, present the current state of knowledge and the solutions used. At the beginning, the main issues, applicable standards and regulations on which this work was based were discussed. Next, image processing methods are presented, both using classical methods and those using neural networks and machine learning. Basic issues in the field of photometry and radiometry were also presented. The following sections present the single board computers and cameras used with them, along with their specifications and an overview of their possibilities. Additionally, the quality of cameras that can support this task is analysed. This chapter also presents methods for evaluating the proposed algorithms.

The chapter 3. Detection of Foreign Object Debris presents the prepared *PUT dataset* consisting of 1480 FOD type object images, corresponding to FAA recommendations. Then, the concept of the proposed system for detecting such objects for use at the airport is presented and discussed. In this research area, the results obtained using classical image processing methods (k-means) were compared with the fine-tuned neural networks such as GoogLeNet and YOLOv5. The MATLAB and Google Colab tools were used to solve the task.

Chapter 4. Detection of airport horizontal markings presents dataset prepared in the airport zone with limited access, such as runways, taxiways or other airport surfaces and service roads. The result was the preparation of a unique *PLAVS1* dataset consisting of 98 GB of video materials (more than 300 minutes) of recordings from areas with limited access. Then, the proposed solutions for detecting horizontal airport markings and the experimental results are discussed. The developed algorithm is presented and the effect of resolution on the obtained results is examined. Then, the possibility of running the selected algorithms on Single Board Computers is verified, and the energy consumption and energy efficiency are analysed.

The next, chapter 5. Quality classification of airfield ground lighting is divided into two main subsections. The first, vision classification of the airport navigation lighting system, presents the concept of assessing the wear of lamps based on the destruction and tarnishing of prisms installed in the lamps. The author's *PLAVS2* dataset, consisting of over 1000 photos of airport lighting system lamps with different wear, the algorithm for detecting lamps and determining their orientation, and then the classification of the prism using artificial neural networks, are discussed. The selection of neural networks and the possibilities of their use in the proposed system are precisely analysed. The second subsection presents the classification of lamps based on the colour of the light they emit. Thanks to this solution, it is possible to determine what standards a given lamp should meet (the colour determines its location and function, and thus the reference to the standard). Then, the concept of a system for inspecting the chromaticity of navigation lighting in accordance with the applicable standards is presented. The measurement distance was precisely selected and software for airport services was prepared.

Chapter

2. State of the art

2.1. Vision inspection of aerodrome

The research presented in this thesis puts emphasis on vision inspection of aerodrome. As mentioned earlier, the focus was on 3 main research fields. For this reason, this chapter will present the most important issues in this area, present the current state of knowledge and the solutions used.

2.1.1. Foreign Object Debris detection

The International Civil Aviation Organization (ICAO) and European Union Aviation Safety Agency (EASA) emphasizes the importance of implementing various procedures and practices to prevent Foreign Object Debris (FOD) at airports [3], [13], [14]. They recommend specific measures to ensure that foreign objects do not make their way onto critical areas such as runways, taxiways, and aprons. This includes establishing appropriate procedures and conducting regular inspections of these areas to detect and remove any foreign objects that might pose a threat to aircraft safety [3].

Similarly, the Federal Aviation Administration (FAA) in the United States has issued multiple recommendations aimed at mitigating the risk of FOD [15]. These recommendations include regular inspections of airport surfaces to identify and remove debris, ensuring that runways, taxiways, and aprons are clear of obstructions, and inspecting vehicles and equipment operating in these areas to prevent them from inadvertently introducing FOD.

In addition to these measures, aviation agencies underscore the importance of training airport personnel and aircraft crews to recognize and report FOD. Implementing a comprehensive FOD prevention program involves establishing a system for the quick and efficient identification and removal of FOD. Proper training and education of relevant personnel are crucial components of such a program, as they help to significantly reduce the occurrence of FOD and minimize potential damage to aircraft and ground equipment.

Addressing the issue of FOD detection requires reliable, fast, and effective solutions. Currently, many airports rely heavily on manual labour and human resources for FOD detection. To enhance the efficiency and accuracy of FOD detection, various advanced systems have been developed and implemented. Examples include the Tarsier Radar system from the UK, the FODetect system from Israel, the FODFinder system from the US, and the iFerret system from Singapore [55]. These systems utilize different technologies such as radar-based detection, optical camera-based detection, and multisensory fusion detection. Radar-based systems are particularly effective for detecting larger objects but may struggle with smaller items like nuts and rubber pieces. Conversely, while optical cameras can detect FOD, they are not typically used for this purpose. If the specific characteristics of FOD in optical images were leveraged for detection, it could greatly reduce FOD-related damage and improve runway utilization rates. Despite the use of optical images in the iFerret system, the detection performance for smaller objects remains suboptimal. Figure 2-1 shows the division of methods for detecting or removing FOD objects in aerodromes, where the focus is on the division according to the method of detecting the object.

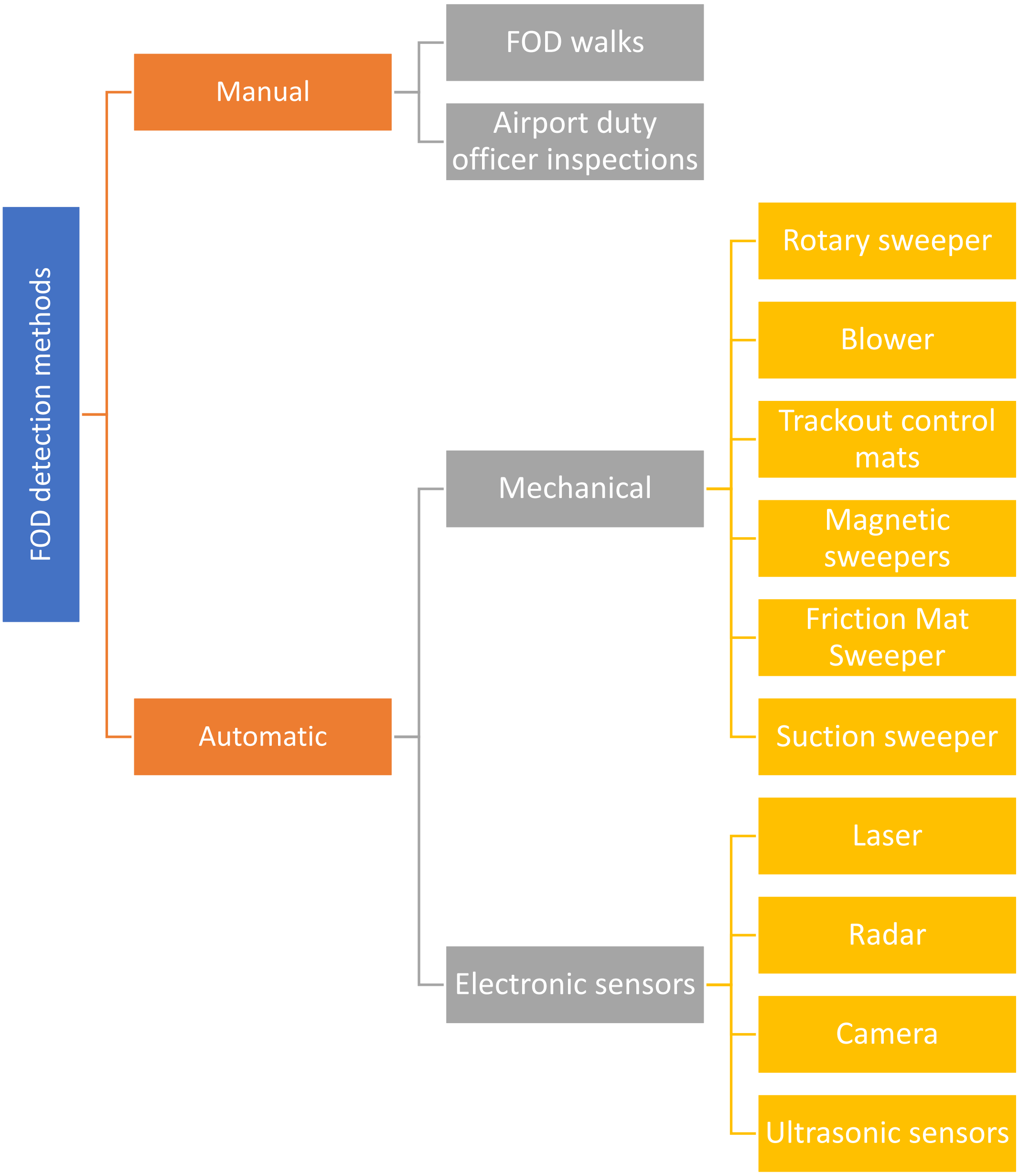

Figure 2-1 Division of methods for detecting or removing FOD objects in aerodromes

Recent years have seen growing interest in the development of advanced FOD detection technologies, including vision systems that use high-resolution cameras and sophisticated image-processing algorithms. These systems provide real-time information about the location and type of debris, allowing airport authorities and maintenance personnel to take immediate action to remove FOD and prevent potential safety incidents. Using vision systems, it is also possible to prevent other types of threats to aircraft, such as bird strikes, which are particularly dangerous during take-off and landing manoeuvres [56]. A comprehensive assessment of FOD detection methodologies can be articulated concerning their spatial resolution and area coverage, showed in Figure 2-2 [57].

Automatic FOD detection techniques using electronic sensors can be divided into four categories, namely ultrasonic sensors, camera detection, radar detection and hybrid detection methods, as in Figure 2-2. Laser systems are distinguished by their high resolution and medium coverage area. These systems offer precise and detailed detection capabilities, which makes them effective for identifying small objects. However, their limited coverage area indicates that they may not be optimal for larger airport environments requiring extensive surveillance. Radar systems exhibit moderate resolution, and a larger coverage area compared to laser systems. This characteristic makes them suitable for detecting objects over larger distances, although their moderate resolution may restrict their ability to accurately identify smaller debris. Camera systems, which are crucial to this analysis, provide a balanced combination of resolution and coverage area. They offer a relatively high coverage area while maintaining moderate resolution. This balance makes them advantageous for airport environments that require a broad surveillance with sufficient resolution to identify various types of FOD. The vision information provided by camera systems is a significant benefit, facilitating the easy identification and verification of detected objects. Ultrasonic sensors, located in the low resolution and low coverage area quadrants, are less suitable for extensive FOD detection in airports. Their limited range and resolution confine their use to smaller areas where detailed precision is less critical. Hybrid systems, situated in the quadrant of high resolution and high coverage area, represent the most comprehensive solution. These systems integrate the strengths of multiple detection technologies, offering extensive coverage with high-resolution capabilities. This makes them ideal for large and complex environments such as airports. However, the complexity and potential cost associated with hybrid systems may be higher than those of single-technology solutions.

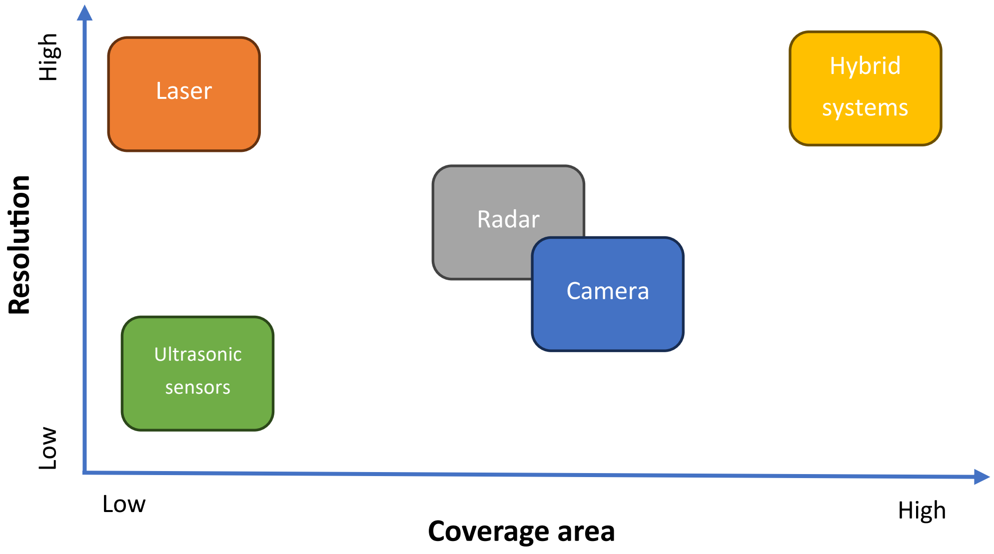

Figure 2-2 Evaluation of FOD detection methodology depending on coverage area and resolution [38]

Among the analysed solutions, FOD detection based on image analysis has been explored using datasets such as the Foreign Object Debris in Airports (FOD-A) dataset, which contains up to 2000 photos and several classes. For instance, one study [58] presents a solution that employs video-based image processing techniques to detect FOD on airport runways. This system uses a background subtraction algorithm to detect moving objects, followed by image processing techniques to classify them as FOD or non-FOD. Tested with a runway video footage dataset, the system achieved a detection rate of 96.67% and a false alarm rate of 5.26%.

Another innovative approach [59] involves the use of unmanned aerial vehicles (UAVs) combined with artificial intelligence (AI) to detect FOD on runways. This system utilizes an object detection algorithm based on the YOLOv3 model and a convolutional neural network (CNN) for FOD classification. Tested with UAV footage, the system achieved a detection accuracy of 94.5%.

Similarly, another study [60] utilized the YOLOv3 model for FOD detection on runways, employing transfer learning to fine-tune the model. This approach yielded a detection rate of 95.67% with high accuracy.

Furthermore, a system [61] using random forest classification was proposed to detect FOD in the data from optical imaging sensors. This system extracts features from image data and trains a random forest classifier to differentiate between FOD and non-FOD. The testing with a runway image dataset resulted in a detection rate of 93.1% and a false alarm rate of 5.5%.

Furthermore, a study [62] explores the integration of computer vision and UAV technologies for collecting images of FOD in airfields. The proposed system, which was tested using the FOD-A data set consisting of more than 19000 FOD images, demonstrated a detection rate of 95.2%. This approach has the potential to improve the efficiency and accuracy of FOD detection, thereby improving aviation safety.

2.1.2. Video based detection of airport horizontal markings

The task of detecting lines and lanes has seen significant development, primarily within the domain of Advanced Driver Assistance Systems (ADAS). Initially, ADAS were designed as passive systems that provide basic assistance without active intervention. However, with the advent of new technologies and tools, these systems have evolved to offer more advanced functionalities, transitioning from passive to active assistance. This evolution allows ADAS to perform complex tasks such as lane keeping, adaptive cruise control, and autonomous driving features [63].

Various types of horizontal markings, including multi-coloured lines and light navigation points, are utilized on ground surfaces to facilitate the proper execution of procedures required for air operations. These markings assist pilots in determining crucial elements such as the central axis of runways and taxiways, touchdown points, runway boundaries, and the aircraft's position relative to the runway's end. Despite advancements in onboard instruments, flight personnel continue to rely on visual cues and aids. Figure 2-3 presents a segment of a satellite image depicting the runway at Poznań–Ławica Airport.

Figure 2-3 Runway markings visible in the satellite image of the Poznań–Ławica Airport (Google Maps)

The primary markings crucial for the operator assist system are the runway centre line markings, represented by white stripes. These stripes are 0.9 meters wide, 30 meters long, and spaced 20 meters apart. Positioned along the runway axis, they serve as reference points for the measurement platform used to assess the performance quality of centre line lamps. Figure 2-4 provides an illustration of horizontal road markings on airport runways and taxiways, accompanied by descriptions.

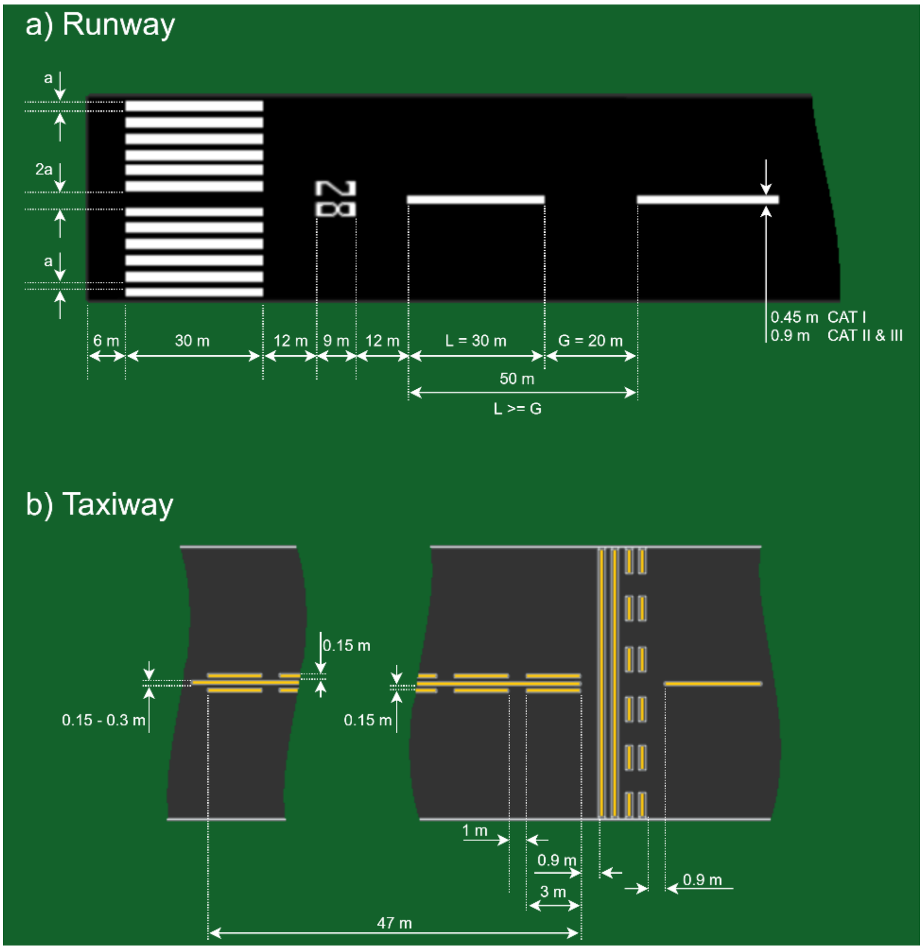

Figure 2-4 Basic horizontal markings on the runway (a) and taxiway (b) [30]

These markings are extensive and include both dashed and continuous lines, often appearing adjacent to each other. Their placement varies depending on the designation, indicating runway exits, holding points, stops, intersections, or hazardous areas. Despite their diverse functions, all markings adhere to strict descriptions and are uniformly coloured white and yellow. In cases where a marking lacks sufficient contrast with the pavement, a black outline is added. An important observation during testing and recording is the wear of airport markings caused by rubber deposits from aircraft tyres adhering to the surface. This wear significantly affects the visibility of horizontal signs and in-pavement light points.

The aspect of line detection remains a pertinent and actively researched area in scientific literature [64], [65]. Numerous algorithms and techniques have been developed to enhance the accuracy and reliability of line detection. Despite advancements, these methods can face limitations under certain conditions. For example, detecting lines on airport runways presents unique challenges that differ from typical roadway scenarios. The precision required for guiding measurement equipment, such as mobile measurement trailers used for assessing the light intensity of airport lamps, is significantly higher.

Under these specific conditions, traditional line detection algorithms may struggle to deliver the necessary accuracy and reliability. Environmental factors such as varying light conditions, weather changes, and the reflective properties of runway surfaces can all impact the performance of these algorithms. Therefore, specialized techniques are often required to ensure the precise detection of runway lines to facilitate the accurate measurement of airport lamp intensity [28], [29].

Recent studies and ongoing research continue to address these challenges, seeking to improve the robustness and precision of line detection algorithms in diverse and demanding environments. By refining these techniques, researchers aim to support critical applications that rely on accurate line detection, thereby enhancing the safety and efficiency of both automotive and aeronautical operations.

To effectively analyse the potential applications of vision inspection systems within a measurement platform designed to test the quality of airport lamp operations, it is crucial to segment the system into distinct areas of activity. Each area can benefit from different types of cameras tailored to specific inspection tasks. This makes it possible to optimize the inspection process and ensure accurate and efficient measurement of the performance of airport lighting.

As highlighted in the Introduction, the task of detecting lines and lanes has primarily been developed for vehicles navigating standard roadways. A variety of methods and algorithms have been created for this purpose, each with its unique approach to road detection. These methodologies predominantly emphasize road models, edge detection, vanishing point detection, colour segmentation, and the Hough transform. There are numerous variations and combinations of these methods. According to the paper [66], the Hough transform combined with basic image processing remains one of the most robust techniques. This algorithm for detecting road boundaries fundamentally relies on edge detection. When applied to the relatively small markings on typical car roads, additional processing to achieve a bird’s eye view is quite beneficial. However, for a vision system used to monitor the trajectory of a measurement platform designed to test airport lamps, such an approach is less practical due to the significantly larger size of the runway markings. Nevertheless, the concept of detecting horizontal markings using edge detection, possibly following a colour filtration process, is useful for algorithm development. Figure 2-5 shows selected line detection methods used in vision systems.

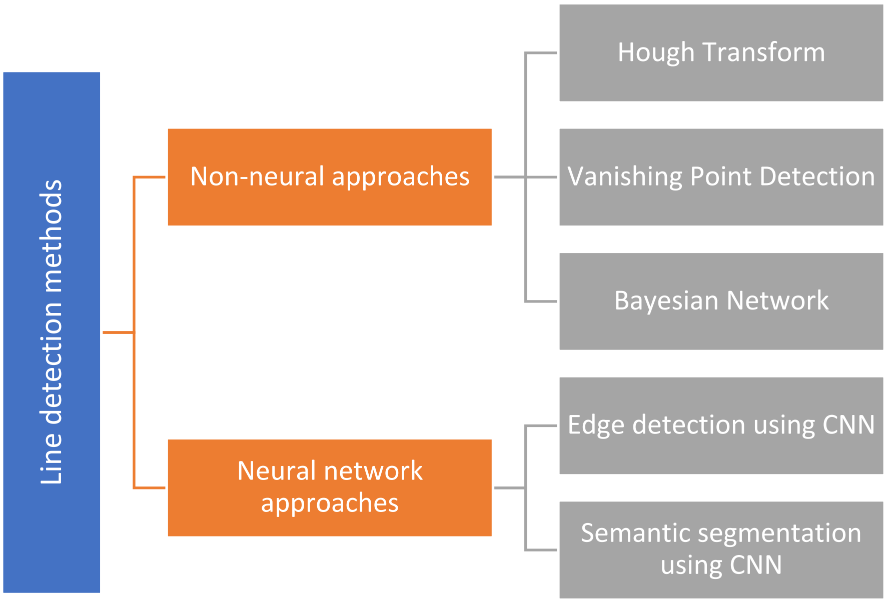

Figure 2-5 Selected line detection methods used in vision systems

The methodology for correcting the trajectory of the measurement platform for testing airport lamp quality may parallel that described in the paper [67]. Positioning is achieved by detecting lane lines, and then the vehicle's lane change is assessed on the basis of the relative positions of these detected features. For the measurement platform, the central reference point is the centre line of the runway. After the camera system calibration, a line will be programmed to guide the operator. Crossing this line on either side of the frame will trigger a command for the operator to adjust the direction of movement.

More sophisticated solutions can involve assessing environmental objects and training Bayesian network models [68]. However, at an airport, this approach is less effective due to the minimal and relatively static details of the surrounding environment during a runway traversal. The most effective method to determine the trajectory of the measuring platform for airport lamp testing is to use surface markings as references.

Another intriguing positioning method for the measurement platform in airport environments involves landmark-based vehicle localization [69]. This method utilizes runway endpoints as landmarks. The paper details two critical components: detecting lane endpoints and evaluating the accuracy of the estimation. Here, a single camera was used. Enhancing the algorithm could involve incorporating a tool that automatically addresses incorrect readings of road markings with the help of a convolutional neural network (CNN) [70].

A modern solution for car line detection, as described in [71], involves predicting the occurrence of lines and estimating distances using vanishing points (VP). This method relies on detecting the VP in the area where the edge directional feature information is concentrated, requiring the intersection of two straight lines in this zone. This point can determine the vehicle's optimal trajectory, typically the lane's centre. Edge detection in this method uses the Hough transform.

An interesting algorithm for detecting less visible road markings is elaborated in [72]. It is designed to resist interference from lighting and environmental conditions and operates on the basis of live video processing with charge-coupled device (CCD) cameras using an original mask. Demonstrated examples show their significant advantages over the Prewitt and Canny algorithms, suggesting that a similar approach could be beneficial for detecting the central axis of a runway.

Line detection can also be implemented using solutions that require higher computational power due to the complexity of deep learning methods. Paper [73] details a methodology for detecting lane lines based on object feature distillation. The authors used different decoders for feature detection to enhance the effectiveness of a neural network-based framework without incurring additional costs, verified with methods such as SCNN, DeepLabv1, and ResNet. Modifications during the model preparation stage were sufficient to achieve better F1 Measure performance on the CuLane dataset. However, the manuscript mentions using a workstation with specifications such as an Intel @ CoreTM i7-6800K CPU @ 3.40 GHz and an NVIDIA 2080 Ti graphics card [73], which is impractical for mobile applications with less powerful computational capabilities.

The airport environments housing the tested lamps can be likened to roadways designated for vehicular traffic, thus presenting a comparable specificity to that encountered in the detection of road signs, a challenge addressed by algorithms facilitating the operation of lane-keeping assistants in contemporary passenger vehicles. With the ongoing advancements in technology and automation, the automotive industry has undergone significant transformations, leading to the creation of numerous datasets aimed at validating algorithms, such as the well-known KITTI dataset [74]. These resources serve as invaluable tools for conducting laboratory testing of methods that hold potential for real-world implementation. Existing systems primarily puts emphasis on collision avoidance and alerting drivers to potential obstacles on the road through the utilization of vision systems [45].

Another pertinent aspect pertains to the estimation of distances between vehicles, achieved through algorithms designed to detect vehicle lights during nighttime conditions and normalize the angle of their illumination [75]. Subsequent systems have expanded to encompass omnidirectional monitoring of the vehicle's surroundings [76], a feature of paramount importance on roadways but not always applicable to other contexts. In environments characterized by significant width and frequently imperceptible central lines, navigation aids may benefit from the fusion of semantic segmentation and monocular depth estimation [77], or through the implementation of algorithms capable of accurately reproducing and denoising captured images [78].

While current monocular camera-based assessment and driving assistance systems [79] offer valuable insights into driving behaviour, they may not be entirely effective in environments like airport runways, where the distances between markings are considerably greater. Consequently, future research endeavours may focus on identifying additional markings on aerodrome, mirroring initiatives aimed at enhancing safety on public roads [80].

2.1.3. Inspection of airport in-pavement navigational lights

The increasing requirements set by European and global aviation safety agencies have been driving more stringent oversight of lighting on airport surfaces, including runways and taxiways [4]. Most of currently used airport lamps are equipped with halogen bulbs, which have limited lifespans. A decrease in lamp luminous efficiency is determined by the soiling of prisms (for example, from adhering, powdered rubber from aircraft tyres). Figure 2-6 provides an illustration of an in-pavement navigation lighting lamp situated on an airport taxiway.

Figure 2-6 Airport taxiway centreline in-pavement lamp [41]

Figure 2-7 depicts a new prism alongside a damaged one after the winter season, illustrating the importance of proper maintenance and adherence to regulatory standards. The fixtures of the lamps and their prisms are susceptible to damage from runway maintenance machinery, particularly during winter snow clearance operations.

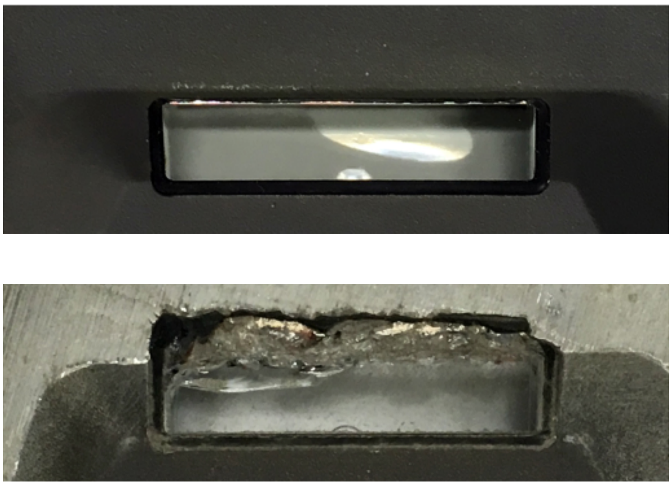

Figure 2-7 In-pavement navigation light prisms – new (top) and damaged (bottom) [28]

In-pavement lamps, also known as runway and taxiway centre line lights or touchdown zone lamps, play a crucial role in providing essential visual guidance to pilots during take-off, landing, and taxiing, particularly in low visibility conditions [3], [4], [24]. Metal brushes can scratch the lamp fixtures and chip their prisms, necessitating the replacement of damaged lamps [28], [29], [51]. Such machinery can inadvertently cause abrasions and fractures on the lamp casings and prisms, necessitating their replacement due to compromised structural integrity. The degradation of luminous efficiency can also occur due to weather conditions and runway operations, such as the accumulation of sticky, powdered rubber from aircraft tyres [81].

As mentioned earlier, the average intensity of the main beam and the colour of the light emitted by aeronautical ground lights are critical for aviation safety. Both the International Civil Aviation Organization [3] and the European Union Aviation Safety Agency [4] have established regulations that address the quality of this lighting [82], including specific requirements for chromaticity and light intensity [28]. These standards are designed to ensure that the lights are easily distinguishable by pilots, even in poor visibility conditions [83]. To maintain compliance with ICAO and EASA regulations, also regular inspection of chromaticity is essential [84]. These inspections can be conducted using specialized equipment, such as spectrophotometers or colorimeters, which deliver precise measurements of colour parameters [33]. By routinely performing these assessments, airports can detect any deviations from the required colour standards and implement corrective measures to ensure aviation safety [85].

For instance, at the Poznań–Ławica Airport, there are approximately 356 in-pavement lamps spread over a distance of about 2.5 km. The performance of all these lamps is specified in the European Aviation Safety Agency standard outlined in Chapter U — Colours for aeronautical ground lights, markings, signs, and panels [4]. This document delineates the illumination intensity of individual lights and their dependence on the angle of incidence. The prescribed values vary on the basis of the lamp type and light colour. Furthermore, the standards define requirements specific to the airport category. One of the critical parameters is the minimum luminous intensity for the main beam, which varies across different angular ranges depending on the lamp type. The intensity is expressed in candelas and depends on the beam angle. Figure 2-8a presents an example isocandela diagram for taxiway centre line lights.

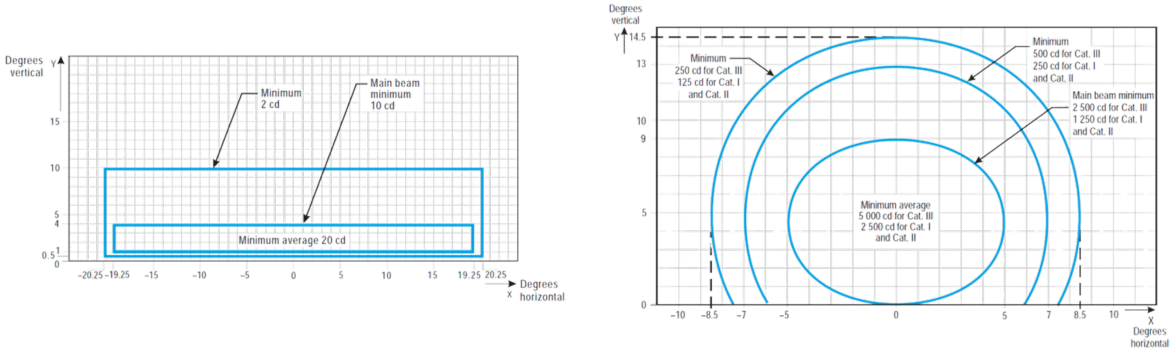

(a) (b)

Figure 2-8 Selected isocandela diagrams for in-pavement airport lamps [4]: (a) Isocandela diagram for taxiway centre line (7.5 m, 15 m, 30 m spacing), no-entry bar, and stop bar lights in curved sections intended for use in runway visual range conditions of 350 m, (b) Isocandela diagram for runway centre line light with 15 m longitudinal spacing (white light) and rapid exit taxiway indicator light (yellow light)

Typically, new fixtures used on taxiways significantly exceed the parameters beyond the minimum values specified by the standards. This is primarily due to the requirements for light intensity on the taxiway, where the main role of the light points is aircraft navigation while on the ground [86].

The standards for the intensity of the runway centre line lights (Figure 2-8b) vary depending on the category required at the airport. These fixtures must meet the highest intensity values within the range of 0 to 9 degrees in the vertical axis and -5 to 5 degrees in the horizontal axis for the main beam.

Light, functioning as an electromagnetic wave, reaches the human eye and is focused onto the retina. Here, specialized cells known as cones are located, which, upon stimulation by light, transmit signals to the brain. Each of the three types of cones responds to a distinct range of electromagnetic wavelengths. Cones sensitive to short wavelengths exhibit the strongest response to wavelengths around 420 nm (blue), while those responsive to medium wavelengths peak at around 530 nm (green). Cones sensitive to long wavelengths demonstrate the strongest response to wavelengths around 570 nm. This understanding forms the basis for constructing instruments designed to measure colours [87].

Radiometry is a fundamental branch of optics concerned with the quantitative measurement and characterization of light. This discipline encompasses the precise assessment of spectral radiation, which denotes the radiant power emitted, transmitted, or received per unit wavelength. Spectral radiation is typically quantified in units such as watts per square meter (W/m^2) or microwatts per square centimetre ($\mu W/cm^2$), depending on the specific application requirements and scale of measurement [88].

Photometry is concerned exclusively with visible light and evaluates it based on how the human eye experiences brightness. It adjusts the measurement of light intensity according to the luminous efficiency curve, which represents the eye's varying sensitivity to different wavelengths [89], [90].

The $v(\lambda)$ curve (Figure 2-9), representing the human eye's average sensitivity to different wavelengths of light, has been progressively refined, particularly through revisions in the CIE (International Commission on Illumination) standards. Below is a summary of the key developments [89], [90]:

- CIE 1931 (blue): The initial luminous efficiency function, created from early experiments with a small sample size and basic equipment, remains in widespread use today.
- CIE 1978 (orange): This update enhanced the accuracy of the sensitivity measurements, taking advantage of improved experimental methods and technology.
- CIE 2005 (green): The most recent revision integrated contemporary research, offering more precise data and reflecting a more comprehensive analysis of the human population's visual response.

The modifications implemented over the years have minimal impact on the subject matter addressed in the dissertation, and the applicable aviation safety regulations and recommendations are based on standards established in 1931 [4].

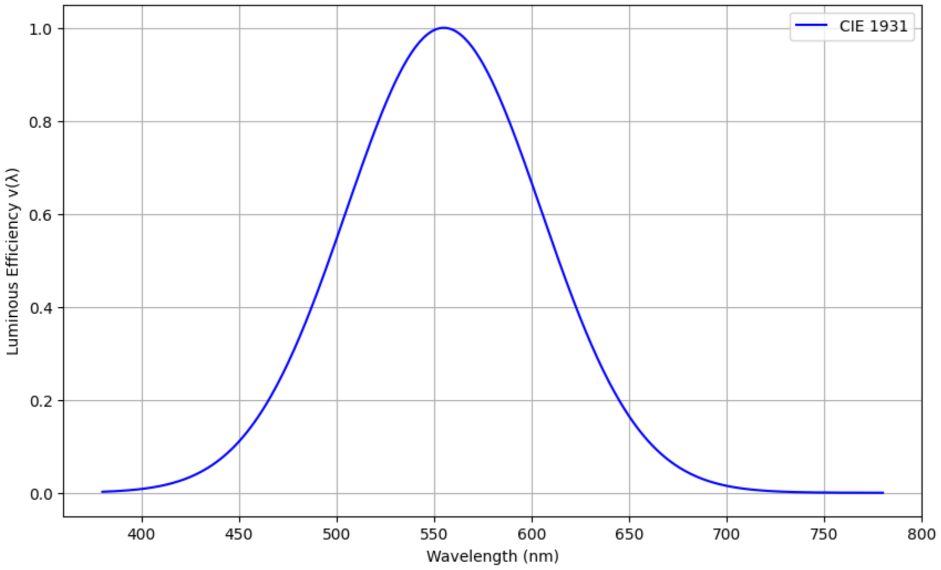

Figure 2-9 The $v(\lambda)$ curve from 1931

The nanometre (nm) is the standard unit used to express wavelengths of electromagnetic radiation, particularly within the visible spectrum, which spans approximately from 400 nm (violet) to 700 nm (red). Relative responsivity refers to the sensitivity of optical detectors or sensors across different wavelengths relative to a standard response curve, providing insight into their spectral sensitivity characteristics [88].

Normalized responsivity is a derived metric that standardizes the responsivity of a sensor against a reference value, facilitating comparative analyses across different sensor types or measurement systems. The mnemonic VBGYOR represents the sequence of Violet, Blue, Green, Yellow, Orange, and Red colours in the visible spectrum, corresponding to specific wavelength ranges perceived by the human eye [88].

The conversion from radiometric to photometric measurements requires integrating the spectral energy distribution with the eye's photopic response curve [88]. This approach reflects the fact that human visual sensitivity changes with wavelength. The fundamental equation for this conversion is [88]:

$$\Phi_v = K_{cd} \int_0^\infty v(\lambda)\Phi_e(\lambda)\mathrm{d}\lambda \tag{1}$$

where:

- The integration limits are technically standardized from 380 to 780 nm in 5 nm steps
- Φ_v – photometric quantity (luminous flux in lumens)
- K_{cd} – maximum luminous efficacy (683 lm/W for photopic vision)

- $v(\lambda)$ – photopic luminosity function, which describes the human eye's sensitivity under well-lit conditions
- $\Phi_e(\lambda)$ – spectral radiometric value (radiant flux in watts per nanometer).

Lux, the SI unit of illuminance, quantifies the amount of luminous flux incident per unit area on a surface, directly influencing perceived brightness. Candela (cd), the SI unit of luminous intensity, measures the amount of light emitted in a specific direction by a source, crucial for assessing the brightness of light sources and their visual impact [88].

RGB (Red, Green, Blue) signifies the additive colour model wherein various intensities of red, green, and blue light are combined to produce a wide spectrum of colours, prevalent in digital displays and imaging technologies. The CIE 1931 colour space, established by the International Commission on Illumination, provides a rigorous mathematical framework for representing u perception based on human visual responses, essential in colour science and related fields [91]. This colour space is a standard for describing how the human eye perceives colour. Developed by the CIE in 1931, it is also known as the CIE XYZ colour space [92], defined by theoretical (non-negative) matching functions $\bar{x}(\lambda)$, $\bar{y}(\lambda) = v(\lambda)$, $\bar{z}(\lambda)$, which are used to calculate the following, always non-negative coordinates (X, Y, Z) for any colour perceived by humans with spectral energy density $f(\lambda)$ [93]. Figure 2-10 presents CIE 1931 XYZ Colour Matching Function.

$$\mathrm{X} = \int_0^\infty f(\lambda)\bar{x}(\lambda)\mathrm{d}\lambda \tag{2}$$

$$\mathrm{Y} = \int_0^\infty f(\lambda)\bar{y}(\lambda)\mathrm{d}\lambda \tag{3}$$

$$\mathrm{Z} = \int_0^\infty f(\lambda)\bar{z}(\lambda)\mathrm{d}\lambda \tag{4}$$

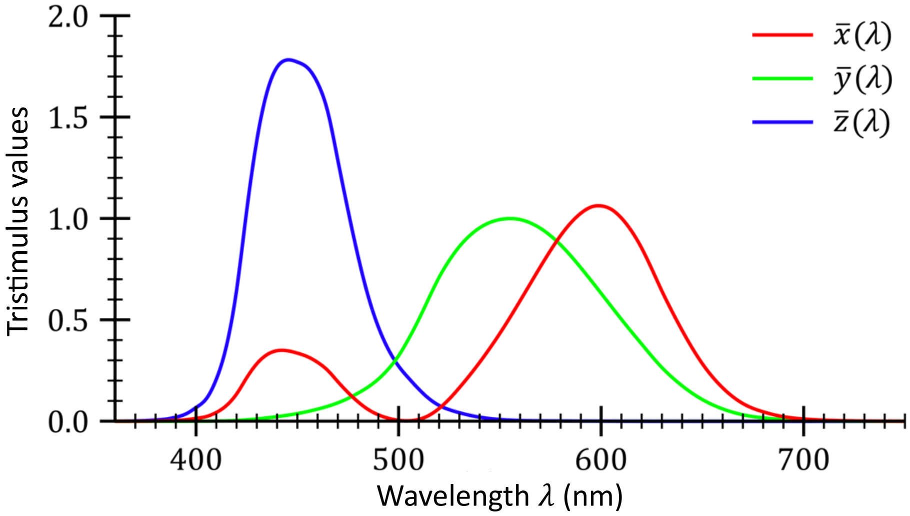

Figure 2-10 CIE 1931 XYZ Colour Matching Function [90]

This space is widely used as a reference for colour measurement in fields such as colour science, colourimetry, and colour management. It has been adopted by numerous organizations, including the International Organization for Standardization (ISO) and the Society of Motion Picture and Television Engineers (SMPTE), as a standard for colour measurement and calibration. Figure 2-11 shows the CIE 1931 colour space chromaticity diagram.

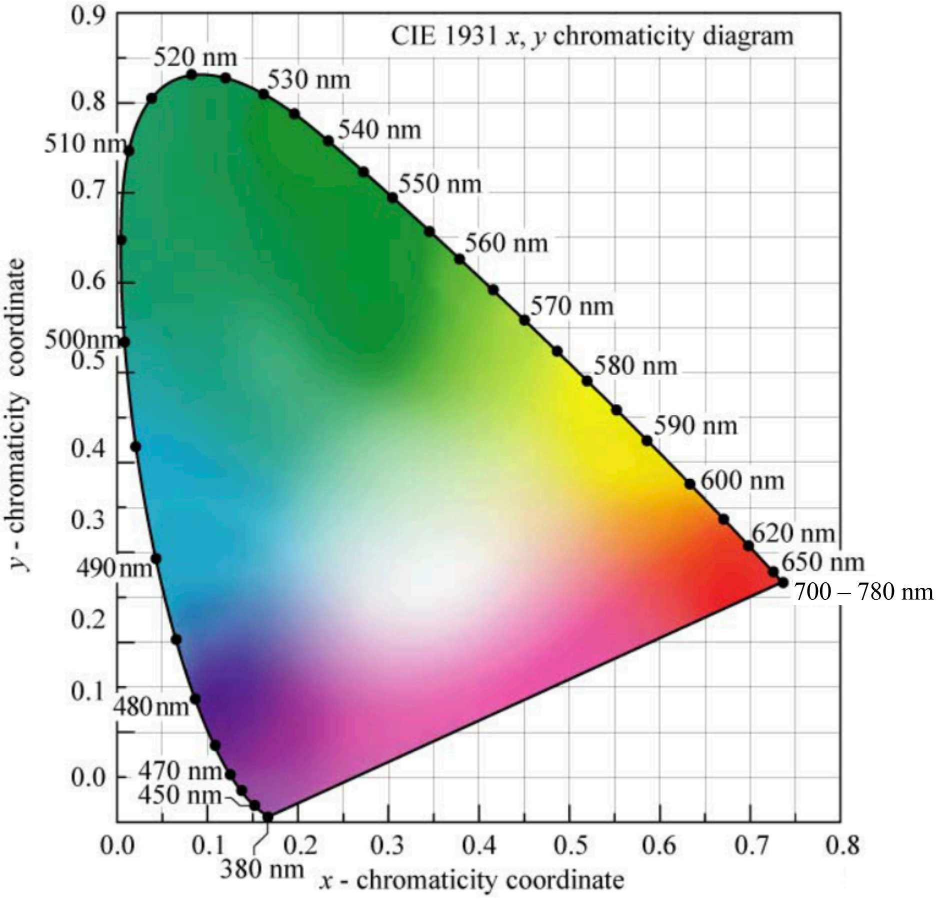

Figure 2-11 The CIE 1931 colour space chromaticity diagram [93]

The x, y coordinates in the CIE 1931 colour space represent the chromaticity of the colour, which refers to the hue and saturation, excluding the brightness. To achieve this conversion, the XYZ coordinates from the sensors need to be normalized. This normalization process involves dividing each of the XYZ values by the sum of all three values $X + Y + Z$. This step adjusts the coordinates to reflect the relative amounts of each primary colour present in the light [94]. In the chromaticity diagram of the CIE 1931 colour space, the wavelength range of 700 to 780 nm is represented, as the variations within this spectrum are not discernible to human vision.

The equations used to perform this conversion are straightforward. By normalizing the XYZ values, it is possible to obtain the relative proportions necessary to calculate the chromaticity coordinates. The specific equations (5) and (6) used for this conversion are [93]:

$$x = \frac{X}{X + Y + Z} \tag{5}$$

$$y = \frac{Y}{X + Y + Z} \tag{6}$$

where X, Y, and Z are the normalised tristimulus values.

When the x, y coordinates are calculated, they can be plotted on a chromaticity chart to visualize the colour. The chromaticity graph is a two-dimensional representation that displays all possible chromaticity within the CIE 1931 colour space, providing a comprehensive view of colour data. This chart helps in understanding and verifying the colour properties of the tested light sources.

To ensure accurate results across the broadest possible spectrum of lamps, the decision was made to set the gain factor to 1. This setting allows for testing at close range without the risk of quickly saturating the sensor. By preventing sensor saturation, the measurements remain reliable and precise, particularly when dealing with high-intensity light sources. This approach maximizes the accuracy of the colour measurements and ensures that the data collected is valid for a wide variety of lamp types.

Changes in airport lighting colour can result from various factors such as the aging of the lighting system, environmental influences, and even changes in the composition of the surrounding air. Regular chromaticity measurements are essential for airports to comply with ICAO and EASA regulations, ensuring that pilots can consistently recognize the colours of the navigational lighting system [95]. The ICAO has also specified chromaticity requirements for the instrument landing system (ILS), which vary depending on the system category, similar to luminous intensity standards [4], [24].

The EASA chromaticity standards are defined within the International Commission on Illumination (CIE) 1931 colour space. Figure 2-12 provides an example chart illustrating the EASA regulations regarding the colours of navigation lighting.

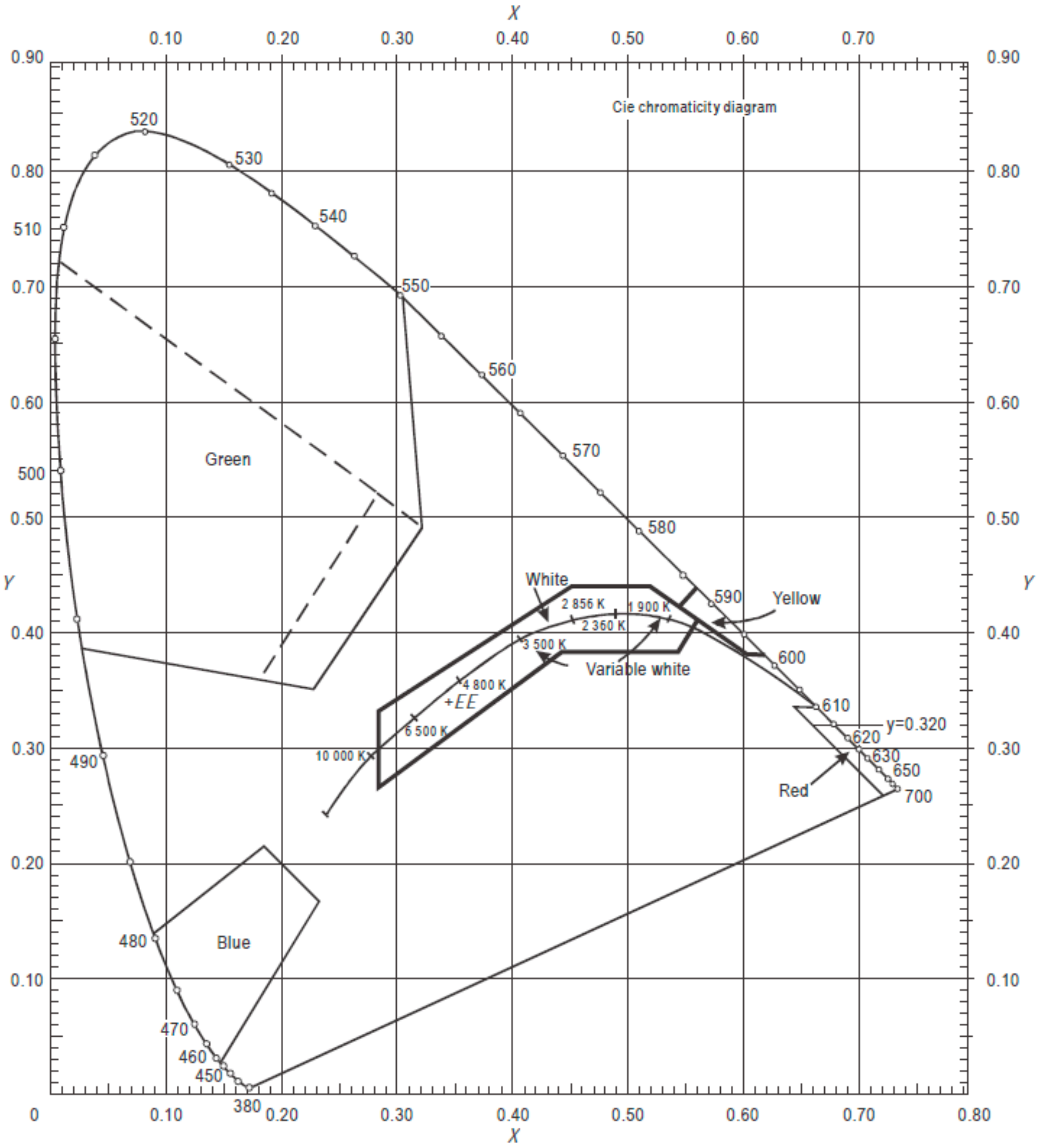

Figure 2-12 Colours for aeronautical ground lights (filament-type lamps) [4][*]

The chromaticity requirements for airport lighting vary depending on the type of lamp and its location. The equations defining the boundaries of individual colours in the CIE 1931 colour space, illustrated in Figure 2-12, are as follows [4]:

- Red:
  - Purple boundary: $y = 0.980 - x$
  - Yellow boundary: $y = 0.335$

---

[*] The presented chromaticity diagram comes directly from the EASA documentation "Certification Specifications and Guidance Material for Aerodrome Design (CS-ADR-DSN)" [4], where the axes are marked with capital *X* and *Y*, although they should be lower case x and y, in accordance with those used in subsequent equations. Furthermore, the point associated with 700 nm in the other charts is designated as 700 - 780 nm, since the variations within this range are undetectable by the human visual system.

- Yellow:
    - Red boundary: $y = 0.382$
    - White boundary: $y = 0.790 - 0.667x$
    - Green boundary: $y = x - 0.120$

- Green:
    - Yellow boundary: $x = 0.360 - 0.080y$
    - White boundary: $x = 0.650y$
    - Blue boundary: $y = 0.390 - 0.171x$

- Blue:
    - Green boundary: $y = 0.805x + 0.065$
    - White boundary: $y = 0.400 - x$
    - Purple boundary: $x = 0.600y + 0.133$

- White:
    - Yellow boundary: $x = 0.500$
    - Blue boundary: $x = 0.285$
    - Green boundary: $y = 0.440$
      $y = 0.150 + 0.640x$
    - Purple boundary: $y = 0.050 + 0.750x$
      $y = 0.382$

- Variable white:
    - Yellow boundary: $x = 0.255 + 0.750y$ $y = 0.790 - 0.667x$
    - Blue boundary: $x = 0.285$
    - Green boundary: $y = 0.440$ $y = 0.150 + 0.640x$
    - Purple boundary: $y = 0.050 + 0.750x$ $y = 0.382$

To verify the parameters of navigation lighting, specialized devices are employed, including measurement platforms [28] and drones [26], [31]. Traditionally, the primary focus has been on the intensity of the light [51], [96], as a reduction in intensity can result from damage to the lamp prism. However, there is a growing emphasis on examining airport areas [40] and the chromaticity of the light emitted by airport navigation lighting.

To maintain the integrity of in-pavement lamps and ensure their continued functionality, regular inspection and maintenance are imperative [33]. Traditionally, the inspection process for in-pavement lamps has been manual, characterized by its time-consuming nature, labour intensiveness, and susceptibility to human error. Consequently, there is a growing demand for automated systems [26], [31] capable of accurately and efficiently assessing the condition of in-pavement lamps and identifying any signs of damage or wear [39], [40].

In recent years, the convergence of computer vision and artificial intelligence (AI) has emerged as a promising avenue for automating the inspection and maintenance of critical infrastructure, including in-pavement lamps. The next stage of an intelligent vision system designed for the automated detection and classification of prism defects in in-pavement lamps [30], [46], [47] has been proposed. The system leverages a sequence of vision images captured by a camera installed on the inspection vehicle, alongside an AI-based algorithm, to analyse the images and identify any defects or anomalies in the prisms. This approach offers significant advantages over traditional manual inspection methods, including enhanced speed, accuracy, and efficiency.

Periodic assessments of the correctness of airport lighting can be conducted using special devices that are commercially available and designed for specific airports. For example, the device offered by FB Technology enables the examination of the light beam intensity level emitted by both inset and surface fixtures [97]. A noteworthy feature is the creation of a dataset from previously taken measurements, allowing for the observation of the degree of wear of individual lamps, consequently facilitating the selection of the appropriate lighting maintenance method. The measurement kit can be installed on any vehicle, either at the front or at the rear, thanks to the use of a special frame. Communication between the sensors and a laptop or tablet is wireless, via the WiFi network, or, when not possible due to airport procedures, via an Ethernet cable. Additionally, the manufacturer offers the optional use of the DGPS (Differential Global Positioning System) system for the localization of measurement points. However, this requires interference with stationary airport installations. The lamp inspection is carried out while the vehicle is in motion, with a speed limit of 60 km/h during measurement. Inspection can be carried out independently of atmospheric conditions and time of day. Correct approach to the fixtures is assisted by the live camera preview transmitted to the driver's cabin.

DeWiTec offers the Dalmas AFL Analysis device, which also examines both in-pavement and elevated fixtures [98]. It takes the form of a trailer attached to any vehicle with a tow bar. Only one person is needed to perform the inspection. Measurements can be taken under any lighting and atmospheric conditions. In contrast to competitive products, the driving speed during the inspection is lower, ranging from 25 to 35 km/h. The driver is provided with several conveniences to precisely carry out the inspection. The device guides the driver to the starting point of the measurement and then to each subsequent lamp. Additional conveniences include two cameras and a laser line that indicates the direction. All information is available online in software dedicated to a specific airport. Reporting occurs immediately after measurements are taken, along with maintenance recommendations and necessary data and charts.

However, the aspect of high costs associated with the aforementioned commercial devices [97], [98] served as motivation to develop a new, low-budget device with high utility value, tailored to the requirements of the Poznań–Ławica Airport, enabling quick, daily inspection of runway lighting [28]. This led to the creation of a proprietary device with characteristics similar to those of commercial devices [30].

The scientific literature has explored the issue of chromaticity measurement using integrated electronic sensors. A crucial aspect is ensuring accurate measurement within a specific colour space or achieving correct conversion. Ref. [99] presents a method for calculating and specifying light source chromaticity using the CIE2015 10° colour matching functions (CMFs). This reference offers methodological recommendations to enhance the evidential value of laboratory-based psychophysical experiments that investigate how the spectral power distribution of light sources affects subjective evaluations of colour appearance in scenes. However, it does not discuss the use of specific electronic systems.

Chromatic verification of light sources was also addressed in Ref. [25], which focused on LED sources. For the CIE 1931 colour space, the values of illuminance and correlated colour temperature (CCT) were determined. The measuring apparatus included a spectrophotometer and recommended sphere geometries, which necessitate the disassembly of the tested light source to obtain measurement results.

In Ref. [100], the authors introduced a microprocessor system designed for capturing, processing, and managing s, allowing for the analysis of any non-self-luminous object's. During experimental tests, a TCS3414CS colour sensor was utilized. This study did not reference international standards and requirements for colour space, and the colour obtained was not categorized within the limits set by the CIE 1931 colour space.

A mobile solution for chromaticity evaluation has been proposed using a smartphone-based system that approximates colour regions on the CIE 1931 x, y chromaticity diagram [101]. These tests were limited to assessing the chromaticity of the measurement scene, followed by lighting adjustments to the selected setting.

This dissertation puts emphasis on two critical aspects of assessing the correct functioning of airport navigation lighting, proposing systems:

- for detecting in-pavement lamps and classifying prisms, assessing its mechanical wear
- for the chromaticity evaluation of the emitted light beam.

2.2. Image processing techniques for vision inspection

Modern video monitoring systems have built-in algorithms called IVA (Intelligent Video Analysis) [102]. These algorithms are intended for typical tasks related to urban monitoring. The deployment of Intelligent Video Analysis within surveillance systems encompasses a range of applications, including the detection, tracking, and classification of moving objects, the creation of density maps, people counting, the identification of vehicles traveling in the wrong direction, and even fire detection. These functionalities have collectively driven the advancement of sophisticated intelligent systems [102].

In order to detect the objects, it is possible to use classic image analysis techniques embedded in OpenCV [103]. Open Source Computer Vision Library is an open-source computer vision and machine learning software library. It was initially developed by Intel in 1999, and later supported by Willow Garage and Itseez (now part of Intel) [104]. OpenCV is designed to provide a common infrastructure for computer vision applications and to accelerate the use of machine perception in commercial products. The library includes more than 2500 optimized algorithms, which can be used for a wide range of applications including facial recognition, object detection, 3D model extraction, image stitching, and motion tracking. It is written in C++ and has interfaces for Python, Java, and MATLAB/OCTAVE, supporting multiple platforms such as Windows, Linux, Android, and macOS. OpenCV facilitates real-time operation, and its modular structure enables developers to tailor functionalities for specific projects, ensuring efficient processing and lower computational overhead. With its extensive functionalities and adaptability, OpenCV has become a fundamental tool in the field of computer vision and is widely adopted in both academic research and industry applications [104].

Video and image analysis in MATLAB harnesses the software's advanced computational and visualization capabilities to process, analyse, and interpret visual data [105]. MATLAB equips users with an extensive array of tools and functions specifically tailored for image and video processing tasks. The Image Processing Toolbox offers a diverse set of algorithms for image enhancement, filtering, and transformation. These capabilities allow users to execute operations such as edge detection, image segmentation, and morphological transformations, facilitating the extraction of meaningful features from images. For video analysis, MATLAB's functionality encompasses the reading, processing, and analysis of video frames. The Computer Vision Toolbox provides essential functions for object detection, motion estimation, and tracking, supporting the development of sophisticated video analytics applications. MATLAB's support for various video formats and its tools for frame-by-frame analysis are crucial for tasks such as object tracking and activity recognition [105].

A significant feature of MATLAB in video and image analysis is its integration with deep learning frameworks. It is possible to design and train convolutional neural networks and other deep learning models directly within MATLAB [106]. The Deep Learning Toolbox enables the implementation of intricate neural network architectures for tasks including image classification, object detection, and semantic segmentation. Pre-trained models like AlexNet, VGG-16, and ResNet can be fine-tuned for specific applications, thereby expediting the development process [105]. Additionally, MATLAB's extensive support for hardware integration facilitates real-time image and video processing. Users can deploy algorithms to embedded systems, GPUs, and cloud platforms, ensuring scalability and performance. MATLAB also provides a versatile environment for prototyping and testing, with capabilities to simulate various image and video processing scenarios, further enhancing its utility in research and development [105]. Figure 2-13 shows selected image processing methods for object detection.

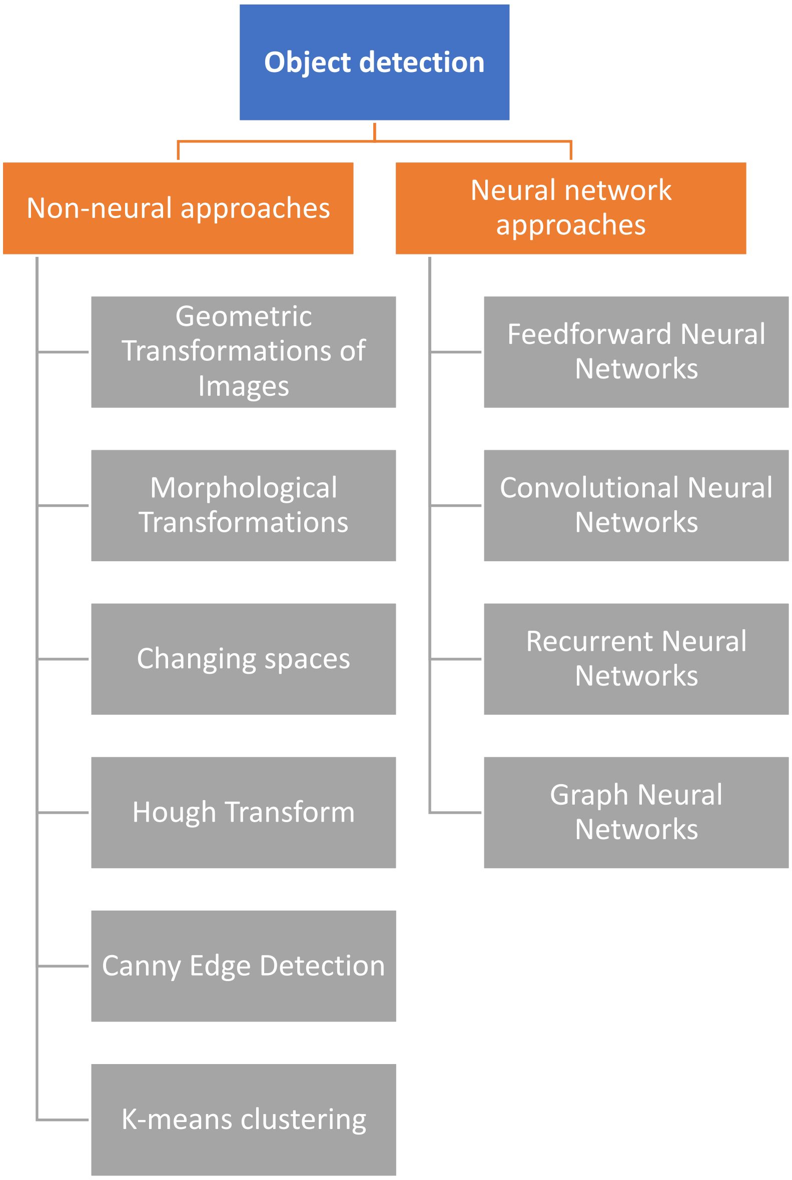

Figure 2-13 Selected image processing methods for object detection

Numerous libraries and tools are available for constructing and training neural networks. Among these, TensorFlow and Keras libraries, both operating within the Python ecosystem, are prominent. Additionally, the Deep Network Designer tool in the MATLAB environment is particularly suitable for testing and validating pre-trained neural network models.

Developed by Google, TensorFlow [107] is an open-source framework that supports the creation and training of machine learning models, including deep neural networks. TensorFlow is highly versatile, enabling efficient computation and scalability across various platforms, from desktops to mobile devices, and edge computing environments. It provides robust support for deep learning research and production deployment, featuring a comprehensive ecosystem with tools like TensorBoard for visualization and TensorFlow Serving for model deployment.

Initially an independent project and now integrated into TensorFlow, Keras [108] is a high-level neural networks API written in Python. It is designed to enable fast experimentation with deep learning models. Keras offers a user-friendly interface, reducing the complexity of implementing common neural network operations and architectures. It acts as a convenient wrapper for the lower-level operations provided by TensorFlow, simplifying the process of model development and training.

Deep Network Designer, part of MATLAB's Deep Learning Toolbox [109], provides a graphical interface for designing, analysing, and testing deep neural networks. It facilitates the import and customization of pre-trained models, allowing users to fine-tune and validate these models against their own datasets. The Deep Network Designer supports interactive network construction, making it accessible for users with varying levels of expertise in deep learning. Additionally, it integrates seamlessly with MATLAB's comprehensive suite of tools for data analysis, visualization, and simulation, enhancing its utility for research and development in neural network applications. Figure 2-14 shows selected libraries and toolboxes for image processing.

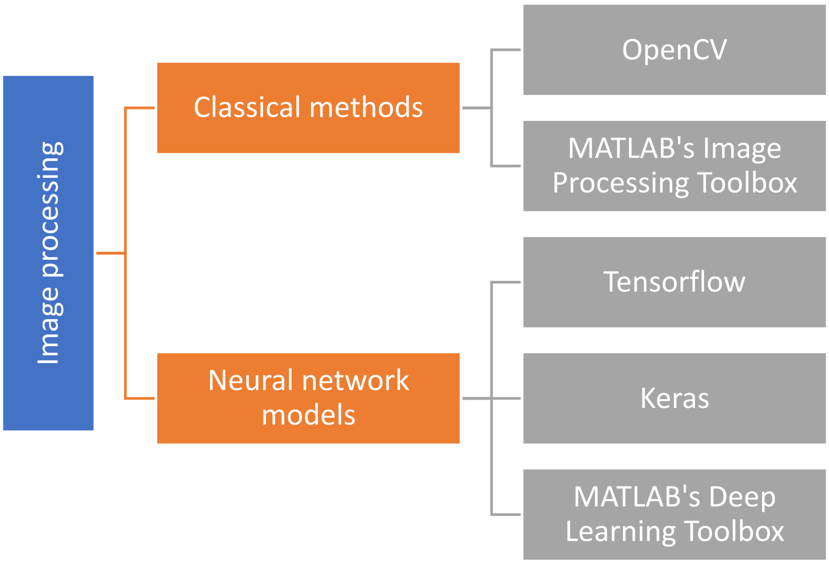

Figure 2-14 Selected libraries/toolboxes for image processing

2.2.1. Classical methods for vision analysis of aerodrome

The development of computers and embedded systems has made it possible to use algorithms that effectively process images recorded in digital form [91], [110], [111], [112], [113], [114],

[115]. From the point of view of this dissertation, the most important operations that may be helpful are [91], [103]:

- Geometric Transformations of Images

These transformations include scaling, translation, rotation, affine transformation, and perspective transformation.

  - Scaling

Scaling alters the size of an image. It is achieved using the `*cv2.resize()*` function. The scaling operation is mathematically represented as:

$$(x', y') = (sx, sy) \tag{7}$$

where (x, y) are the coordinates of a pixel in the original image, and s is the scaling factor. In OpenCV, scaling can be done by specifying the desired output size or the scaling factors along the x and y axes.

  - Translation

Translation shifts an image by moving it along the x and y axes. This operation is described by the following equations:

$$(x', y') = (x + t_x, y + t_y) \tag{8}$$

where t_x and t_y are the translation distances along the x and y axes, respectively. In OpenCV, translation is performed using an affine transformation matrix:

$$T = \begin{bmatrix} 1 & 0 & t_x \\ 0 & 1 & t_y \end{bmatrix} \tag{9}$$

  - Rotation

Rotation turns an image around a specified pivot point. The rotation transformation is represented by:

$$(x', y') = (x \cos \Theta - y \sin \Theta, \qquad x \sin \Theta + y \cos \Theta) \tag{10}$$

where Θ is the angle of rotation.

- Image Thresholding

Image thresholding is a fundamental technique in image processing, widely used for segmenting images and extracting meaningful information. It plays a crucial role in various applications, such as object detection, image enhancement, and medical imaging [110].

Thresholding is the process of converting grayscale or colour images into binary images, where pixels are classified into two categories based on their intensity values: foreground (object) and background. The main objective of thresholding is to separate objects or regions of interest from the background, making subsequent analysis and interpretation easier [110].

One of the simplest thresholding techniques is the binarization method, where a single threshold value is applied to the entire image. This method assumes that the intensity histogram of the image has two distinct peaks, separating the foreground from the background. Mathematically, the binarization operation $T(x, y)$ can be expressed as:

$$T(x,y) = \begin{cases} 0 & \text{if } I(x,y) < \mathrm{T} \\ 255 & \text{otherwise} \end{cases} \tag{11}$$

where $I(x, y)$ represents the intensity value of the pixel at coordinates (x, y), and T is the threshold value [110].

- Morphological Transformations

Morphological transformations are one of the most important operations in computer image analysis, because - properly combined into sets - they allow for the most complex operations related to the analysis of the shape of image elements, their interconnection and enable complex simulation processes [110], [111]. Basic morphological transformations are the starting point for creating more complex operations related to the analysis of the shape of objects and their important arrangement. Unfortunately, their biggest drawback is their high computational complexity, as a result of which they became popular in image analysers only in the second half of the 1980s [111]. The fundamental concept of morphological transformations is the so-called structural element of the image. It is a certain section of the image (in the case of a discrete representation of the image - a certain subset of its elements) with one point highlighted (the so-called central point). The most frequently used structural element is a circle with a unit radius [111].

- Erosion

To define the erosion frame, it is assumed that there is an irregular area X and a circle B with radius r, which will be a structural element [111]. The centre of point B is taken as the centre point of the structural element. Therefore, the erosion of figure X by element B can be defined in two different ways:

- the eroded figure is the set of centres of all angles of radius r, which are entirely contained within area X;
- Circle B rolls on the inside of the edge of the figure. Next positions of the centre of circle B determine the edge of the eroded figure.

In computer implementations, unit erosion involves the removal of all image points with a value of 1 that have at least one neighbour with a value of 0. Erosions can also be interpreted mathematically as the so-called A minimal filter is an operator in which each point is assigned the minimum of the values of its neighbours [110], [111]. Figure 2-15 shows an illustrative erosion process [110], [113].

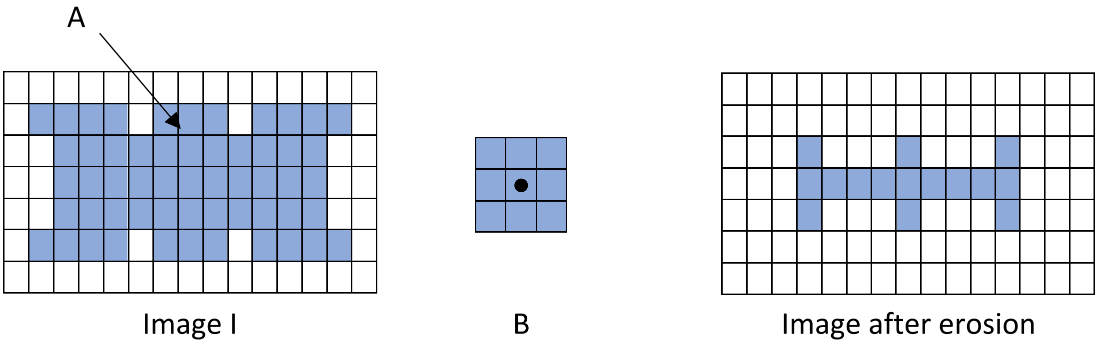

Figure 2-15 Illustration of erosion process

- Dilation

Dilation is the opposite transformation to erosion [111]. To define the dilation frame, it is assumed that there is an irregular area (figure) in the image X and a circle B with radius r, which will be a structural element [110], [111]. Therefore, the expansion joints of figure X with element B can be defined in three different ways:

- the figure after dilation is the set of the means of all angles B, for which at least one point coincides with any point of the starting figure.

        - circle B rolls on the outside of the edge of the figure. Next positions of the centre of circle B define the edge of the figure after the expansion joint.
        - similarly to erosion, expansion joints can be defined as a maximum filter.

    - Opening and closing

The image transformations described earlier (dilation and erosion) unfortunately have a significant drawback [111]. They significantly change the surface area of the transformed areas. Erosion reduces it and dilatation increases it. To eliminate this defect, two transformations were performed, which were a composite of the previous ones [110], [111]. These are opening and closing. The opening consists in rolling circle B on the inside of the edge of the figure and discarding all the points that cannot be reached by the circle. Closing consists in rolling circle B on the outside of the edge of the figure and adding to it all the points that cannot be reached by the circle. Unlike erosion and dilation, in the transformations discussed here it was consider the area around B, not just its centre [111].

- Changing colour spaces

Colour spaces are fundamental in image processing for representing and manipulating colour data. Among these, HSV (Hue, Saturation, Value) or HSB (Hue, Saturation, Brightness) is one of widely used and stands out from RGB (Red, Green, Blue) [116]. HSV categorizes colour information into three components: Hue, which signifies the dominant wavelength; Saturation, indicating colour intensity or purity; and Value, representing colour brightness.

Converting RGB to HSB involves a sequence of mathematical operations to translate RGB values into the corresponding HSB (or HSV) values [116]. Initially, RGB values are normalized to a 0 to 1 range for consistent computation. Subsequently, the maximum (Value) and minimum (Saturation) values among the RGB components are identified to calculate the corresponding HSB components [116].

This conversion process ensures that the HSB/HSV representation is particularly intuitive for a variety of image processing tasks, including colour segmentation and adjustment. It facilitates straightforward manipulation of attributes such as brightness and intensity, which are critical in applications presented in the doctoral thesis, where white is a neutral colour, as opposed to the HCL (Hue, Chroma, Luminance) space.

Furthermore, HSV's capability to separate intensity (Value) from colour information (Hue and Saturation) proves beneficial in situations where independent manipulation of colour perception without affecting brightness is necessary. This feature supports tasks such as colour-based object detection in computer vision and artistic colour correction in graphic design [116].

However, it is important to acknowledge that converting between colour spaces, such as RGB and HSV (HSB), involves computational complexity [117]. Each transformation step, from normalization to Hue calculation, demands meticulous handling to maintain accuracy and prevent artifacts in resultant images [116]. Additionally, HSV's perceptual uniformity makes it preferable over RGB in applications where human interpretation of colour fidelity is crucial. In OpenCV, for HSV, hue range is [0, 179], saturation range is [0, 255], and value range is [0, 255] [103].

- The *R,G,B* values are divided by 255 to change the range from 0..255 to 0..1 [116]:

$$R' = \frac{R}{255} \tag{12}$$

$$G' = \frac{G}{255} \tag{13}$$

$$B' = \frac{B}{255} \tag{14}$$

$$C_{\max} = \max\,(R', G', B') \tag{15}$$

$$C_{\min} = \min\,(R', G', B') \tag{16}$$

$$\Delta = C_{\max} - C_{\min} \tag{17}$$

- Hue calculation in OpenCV library:

$$\overline{H} = \begin{cases} 60 \times \dfrac{G' - B'}{\Delta} + 0 & \text{if } C_{\max} = R' \text{and } G' \geq B' \\ 60 \times \dfrac{G' - B'}{\Delta} + 360 & \text{if } C_{\max} = R' \text{and } G' < B' \\ 60 \times \dfrac{B' - R'}{\Delta} + 120 & \text{if } C_{\max} = G' \\ 60 \times \dfrac{R' - G'}{\Delta} + 240 & \text{if } \mathrm{C}_{\max} = B' \end{cases} \tag{18}$$

$$H = \frac{1}{2} \times \overline{H} \tag{19}$$

- Saturation calculation in OpenCV library:

$$\mathrm{S} = \begin{cases} 0 & \text{if } C_{\max} = 0 \\ \dfrac{\Delta}{C_{\max}} & \text{if } C_{\max} \neq 0 \end{cases} \tag{20}$$

- Value calculation in OpenCV library:

$$\mathrm{V} = C_{\max} \tag{21}$$

- Edge Detection

One of the important operations in vision inspection systems is the detection of object edges. The image gradient is a crucial concept in image processing and computer vision, representing the direction and rate of the most significant intensity change at each pixel in an image. Mathematically, the gradient is a vector containing the partial derivatives of the image intensity function with respect to the spatial coordinates. The gradient magnitude highlights edges in the image, as edges correspond to regions with significant intensity changes. The preferred method for determining the edge strength and direction at any given point (x, y) in an image f is the gradient, represented as ∇f and defined as the vector [110].

$$\nabla \mathrm{f}(x, y) \equiv \mathrm{grad}[\mathrm{f}(x, y)] \equiv \begin{bmatrix} \mathrm{g_x}(x, y) \\ \mathrm{g_y}(x, y) \end{bmatrix} = \begin{bmatrix} \dfrac{\partial \mathrm{f}(x, y)}{\partial x} \\ \dfrac{\mathrm{df}(x, y)}{\mathrm{d}i} \end{bmatrix} \tag{22}$$

To implement the edge detection process, masks defined in Table 2-1 are typically used, which are the core of the two-dimensional high-pass filtering process [110], [113], [118].

Table 2-1 Typically used masks in edge detection process

Operator	Mask template	
Roberts	$\begin{array}{\|c\|c\|}\hline -1 & 0 \\ \hline 0 & 1 \\ \hline \end{array}$	$\begin{array}{\|c\|c\|}\hline 0 & -1 \\ \hline 1 & 0 \\ \hline \end{array}$
Prewitt	$\begin{array}{\|c\|c\|c\|}\hline -1 & -1 & -1 \\ \hline 0 & 0 & 0 \\ \hline 1 & 1 & 1 \\ \hline \end{array}$	$\begin{array}{\|c\|c\|c\|}\hline -1 & 0 & 1 \\ \hline -1 & 0 & 1 \\ \hline -1 & 0 & 1 \\ \hline \end{array}$
Sobel	$\begin{array}{\|c\|c\|c\|}\hline -1 & -2 & -1 \\ \hline 0 & 0 & 0 \\ \hline 1 & 2 & 1 \\ \hline \end{array}$	$\begin{array}{\|c\|c\|c\|}\hline -1 & 0 & 1 \\ \hline -2 & 0 & 2 \\ \hline 1 & 0 & 1 \\ \hline \end{array}$

A more advanced edge detection algorithm is Canny edge detection algorithm [119]. The Canny edge detection algorithm is composed of several key steps [110]:

1. Begin by smoothing the input image using a Gaussian filter to reduce noise.

$$\mathrm{G}\,(x,y) = \mathrm{e}^{-\frac{x^2+y^2}{2\sigma^2}} \tag{23}$$

$$f_{\mathrm{s}}(x,y) = \mathrm{G}(x,y) \star \mathrm{f}(x,y) \tag{24}$$

with $\mathrm{f}(\mathrm{x},\mathrm{y})$ as input image.

2. Next, calculate the gradient magnitude and direction for the image.

$$M_{\mathrm{S}}(x,y) = \|\nabla f_{\mathrm{s}}(x,y)\| = \sqrt{\mathrm{g}_{\mathrm{x}}^2(x,y) + \mathrm{g}_{\mathrm{y}}^2(x,y)} \tag{25}$$

$$\alpha(x,y) = \tan^{-1}\left[\frac{\mathrm{g}_{\mathrm{y}}(x,y)}{\mathrm{g}_{\mathrm{x}}(x,y)}\right] \tag{26}$$

With $\mathrm{g}_{\mathrm{x}}(x,y) = \frac{\partial \mathrm{f}_{\mathrm{s}}(x,y)}{\partial x}$ and $\mathrm{g}_{\mathrm{y}}(x,y) = \frac{\partial \mathrm{f}_{\mathrm{s}}(x,y)}{\partial y}$. $\|\nabla \mathrm{f}_{\mathrm{s}}(x,y)\|$ and $\alpha(x,y)$ are arrays of the same size as the image from which they are computed.

3. Then, perform nonmaxima suppression on the gradient magnitude to thin out the edges.

Nonmaxima suppression is employed to thin edges in the gradient magnitude image, guaranteeing that the detected edges are only one pixel wide. This enhances the precision of edge detection. The procedure comprises several critical steps:

i. Gradient Computation:
   - Initially, compute the gradient magnitude and direction at each pixel within the smoothed image. The gradient magnitude provides the intensity of the edges, while the gradient direction denotes the orientation of these edges.

ii. Edge Thinning:
   - For each pixel in the gradient magnitude image, the algorithm evaluates the pixel’s gradient direction and compares the pixel's gradient magnitude with the magnitudes of its neighbouring pixels along the gradient direction.
   - Specifically, for a pixel at location (x, y), if the gradient direction approximates 0°, 45°, 90°, or 135°, the pixel is compared with its two neighbors along that direction:
     - 0° (horizontal): Compare with the pixels at $(x-1, y)$ and $(x+1, y)$
     - 45° (diagonal): Compare with the pixels at $(x+1, y+1)$ and $(x-1,\ y-1)$
     - 90° (vertical): Compare with the pixels at $(x, y-1)$ and $(x, y+1)$
     - 135° (diagonal): Compare with the pixels at $(x-1, y+1)$ and $(x+1, y-1)$.

iii. Suppression:
   - If the pixel's gradient magnitude $\mathrm{M}(x, y)$ is greater than those of its neighbors, it is retained as a potential edge. Otherwise, it is suppressed (set to zero).
   - This operation effectively narrows down the edges to a single-pixel width and eliminates pixels that are not local maxima of the gradient magnitude in the gradient direction.

4. Finally, implement double thresholding along with connectivity analysis to identify and connect the edges.

$$\mathrm{g}_{\mathrm{NL}}(x, y) = \mathrm{g}_{\mathrm{NL}}(x, y) - \mathrm{g}_{\mathrm{NH}}(x, y) \tag{27}$$

- Hough Transform

A typical line drawing technique will be to use the Line Hough Transform [120]. Then the following parametric equation of the line is considered:

$$\rho = x\cos\alpha + y\sin\alpha \tag{28}$$

The task of detecting a straight line comes down to determining a pair of parameters (ρ,α), which uniquely describes a straight line in the plane [120]. The process of determining the transform is illustratively presented in Figure 2-16.

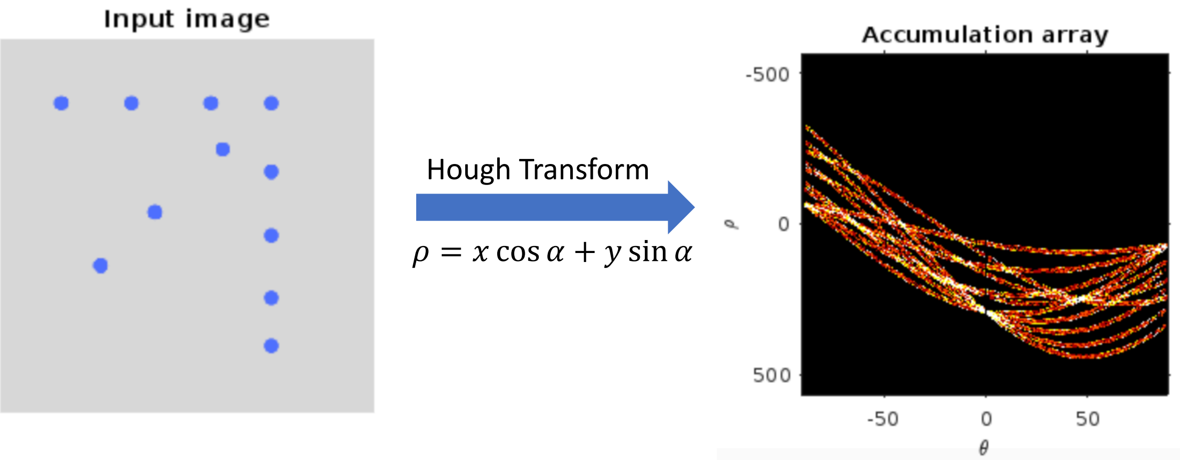

Figure 2-16 Example of input image I and accumulation array A, obtained by applying the Hough Transform for straight lines

Figure 2-16 shows an example of the input image I, showing an object consisting of several points, and the accumulation table A corresponding to this image, which is the result of applying the Hough Transform [120]. In the accumulation table A, one can observe characteristic sinusoidal curves $\rho = \frac{y}{\cos\gamma}\sin(\alpha+\gamma)$, where $\tan\gamma = \frac{s}{y}$, generated by the points of the object in the input image I. The equivalent of each curve in parameter space, there is a bunch of straight lines in image B, the vertex of which is the point $(x,\ y)$ of object $\mathrm{b(I)}$ [120].

One of the issues discussed will be circle detection, then one of the possible detectors is the use of the Circle Hough Transform [120]. The resulting form of the Hough Transform for circles will then be:

$$\mathrm{H}\,(x_S, y_S, \mathrm{r}) = \int_{-\infty}^{\infty}\int_{-\infty}^{\infty} \mathrm{I}\,(x,y)\delta((x-x_S)^2 + \ (y-\ y_S)^2 - \ \mathrm{r}^2)\,\mathrm{d}x\,\mathrm{d}y \tag{29}$$

where $\mathrm{x_S}, \mathrm{y_S}$ are the coordinates of the centre of the circle with radius r [120].

- K-means clustering

The k-means algorithm, widely regarded as one of the most effective clustering techniques, is instrumental in Foreign Object Debris (FOD) detection by segmenting an image into various regions, thereby aiding in the identification of FOD objects. This algorithm functions by partitioning a dataset into *k* unique, non-overlapping clusters. When applied to pixel clustering based on, the objective is to group pixels such that those within the same cluster exhibit similar *s*, while pixels in different clusters display distinct variations.

The k-means algorithm initiates by randomly selecting *k* centroids, which act as the initial cluster centres in a three-dimensional space, typically RGB (red, green, blue). During the Assignment Step, each pixel is assigned to the nearest centroid by calculating the Euclidean distance in the RGB space, thus segmenting the image into *k* clusters, with each cluster containing pixels closest to the corresponding centroid. In the subsequent Update Step, the centroids are recalculated as the mean positions of all pixels within each cluster, determined by averaging their RGB values. This iterative process continues until convergence, which is achieved when the centroids stabilize and show no significant changes between iterations, or when a predefined number of iterations is completed. This method ensures the resulting clusters are as compact and distinct as possible for the selected number of clusters *k* [121].

Given a collection of data points $(x_1, x_2, \dots, x_n)$, where each point is represented as a *d*-dimensional vector in real space, the k-means clustering algorithm seeks to divide these *n* data points into *k* clusters $S = (S_1, S_2, \dots, S_k)$, with $k \leq n$. The primary goal of this partitioning is to minimize the sum of the squared differences within each cluster, which is also known as the within-cluster sum of squares (WCSS) or variance [121]. Mathematically, the objective is to determine the cluster sets that achieve the minimal WCSS [121]:

$$\arg\min_{S} \sum_{i=1}^{k} \sum_{x \in S_i} \|x - \mu\|^2 = \arg\min_{S} \sum_{i=1}^{k} |S_i| \, Var\, S_i \tag{30}$$

where μ_i is the average, often referred to as the centroid, of the points within the cluster S_i. This centroid is calculated as follows [121]:

$$\mu_i = \frac{1}{|S_i|} \sum_{x \in S_i} x_i \tag{31}$$

$|S_i|$ represents the number of elements in the cluster $|S_i|$, and $\|\cdot\|$ denotes the standard L2 norm.

This optimization problem can also be understood as minimizing the sum of squared differences between pairs of points within each cluster [121]:

$$\arg\min_{S} \sum_{i=1}^{k} \frac{1}{|S_i|} \sum_{x,y \in S_i} \|x - y\|^2 \tag{32}$$

2.2.2. Machine learning techniques according EASA guidance

Machine learning, a branch of artificial intelligence (AI), centres on enabling computers to learn from data and enhance their performance through experience. Unlike traditional programming, where explicit instructions dictate behaviour, machine learning involves training algorithms to identify patterns and relationships within extensive datasets. These algorithms subsequently use the discovered patterns to make informed decisions and predictions. As machine learning systems are exposed to more data, their effectiveness and accuracy improve progressively. The abundance and quality of data available to these systems directly influence their predictive precision and overall performance.

Machine learning, including its components such as deep learning technology and neural networks, is intricately nested within the broader field of artificial intelligence. AI utilizes data to make decisions and predictions. Machine learning algorithms enable AI systems to further learn from data autonomously, enhancing their intelligence without requiring explicit programming. Artificial intelligence serves as the overarching category encompassing all subsets of machine learning. Machine learning represents the initial subset, followed by deep learning, which includes neural networks as its component parts (Figure 2-17).

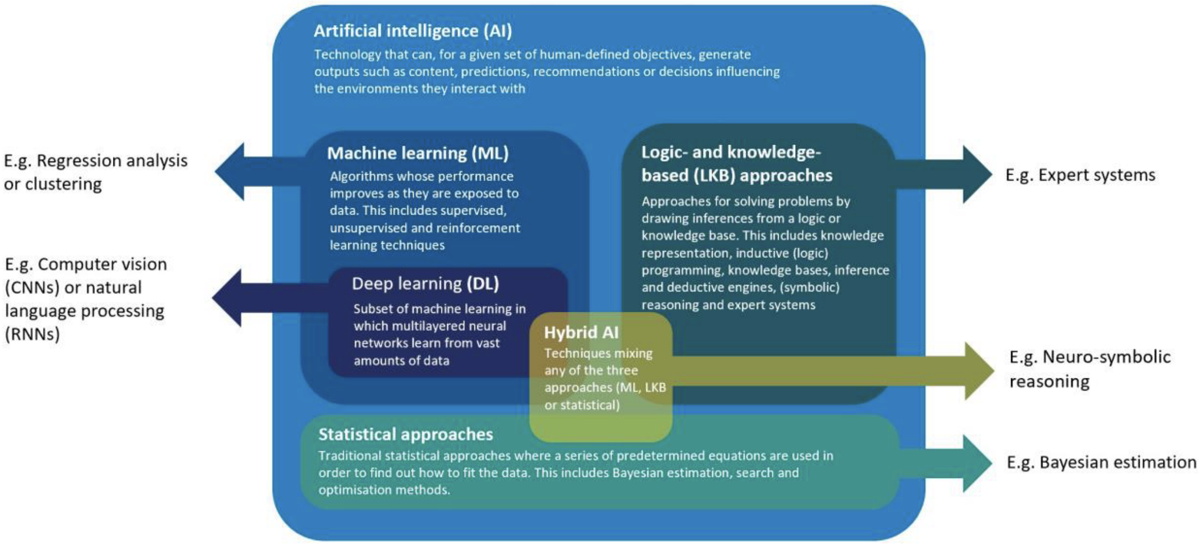

Figure 2-17 AI taxonomy based on EASA [14]

Following the detection and classification of objects, it may be appropriate to use convolutional neural networks. Convolutional Neural Networks (CNNs) are a class of deep learning models particularly effective for processing data with grid-like topology, such as images. The CNN architecture is designed to automatically and adaptively learn spatial object hierarchies through backpropagation using multiple building blocks such as convolutional layers, pooling layers, and fully connected layers. It is EASA in its document [14] that recommends the use of artificial intelligence and machine learning to support the safety of air operations, especially in the field of aerodromes.

Each network type offers distinct methodologies for object detection and image processing. Convolutional Neural Networks (CNN) are predominant in image segmentation and object detection tasks, employing region-based approaches (e.g., R-CNN) and single-shot detectors (e.g., SSD, YOLO) to identify and classify objects within images [122], [123].

Recurrent Neural Networks (RNN), particularly in combination with CNNs, are effective in video analysis, capturing temporal dynamics in image sequences. They process frames sequentially, maintaining temporal dependencies crucial for tasks like action recognition and event detection.

Graph Neural Networks (GNN), though not traditionally used for image processing, have been applied in relational reasoning tasks, such as scene graph generation, where understanding object relationships is essential.

Due to the properties of network features of image processing capabilities, this thesis puts emphasis on Convolutional Neural Networks (CNN) and Recurrent Neural Networks (RNN), with particular emphasis on the former, which are particularly often used for image segmentation and object detection. A summary of the selected network properties depending on their architecture is presented in Table 2-2.

Table 2-2 Selected neural network architectures for image processing

Network Type	Architecture	Image Processing Capabilities
Feedforward Neural Networks (FNN)	Input, hidden, and output layers; data flows unidirectionally	Basic classification and regression
Convolutional Neural Networks (CNN)	Convolutional layers, pooling layers, fully connected layers; exploits spatial hierarchies	Image segmentation, object detection, feature extraction
Recurrent Neural Networks (RNN)	Sequential processing with hidden states; captures temporal dependencies	Video analysis, sequence prediction in image frames
Graph Neural Networks (GNN)	Node feature aggregation from neighbours; relational reasoning	Scene graph generation, object relations understanding

- Feedforward Neural Networks

Feedforward Neural Networks (FNN) represent the simplest form of neural networks, where data flows unidirectionally from input to output through multiple layers. An FNN typically consists of an input layer, several hidden layers, and an output layer. Each neuron in a layer is connected to every neuron in the subsequent layer, with no feedback connections [124]. The activation function f introduces non-linearity, allowing the network to learn complex mappings. Common activation functions include ReLU, Sigmoid, and Tanh. FNNs are primarily used for classification and regression tasks. However, they lack the ability to capture spatial and temporal dependencies, making them less suitable for tasks involving sequential or structured data [124].

- Convolutional Neural Networks

Convolutional neural networks (CNNs) have their origins in the study of the brain's visual cortex and have been applied to image recognition tasks since the 1980s [125]. In recent years, due to advancements in computational power, the availability of extensive training datasets, and the optimization techniques for training deep neural networks [106], CNNs have attained superhuman performance on certain complex vision tasks. These networks are integral to image search engines, autonomous vehicles, automated video classification systems, and more [125]. Additionally, CNNs have proven effective beyond visual perception, excelling in tasks such as voice recognition and natural language processing (NLP).

Computing the output of a neuron in a convolutional layer [125]:

$$\mathrm{z}_{\mathrm{i,j,k}} = \mathrm{b}_{\mathrm{k}} + \sum_{\mathrm{u}=1}^{\mathrm{f_h}} \sum_{\mathrm{v}=1}^{\mathrm{f_w}} \sum_{\mathrm{k}'=1}^{\mathrm{f_{n'}}} \mathrm{x}_{\mathrm{i',j',k'}} \cdot \mathrm{w}_{\mathrm{u,v,k',k}} \text{ with } \begin{cases} \mathrm{i}' = \mathrm{u} \cdot \mathrm{s_h} + \mathrm{f_h} - 1 \\ \mathrm{j}' = \mathrm{v} \cdot \mathrm{s_w} + \mathrm{f_w} - 1 \end{cases} \tag{33}$$

- $\mathrm{z}_{\mathrm{i,j,k}}$ is the output of the neuron located in row i, column j in feature map k of the convolutional layer (layer l)
- $\mathrm{s_h}$ and $\mathrm{s_w}$are the vertical and horizontal strides, $\mathrm{f_h}$ and $\mathrm{f_w}$ are the height and width of the receptive field, and $\mathrm{f_{n'}}$ is the number of feature maps in the previous layer (layer $\mathrm{l} - 1$)
- $\mathrm{x}_{\mathrm{i',j',k'}}$ is the output of the neuron located in layer $\mathrm{l} - 1$, row i', column j', feature map k' (or channel k' if the previous layer is the input layer)
- $\mathrm{b_k}$ is the bias term for feature map k (in layer l)
- $\mathrm{w}_{\mathrm{u,v,k',k}}$ is the connection weight between any neuron in feature map k of the layer l and its input located at row u, column v (relative to the neuron's receptive field), and feature map k'.

- Recurrent Neural Networks

Recurrent neural networks (RNNs) represent a sophisticated class of neural architectures capable of forecasting future events to a certain extent [125]. These networks are adept at analysing temporal data, such as stock market prices, to provide recommendations on optimal buying or selling times. In the context of autonomous driving, RNNs can predict vehicle trajectories, thereby enhancing safety by preventing potential collisions. Unlike traditional neural networks that operate on fixed-size inputs, RNNs have the flexibility to process sequences of varying lengths, making them particularly valuable for tasks involving sentences, documents, or audio inputs. This capability is instrumental in natural language processing (NLP) applications, including automatic translation, speech-to-text conversion, and sentiment analysis [125].

Furthermore, RNNs exhibit a remarkable degree of creative potential due to their predictive abilities. For instance, they can be employed to generate musical compositions by predicting the most probable subsequent notes in a melody and iteratively selecting from these predictions. This method has been utilized in projects such as Google's Magenta to produce novel melodies. Similarly, RNNs are capable of generating coherent sentences, crafting image captions, and performing a variety of other generative tasks, demonstrating their versatility and creative prowess in multiple domains [125].

Similar to feedforward neural networks, it is possible to determine the output of an entire layer in a single step for an entire mini-batch by utilizing a vectorized version of the equation [125].

$$\mathrm{Y}_{(\mathrm{t})} = \phi\left(\mathrm{X}_{(\mathrm{t})} \cdot \mathrm{W}_{\mathrm{x}} + \mathrm{Y}_{(\mathrm{t}-1)} \cdot \mathrm{W}_{\mathrm{y}} + \mathrm{b}\right) = \phi\left(\left[\mathrm{X}_{(\mathrm{t})} \quad \mathrm{Y}_{(\mathrm{t}-1)}\right] \cdot \mathrm{W} + \mathrm{b}\right) \text{ with } \mathrm{W} = \begin{bmatrix} \mathrm{W}_{\mathrm{x}} \\ \mathrm{W}_{\mathrm{y}} \end{bmatrix} \tag{34}$$

Outputs of a layer of recurrent neurons for all instances in a mini- batch [125]:

- $\mathrm{Y}_{(\mathrm{t})}$ is an $\mathrm{m} \times \mathrm{n}_{\mathrm{neurons}}$ matrix containing the layer's outputs at time step t for each instance in the mini-batch (m is the number of instances in the mini-batch and $\mathrm{n}_{\mathrm{neurons}}$is the number of neurons)
- $\mathrm{X}_{(\mathrm{t})}$ is an $\mathrm{m} \times \mathrm{n}_{\mathrm{inputs}}$ matrix containing the inputs for all instances (ninputs is the number of input features)
- W_{x} is an $\mathrm{n}_{\mathrm{inputs}} + \mathrm{n}_{\mathrm{neurons}}$ matrix containing the connection weights for the inputs of the current time step
- W_{y} is an $\mathrm{n}_{\mathrm{neurons}} \times \mathrm{n}_{\mathrm{neurons}}$ matrix containing the connection weights for the outputs of the previous time step
- The weight matrices $\mathrm{W}_{\mathrm{x}}$and W_{y} are often concatenated into a single weight matrix W of shape $(\mathrm{n}_{\mathrm{inputs}} + \mathrm{n}_{\mathrm{neurons}}) \times \mathrm{n}_{\mathrm{neurons}}$
- b is a vector of size $\mathrm{n}_{\mathrm{neurons}}$containing each neuron's bias term.

- Graph Neural Networks

Graph Neural Networks (GNN) extend neural networks to graph-structured data, where relationships and interactions among entities are crucial [126]. The basic operation involves aggregating features from neighbouring nodes.

GNNs are pivotal for applications requiring relational reasoning, such as social network analysis, molecular biology, and recommendation systems. They have also been employed in scenarios like scene graph generation and object relations understanding, although they are less common in traditional image processing [126].

2.3. Embedded systems for vision monitoring tasks

As part of the doctoral dissertation, selected Single Board Computers (SBC) and cameras that could be implemented in individual solutions were analysed. The Figure 2-18 shows a schematic concept of the system, and in the subsequent parts of the chapter the parameters and capabilities of individual embedded systems and cameras are compared. The result of the system is the result of the Intelligent Video Analysis (IVA), as a use of advanced algorithms and machine learning techniques to automatically process and analyse video footage.

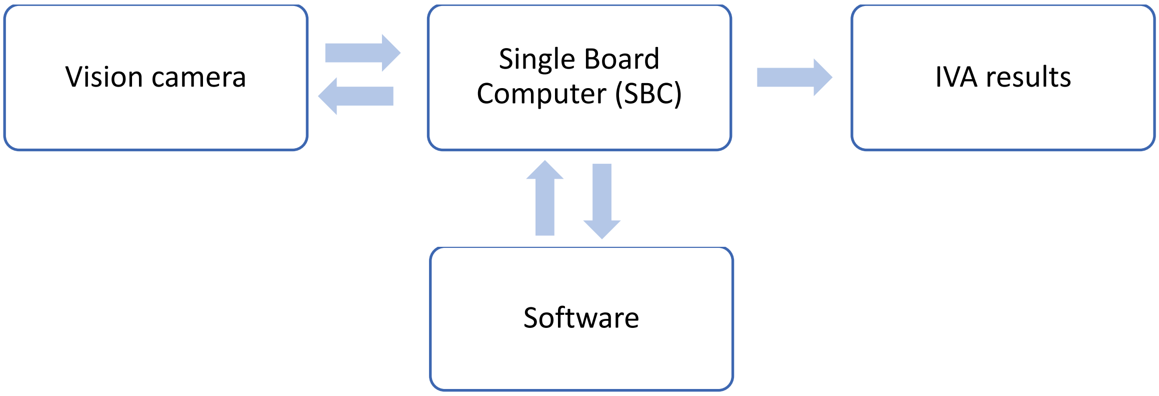

Figure 2-18 Conceptual diagram of a video analysis system

2.3.1. Possibilities of processing video sequences in embedded systems

Systems for identification based on the recognition of individual characters and events in video sequences are becoming increasingly common and utilized in various domains. They rely on both classical image processing methods and neural networks, whose usage is growing in popularity. Cameras are installed in cars and autonomous vehicles [127], [128], [129], [130], for urban surveillance purposes [5], as well as in specialized applications such as airport runway light inspection [28], [29]. These systems assist operators in observing urban spaces or machine surroundings and in monitoring ongoing events, responding to them as necessary. In certain cases, they are capable of entirely eliminating the human factor by automatically issuing specific commands to other systems [47], [131].

For the research and testing phases, five specific Single Board Computers were selected and evaluated during tests:

- Raspberry Pi 4B
- Google Coral
- NVIDIA Jetson Nano
- NVIDIA Jetson Xavier AGX
- NVIDIA Jetson Orin AGX.

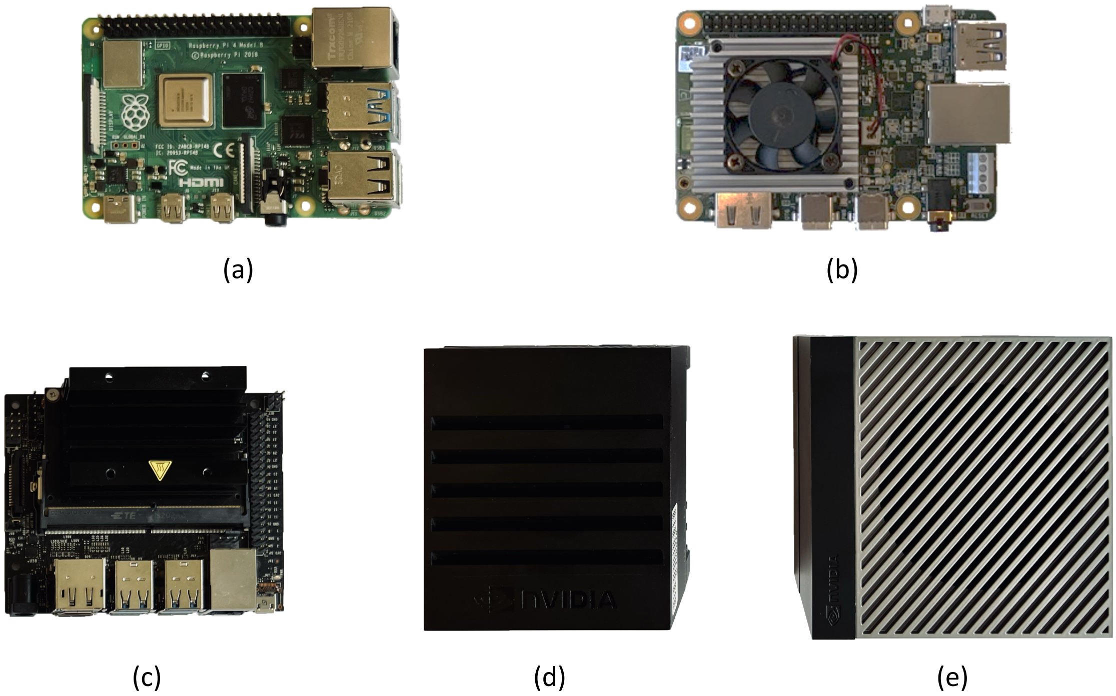
(a) (b)

(c) (d) (e)

Figure 2-19 Single Board Computers (SBC) used during experimental tests [44], [46]:
(a) Raspberry Pi 4B, (b) Google Coral, (c) NVIDIA Jetson Nano, (d) NVIDIA Jetson Xavier AGX, and (e) NVIDIA Jetson Orin AGX

First microcomputer, Raspberry Pi 4B (Figure 2-19a), is distinguished by its powerful hardware, featuring a Broadcom BCM2711 64-bit Quad-Core Advanced RISC Machine (ARM) Cortex-A72 processor [132], which operates at a clock speed of 1.5 GHz and utilizes the ARMv8-A architecture. This specific model is equipped with 8 GB of Low Power Double Data Rate 4 (LPDDR4) RAM, providing substantial memory capacity for various applications. One notable aspect of the Raspberry Pi 4B is its single power mode, simplifying its power management. The detailed specifications of this device, including its power requirements and other relevant technical data, are outlined in Table 2-3. This configuration ensures that the Raspberry Pi 4B can handle demanding tasks efficiently, making it suitable for a wide range of projects and applications, including those requiring significant computational power and memory resources. Its advanced processor and ample RAM contribute to its versatility and performance, supporting both basic and complex operations effectively.

Table 2-3 Performance characteristics of Raspberry Pi 4B 8GB

Property	**Mode**
	-
Max power [W]	6
Online CPU	4
CPU max frequency [MHz]	1500
GPU TPC	4
GPU max frequency [MHz]	500

Figure 2-20 illustrates a performance comparison represented by individual models from the Raspberry Pi series [133].

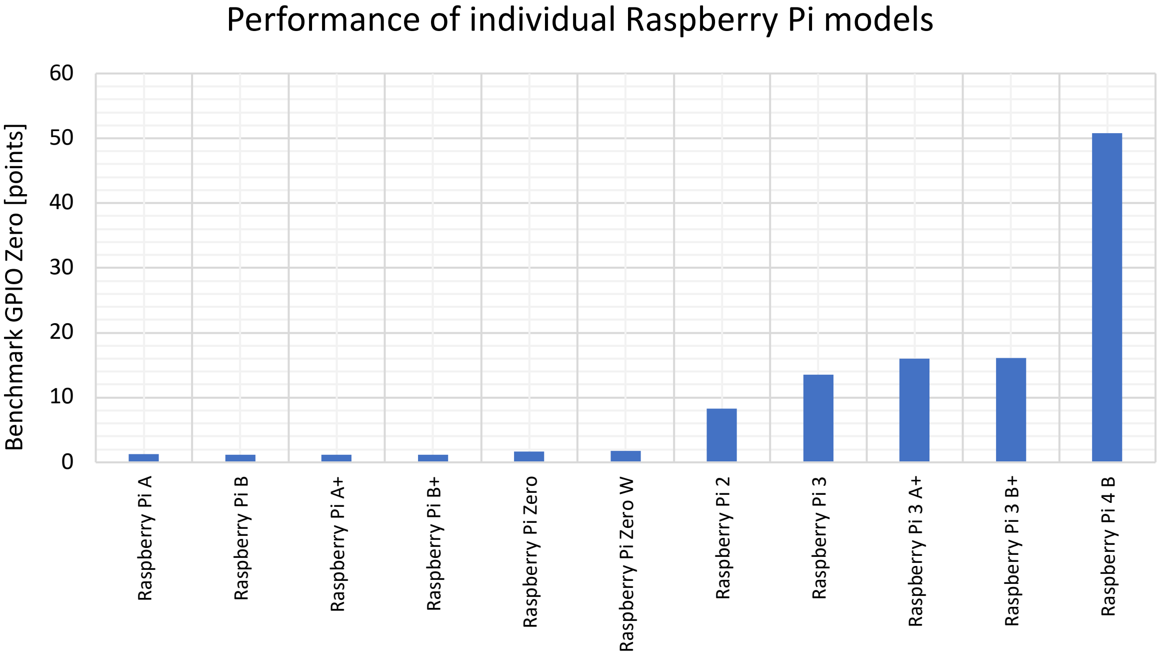

Figure 2-20 Performance comparison of individual Raspberry Pi models [47]

The analysis of the chart reveals that modules from Type A to Zero W exhibit similar computational power, which significantly differs from the other models equipped with more efficient ARM architecture units. Models from 2 to 3 B+ show an increasing performance trend, but the 4B model outperforms its predecessors. Due to the necessity of processing vision sequences, the choice of this unit, characterized by the highest computational power in the entire Raspberry Pi family, was indispensable.

Figure 2-21, on the other hand, presents a comparison of power consumption among the discussed Raspberry Pi family [133]. As the device's performance increases, so does its energy demand. Raspberry Pi 4 B demonstrates the highest performance but also requires the highest power for operation and necessary computations. The latest models exhibit a significant increase in performance with limited energy demand at low loads compared to their predecessors. A more than threefold improvement in computational power does not entail a significant increase in electricity consumption.

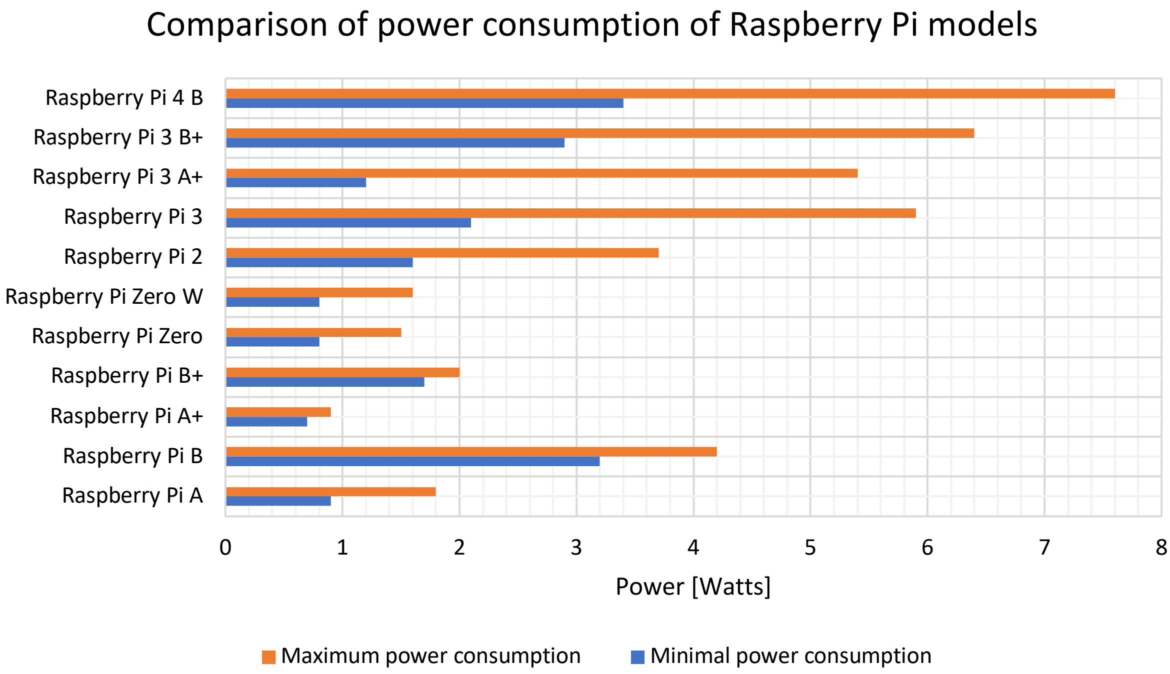

Figure 2-21 Comparison of power consumption of Raspberry Pi models [47]

The Google Coral platform, depicted in Figure 2-19b, features a System-on-Module (SOM) chip that integrates various components essential for AI and machine learning applications [134]. This SOM chip includes built-in eMMC memory and is powered by an integrated circuit based on the NXP i.MX 8M architecture. The NXP i.MX 8M incorporates a Quad-Core ARM Cortex-A53 processor along with an ARM Cortex-M4F core, offering a balance of high-performance processing and low-power efficiency. This architecture is well-suited for handling complex computational tasks, including neural network inference and real-time data processing.

One of the standout features of the Google Coral platform is its Edge TPU (Tensor Processing Unit) accelerator coprocessor. The Edge TPU is specifically designed to accelerate machine learning inference tasks, enabling fast and efficient execution of neural network models directly on the device. This hardware acceleration significantly enhances the performance and responsiveness of AI applications, making the Google Coral platform ideal for edge computing deployments where low latency and real-time processing are critical [134].

In terms of memory, the Google Coral platform is equipped with 1 GB of RAM, providing sufficient memory capacity for running machine learning models and processing data. Additionally, it includes 8 GB of eMMC memory, which serves as onboard storage for storing applications, models, and other data [134].

The combination of powerful processing capabilities, hardware acceleration with the Edge TPU, and ample memory and storage capacity make the Google Coral platform a compelling choice for developers and researchers working on AI-driven applications. Its compact form factor and support for popular machine learning frameworks such as TensorFlow Lite further enhance its versatility and suitability for a wide range of edge computing and IoT applications [134].

Nvidia Jetson Nano microcomputer was the third tested device (Figure 2-19c). This unit boasts a quad-core ARM A57 processor clocked at 1.43 GHz and 2 GB of 64-bit LPDDR4 RAM. Notably, Nvidia Jetson Nano is also equipped with a 128-core Maxwell graphics processor clocked at 921 MHz [135]. This configuration endows the unit with significantly enhanced capabilities for executing machine learning-based operations compared to the Raspberry Pi 4B. Depending on the neural network model utilized, the performance of Nvidia Jetson Nano in this comparison may even exceed that of Raspberry Pi 4B by up to threefold [133], [136]. This microcomputer also offers operation in two modes: energy-efficient (5W) and MAXN (10W). This allows users to balance performance and power efficiency based on their specific needs. Table 2-4 provides a summary of these features and power modes [137].

Table 2-4 Comparison of NVIDIA Jetson Nano operating modes

Property	**Mode**	
	MAXN	**5W**
Max power [W]	10	5
Online CPU	4	2
CPU max frequency [MHz]	1479	918
GPU TPC	1	1
GPU max frequency [MHz]	921.6	640
RAM max frequency [MHz]	1600	1600

The fourth microcomputer utilized in the experiments was the NVIDIA Jetson Xavier AGX (Figure 2-19d). This powerful device features an octa-core, 64-bit ARM®v8.2 processor, complemented by an 8MB L2 cache and a 4MB L3 cache. It boasts a 512-core NVIDIA Volta™ GPU and 64 Tensor cores, which significantly enhance its parallel processing capabilities and make it exceptionally suited for AI and deep learning tasks [138]. Additionally, it includes two

NVIDIA Deep Learning Accelerator (NVDLA) engines, which further boost its ability to handle complex neural network computations efficiently. The Jetson Xavier AGX is equipped with 32 GB of 256-bit LPDDR4x memory, providing ample space for handling large datasets and high-speed operations. It also includes 32 GB of embedded Multi-Media Card (eMMC) memory for onboard storage, ensuring that it can store and access data quickly and efficiently. From an experimental and practical perspective, the NVIDIA Jetson Xavier AGX is particularly notable for its versatility in power management. It supports eight different power modes: MAXN, 10W, 15W, 30W, 30W 6CORE, 30W 4CORE, 30W 2CORE, and 15W DESKTOP. These modes allow users to tailor the device's performance and power consumption to suit specific needs, balancing computational demands with energy efficiency. The details of these power modes are summarized in Table 2-5. This configurability makes the Jetson Xavier AGX an attractive option for a variety of applications, from power-sensitive environments to scenarios requiring maximum computational power. Its robust hardware and flexible power options enable it to deliver optimal performance across a wide range of use cases, making it a valuable asset for experimental AI and robotics projects [137].

Table 2-5 Comparison of NVIDIA Jetson Xavier AGX 32GB operating modes

Property	**Mode**							
	MAXN	**10W**	**15W**	**30W**	**30W 6CORE**	**30W 4CORE**	**30W 2CORE**	**15W DESKTOP**
Max power [W]	n/a	10	15	30	30	30	30	15
Online CPU	8	2	4	8	6	4	2	4
CPU max frequency [MHz]	2265.6	1200	1200	1200	1450	1780	2100	2188
GPU TPC	4	2	4	4	4	4	4	4
GPU max frequency [MHz]	1377	520	670	900	900	900	900	670
RAM max frequency [MHz]	2133	1066	1333	1600	1600	1600	1600	1333

The fifth single board computer, the NVIDIA Jetson Orin AGX (Figure 2-19e), is the latest innovation in NVIDIA's lineup of embedded AI computing devices. This cutting-edge platform marks a substantial advancement in both performance and energy efficiency, making it a pivotal tool for the development and deployment of AI and robotics applications. The Jetson Orin AGX offers high-performance computation capabilities within an energy-efficient and compact module, ideal for a wide range of AI-driven tasks. At the core of the NVIDIA Jetson Orin AGX is the Orin system-on-a-chip (SoC), which integrates next-generation GPU architecture, advanced ARM CPU cores, and high-speed memory technology. This combination ensures that the Jetson Orin AGX delivers exceptional computational performance, capable of handling intensive AI workloads and complex algorithms with ease. The advanced GPU architecture enhances parallel processing capabilities, while the ARM CPU cores provide robust general-purpose processing power. Additionally, the high-speed memory technology ensures rapid data access and processing, further boosting the system's overall performance. This sophisticated AI computing platform is designed to support a variety of applications, including autonomous machines, medical devices, industrial robots, and more. Its compact form factor does not compromise on power, making it a versatile solution for developers seeking to implement AI and machine learning functionalities in their projects. The NVIDIA Jetson Orin AGX thus stands out as a significant leap forward in embedded AI computing, combining powerful performance with energy efficiency to meet the demanding needs of modern AI applications.

One of the key advantages of the Jetson Orin AGX is its support for a wide range of high-speed interfaces. It includes PCIe Gen 4 and USB4, which facilitate the connection of various peripheral devices, such as sensors, cameras, and other input/output devices. This versatility allows for the integration of multiple components, enhancing the system's overall functionality and performance. Additionally, the unit features Gigabit Ethernet and Wi-Fi capabilities, ensuring fast and reliable data transmission, which is essential for networking applications.

In terms of energy efficiency, the Jetson Orin AGX stands out as the most efficient embedded device in this comparison. It supports four distinct power modes: MAXN, 15W, 30W, and 50W. These modes provide flexibility in power consumption and performance, enabling the device to adapt to different operational requirements and conserve energy when full computational power is not needed.

The summarized specifications and capabilities of the Jetson Orin AGX are presented in Table 2-6, highlighting its superior performance and versatility in supporting high-speed data processing and connectivity needs across various applications [139].

Table 2-6 Comparison of NVIDIA Jetson Orin AGX 64GB operating modes

Property	**Mode**			
	15W	**30W**	**50W**	**MAXN**
Max power [W]	15	30	50	n/a
Online CPU	4	8	12	12
CPU max frequency [MHz]	1113.6	1728	1497.6	2201.6
GPU TPC	3	4	8	8
GPU max frequency [MHz]	420.75	624.75	828.75	1301
RAM max frequency [MHz]	2133	3200	3200	3200

Additionally, to compare the performance of embedded systems, a virtual machine was presented. The utilization of a robust virtual machine with advanced hardware specifications provided a computational environment conducive to conducting comprehensive laboratory testing and analysis. The Intel Core i7-7700HQ CPU, with its high clock speed and multiple cores, offered significant processing power, enabling efficient execution of complex algorithms and simulations. The substantial RAM capacity of 15.6 GB ensured ample memory resources for handling large datasets and running memory-intensive applications without performance degradation. This was particularly advantageous for processing and analysing the vast amount of data generated during experimental testing. The SVGA3D graphics card, hosted by the NVIDIA GeForce GTX 1050Ti, provided enhanced graphical capabilities, facilitating the visualization of experimental results with high fidelity and detail. This was essential for accurately interpreting and analysing vision data, such as images and videos, obtained from the embedded systems under evaluation. The choice of Ubuntu 18.04.5 LTS 64-bit as the operating system offered stability, security, and compatibility with a wide range of software tools and libraries commonly used in scientific and engineering applications. Additionally, the 64-bit architecture allowed for efficient utilization of system resources and support for handling large datasets and complex computations.

The equipment parameters are summarized in Table 2-7 based on [132], [135], [140]. This evaluation aimed to select a device suitable for developing a measurement platform to assess the operational quality of airport lamps. Key criteria included compact size and high performance. To compare the performance of three devices under consideration, benchmarks were conducted using two different benchmarks: TTSIOD 3D Renderer (utilizing Phong Rendering with Soft-Shadow Mapping) and PyBench (evaluating Total For Average Test Times). In the former benchmark, a higher FPS value indicates superior performance, while in the latter, increased computing time signifies inferior performance. In both benchmarks, a virtual machine exhibited the best performance, serving as a benchmark for workstation performance. Notably, the Nvidia Jetson Nano outperformed the others in the TTSIOD 3D Renderer benchmark, owing to its superior graphics processor. Conversely, the Raspberry Pi 4 Model B showcased a more efficient CPU processor, as evidenced by its performance in the PyBench benchmark.

A critical aspect in designing such devices is evaluating computational efficiency. This efficiency, in the context of video sequence analysis, is directly influenced by factors like image resolution and the number of frames per second that can be processed. Another key factor is power consumption; it needs to be minimized to reduce the overall size and weight of the device, predominantly the batteries, and to lessen the frequency of recharging.

The mean frames per second (FPS) was computed using equation (35), where the FPS variable represents the result, n denotes the total number of video frames statistically measured, and T signifies the total processing time for the entire set of n frames executed by the algorithm.

$$\overline{FPS} = \frac{\mathrm{n}}{\mathrm{T}} \tag{35}$$

Table 2-7 Performance comparison of virtual machine and Single Board Computers

Property	**Virtual machine**	**Raspberry Pi 4 model B**	**NVIDIA Jetson Nano**
Processor	Intel Core i7-7700HQ CPU 2.80GHz – 3.8 GHz × 4	BCM2711 Cortex A72 Quad Core 1.5 GHz	ARM Cortex A57 1.43GHz
RAM	15.6 GB	8 GB	4 GB
Graphics	SVGA3D (host: NVIDIA GeForce GTX 1050Ti (4096 MB memory)	Broadcom VideoCore VI	GPU NVIDIA Maxwell 128-core NVIDIA CUDA
Operating system	Ubuntu 18.04.5 LTS 64-bit	Raspbian Buster 10	Ubuntu 18.04 LTS 64-bit
TTSIOD 3D Renderer **Phong Rendering With Soft-Shadow Mapping**	146.04 FPS	32.75 FPS	41.25 FPS
PyBench **Total For Average Test Times**	1345 milliseconds	5679 milliseconds	7084 milliseconds

Table 2-8 presents an overall comparison of the devices used at work, showing the most important technical data based on [132], [134], [135], [138], [139].

Table 2-8 Comparison of parameters of Single Board Computers used in dissertation

Property	Raspberry Pi 4B	Google Coral	NVIDIA Jetson Nano	NVIDIA Jetson Xavier AGX	NVIDIA Jetson Orin AGX
CPU	Quad-core Cortex-A72 (ARM v8)	Quad-core Cortex-A53 (ARM v8)	Quad-core ARM Cortex-A57	8-core NVIDIA Carmel ARM v8.2 64-bit	12-core ARM Cortex-A78AE v8.2
GPU	Broadcom VideoCore VI	GC7000 Lite Graphics Processor	128-core Maxwell	512-core Volta with Tensor Cores	2048-core Ampere with Tensor Cores
RAM	2GB, 4GB, or 8GB LPDDR4	1GB LPDDR4	4GB LPDDR4	32GB LPDDR4x	32GB LPDDR5
Storage	microSD	8GB eMMC, microSD	microSD, 16GB eMMC (optional)	32GB eMMC	64GB eMMC
AI Performance	N/A	4 TOPS (Edge TPU)	0.5 TFLOPS (FP16)	32 TOPS (INT8)	200 TOPS (INT8)
Connectivity	2 × USB 3.0, 2 × USB 2.0, HDMI, Gigabit Ethernet, Wi-Fi, Bluetooth	1 × USB 3.0, HDMI, Gigabit Ethernet	4 × USB 3.0, HDMI, Gigabit Ethernet	4 × USB 3.1, 2 × HDMI, 2 × Gigabit Ethernet	4 × USB 3.2, 2 × HDMI, 2 × Gigabit Ethernet
Camera Interface	2-lane MIPI CSI-2	4-lane MIPI CSI-2	2-lane MIPI CSI-2	16-lane MIPI CSI-2	16-lane MIPI CSI-2
Power Consumption	3W idle, 7.6W max	5-10W	5-10W	30W typical, 50W max	40W typical, 60W max
Dimensions	85.6 × 56.5 mm	88 × 60 × 24 mm	100 × 80 × 29 mm	105 × 105 × 72 mm	100 × 87 × 65 mm
Weight	46g	45g	140g	280g	700g
Special Features	Dual monitor support, GPIO pins	Integrated Edge TPU for ML tasks	Low-power AI computing	Advanced AI capabilities, Multiple camera support	High-end AI and robotics applications

As noted, the advancements in microcontroller technology have paved the way for the implementation of increasingly sophisticated image processing algorithms and the handling of complex video sequences. These technological strides are particularly beneficial as they enable the creation of portable devices that can be powered by batteries due to their low energy consumption. The development and design of prototypes for mobile vision processing solutions are greatly aided by the availability of a wide array of minicomputers from well-known families such as Raspberry Pi and NVIDIA Jetson. It's also noteworthy that industrial versions of these minicomputers can be utilized, which offer not only professional-grade performance but also durability for long-term operations [141].

Typically, manufacturers of evaluation platforms provide performance metrics for the microprocessors they use. Specialized websites (for example, on the [142] website) offer comparisons of various performance metrics such as integer math operations, floating-point math operations, finding prime numbers, sorting random strings, data encryption, and data compression. These metrics, however, are often not directly comparable to image processing performance, especially when the algorithms in question include conditional instructions.

Moreover, the assessment of computational performance is detailed on websites like [143], where the focus is on popular deep neural network solutions. Performance results are usually presented in terms of Samples/sec for various NVIDIA Jetson models, factoring in power requirements. It's important to note that these neural networks typically operate at relatively low resolutions, and the consumption analysis often does not consider the different power supply modes available. For instance, information is available indicating that each NVIDIA Jetson module was tested at maximum performance settings (MAXN).

The efficiency of video sequence processing has also been discussed extensively in scientific literature. For example, the [144] paper reviews various algorithms including the Canny edge detection algorithm, road line tracking, face and eye recognition, motion detection, and object detection. The Raspberry Pi 4 served as the experimental platform in this study, with maximum power and frequency values for the CPU and GPU provided, although specific values for individual algorithms were not detailed. Additionally, the Raspberry Pi 4 module was utilized in the research documented in manuscript [145], where the author investigated frame rate, frame transfer delay, and frame processing time, though energy consumption was not explored.

Performance analyses for the NVIDIA Jetson family modules can also be found in various publications. For instance, paper [146] describes a vision system designed to recognize fiducial markers including the ARTag type. This system comprises two Logitech HD Pro Webcam C920 cameras and a NVIDIA Jetson TX2 module that handles digital image processing. Performance and power consumption of the NVIDIA Jetson Orin AGX are analysed in manuscript [147], focusing on mean Average Precision (mAP) as a function of FPS and different image sizes. The task of line detection using the NVIDIA Jetson Xavier NX is discussed in [148], where the authors proposed a CNN Encoder-Decoder network architecture, testing their solution at various image resolutions up to 1280 × 720. In these studies, energy consumption was not a focus.

A comprehensive benchmark analysis of NVIDIA Jetson Platforms (Nano, TX2, NX, and AGX) is presented in paper [149]. This study includes measurements of resource usage and power consumption without considering the impact of image resolution. Furthermore, performances of single-board computers such as the NVIDIA Jetson Nano, NVIDIA Jetson TX2, and Raspberry PI4, using a Convolutional Neural Network (CNN) algorithm created with a fashion product images dataset, are compared in [136]. The authors examined metrics like processing power (CPU, GPU), memory (RAM, cache), power consumption, and cost. However, they did not conduct an analysis of frame rate processing speed (FPS).

2.3.2. Parameters evaluation of cameras in embedded systems

The advancement of embedded systems has facilitated sophisticated real-time analysis of video sequences. This progress is largely attributed to TinyML [150], which has enabled the integration of machine learning into small devices that are constrained by efficiency and power consumption. To fully exploit the potential of this technology, one must possess a comprehensive understanding of its applications, algorithms, hardware, and software. In particular, video signal processing necessitates the use of relatively high-performance modules [46].

Vision systems equipped with cameras for acquiring video data are extensively used in various fields. They are integral to autonomous vehicles and cars [127], [128], city monitoring systems [5], and specialized applications, such as the measurement platform for testing the quality of airport lamps [28]. This platform is designed to measure the luminous efficiency of in-pavement lamps at airports, assessing their wear and tear. The system then classifies each lamp, determining whether it is unusable or needs replacement. The decrease in luminous efficiency can be attributed to adverse weather conditions and the routine operation of runways and taxiways, especially during snow removal activities.

Embedded systems that facilitate the analysis of data from cameras offer the advantage of achieving satisfactory results while maintaining relatively low purchase costs compared to traditional computing units [30], [47]. These systems support connectivity with vision cameras through both the MIPI CSI-2 and USB interfaces. A detailed comparison of the features of these interfaces is presented in Table 2-9 [151].

Table 2-9 MIPI Camera vs USB Camera – a feature-by-feature comparison

Features	**MIPI CSI-2**	**USB 3.0**
Availability on SoC	Many (Typically 6 lanes available)	On high-end SoCs
Bandwidth	320 MB/s/lane 1280 MB/s (with 4 lanes)	400 MB/s
Cable Length	< 30 cm	< 5 meters
Space Requirements	Low	High
Plug-and-play	Not supported	Supported
Development Costs	Medium to High	Low

To compare the cameras, a standard ISO 12233 test chart [152] can be utilized. This chart is widely used to determine the resolving power of a camera sensor and/or its lens under laboratory conditions. It is a benchmark tool frequently employed in various tests of photographic equipment due to its precision and reliability. The ISO 12233 test chart helps in assessing the camera's ability to capture fine details and its overall image quality.

The ISO 12233 test chart is a comprehensive tool featuring numerous patterns that challenge a camera's resolving power, contrast, and clarity. By analysing how well a camera can reproduce these patterns, one can evaluate its performance in terms of sharpness and detail resolution. This makes it an essential component in the comparison of different cameras, especially when determining their suitability for specific applications such as machine learning and image processing within embedded systems.

In practical terms, using the ISO 12233 test chart involves capturing images of the chart under controlled lighting conditions. These images are then analysed to measure various parameters such as spatial resolution, line pairs per millimetre (lp/mm), and overall image fidelity. This standardized approach ensures that the camera's capabilities are accurately assessed, providing a clear benchmark for comparing different models.

Figure 2-22 presents a visual representation of the ISO 12233 test chart, showcasing the various patterns and details used for testing. This figure is crucial for understanding the specific elements that are evaluated during the camera comparison process.

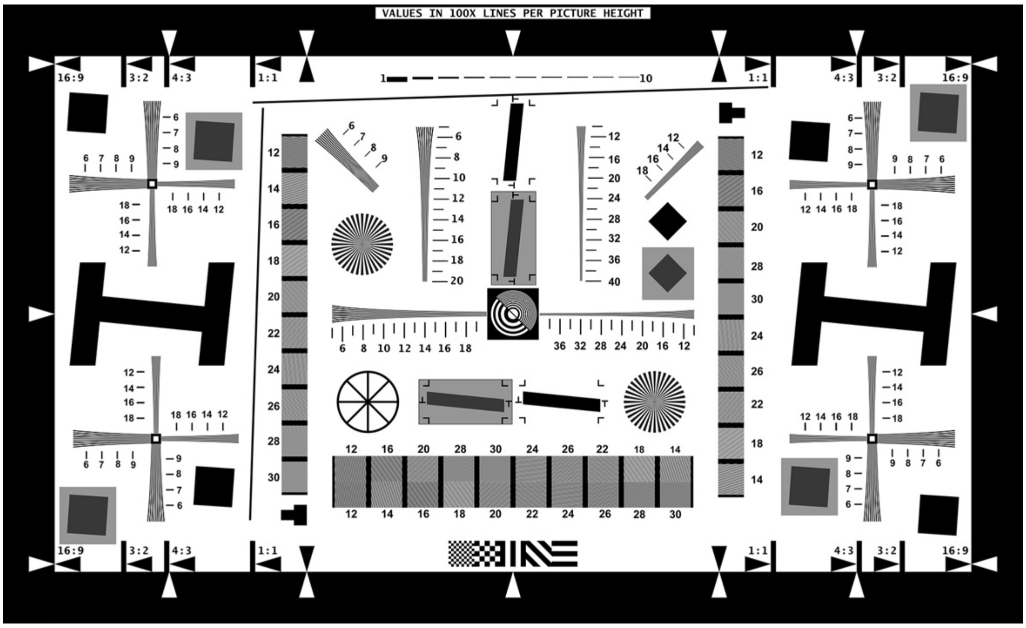

Figure 2-22 ISO 12233 Standard Test Chart [152]

The smooth variation in the thickness of the test field lines on the ISO 12233 chart allows for precise identification of the point at which the lens (and the sensor) can no longer resolve details. Resolution is measured in lines per picture height (lph). For instance, if the most densely packed but still discernible lines on the test field correspond to the number 16, it indicates that 1600 lines can be recognized along the entire height of the horizontal frame. It's important to note that vertical and horizontal resolutions are typically not the same, and the smaller of the two readings is considered the test result.

To determine the resolution score, the results need to be processed by converting the highest achieved resolution in the frame centre to a 1-megapixel matrix. This conversion involves dividing the result by R, where R represents the number of millions of pixels (megapixels) in the camera sensor used for the test. This standardization allows for direct comparison of image resolution obtained from cameras with sensors of different resolutions. By converting the resolution to a 1-megapixel standard, one can accurately assess the performance of the lens and camera combination. This method also facilitates the evaluation of whether using a camera with a higher resolution sensor would yield proportionally higher image resolution. Essentially, this conversion provides a clear understanding of the efficiency and effectiveness of the lens and camera together, independent of the sensor’s pixel count.

This approach is particularly useful in embedded system applications where high image quality is critical, but resources may be limited. By understanding the actual resolving power of the camera system, developers can make informed decisions about the best equipment to use for specific tasks, such as machine learning and image analysis. The conversion ensures that the performance of different cameras can be objectively compared, ensuring that the chosen system meets the necessary requirements for high-quality vision data processing.

During laboratory tests, four cameras were evaluated, each offering distinct specifications tailored to various applications. Below are the characteristics of each camera.

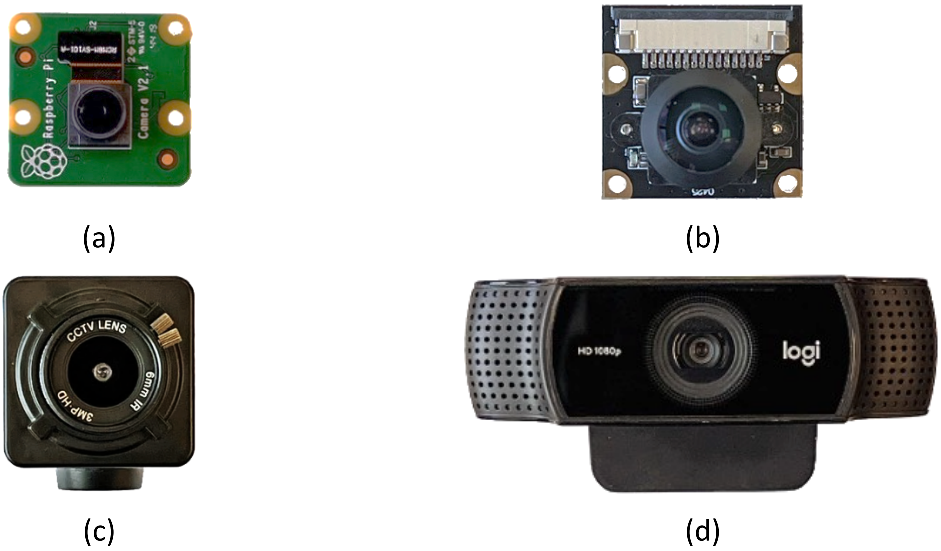

Figure 2-23 Selected cameras [46]: (a) Raspberry Pi Camera HD v2 with a viewing angle of 62.2°, (b) Waveshare 16579 160°, (c) Camera IMX477 with 6mm CS-Mount lens and (d) Camera Logitech C922

The camera modules are equipped with the IMX219 sensor (Figure 2-23a, b), featuring a resolution of 8 megapixels and a viewing angle of either 62.2 degrees (Figure 2-23a) or 160 degrees (Figure 2-23b). These cameras offer the capability to record video sequences in multiple modes, including 1080p30, 720p60, and 640 × 480p90. Both cameras are designed with a CSI (Camera Serial Interface) connector, facilitating easy integration with compatible hardware platforms. However, despite having identical sensors, camera (Figure 2-23b) is not compatible with the Raspberry Pi 4B and Google Coral microcomputers. While both cameras share the same sensor, compatibility issues may arise due to differences in firmware, driver support, or interface configurations between the two camera modules. As a result, camera (Figure 2-23b) cannot be utilized with the Raspberry Pi 4B and Google Coral microcomputers.

To address this compatibility issue, relevant libraries have been developed and made available for servicing these camera modules via devices from the NVIDIA Jetson family [153]. The NVIDIA Jetson family of microcomputers provides robust support for a wide range of camera modules and peripherals, offering developers a versatile platform for building AI and computer vision applications. By leveraging these libraries and the NVIDIA Jetson platform, users can effectively utilize camera modules with the IMX219 sensor, ensuring seamless integration and optimal performance in their projects.

The camera housed in a protective metal casing features an IMX477 sensor (Figure 2-23c), boasting a resolution of 12.3 megapixels in the 1/2.3" format, with a maximum image resolution of 4056 × 3040 pixels. It is equipped with a 6 mm focal length lens. To facilitate connectivity with microcomputers, a CSI to HDMI adapter is employed. This setup enables recording in two primary modes: 60 frames per second (FPS) in full 4k2k resolution and 60 FPS in 1080p [154].

On the other hand, the Logitech C922 camera (Figure 2-23d) offers a maximum resolution of 1080p at 30 FPS and 720p at 60 FPS, with a viewing angle of 78 degrees. This camera is operated via the USB interface [155].

Both cameras serve distinct purposes and offer unique capabilities. The camera with the IMX477 sensor, with its high resolution and 60 FPS recording capability in full 4k2k resolution, is well-suited for applications requiring detailed imaging and high frame rates, such as surveillance, scientific imaging, and video production.

Conversely, the Logitech C922 camera, with its USB interface and maximum resolution of 1080p at 30 FPS, is ideal for video conferencing, live streaming, and casual video recording applications. Its wide viewing angle of 78 degrees provides a good field of view for capturing group settings or wider scenes.

Table 2-10 presents an overall comparison of cameras used in dissertation, showing the most important technical data based on [153], [154], [155].

Table 2-10 Comparison of parameters of cameras used in Single Board Computers

Parameter	Raspberry Pi Camera HD v2	Waveshare 16579	Camera IMX477 with 6mm CS-Mount Lens	Logitech C922
Image Sensor	Sony IMX219	OmniVision OV5647	Sony IMX477	HD CMOS
Resolution	8 Megapixels (3280 × 2464)	5 Megapixels (2592 × 1944)	12.3 Megapixels (4056 × 3040)	2 Megapixels (1920 × 1080)
Lens	Fixed Focus	Fisheye Lens	6mm CS-Mount Lens	Autofocus
Field of View (FOV)	62.2°	160°	~66° (depending on lens configuration)	78°
Max Frame Rate	30 FPS (at 1080p)	30 FPS (at 1080p)	60 FPS (at 1080p)	30 FPS (at 1080p) / 60 FPS (at 720p)
Video Modes	1080p30, 720p60, 640 × 480p60/90	1080p30, 720p60, 640 × 480p60/90	1080p60, 4K15	1080p30, 720p60
Connectivity	CSI-2	CSI-2	CSI-2	USB 2.0
Dimensions	25 × 23 × 9 mm	25 × 24 × 21 mm	38 × 38 × 18.4 mm (excluding lens)	95 × 71 × 43 mm
Weight	3g	10g	11.5g (excluding lens)	162g
Special Features	-	Wide-angle view, Infrared support	High resolution, Manual focus lens	Built-in microphone, Low-light correction

The use of video cameras also requires calibration of selected devices, because they often introduce image distortions. The two main types of distortion are radial distortion and tangential distortion. Radial distortion causes straight lines to appear curved. The radial distortion becomes greater the further the points are from the centre of the image.

Radial distortion can be represented by the following equation [156]:

$$x_{\text{distorted}} = x(1 + k_1 r^2 + k_2 r^4 + k_3 r^6) \tag{36}$$

$$y_{\text{distorted}} = y(1 + k_1 r^2 + k_2 r^4 + k_3 r^6) \tag{37}$$

where:

- k – lens distortion coefficients associated with radial distortion. These parameters quantify the extent to which radial distortion affects the image. Higher values of these coefficients correspond to increased distortion, particularly at the edges of the image.

- r – the distance of an image point from the optical centre of the lens (distortion centre), measured in image coordinates (in pixels or normalized units). This distance is critical, as radial distortion intensifies with increasing distance from the image centre.

Tangential distortion arises due to the misalignment of the camera lens with respect to the imaging plane. This misalignment results in certain regions of the captured image appearing closer than anticipated. The extent of tangential distortion can be quantified as follows [156]:

$$x_{\mathrm{distorted}} = x + \ [2p_1xy + \ p_2(r^2 + 2x^2)] \tag{38}$$

$$y_{\mathrm{distorted}} = y + \ [\,p_1(r^2 + 2x^2) + \ 2p_2xy] \tag{39}$$

In summary, it is essential to determine five specific parameters, referred to as distortion coefficients, which are expressed as follows [156]:

$$\text{Distortion coefficients} = (\,k_1 \ \ k_2 \ \ p_1 \ \ p_2 \ \ k_3) \tag{40}$$

where:

- p – coefficients of tangential distortion. Tangential distortion arises when the lens is not perfectly aligned with the image plane. These parameters characterize this non-linear distortion, which depends on the position of the point within the image.

2.3.3. Comparison of the quality of micro cameras in single board computers

Due to the need to use a vision system in the proposed solution, it was justified to assess the quality of micro cameras in single board computers, capable of analysing the image of the tested lamps and prisms. As part of laboratory tests, a comprehensive evaluation was conducted involving a series of photographs and video recordings of video sequences based on a standard ISO 12233 test chart [46].

The cameras were meticulously positioned at appropriate distances to enable a thorough investigation of lens distortion and image detail across various regions, including the centre and peripheral areas. Subsequently, a subjective assessment of the acquired resolutions was conducted for each camera setting and selected areas of interest.

To ensure consistent and uniform illumination, an Aputure Amaran 100x studio lamp paired with the Godox QR-P90 parabolic softbox was utilized. This setup facilitated the acquisition of high-quality images with uniform lighting conditions, crucial for accurate assessment.

Figure 2-24 provides a visual comparison of the images obtained from the tested micro cameras, showcasing the differences in image quality, clarity, and resolution. This comparative analysis allows for a qualitative evaluation of each camera's performance under controlled conditions. Table 2-11 shows a comparison of EXIF data from the obtained images of the tested cameras.

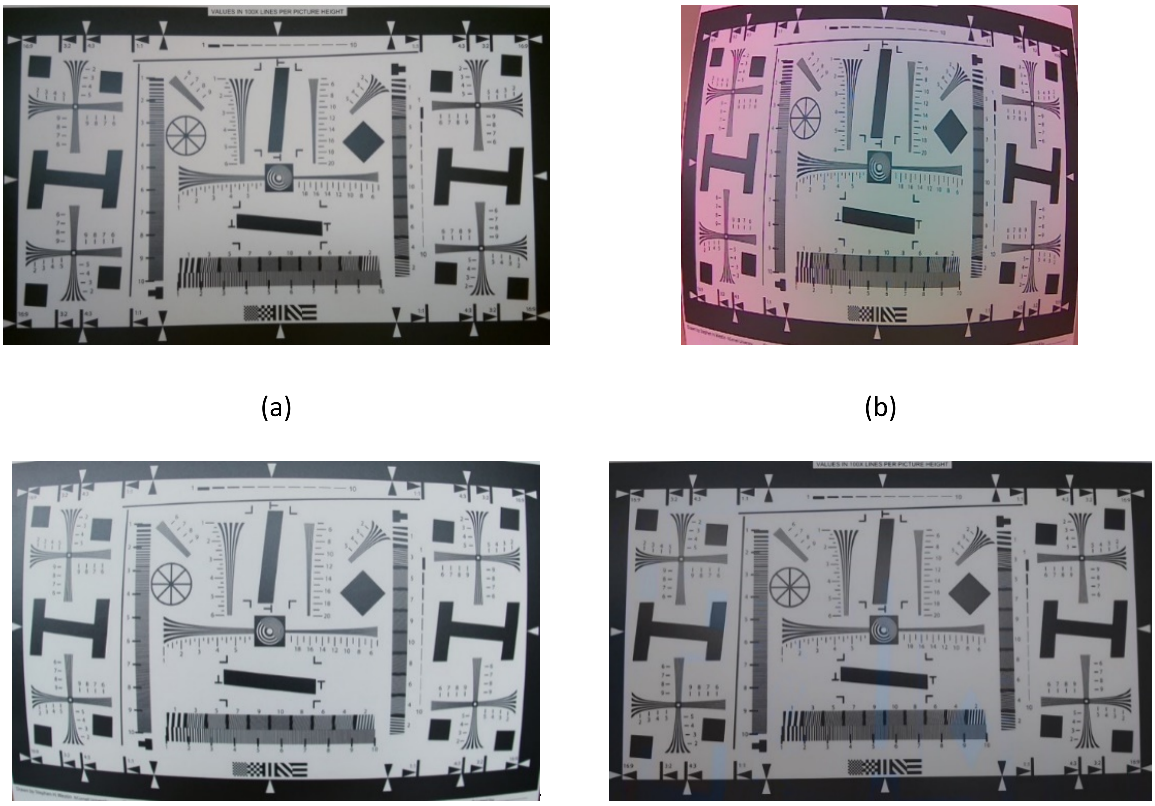

(a) (b)

(c) (d)

Figure 2-24 Comparison of ISO 12233 standard test chart images obtained with tested cameras [46]: (a) Image from Raspberry Pi Camera HD v2, (b) Image from Waveshare 16579 camera, (c) Image from Camera IMX477 with 6 mm CS-Mount lens, (d) Image from Logitech C922 camera

Table 2-11 Comparison of EXIF data from the obtained images of the tested cameras

Camera model	**Raspberry Pi Camera HD v2**	**Camera Waveshare 16579**	**Camera IMX477 with 6mm CS-Mount lens**	**Camera Logitech C922**
Colour space	RGB	RGB	RGB	RGB
Colour profile	sRGB I EC61966-2.1	sRGB IEC61966-2.1	sRGB IEC61966-2.1	sRGB IEC61966-2.1
Focal length	3 mm	6 mm	6 mm	3.7 mm
Aperture value	f/2.0	f/2.35	f/2.0	f/2.0
Exposure time	1/64	1/64	1/64	1/64
ISO	50	50	50	50

Furthermore, Figure 2-25 presents a detailed comparison of a selected fragment from the acquired images, focusing on specific areas of interest. This close-up comparison enables a more granular assessment of image detail, allowing for the identification of any distortions or artifacts present in the captured images.

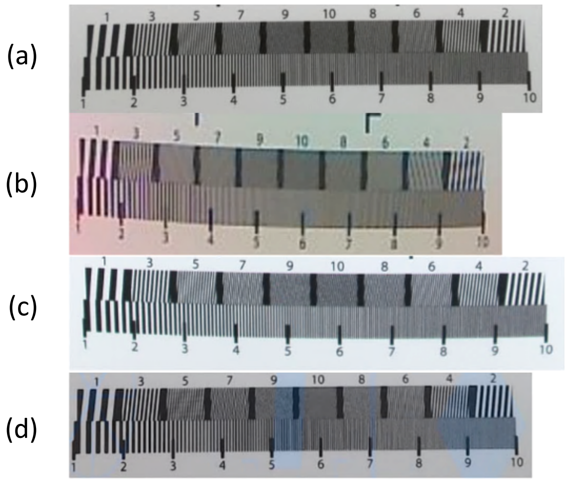

Figure 2-25 Comparison of image fragments of test charts obtained with the tested cameras [46]

Among the tested cameras, the Waveshare 16579 camera exhibited the most pronounced drawbacks, particularly when using the wide-angle lens with a viewing angle of 160° (Figure 2-25b). While it demonstrated good sharpness and quality in the frame centre, the image quality significantly degraded outside of this area, characterized by unreadable details and high vignetting. Additionally, the camera tended to produce reddish photos in daylight due to the absence of an IR filter in the CCD sensor. However, this lack of an IR filter enabled the camera to capture images in low-light conditions using IR LEDs. Consequently, the suitability of this camera for applications requiring high image detail appears limited.

On the other hand, the Logitech C922 camera yielded satisfactory results, but its configuration options were restricted due to its design primarily intended for webcam use. Although satisfactory results were achieved during testing, inconsistencies were observed, making reproducibility challenging (Figure 2-25d).

In contrast, the Raspberry Pi Camera HD v2 delivered high-quality images with detailed resolution (Figure 2-25a). Notably, it offers comprehensive manual configuration options, making it a popular choice among users. However, its design limitations preclude the use of universal lenses.

The IMX477 camera, equipped with a 6 mm CS-Mount lens, emerged as the top performer for the applications discussed in this dissertation, as evidenced by the resulting image (Figure 2-25c). Its design allows for the utilization of professional DSLR lenses, such as those from the Canon EOS EF line, enabling customized adaptation to the specific requirements of systems testing mechanical wear of airport lamps. Moreover, the camera features a durable housing and supports connection via HDMI interface with a converter to CSI, simplifying its integration into the measuring platform for quality testing of airport lamps. This comprehensive set of features and capabilities makes the IMX477 camera an ideal choice for demanding applications where image quality, adaptability, and reliability are paramount.

2.4. Methods for assessing the effectiveness of algorithms

The evaluation of algorithm performance is crucial in computer science, particularly in the field of machine learning and data mining [157]. One of the most informative tools for this purpose is the confusion matrix, which provides a detailed breakdown of the classification outcomes. This chapter delves into the various aspects of the confusion matrix and explores different metrics derived from it to assess the effectiveness of algorithms [108], [157], [158].

A confusion matrix is a table used to describe the performance of a classification model on a set of test data for which the true values are known. It compares the actual target values with those predicted by the model [158]. The matrix itself is a 2 × 2 table for binary classification, with the following elements:

- True Positives (TP): Instances correctly classified as positive
- True Negatives (TN): Instances correctly classified as negative
- False Positives (FP): Instances incorrectly classified as positive (Type I error)
- False Negatives (FN): Instances incorrectly classified as negative (Type II error).

This matrix helps in understanding not only the accuracy of a model but also its ability to differentiate between classes.

The confusion matrix allows for the calculation of several critical performance metrics, including [158]:

- Accuracy:

$$\mathrm{Accuracy} = \frac{\mathrm{TP} + \mathrm{TN}}{\mathrm{TP} + \mathrm{TN} + \mathrm{FP} + \mathrm{FN}} \tag{41}$$

Accuracy measures the proportion of total correct predictions. However, it can be misleading in cases of class imbalance.

- Precision (Positive Predictive Value):

$$\mathrm{Precision} = \frac{\mathrm{TP}}{\mathrm{TP} + \mathrm{FP}} \tag{42}$$

Precision indicates the percentage of positive predictions that are actually correct. It is particularly useful when the cost of false positives is high.

- Recall (Sensitivity or True Positive Rate):

$$\mathrm{Recall} = \frac{\mathrm{TP}}{\mathrm{TP} + \mathrm{FN}} \tag{43}$$

Recall measures the ability of the model to identify all relevant instances. It is crucial in contexts where missing a positive case has significant consequences.

- Specificity (True Negative Rate):

$$\text{Specificity} = \frac{\text{TN}}{\text{TN} + \text{FP}} \tag{44}$$

Specificity evaluates the ability of the model to identify negative instances correctly. It is important in situations where the cost of false positives is high.

- F1 Score:

$$\text{F1} = 2 * \frac{\text{Precision} \ * \text{Recall}}{\text{Precision} + \text{Recall}} \tag{45}$$

The F1 score provides a balance between precision and recall, especially useful when dealing with imbalanced datasets.

- Balanced Accuracy:

$$\text{Balanced Accuracy} = \frac{\text{Sensitivity} + \text{Specificity}}{2} \tag{46}$$

This metric accounts for class imbalance by averaging the sensitivity and specificity.

In addition to the basic metrics, several other measures can provide deeper insights into the model's performance [158]:

- Positive Predictive Value (PPV) and Negative Predictive Value (NPV):

$$\text{PPV} = \frac{\text{TP}}{\text{TP} + \text{FP}} \tag{47}$$

$$\text{NPV} = \frac{\text{TN}}{\text{TN} + \text{FN}} \tag{48}$$

These values help understand the probability that positive and negative predictions are correct, respectively.

- ROC Curve and AUC (Area Under the Curve):

The ROC curve plots the true positive rate against the false positive rate at various threshold settings. The AUC represents the likelihood that the model ranks a randomly chosen positive instance higher than a randomly chosen negative one.

- Precision-Recall Curve:

Particularly useful in imbalanced datasets, this curve plots precision against recall. It is often more informative than the ROC curve when the positive class is rare.

Despite its usefulness, the confusion matrix has limitations. For instance, it does not account for the costs associated with different types of errors. Moreover, metrics such as accuracy can be misleading in highly imbalanced datasets, where precision, recall, and the F1 score might provide a clearer picture of the model's performance.

The confusion matrix and its derived metrics are indispensable tools for evaluating the performance of classification algorithms. By providing detailed insights into the true positives, true negatives, false positives, and false negatives, it allows researchers to fine-tune models and achieve better accuracy, precision, and recall. Understanding and appropriately applying these metrics is critical in developing effective and reliable algorithms across various applications in computer science [108], [157], [158].

- Mean Average Precision (mAP):

Mean Average Precision (mAP) is a standard metric in machine learning for assessing the accuracy of a model's predictions, particularly in object detection tasks. This metric evaluates the extent to which the predicted bounding boxes for objects align with the actual ground truth boxes. It does so by considering both precision, which is the ratio of correctly identified objects (true positives) to the total number of objects identified (both true positives and false positives), and recall, which is the ratio of correctly identified objects to the total number of actual objects present (true positives and false negatives) [159].

- Mean Average Precision 50-95 (mAP50-95):

mAP50-95 denotes the mean Average Precision computed across multiple Intersection over Union (IoU) thresholds, usually ranging from 0.50 to 0.95, with increments of 0.05. IoU is a metric that measures the degree of overlap between predicted bounding boxes and ground truth boxes in object detection tasks. The mAP50-95 metric offers a more detailed and rigorous evaluation of a model's performance by accounting for different levels of overlap, thereby providing a more stringent and nuanced assessment than mAP computed at a single IoU threshold, such as mAP50 [159].

Chapter

3. Detection of Foreign Object Debris

3.1. FOD detection system concept

The system concept revolves around a camera and an embedded device installed within the vehicle of airport services, traversing critical areas of manoeuvring areas. The primary objective is to enhance the detection of Foreign Object Debris (FOD) by enabling the system's deployment across multiple vehicles, thereby expanding coverage and improving safety protocols.

Figure 3-1 illustrates a block diagram outlining the FOD detection system's workflow. The process initiates with video capture facilitated by a camera affixed to the vehicle's hood. Subsequently, the captured video signal is transmitted to the embedded system, where a sequence of operations unfolds. Initially, the video undergoes preprocessing to enhance its quality and optimize for further analysis. Following preprocessing, the system executes FOD detection algorithms, identifying and isolating objects of interest within the captured footage. Once potential FOD items are identified, the system proceeds with classifying these objects to determine their nature and associated risks.

In the final phase of the workflow, upon successful detection and classification of FOD, the user is promptly notified, signalling the need for immediate removal or mitigation measures. This real-time feedback mechanism ensures swift response and intervention, thereby mitigating potential hazards and minimizing operational disruptions at the airport.

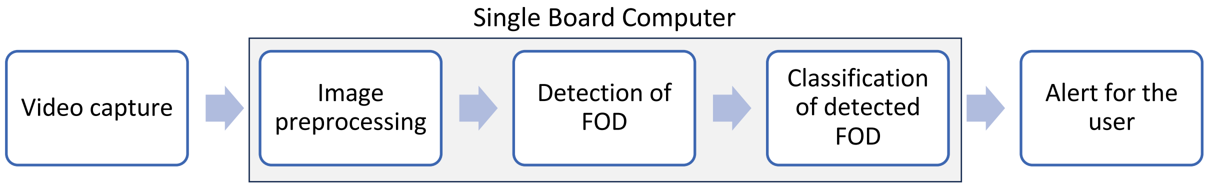

Figure 3-1 Block diagram of information processing in the proposed FOD detection system

By integrating advanced imaging technology with embedded processing capabilities, the FOD detection system offers a proactive approach to enhancing safety protocols in airport operations. Its ability to seamlessly integrate into existing vehicle fleets and provide timely alerts underscores its potential to bolster operational efficiency and ensure the integrity of runway surfaces, ultimately contributing to safer air travel experiences.

Figure 3-2 illustrates the practical implementation of the system concept at the Poznań–Ławica Airport, where a camera is strategically mounted on the front of the vehicle. This setup allows for real-time monitoring of critical areas within the airport premises, facilitating early detection of Foreign Object Debris and other potential hazards.

Figure 3-2 The concept of the FOD detection system (camera mounted on the front of a car moving along the runway at the Poznań–Ławica Airport) [37]

3.2. Datasets of aerodrome FODs

3.2.1. Standard FOD-A dataset

The issue of detecting FOD on aerodromes requires analysing available public datasets of such objects. The Foreign Object Debris in Airports (FOD-A) dataset [160] stands as a pivotal resource tailored to support the development and assessment of Foreign Object Debris (FOD) detection systems, as depicted in Figure 3-3. Comprising an extensive collection of over 30000 high-resolution (2048 × 1080 to 4272 × 2848 pixels) JPG images sourced from various airports worldwide, this dataset offers a diverse array of scenarios to facilitate robust system evaluation and validation.

The images within the FOD-A dataset are captured using a spectrum of cameras, including RGB cameras and thermal cameras, thus encompassing a broad spectrum of imaging modalities. This diversity ensures comprehensive coverage across different weather conditions, lighting scenarios, and types of debris encountered in airport environments, enhancing the dataset's utility for system testing and benchmarking.

Figure 3-3 Examples of images from dataset of the Foreign Object Debris in Airports (FOD-A) [160]

Crucially, the FOD-A dataset is enriched with meticulous annotations for each image, documenting the precise location and nature of debris present within the scene. These annotations are curated by trained personnel, guaranteeing a high degree of accuracy and consistency across the dataset. Such annotations serve as invaluable ground truth data, facilitating supervised learning approaches and enabling the development of highly accurate FOD detection algorithms.

The dataset reveals that the "Bolt" class is the most prominent, containing a notable 3300 images. This significant number suggests that bolts are either highly prevalent or particularly emphasized within the dataset. Following the bolts, the "Pliers" and "Wrench" classes also stand out, with 2884 and 2568 images respectively, highlighting their considerable importance. Classes like "Washer" and "Wire" also feature prominently, each boasting over 2000 images—2139 and 2138, respectively—indicating a similar level of representation. The "Plastic part" class is another well-represented category, with 2008 images. Conversely, at the lower end of the dataset, categories such as "Tape" and "Screw driver" have the least number of images, with just 127 and 157 respectively.

Additional classes with fewer images include "Hose" (294 images), "Adjustable wrench" (472 images), and "Wood" (206 images). In the mid-range, classes such as "Nut" (1303 images), "Hammer" (760 images), and "Metal part" (970 images) have a moderate number of images, ranging between 500 and 1500. Table 3-1 shows the distribution of FOD object types in the dataset.

Table 3-1 Division of class of FOD images in FOD-A dataset

FOD object type	Number of images
Battery	1059
Clamp part	917
Nut	1303
Washer	2139
Cutter	1352
Nail	1193
Hose	294
Bolt nut set	514
Paint chip	968
Screw driver	811
Tape	127
Bolt washer	1017
Fuel cap	548
Plastic part	2008
Wire	2138
Label	1310
Pliers	2884
Adjustable clamp	544
Hammer	760
Pen	483
Soda can	950
Bolt	3300
Metal part	970
Rock	662
Wrench	2568
Luggage tag	1686
Metal sheet	394
Adjustable wrench	472
Luggage part	738
Screw driver	157
Wood	206
Total:	34472

Moreover, alongside image and annotation data, the FOD-A dataset encompasses comprehensive metadata for each image, including critical information such as location, date, and time of capture. This contextual metadata enhances the dataset's richness and enables researchers to analyse FOD occurrences in relation to environmental factors and operational contexts.

As part of their evaluation process, the authors employed a total of 19975 photographs to train, validate, and test the system, encompassing a wide range of scenarios across 107 distinct classes. This meticulous selection process ensured the representation of diverse objects encountered in airport environments, covering various shapes, sizes, and materials commonly associated with Foreign Object Debris (FOD).

The dataset was thoughtfully curated to include photographs captured under different lighting conditions and against diverse backgrounds, thereby simulating the real-world variability encountered in airport settings. This diversity in lighting and background conditions is essential for training robust FOD detection algorithms capable of generalizing well to unseen scenarios and environmental contexts.

It is worth noting the disadvantages of this defect, which does not meet the FAA recommendations regarding the ratio of the number of photos/items found on aerodromes. This database also has photos of different resolutions and taken with different cameras.

3.2.2. New dataset based on FAA requirements

However, it was decided to prepare its own *PUT dataset* of FOD objects in order to develop this field, but also to provide a dataset of video recordings with FOD objects, as such a dataset was not found. Preparation of the dataset began with collecting characteristic FOD objects occurring at aerodrome, based on FAA requirements [15] and cooperation with experts from the Poznań–Ławica Airport. Four main classes of objects were chosen.

Additionally, according to the reports [15], metal FODs constitute approximately 60% of all unwanted objects found on airport roads, so the focus was mainly on objects made of this material. The created dataset consists of 180 FOD objects captured in 1480 photos. Table 3-2 shows the division of the collected FOD objects [161]. The dataset was created in the frame of a master's degree dissertation, conducted in the Division of Electronic Systems and Signal Processing at the Poznan University of Technology [162].

Table 3-2 Division of class of collected FOD images for *PUT dataset*

FOD object type	Number of images
Metal	1200
Plastic	160
Concrete	80
Wood	40
Total:	1480

Figure 3-4 shows sample images from author's FOD dataset with selected objects of various sizes and structures at airport ground surfaces.

Figure 3-4 Examples of images of FOD from *PUT dataset* [161]

The items were arranged at aerodrome (taxiways, runways, apron/ramp). Due to the close resemblance of metal and concrete objects to the concrete background, distinguishing these materials presents a significant challenge for algorithms. A total of 300 photographs were taken from a distance of 2 meters at a 45° angle. Each image contains a maximum of one FOD object, and additional photographs of the concrete slab alone were also captured. The images, taken at a resolution of 4272 × 2848, ensured high-quality photography. Figure 3-5 illustrates the setup for photographing. The constructed dataset was subsequently augmented to facilitate a more comprehensive evaluation of the algorithms employed.

Figure 3-5 Visualization of the photo station for *PUT dataset*

For the prepared dataset, the annotation process was conducted using Roboflow tools [163]. Ground truth-augmented training data, as illustrated in Figure 3-6, refers to datasets enhanced by augmenting the annotations of manually verified or labelled data points. These annotations act as precise reference points for machine learning models. Augmentation techniques encompass adding new samples, refining existing annotations, or integrating synthetic data, all while preserving the integrity of the original ground truth labels. This approach enhances the diversity, robustness, and generalization capabilities of machine learning models by providing a more comprehensive and varied training dataset.

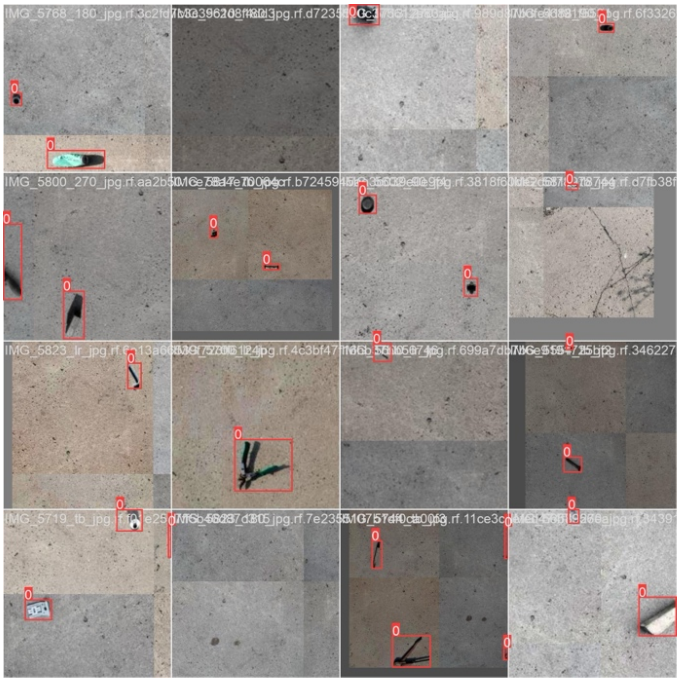

Figure 3-6 Ground truth augmented *PUT dataset* of FOD detection [38]

3.3. Application of image processing methods for FOD detection

The image processing sequence of the algorithm (Figure 3-7) includes calculating the average of the image, applying a blur, resizing the image to a vector, and clustering pixels based on using the k-means algorithm. The process then involves selecting the contour group that most differs from the average background, creating a mask for this selected group to segment the image, converting the segment to grayscale, detecting contours in the grayscale image, and selecting a contour larger than a specified threshold but smaller than a certain percentage of the image area. The algorithm then calculates the centre and radius of the selected contour and draws a circle around it on the original image [38]. Figure 3-8 illustrates an example of accurate FOD detection using classical methods using *PUT dataset*.

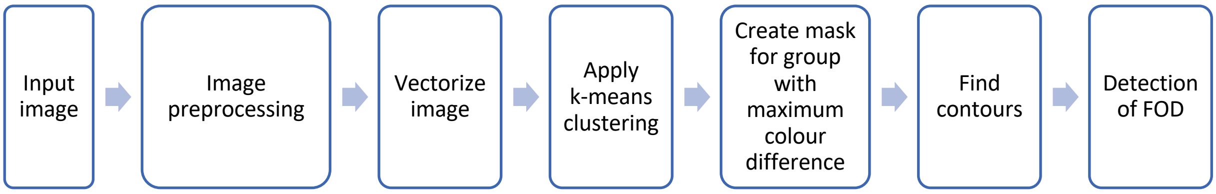

Figure 3-7 Block diagram of FOD detection using k-means method

Figure 3-8 Example of correct FOD detection using k-means method [38]

Table 3-3 presents the accuracy metrics for the k-means algorithm, demonstrating that its performance is significantly impacted by the resolution of the FOD input images from *PUT dataset*. The data indicate that higher resolutions initially enhance accuracy due to the greater detail and clearer clustering patterns they provide. However, beyond a specific resolution threshold (notably, when increasing from 400 × 400 to 600 × 600), the benefits of higher resolution diminish, and accuracy improvements plateau or even decrease. This suggests that while higher resolution can facilitate more precise clustering, there is a limit to its effectiveness. Thus, selecting an optimal image resolution is essential for maximizing the efficiency of k-means clustering in image analysis applications [38].

Table 3-3 Accuracy of the k-means method for FOD detection on *PUT dataset*

Input image resolution	**Accuracy**
256 × 256	65.54%
400 × 400	73.94%
600 × 600	68.53%

Due to the low effectiveness of the algorithm for detecting FOD objects at aerodromes based on the k-means method, it was decided to use neural networks in further experiments.

3.4. Improvement of FOD detection using convolutional neural network

In this issue, a series of experiments were conducted, testing different models of neural networks for detecting FOD objects in the image. It was decided to use the MATLAB, Roboflow and Google Colab environments.

The MATLAB environment has the ability to design its own neural networks, but also to use pre-trained models, such as AlexNet, VGG16, VGG19, GoogLeNet, ResNet-50 or Inception-v3. The Roboflow environment, on the other hand, has pre-trained models from the YOLO group (YOLOv5, YOLOv6, YOLOv9, YOLOv10) and an original network model, currently Roboflow 3.0 Object Detection.

The author analysed the possibility of using GoogLeNet models implemented in the MATLAB and YOLOv5 environments using Google Colab. The experiments were performed on the FOD-A dataset, and then the model with the best performance was validated on the *PUT dataset*.

The architecture employed in this study was grounded on the GoogLeNet convolutional neural network, featuring 144 values and 170 connections. With a FOD-A dataset encompassing 19975 images, 30% of which were allocated for validation, the robustness of the outcomes was assessed. To align with the network's specifications, images initially sized at 400 × 400 pixels were resized to 224 × 224 pixels. This adaptation was necessary as it corresponds to the dimensions compatible with the neural network's requirements. The implementation phase leveraged the MATLAB 2022a environment, harnessing the capabilities of the Deep Network Designer tool.

Originating from the efforts of Google researchers in 2014, GoogLeNet represents a significant stage in the development of deep convolutional neural networks. Its foundation lies in the "Inception" architecture, which intricately employs layers of convolutions and pooling to distil salient features from images. What sets GoogLeNet apart is not only its depth but also its computational efficiency. The incorporation of techniques like "1 × 1 convolutions" to streamline intermediate representations and the adoption of global average pooling instead of conventional fully connected layers underscores its architectural ingenuity.

Furthermore, the study delved into data augmentation techniques, experimenting with random rotation, rescaling, and axis-specific reflections to enrich the dataset. Rigorous analysis ensued during the parameter selection phase, culminating in an impressive 95.73% classification accuracy during final validation. The training regimen demanded significant computational resources, spanning 1422 minutes on an Intel Core i7-3770 3.40 GHz CPU. With a training cycle encompassing 30 epochs and 3270 iterations (averaging 109 iterations per epoch), validation intervals were set at every 50 iterations. The learning dynamics and loss evolution are elucidated in Figure 3-9.

At its core, the network operates by accepting input images sized at 224 × 224 × 3, denoting height, width, and RGB channels, respectively, as its inaugural layer (*imageInputLayer*). Subsequently, a convolutional layer housing 64 filters, each spanning 7 × 7 dimensions with a stride of 2, constitutes the network's foundational architecture (*convolution2dLayer*).

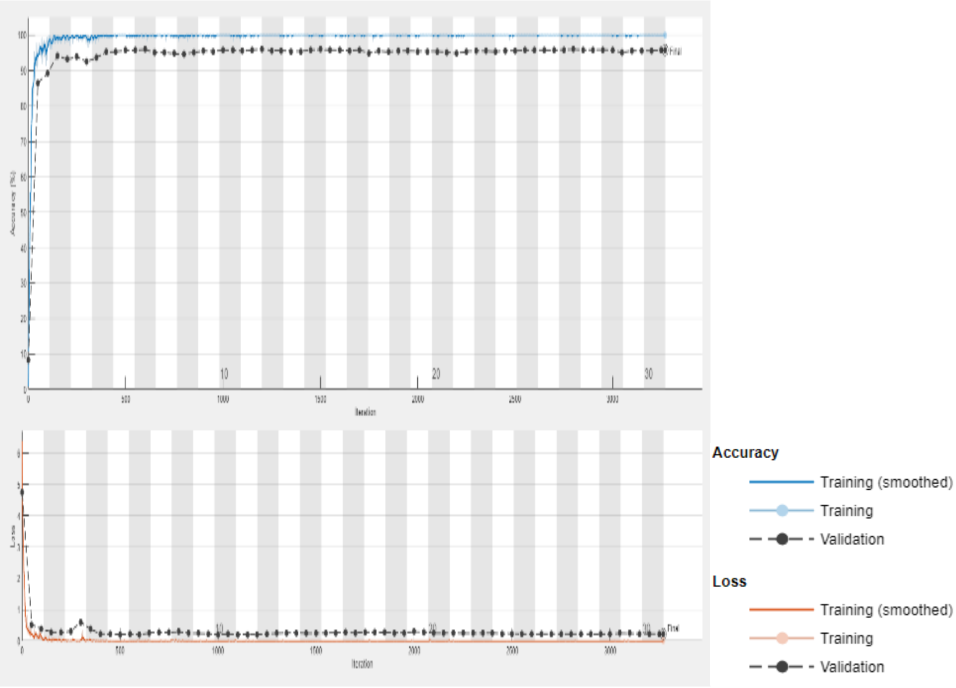

Figure 3-9 GoogLeNet FOD-A training and validation accuracy and loss graph [37]

The output from this layer is then fed into a rectified linear unit (ReLU) activation function (*reluLayer*), enhancing the network's ability to capture nonlinear relationships within the data. Subsequently, a max-pooling layer with a size of 3 × 3 and a stride of 2 (*maxPooling2dLayer*) downsamples the feature maps, reducing their spatial dimensions while retaining important features.

Following the pooling layer, a cross-channel normalization layer (*crossChannel-NormalizationLayer*) is employed to normalize the responses across feature maps, enhancing the network's generalization capabilities. This layer is succeeded by another convolutional layer featuring 64 filters of size 1 × 1 (*convolution2dLayer*), followed by yet another ReLU activation layer.

The subsequent layer is another convolutional layer with 192 filters of size 3 × 3 (*convolution2dLayer*), followed again by a ReLU activation layer and another cross-channel normalization layer. This pattern of alternating convolutional and activation layers is repeated in blocks with varying filter sizes and numbers of filters. The outputs of these layers are then concatenated using concatenation layers (*depthConcatenationLayer*), merging them into a single tensor.

Finally, the network concludes with a fully connected layer (*fullyConnectedLayer*), which produces the classification probabilities for the input image. During training, the network utilizes backpropagation to minimize the classification error between the predicted and actual labels. Notably, the model incorporates multiple branches, allowing it to learn different features at different scales, thereby enhancing its accuracy and robustness.

Due to the best results, it was decided to analyse the network metrics obtained depending on the input image. YOLOv5, a cutting-edge object detection network, utilizes a single-stage architecture that processes entire images in a single forward pass, facilitating real-time detection. This network harnesses convolutional neural networks (CNNs) to simultaneously predict bounding boxes and class probabilities from full images, employing anchor boxes to enhance localization accuracy. Its efficiency lies in the concurrent execution of classification and localization, yielding high detection speed and precision. The architecture of YOLOv5 integrates feature pyramid networks (FPN) to identify objects at multiple scales, thus improving its robustness in detecting varied object sizes and managing complex backgrounds in image processing tasks.

Table 3-4 shows the network metrics of FOD detection using YOLOv5 and FOD-A dataset at a resolution of 300 × 300, the YOLOv5 model exhibits the highest levels of precision and recall, at 99.0% and 98.8%, respectively, alongside an mAP50 of 99.0%. Nonetheless, the mAP50-95 score is comparatively lower at 88%, which suggests that the model's object detection capability, while precise and accurate, may not be as consistent across different intersection-over-union (IoU) thresholds. Upon increasing the input image resolution to 400 × 400, there is a minor decline in precision to 98.6%, although recall slightly increases to 99%. Concurrently, the mAP50 decreases marginally to 98.9%, and mAP50-95 drops to 87.4%, implying a slight trade-off between precision and recall as well as a modest decrease in overall performance stability. At a resolution of 600 × 600, the model's precision, recall, and mAP50 metrics are similar to those at 300 × 300, with precision at 98.9%, recall at 98.8%, and mAP50 at 99.1%. The mAP50-95 remains stable at 87.6%, indicating that increasing the resolution beyond 300 × 300 does not significantly enhance the model's performance in terms of precision and recall, nor does it detract from it. Overall, these findings suggest that while the YOLOv5 model consistently delivers high precision and recall across different resolutions, optimal performance, particularly in terms of mAP50 and mAP50-95, is achieved at lower resolutions, with diminishing improvements as resolution increases. Figure 3-10 shows the results of FOD detection using YOLOv5 and FOD-A dataset.

Table 3-4 Metrics of FOD detection using YOLOv5 and FOD-A dataset

Input image resolution	Precision	Recall	mAP50	mAP50-95
300 × 300	99.0%	98.8%	99.0%	88.0%
400 × 400	98.6%	99.0%	98.9%	87.4%
600 × 600	98.9%	98.8%	99.1%	87.6%

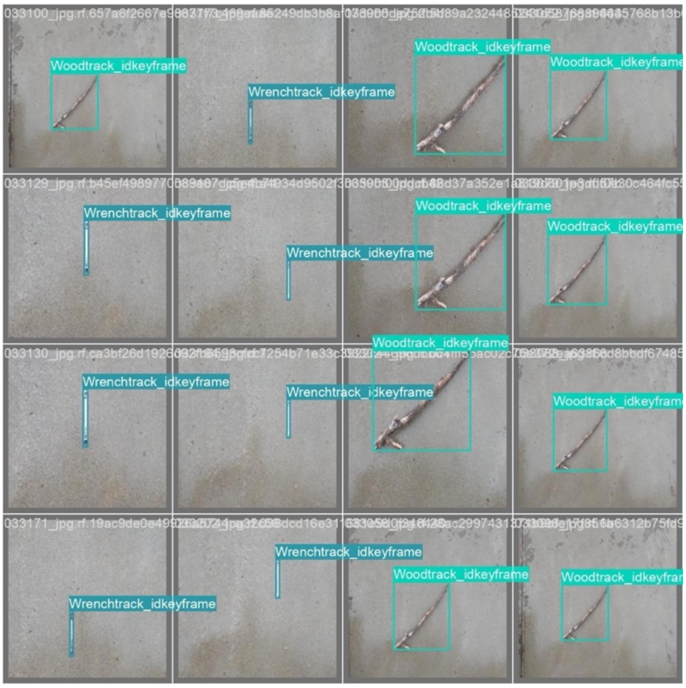

Figure 3-10 Results of FOD detection using YOLOv5 and FOD-A dataset

The YOLOv5 model represents a architecture for object detection, designed to achieve high accuracy and speed. Its configuration is characterized by several key parameters: the number of classes (nc), a depth multiple of 0.33 to control the model's depth, and a width multiple of 0.50 to scale the layer channels. YOLOv5 utilizes a series of predefined anchor boxes at different feature map scales, specifically P3/8, P4/16, and P5/32, to effectively handle objects of varying sizes. The anchors are defined as [10,13, 16,30, 33,23] for P3/8, [30,61, 62,45, 59,119] for P4/16, and [116,90, 156,198, 373,326] for P5/32.

The backbone of YOLOv5 is engineered to efficiently extract features from the input image. Initially, the Focus layer (layer 0) reduces the spatial dimensions by a factor of 2 and increases the channel dimensions to 64. This is followed by a series of convolutional layers and BottleneckCSP modules, designed to capture increasingly abstract representations. Conv layers reduce the spatial dimensions and increase the channel dimensions at layers 1, 3, 5, and 7, corresponding to P2/4, P3/8, P4/16, and P5/32 feature maps, respectively. The BottleneckCSP modules in layers 2, 4, 6, and 8 utilize a cross-stage partial network strategy to balance gradient flow, computational efficiency, and model capacity. Additionally, a Spatial Pyramid Pooling (SPP) layer at layer 8 aggregates multi-scale features to enhance the receptive field.

The head of YOLOv5 constructs the final detection outputs by further processing the features extracted by the backbone. It begins with convolutional and upsampling layers to merge higher-resolution feature maps, enhancing the detection of smaller objects. After a Conv layer (layer 10), an Upsample operation (layer 11) and a Concat operation (layer 12) combine features from different stages of the backbone. This pattern is repeated to progressively refine feature maps at different scales: P3/8 (layer 17), P4/16 (layer 20), and P5/32 (layer 23). Each stage involves additional BottleneckCSP modules to refine the feature representations.

The final detection is executed by the Detect layer (layer 24), which integrates the multi-scale feature maps (P3, P4, and P5) and applies the predefined anchors to predict bounding boxes and class probabilities. This multi-scale approach ensures that YOLOv5 can effectively detect objects of various sizes within an image, maintaining a balance between detection precision and computational efficiency.

The model training was conducted using the Google Colab environment and the Nvidia Tesla T4 GPU architecture. The Nvidia Tesla T4, engineered specifically for machine learning applications, leverages the advanced Turing architecture. With 2560 CUDA cores and 320 Tensor cores, it excels in executing both training and inference tasks within deep learning frameworks efficiently. The Tesla T4 is notable for its ability to perform mixed-precision computations, optimizing operations in FP16 and INT8 formats to greatly enhance throughput and minimize latency. Equipped with 16GB of GDDR6 memory, the Tesla T4 provides ample bandwidth and capacity, enabling seamless processing of extensive datasets and intricate neural networks, thus markedly accelerating the machine learning workflow.

The training and validation metrics for the YOLOv5 model, as depicted in Figure 3-11, exhibit clear patterns throughout the training epochs. The training losses—encompassing box loss, object loss, and classification loss—show a steady decrease, indicating effective learning and convergence by the model. Notably, the box loss decreases to approximately 0.02, and the object loss nears 0.01 in the later stages of training, while the classification loss consistently remains at zero, potentially indicating either the absence of classification tasks or flawless classification from the outset.

In the validation phase, the trends in box and object losses are similar to those observed during training, though they display greater variability, especially in the initial epochs. This variability may be attributed to the smaller size of the validation set or differences in the validation data. Despite this, the validation losses also decline to levels comparable to the training losses, suggesting that the model generalizes effectively.

Performance metrics, including precision, recall, mAP50, and mAP50-95, further illustrate the model's efficacy. Precision and recall both rise quickly and stabilize near 1.0 early in the training process, indicating that the model rapidly learns to detect and classify objects with high accuracy. The mAP50 metric nearly reaches perfect scores, reflecting excellent object detection accuracy at an IoU threshold of 0.5. However, the mAP50-95, which assesses performance over a range of IoU thresholds, stabilizes around 0.6 to 0.7. This suggests that while the model performs exceptionally well at lower IoU thresholds, its consistency diminishes at higher thresholds, possibly due to difficulties in precise localization and classification in more challenging scenarios.

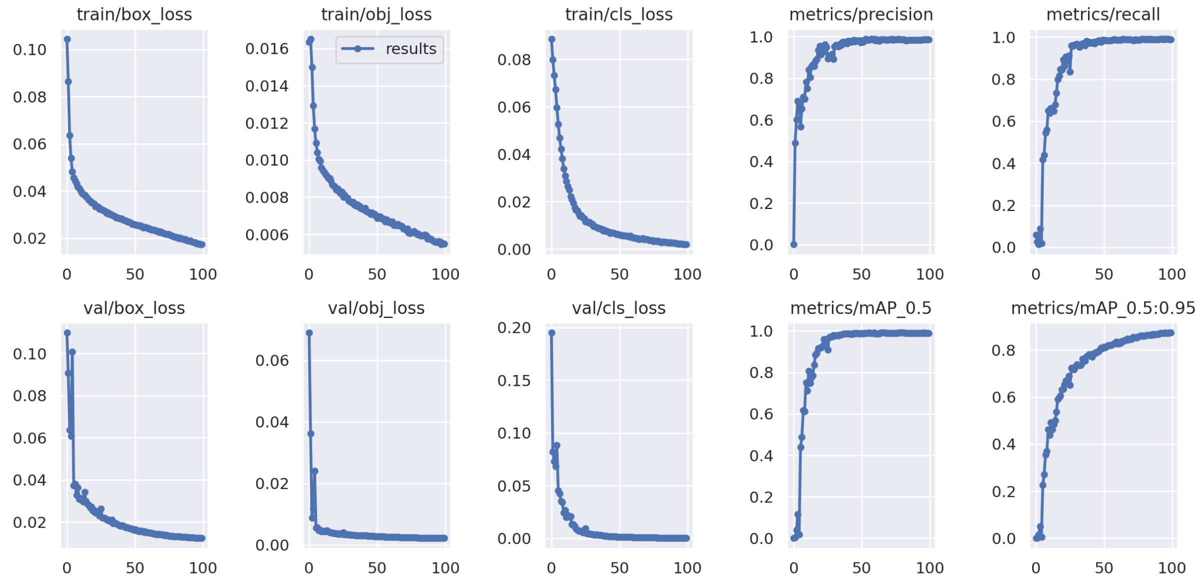

Figure 3-11 YOLOv5 performance metrics for FOD-A dataset

It was also decided to train the YOLOv5 model based on the *PUT dataset* of FOD objects [38]. Figure 3-12 demonstrates the result of FOD detection in an image from *PUT dataset* using YOLOv5.

Figure 3-12 Results of FOD detection using YOLOv5 and *PUT dataset* [38]

Table 3-5 presents the metrics of the proposed neural network model. Precision, a crucial classification metric, measures the proportion of correctly identified positive instances among all instances classified as positive, calculated as the ratio of true positives to the sum of true positives and false positives [38].

Table 3-5 Metrics of FOD detection using YOLOv5 and *PUT dataset*

Input image resolution	Precision	Recall	mAP50	mAP50-95
256 × 256	99.3%	99.3%	99.5%	65.2%
400 × 400	99.3%	99.6%	99.5%	67.9%
600 × 600	99.3%	100%	99.5%	69.5%

The results suggest that increasing the input image resolution generally results in slight improvements in recall and mAP values, while precision remains consistent across different resolutions. Notably, higher resolutions, such as 600 × 600, demonstrate a trend towards enhanced recall and mAP50-95 scores, indicating a better capability to accurately detect objects of various sizes and positions within the image. However, performance gains diminish beyond a resolution of 400 × 400, highlighting potential diminishing returns in accuracy improvement relative to computational cost. Consequently, selecting an optimal resolution requires balancing computational efficiency with the desired detection accuracy in practical applications of YOLOv5 for object detection tasks.

The training and validation metrics for the YOLOv5 model, as illustrated in Figure 3-13, reveal distinct patterns over the course of the training epochs. The training losses, including box loss, object loss, and classification loss, demonstrate a consistent decline, suggesting that the model is effectively learning and converging. Specifically, the box loss decreases to around 0.02 and the object loss approaches 0.01 in the later stages of training, while the classification loss remains at zero, which could imply either the absence of classification tasks or perfect classification from the beginning.

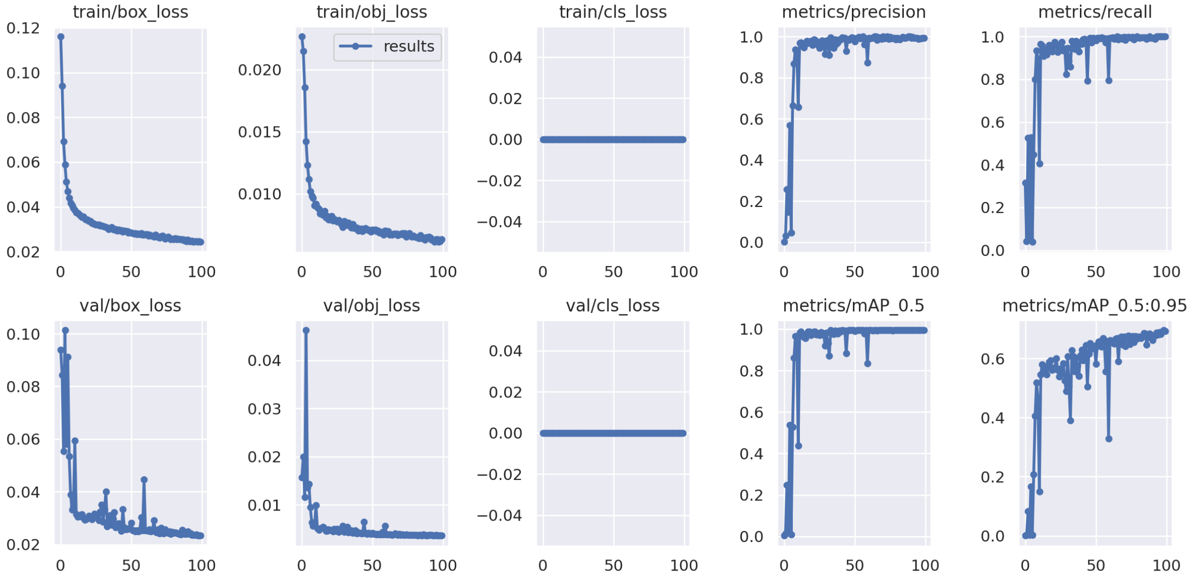

Figure 3-13 YOLOv5 performance metrics for FOD *PUT dataset*

During the validation phase, the trends in box and object losses mirror those seen in training, though they exhibit greater variability, particularly in the initial epochs. This variability could be due to the smaller size of the validation set or differences in the validation data. Nonetheless, the validation losses also reduce to values similar to the training losses, indicating that the model generalizes well.

Performance metrics such as precision, recall, mAP50, and mAP50-95 provide further evidence of the model's performance. Both precision and recall increase rapidly and plateau near 1.0 early in the training process, suggesting that the model swiftly learns to accurately detect and classify objects. The mAP50 metric achieves nearly perfect scores, indicating a high level of accuracy in object detection at an IoU threshold of 0.5. In contrast, the mAP50-95, which measures performance across a range of IoU thresholds, stabilizes around 0.6 to 0.7. This suggests that while the model excels at lower IoU thresholds, its consistency decreases at higher thresholds, possibly reflecting challenges in achieving precise localization and classification in more complex scenarios.

Table 3-6 Comparison of FOD detection algorithms

Paper	Method	Dataset	Accuracy
[58]	Background subtraction	Own dataset (no information)	96.67%
[59]	YOLOv3	Own dataset (1700 images)	94.50%
[60]	YOLOv3	Own dataset (2000 images)	95.67%
[61]	Random forest	Own dataset (1800 images)	93.10%
[62]	YOLOv3	FOD-A Dataset (over 14 000 images)	95.20%
Selected	GoogLeNet	FOD-A Dataset (over 19 000 images)	95.73%
Selected	YOLOv5	FOD-A Dataset (over 19 000 images)	99.00%
Selected	YOLOv5	PUT dataset (1480 images)	99.30%

Table 3-6 provides a comparison of the performance utilized by various authors, revealing a common trend of authors relying on proprietary datasets, often comprising fewer images and not being publicly accessible. Notably, only the authors referenced in [62] conducted testing on the YOLOv3 neural network architecture, achieving a commendable efficiency of 95.2% through the utilization of 14260 images sourced from the FOD-A Dataset. In the present study, a dataset comprising over 19000 images from the same dataset was employed. Impressively, the achieved result surpasses those of other neural network models under comparison, hinting at the judiciousness of model selection and its training methodology. Consequently, the neural network model based on GoogLeNet outperformed its YOLOv3-based counterparts in terms of performance. However, the best results were obtained by the model based on YOLOv5, achieving 99.0% efficiency on the given dataset. Moreover, on the *PUT dataset* with 1480 real photos, the YOLOv5 network model achieved 99.3% accuracy.

Chapter

4. Detection of airport horizontal markings

Lamps in airport ground surfaces are crucial for air navigation, as their visibility is essential for conducting various air operations. Regular checks are needed to maintain their light efficiency, which can degrade due to the use of halogen bulbs or LEDs, as well as the effects of the winter season. During winter, airport areas are cleared of snow using plows with metal brushes, leading to tarnishing, scratching, and even cracking of the prisms of in-pavement lamps, rendering them non-operational. Figure 4-1 illustrates the concept of a measurement platform in a real-world setting (on the runway) with camera mounted on an airport maintenance vehicle.

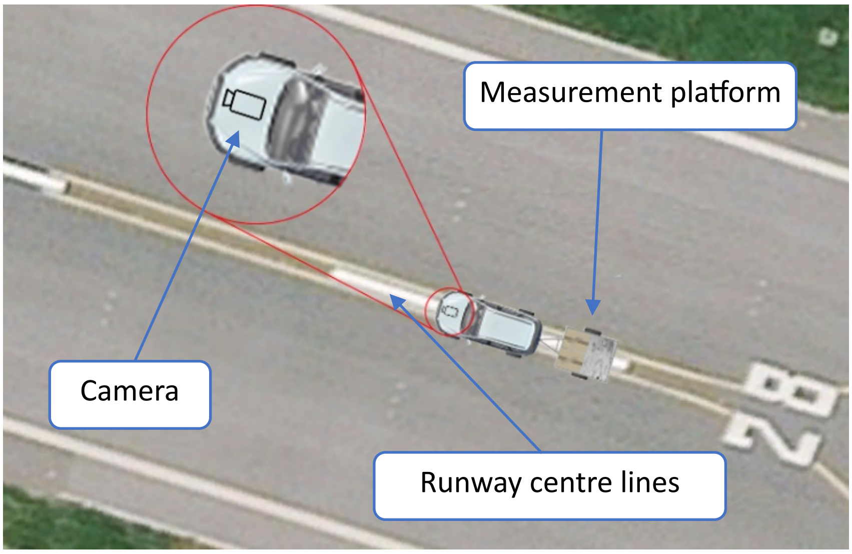

Figure 4-1 Measuring platform for quality testing of airport lamps and camera mounted on the airport maintenance vehicle [37]

To ensure that the platform accurately traverses over the lamps embedded in the runway, a vision system is essential. This system must effectively identify the markings on the runway and other airport areas, subsequently making the necessary trajectory adjustments to enhance measurement precision. The unique characteristics of a runway, which is significantly wider than typical public roads, present additional challenges. One major difficulty is locating appropriate reference points since the edges of the runway often lie outside the camera's frame.

The vision system's primary function on the measuring platform is to facilitate the quality testing of airport lamps. This involves recognizing various runway markings and using these visual cues to navigate and adjust the platform's path accurately. By doing so, the system ensures that the platform aligns correctly with the lamps and other relevant features on the runway, allowing for precise measurements and assessments.

Figure 4-2 illustrates the operational principle of the vision system on the measuring platform. It depicts how the system captures vision data from the runway, processes this information to identify key markings, and uses these markers to guide the platform's movement. This setup is crucial for maintaining the correct trajectory, especially given the expansive width of the runway which complicates the identification of consistent reference points. By effectively managing these visual inputs, the vision system plays a critical role in the accurate and efficient testing of airport lighting systems.

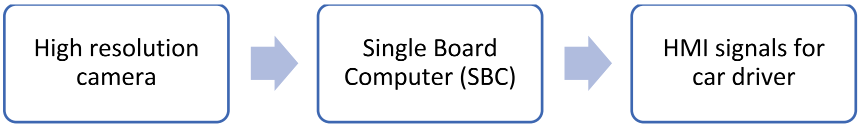

Figure 4-2 Block scheme of airport line tracking system

Modern embedded systems offer the capability to process video sequences efficiently in real-time. Video sequence analysis algorithms can be rooted in traditional image processing techniques as well as in neural networks, which are gaining widespread popularity. Cameras find applications in various fields such as automotive and autonomous vehicles [127], [128], urban surveillance [5], and tracking [164], as well as in specialized contexts like inspection vehicles [28], [29]. These systems assist operators in monitoring urban areas or machinery environments, enabling them to oversee and react to ongoing events. In certain scenarios, these systems can fully eliminate human intervention by automatically issuing specific commands to other systems.

In the context of autonomous vehicles operating within airport premises [28], both the precision of the algorithms and the hardware performance are critically important for ensuring safety. Additionally, these vehicles need to be highly energy-efficient due to the extensive areas they cover within airports and must have sufficient energy reserves for emergency situations. Therefore, managing the lighting and navigation equipment in airport areas is crucial, particularly focusing on the runway centre line, touchdown zone, and taxiway centre line. To ensure accurate movement over the lights being tested, a system is needed to guide the operator or driver in conducting precise measurements despite the width of the runway and the absence of static reference points [28]. These systems are increasingly leveraging vision-based solutions, making the task of detecting runway lines and markings vital for the safe ground movement of aircraft [30]. Moreover, such systems aid in determining the position of measurement platforms during inspections, as the position of lamps is closely linked to the location of horizontal markings on airport surfaces [4]. The method of approaching and detecting lines and supporting the operator was also described in the patent application [45].

Processing video sequences necessitates computing units with varying power levels [165], [166], depending on the chosen algorithm and the image processing operations performed [30], [46]. In mobile applications, finding a balance between system compactness, power consumption, and computational performance is essential. A comparative analysis of available embedded systems is necessary to select the best equipment for specific applications. Due to their small size and relatively low energy requirements, embedded systems can be installed in mobile autonomous vehicles, such as platforms used for quality testing of airport lamps. The need to develop such a platform and test airport lamps systems from increasingly stringent regulations imposed by aviation safety agencies concerning airport lighting inspection [4].

4.1. Dataset of airport horizontal markings

An evident distinction between public roads and airport areas lies in their scale, with airport spaces being significantly larger. To conduct experimental tests, a dataset of video sequences captured at Poznań–Ławica Airport was compiled and named *PLAVS1* (Poznań Lawica Airport Video Set 1). Data collection involved using two different types of cameras: the GoPro Hero+ and the GoPro Hero 8. The resulting dataset is quite extensive, amounting to over 98 GB of video recordings. These recordings include detailed images from restricted areas within the airport, providing a comprehensive basis for this analysis.

The GoPro Hero+ camera is notably resilient to varying weather conditions, which makes it particularly suitable for outdoor use in diverse environments. This camera can be securely mounted on a measurement platform system, ensuring stable and safe data collection. It supports video recording at a maximum resolution of 1920 × 1080 pixels, with a frame rate of 60 frames per second. This high resolution and frame rate are essential for capturing detailed and high-quality video footage necessary for precise analysis. The GoPro Hero+ is equipped with an 8-megapixel CMOS sensor and an aperture value of f/2.8, allowing it to capture clear images even under challenging lighting conditions. Additionally, this camera employs L4.1 (H.264 / MPEG-4 AVC) level coding, which ensures efficient video compression while maintaining quality. The built-in WiFi module is another significant feature, enabling real-time video streaming, which allows for live monitoring and immediate analysis during data collection. The camera's advanced image processing algorithms further ensure optimal image quality, adapting to various lighting scenarios to deliver consistent and clear footage [167].

On the other hand, the GoPro Hero 8 is designed for high-performance and can capture stable, high-quality video in extreme conditions [168]. This camera supports 4K video recording at up to 60 frames per second, 2.7K at up to 120 frames per second, and Full HD (1080p) at up to 240 frames per second. Such versatility in resolution and frame rate options allows for capturing ultra-high-definition footage that is highly suitable for detailed analytical purposes. One of the standout features of the GoPro Hero 8 is its advanced image stabilization technology, which significantly reduces camera shake and ensures smooth footage even during high-motion activities. The camera also excels in still image capture, offering 12-megapixel resolution with HDR capabilities, which enhance details in both highlights and shadows, providing clearer and more detailed photographs. The robust design and technical specifications of the GoPro Hero 8 make it an ideal tool for researchers and scientists working in various challenging environments, ensuring professional-quality video documentation [169].

The video dataset captured at Poznań–Ławica Airport is extensive and rich in detail, providing a substantial foundation for experimental tests. With over 98 GB of video recordings, a comprehensive collection of footage that covers the restricted areas of the airport, capturing essential details needed for thorough analysis. Table 4-1 presents statistics of the locations in recordings in the *PLAVS1* dataset.

Table 4-1 Statistics of *PLAVS1* dataset

Recording location	**Time [minutes]**	**Time [seconds]**	**Size [GB]**
Runway 28-10	89	18	29.21
Runway 10-28	84	25	28.08
Taxiways	102	21	33.02
Other locations	27	15	8.40
Total:	303 minutes 19 seconds		98.70 GB

The *PLAVS1* dataset comprises video recordings collected from various aerodrome locations, each with distinct durations and file sizes. Recordings from Runway 28-10 have a total length of 89 minutes and 18 seconds, with a storage size of approximately 29.21 GB. In comparison, the recordings from Runway 10-28 last for 84 minutes and 25 seconds and occupy 28.08 GB. The Taxiways category contains the longest recordings, amounting to 102 minutes and 21 seconds, and has the largest data size of 33.02 GB. The “Other locations” category features the shortest recordings, with a duration of 27 minutes and 15 seconds and a file size of 8.40 GB. This variation in the length and size of the recordings likely indicates differences in the activity levels or significance of each location captured within the dataset. Figure 4-3 provides a visual representation of the video recordings in GB from aerodrome locations in the *PLAVS1* dataset.

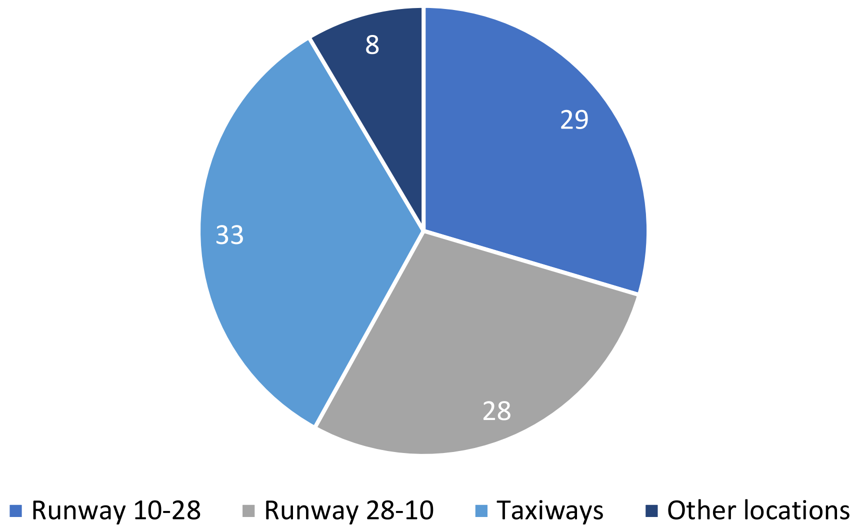

Figure 4-3 Visual representation of the video recordings in GB from aerodrome locations in the *PLAVS1* dataset

The recorded video data plays a crucial role in analysing the performance and quality of airport lamp operations. For instance, Figure 4-4 illustrates sample frames showing various road markings used in airport areas. These include the central axis of the runway, represented by white dashed lines, and the exit tracks and central axes of taxiways, denoted by solid yellow lines. Accurate detection of these markings is essential because the airport lamps are not installed directly on the centre lines but are slightly offset. Therefore, precise detection of the edges of these markings is vital for determining the relative positions of the lamps and for adjusting the approach trajectory accordingly.

Figure 4-4 Sample frames from recordings made at Poznań–Ławica Airport [44]

The advanced capabilities of all used cameras ensure that the recorded footage is of high quality, which is crucial for detailed analysis. The high resolution, frame rates, and image stabilization features enable the capture of clear, detailed, and stable footage, which is necessary for accurately assessing and improving the alignment and functionality of airport lamps. Additionally, the real-time streaming capability provides immediate feedback, allowing for dynamic adjustments and more efficient data collection.

In summary, the combined use of the GoPro Hero+ and Hero 8 cameras, along with the extensive *PLAVS1* dataset recorded at Poznań–Ławica Airport, provides a robust foundation for experimental tests. These tools enable precise, high-quality data collection and analysis, which are essential for evaluating and enhancing the operational quality of airport lighting systems.

4.2. Proposed solution for detection of airport horizontal markings

4.2.1. Standard algorithms for line detection

The algorithm development encompassed fundamental image processing operations aimed at enhancing line detection accuracy and quality. Figure 4-5 illustrates the schematic representation of the program's architecture and workflow.

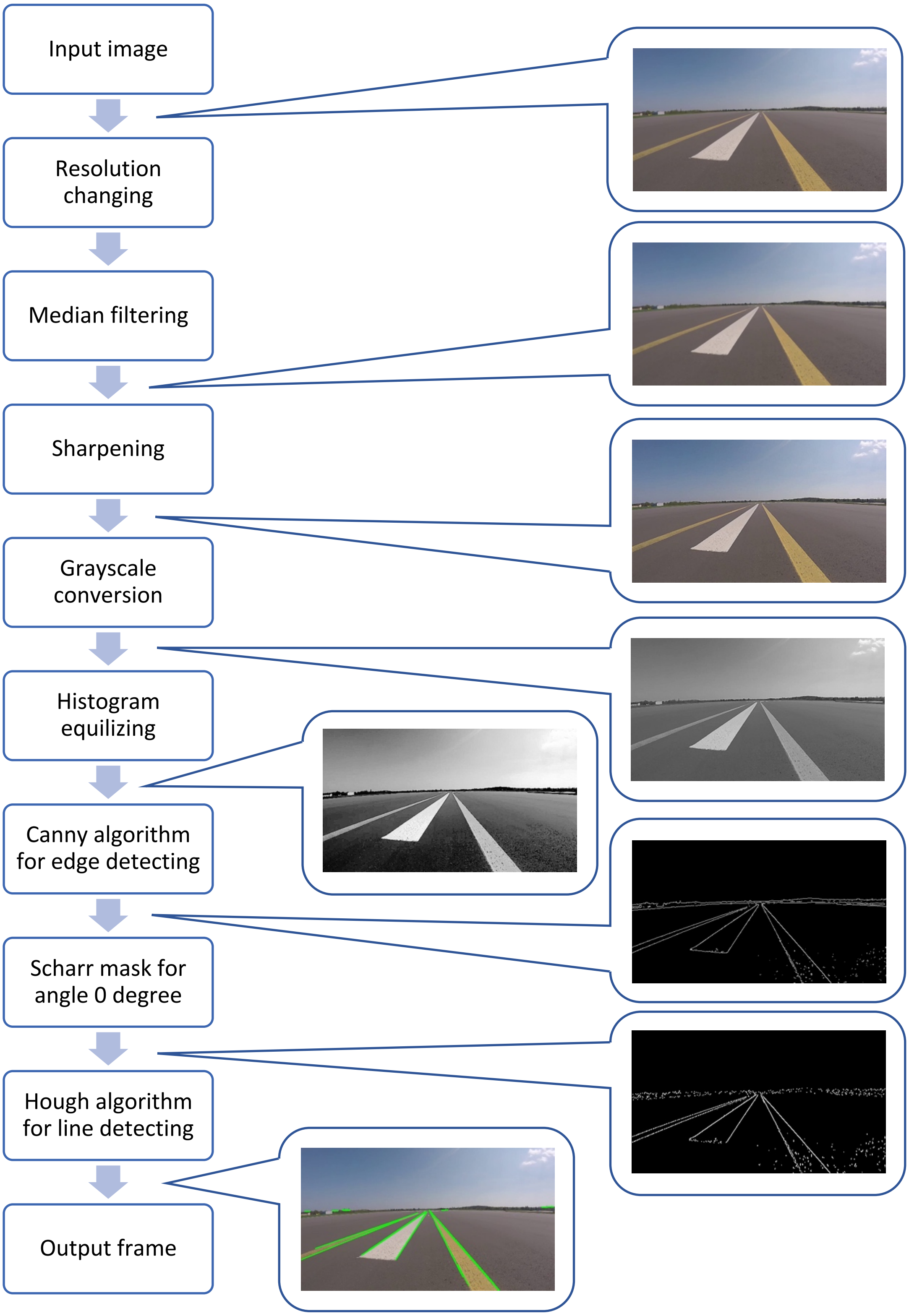

Figure 4-5 Schematic diagram of the program based on line detection using Scharr mask edge detection and Hough Transform

A pivotal objective was to manipulate the frames to distinctly isolate horizontal marks from surrounding objects and the background. Emphasis was also placed on noise reduction and rectifying erroneous detections, alongside detecting vertical edges and mitigating their interference with other elements within the frame. Furthermore, meticulous parameter tuning for the Hough Transform contributed to optimizing performance. Python 3.7.6 served as the programming environment for this endeavour, with the implementation facilitated through the OpenCV library, version 4.2.0.

To expedite the processing of individual stages within the program without sacrificing detail, a strategic approach was adopted. Initially, upon loading each frame, a resolution adjustment was implemented to strike a balance between computational efficiency and retaining essential details. Subsequently, noise reduction was addressed utilizing the *cv2.medianBlur(input, 3)* function, which effectively suppressed noise artifacts without compromising the integrity of visible edges critical for line detection. To further enhance edge visibility, a sharpening operation was executed in the subsequent step. This involved the utilization of a kernel, configured in the form of an array, to accentuate edge contrast and clarity, thereby augmenting the efficacy of subsequent detection processes.

$$\text{kernel} = \begin{bmatrix} 0 & -1 & 0 \\ -1 & 5 & -1 \\ 0 & -1 & 0 \end{bmatrix} \tag{49}$$

Employing the *cv2.filter2D(input, −1, kernel)* function yielded satisfactory outcomes, effectively sharpening the image to accentuate crucial details. Subsequently, a transition from the RGB colour space to grayscale was executed using the standard OpenCV function *cv2.cvt(input, cv2._BGR2GRAY)*. Recognizing the significance of detecting worn lines in airport areas, particularly in high-wear zones like the touchdown area, where accumulated rubber residue from landing aircraft tyres poses visibility challenges, the histogram equalization function *cv2.equalizeHist(input)* was applied. This function served to enhance details that were previously obscured due to low original contrast levels. Following this preprocessing, the image was deemed ready for edge detection using the Canny algorithm, implemented *via cv2.Canny(input, minVal, maxVal)* with specified parameters (minVal = 400 and maxVal = 500). Of particular relevance to the centre line detection task was the identification of vertical edges. By leveraging the Scharr mask configured at a 0-degree angle, with the kernel array meticulously tailored to the task, extraneous edges detected by the Canny algorithm were effectively filtered out, leaving behind only the pertinent vertical edge information.

$$\text{kernel} = \begin{bmatrix} -3 & 0 & 3 \\ -10 & 0 & 10 \\ -3 & 0 & 3 \end{bmatrix} \tag{50}$$

Furthermore, the application of *cv2.filter2D(input, –1, kernel)* further refined the image, enhancing edge clarity and definition. The penultimate step preceding the conclusion of the algorithm involved line detection, accomplished through the utilization of the Hough Transform, specifically the Probabilistic Hough Line Transform available in the OpenCV library. In the culmination of the algorithm's execution, the final frame produced encapsulated the central axis lines superimposed on the original image. These lines serve as pivotal reference points, facilitating the potential expansion of the measurement platform to evaluate airport lighting efficacy with heightened precision. By leveraging this framework, more precise measurements can be obtained, furnishing detailed insights into the spatial relationship between the testing matrix and the examined lamp. Figure 4-6 showcases the resultant output generated by the program's execution, providing a visual representation of the algorithm's effectiveness in action.

Figure 4-6 Result of program based on line detection using Scharr mask edge detection and Hough Transform [30]

One pivotal technique employed in the algorithm's implementation involved the autonomous recognition of road markings, a critical aspect in the realm of intelligent vehicle research, pertinent to both navigation and advanced driver assistance systems [170]. While previous studies predominantly focused on utilizing lane markings for vehicle guidance and operation, the reality demands attention to other vital signage such as arrows and warnings for comprehensive car navigation. The methodology hinged on leveraging support vector machine (SVM) algorithms to mitigate the influence of external factors like varying points of view, ambient brightness, and diverse backgrounds. Experimental validation of the proposed method was conducted using a diverse array of images. The findings underscored impressive recognition accuracy surpassing 97%, with a commendable time consumption per frame standing at 0.26 seconds [170].

Another driving force behind the refinement of the algorithm under discussion stemmed from the imperative to address runway positioning recognition challenges [171]. It was evident that identifying signage and individual markings played a pivotal role in enhancing safety and averting runway incursions. This aspect serves as a crucial adjunct to pilot training and airport ground radar systems, particularly in the context of intricate, expansive airport layouts. Within this project framework, conventional airport signage and markings served as the focal points for detection and recognition purposes. Leveraging the Canny transform facilitated precise line detection, while the Hough Transform was instrumental in identifying prominent lines within images and discerning shorter lines interspersed between them. The culmination of these efforts resulted in remarkable achievements, with authors attaining a commendable accuracy rate of 95.1% for runway sign detection, alongside correct identification of wait positions in 89.2% of instances [171].

This alternative approach to implementing the line detection algorithm minimizes interference with the input form of the image and instead prioritizes computational calculations, offering a distinct technique in constructing image analysis-based algorithms [172]. Employing the same programming environment, bolstered by the support of the OpenCV library (version 4.2.0), alongside additional computational tools such as NumPy and math libraries, facilitated the execution of complex operations. Within this framework, operations such as maximizing values, rounding, calculating means, and generating zero matrices were pivotal in deriving the final result from the input image array.

The algorithm workflow commences with the standard conversion of the frame from RGB to grayscale, followed by the initialization of essential global variables required for subsequent calculations. Subsequently, an array containing left and right threshold intensity values is created, enabling the determination of specific threshold values for both lanes. This is then followed by the initialization of global variables essential for lane extraction. Leveraging the pre-calculated threshold values, the algorithm identifies points corresponding to the left and right lanes, culminating in the generation of an image with marked identified points representing the trajectory of lines painted on airport surfaces upon program completion. Figure 4-7 delineates a block diagram illustrating the program's structure.

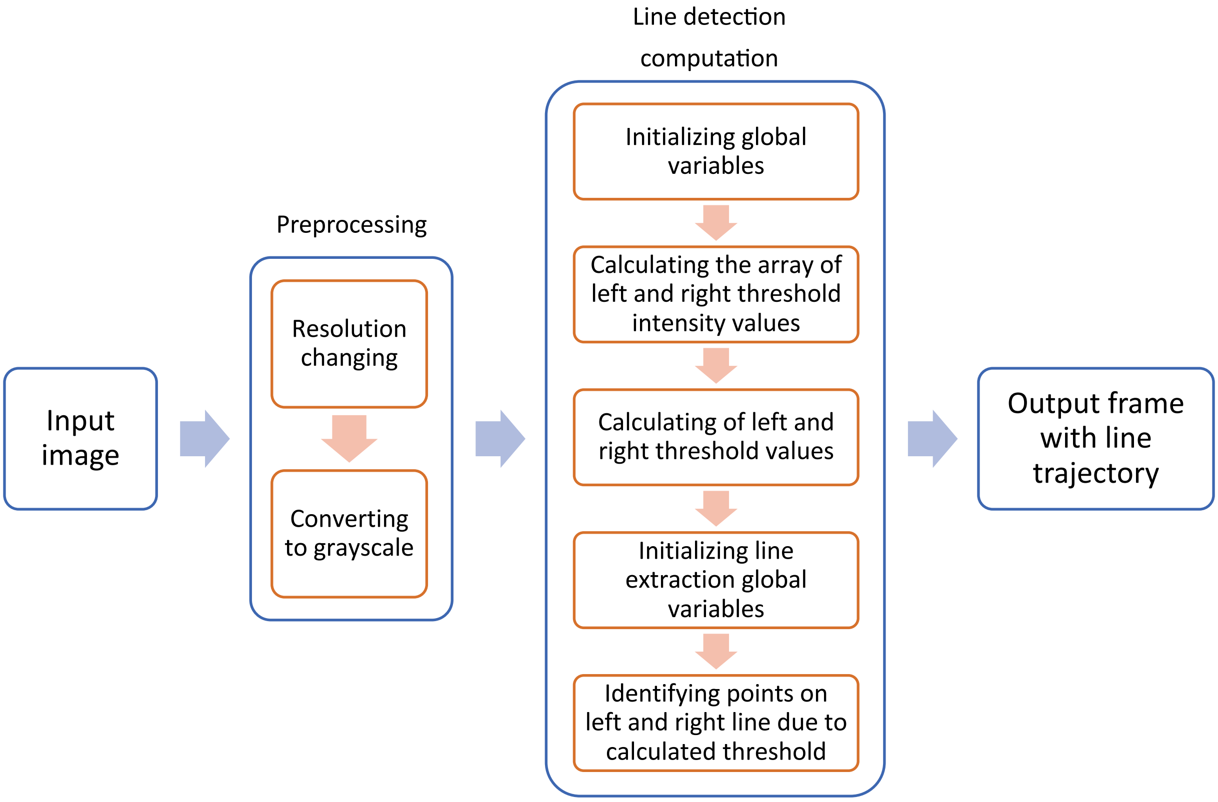

Figure 4-7 Diagram of program for line detection based on hyperbola fitting

The Hough Transform constitutes a pivotal component for line detection within a designated area (Figure 4-8a), as defined by expression (51), wherein ρ denotes the distance from the origin to the nearest point on the detected line, and θ represents the angle between the X-axis and the line connecting the origin to said point. The range of ρ is established by the relation $-R < \rho < +R$, where R denotes the diagonal of the image (52), and θ values are constrained within the range of −90° to 90°. The variables necessary for calculating the diagonal R are rows and cols, corresponding to the number of rows and columns of the processed image.

$$\rho(\theta) = x\cos(\theta) + y\sin(\theta) \tag{51}$$

$$-\sqrt{\mathrm{rows}^2 + \mathrm{cols}^2} < \rho < \sqrt{\mathrm{rows}^2 + \mathrm{cols}^2} \tag{52}$$

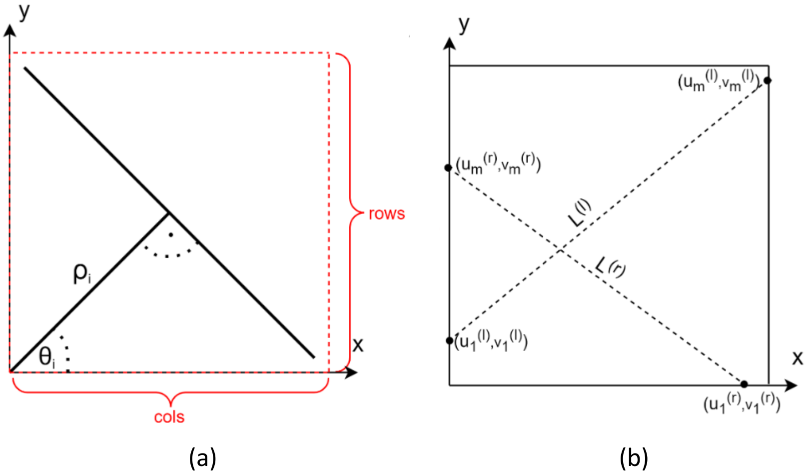

Figure 4-8 Course Hough Transform (a) and image coordinates (b) [30]

When initiating the search process, it's crucial to consider whether it commences from the left or right boundary, thereby setting the maximum range to the respective boundary (Figure 4-8b). By incorporating an additional search zone, tracking the outer lane boundary curves becomes more manageable. The lane points are segregated into two distinct lists, denoted as L(l) for the left line and L(r) for the right line, expressed mathematically as depicted in equations (55) and (56), where u and v represent the x- and y-coordinates in the image reference frame [173].

$$L^{(l)} = \left\{\left(u_1^{(l)}, v_1^{(l)}\right), \left(u_2^{(l)}, v_2^{(l)}\right), \dots, \left(u_m^{(l)}, v_m^{(l)}\right)\right\} \tag{53}$$

$$L^{(r)} = \left\{\left(u_1^{(r)}, v_1^{(r)}\right), \left(u_2^{(r)}, v_2^{(r)}\right), \dots, \left(u_m^{(r)}, v_m^{(r)}\right)\right\} \tag{54}$$

The proposed solution exhibits versatility in its application, extending beyond airport lane detection to encompass a broader scope of obstacle and lane detection systems, leveraging a stereo vision architecture to enhance road safety [174]. Employing fully customized devices, this system adeptly identifies general obstacles, unbound by symmetry or shape constraints, alongside lane positioning. A specific hardware module facilitates geometric transformation, effectively mitigating the perspective effect evident in both left and right stereo images. While lane markings are discerned through the application of morphological filters on the left image, the mapped stereo images collectively aid in detecting clearance ahead of the vehicle. Output from this processing pipeline is conveniently relayed to the Control Display and Control Panel, furnishing the driver with indispensable visual feedback [174].

The detection of road lanes and borders represents a formidable challenge within the realm of autonomous driving systems [175]. Contemporary solutions predominantly rely on lane detection techniques, pivotal for ascertaining road position, determining vehicle-road relative positioning, and analysing vehicle trajectory. Although in-vehicle vision systems serve as the primary approach for road and lane boundary detection, lane detection remains a challenging endeavour owing to the diverse array of road conditions encountered during operation [175].

The devised method for aerodrome line detection, predicated on edge detection principles, exemplifies a vision-based strategy for runway identification, capable of real-time operation with resilience to lighting variations and shadows. Harnessing a front-facing camera mounted on the vehicle, the system employs a sequence of processes to discern lane markings. Leveraging a pair of hyperbolas aligned with lane edges, these trajectories are extracted via the Hough Transform. Notably, this lane detection system demonstrates efficacy across painted and unpainted surfaces, accommodating curved and straight roads amidst diverse weather conditions. Extensive experimentation validates the robustness and real-time operability of the proposed scheme. A critical appraisal of these methodologies, alongside their prospects for future integration, rounds off the discussion, with Figure 4-9 showcasing the outcomes yielded by the implemented program.

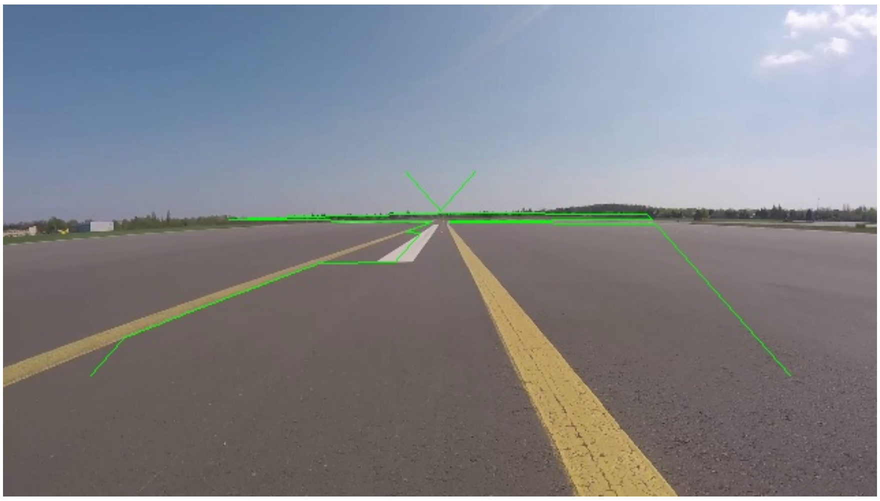

Figure 4-9 Result of running a program for line detection based on an edge detection algorithm [30]

4.2.2. Improved method for line detection

The third algorithm devised for detecting lines in airport areas diverged from the methodologies of the preceding algorithms, yet it adhered to the same programming environment, utilizing Python 3.7.6 and the OpenCV library, version 4.2.0. The fundamental concept revolved around isolating the colour shades corresponding to the lines within the image. Specifically, airport markings typically manifest as white or yellow hues, presenting a stark contrast against the gray or dark gray backdrop of the pavement. To achieve this, the initial step involved transforming the image's resolution and colour space from RGB to HSV. This conversion was pivotal in mitigating distortions arising from uneven lighting conditions, which could otherwise lead to variations in colour intensity [176]. Subsequently, specific thresholds were delineated for the saturation levels and the luminance component associated with white light.

The resultant mask encapsulated regions corresponding to the detected yellow and white colours, wherein pixels attributed to these colours were assigned a value of 255 (indicative of white), while the remaining areas of the frame were assigned a value of 0 (representing black). This binary mask served as input to the Canny algorithm for edge detection, facilitating the identification of line boundaries. Within this algorithm, dedicated functions were allocated to distinct tasks, encompassing colour separation, determination of Regions of Interest (ROI), line detection, and supervisory functions. Figure 4-10 illustrates a comprehensive block diagram elucidating the operational workflow of the program.

The wide-angle lens of the camera provides several benefits, but it also has some drawbacks. One of the primary advantages is that it allows almost the entire width of the runway to be captured in a single frame, which is incredibly useful for monitoring purposes. However, this broad field of view also means that the camera captures many extraneous elements that can introduce noise and interfere with the algorithm's performance. To mitigate this issue, it was decided to manually define a Region of Interest. This ROI encompasses the central part of the image where the critical lines of interest should be located, plus a margin to account for any potential errors. The boundary of this ROI is set just below the horizon line to exclude any horizontal lines that might be mistakenly detected by the algorithm.

Once the ROI is established, the image is processed using the Hough Transform to detect lines. Specifically, the Probabilistic Hough Line Transform was employed, implemented with the function call *cv2.HoughLinesP(input, 1, np.pi/180, 10, 50, 10)*. This function identifies lines within the specified parameters and outputs an image with detected lines superimposed on the original image. These lines correspond to the edges of the stripes painted on the airport runway.

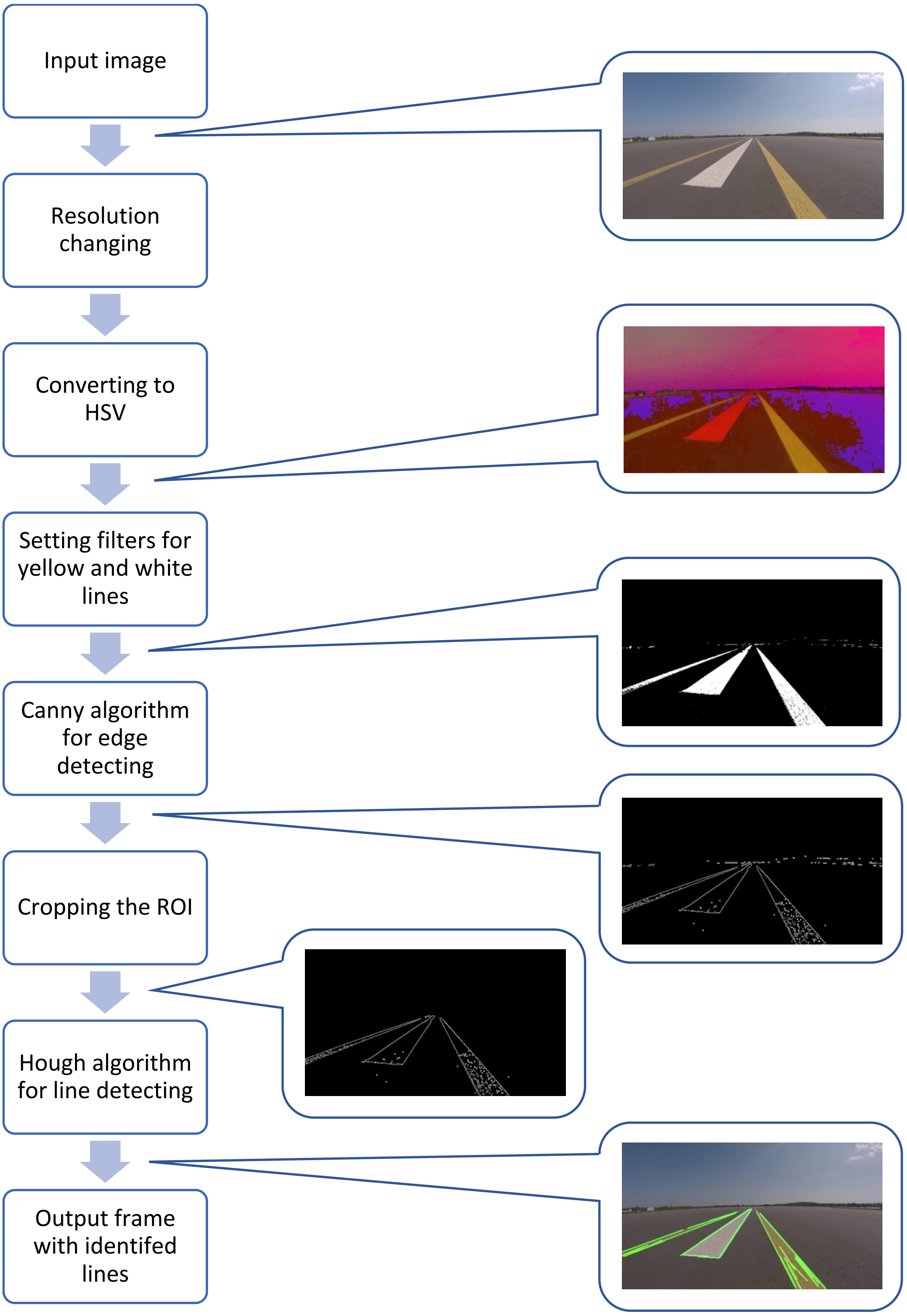

Figure 4-10 Scheme of program based on line detection algorithm using image segmentation based on colours in HSV colour space.

It is particularly noteworthy that this algorithm is highly effective at detecting both white and yellow lines simultaneously. This dual detection capability is achieved by leveraging a different colour space, allowing for more accurate segmentation. For white lines, the colour range from [0, 0, 150] to [60, 40, 255] was used, and for yellow lines, the range from [10, 60, 140] to [30, 255, 255]. The mask for each colour was calculated separately using the *cv2.inRange(input, minVal, maxVal)* function, and then combined using a standard addition operation. The result of this processing is illustrated in Figure 4-11, which shows the detected lines clearly marked on the runway, demonstrating the effectiveness of the algorithm.

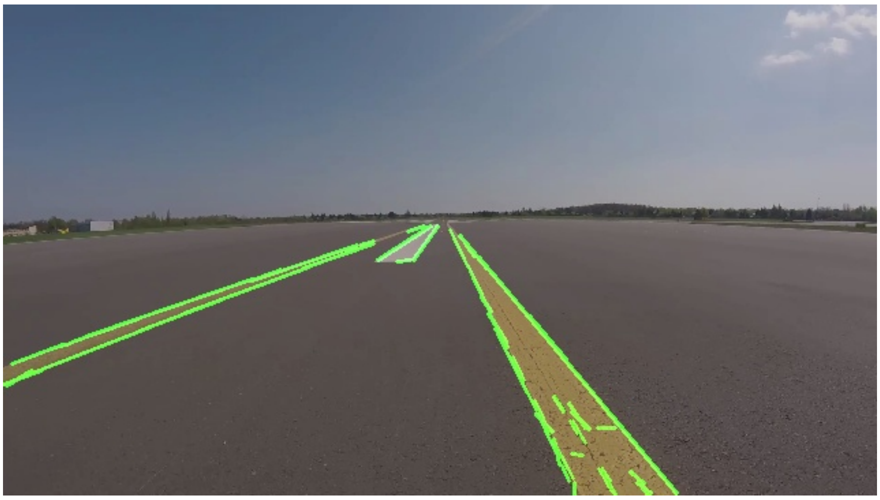

Figure 4-11 Result of program based on a line detection algorithm using image segmentation based on colours in HSV space [30]

A comparable approach to line detection has found application in determining the trajectory of motion for mobile robots [177]. This endeavour underscored the significance of image segmentation, particularly the conversion of colours into an alternative colour space, in enhancing object classification within the image. Notably, in the context of mobile robotics, this task was facilitated by the controlled environment in which the robot operated. Here, the lines exhibited a distinct colour contrast against the background, while the lighting conditions remained uniform, thereby streamlining the selection of an appropriate colour scale range [177].

Conversely, outdoor environments like airports pose a distinct set of challenges owing to the variability in lighting and weather conditions. Moreover, the colour of the lines is subject to constant fluctuation, owing partly to pavement wear and tear. In this regard, leveraging the HSV colour space proves instrumental in circumventing these challenges, primarily due to its hue parameter, which governs the perceived colour tone. Consequently, by amalgamating all colours present in airport markings, it becomes feasible to delineate a mask that effectively segments areas necessitating line edge detection.

4.3. Experimental results of vision algorithms for line detection

During the experimental testing phase of each of the developed algorithms, individual frames containing the results were captured. The experiment encompassed the analysis of 100 frames sourced from diverse recordings obtained during the inspection of airport lighting. Furthermore, the efficiency of line detection and the processing speed of the following algorithms were juxtaposed:

i. Algorithm 1: This entailed preprocessing, histogram equalization, Canny edge detection, Scharr filtering, and Hough Transform
ii. Algorithm 2: This involved preprocessing, thresholding, Canny edge detection, Hough Transform, and hyperbolas fitting
iii. Algorithm 3: This encompassed preprocessing, conversion to HSV colour space, Canny edge detection, and Hough Transform.

The tests were conducted across six different resolutions:

- Full HD (1920 × 1080)
- HD+ (1600 × 900)
- HD (1366 × 768)
- WXGA (1280 × 720)
- nHD (640 × 360)
- 320 × 180.

Consequently, each algorithm yielded an output consisting of 600 frames, each containing marked lines. However, disparities in preprocessing stages and employed methodologies ensured that no two images were identical at the conclusion of detection. Every frame underwent assessment across two categories. The first category pertained to the detection of any line within the airport areas.

$$\mathrm{r\%} = \frac{\sum_{\mathrm{i=1}}^{\mathrm{n}} \mathrm{r_i}}{\mathrm{n}} \times 100 \tag{55}$$

The percentage values representing the performance of the algorithms were determined using equation (55), where the variable r signifies the manually classified result within a specific category, and n denotes the total number of samples or video frames analysed.

The effectiveness, expressed as a percentage, for each algorithm is depicted in Figure 4-12. Notably, Algorithm 2 exhibits substantial deviation from the results obtained by the other two algorithms. This disparity can be attributed primarily to the algorithm's operational mechanism, which relies on mathematical computations rather than image processing operations. Interestingly, Algorithm 2 achieved its highest efficiency at the lowest tested resolution. This phenomenon could be attributed to the reduced level of detail in the frames, simplifying calculations and consequently enhancing line detection efficiency.

Conversely, Algorithms 1 and 3 demonstrate an inverse trend, wherein higher resolutions correspond to improved efficiency. In the case of Algorithm 1, efficiency remains consistently high, exceeding 90%, while for Algorithm 3, it even reaches a perfect score of 100%.

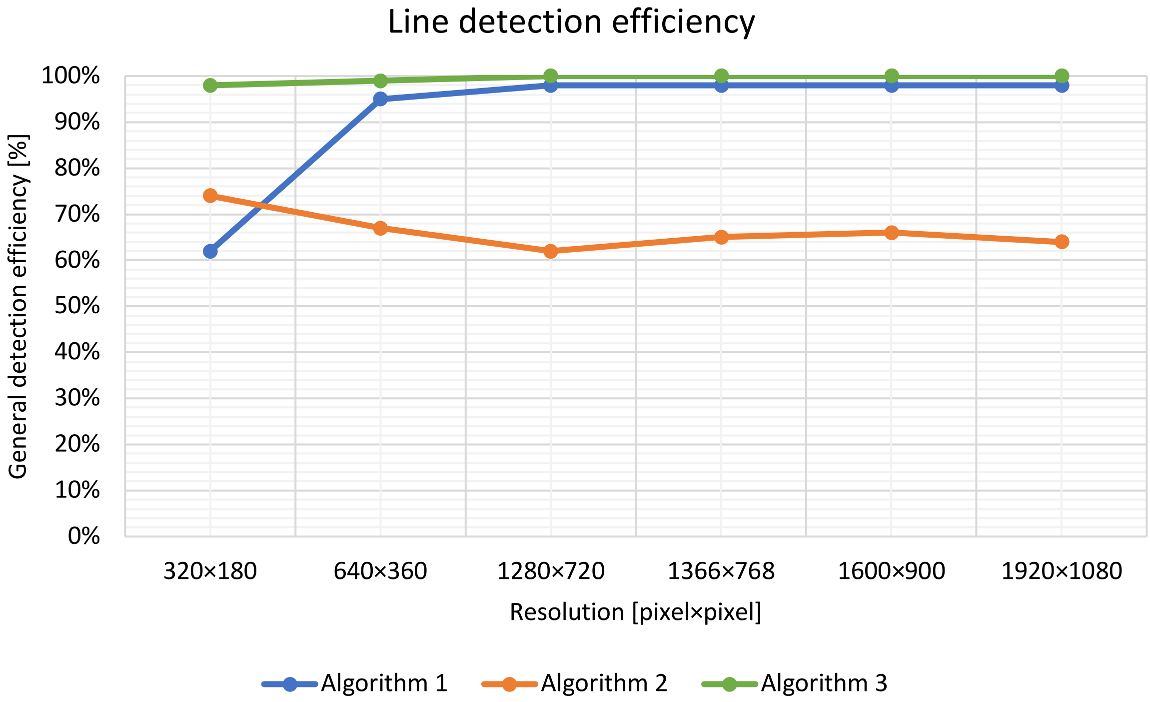

Figure 4-12 Overall detection efficiency depending on resolution and algorithm used [30]

The second step in evaluating the effectiveness of the algorithms involved assessing whether all lines and markings within the critical area of the frame—specifically, the region directly in front of the lens and roughly at the centre of the image—were accurately detected. Figure 4-13 presents a comprehensive list of parameters that measure the degree of line detection efficiency relative to different frame resolutions.

When examining the performance of Algorithms 1 and 3, it was observed that their effectiveness remained relatively consistent in detecting all lines within the critical area for resolutions at or above WXGA. Both algorithms managed to maintain a high level of accuracy in identifying the necessary lines and markings in these higher resolution images. However, a noticeable decrease in detection efficiency occurred for Algorithm 1 when the resolution was reduced. Despite this drop in accuracy at lower resolutions, Algorithm 1 exhibited a significant increase in processing speed, which may be advantageous in certain applications.

In contrast, Algorithm 2, which relies predominantly on computational methods rather than direct image processing, demonstrated considerably poorer performance. Its effectiveness was measured at only 40–45%, indicating that it struggled significantly with accurately detecting the lines and markings within the critical area of the frame. This suggests that Algorithm 2's approach is less suited for tasks requiring precise vision detection, especially when compared to the more image-focused methodologies of Algorithms 1 and 3.

Overall, while Algorithms 1 and 3 provide robust detection capabilities at higher resolutions, the choice of algorithm might depend on the specific requirements of speed versus accuracy, particularly in lower resolution scenarios.

Algorithm 1 exhibits notable shortcomings in accurately identifying both edges of painted lines. This led to classification errors, misinterpreting the failure to detect all lines during processing. Additionally, at higher resolutions, particularly from WXGA upwards, significant background noise was observed, particularly in the form of erroneous edge detections on the black asphalt, a phenomenon absents in the other two algorithms. Furthermore, Algorithm 1 encountered difficulties with lines positioned farther from the camera lens, approximately half the height of the frame, where edges were either not detected at all or incorrectly identified.

Conversely, Algorithm 2 demonstrated robust performance, particularly in scenarios featuring a single white line (central line) within the frame. Satisfactory line detection efficiency extended to scenarios with up to two lines within the camera's field of view, attributed to the algorithm's adaptation for lane determination between two lines. However, Algorithm 2 exhibited limitations in detecting yellow-coloured lines, which were largely unrecognized. In such instances, fragmentary line detection was evident primarily in turns and at greater distances from the camera, disqualifying its suitability for supporting the measurement platform approach to test airport lighting quality.

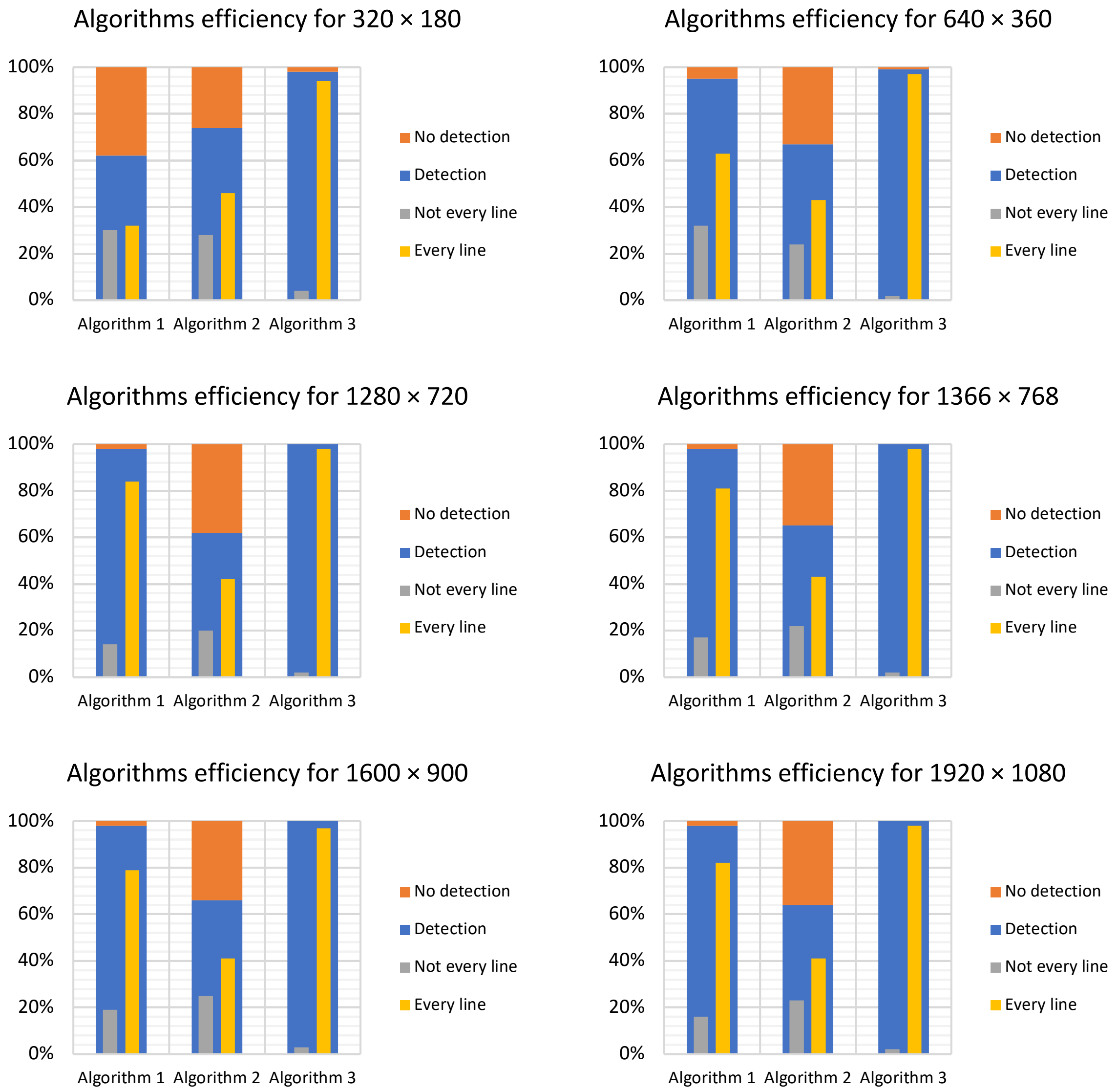

Figure 4-13 Summary of detection performance details for different resolutions [30]

Algorithm 3 emerged as the clear frontrunner, excelling in detecting airport plane markings across various testing scenarios. It consistently identified nearly all edges of visible lines within the frame, regardless of colour (white or yellow). Although noise was present at higher resolutions, starting from nHD and upwards, the use of colour segmentation effectively contained it within the outlines of the lines, preserving result interpretation integrity. These noises primarily comprised small edges detected due to surface texture variations, where the line itself did not constitute a uniform colour area or areas lacking paint. Adjusting length parameters of detected lines could potentially mitigate this issue, but the imperative to identify lines affected by tyre rubber in the touchdown zone rendered such adjustments impractical. Algorithm 3 outperformed its counterparts by seamlessly detecting all lines within this critical area without encountering any obstacles.

4.4. Performance evaluation using single board computer

In order to perform a comprehensive analysis of the proposed algorithm and develop the system, it was necessary to perform an analysis of the performance of individual single board computers. This is also a reference to the tasks set in this dissertation, namely: *Proposals of embedded systems implementations.*

The evaluation of algorithmic performance was conducted using a range of hardware platforms including the Raspberry Pi 4B, NVIDIA Jetson Nano, NVIDIA Jetson Xavier AGX, and NVIDIA Jetson Orin AGX modules. The testing procedure involved the selection of random 10-second segments from the entirety of the video sequences. Moreover, each segment underwent scaling to six different resolutions: 1920 × 1080 (Full HD), 1600 × 900 (HD+), 1366 × 768 (HD), 1280 × 720 (WXGA), 640 × 360 (nHD), and 320 × 180. Figure 4-14 and Figure 4-15 in the analysis depict a comparative evaluation of the mean frames analysed per second across these segments, varying by resolution and the specific embedded system utilized for each algorithm. Notably, power consumption considerations were factored into the experimental design, given the algorithm's computational intensity. Hence, the randomization of sequences was performed once, followed by offline testing.

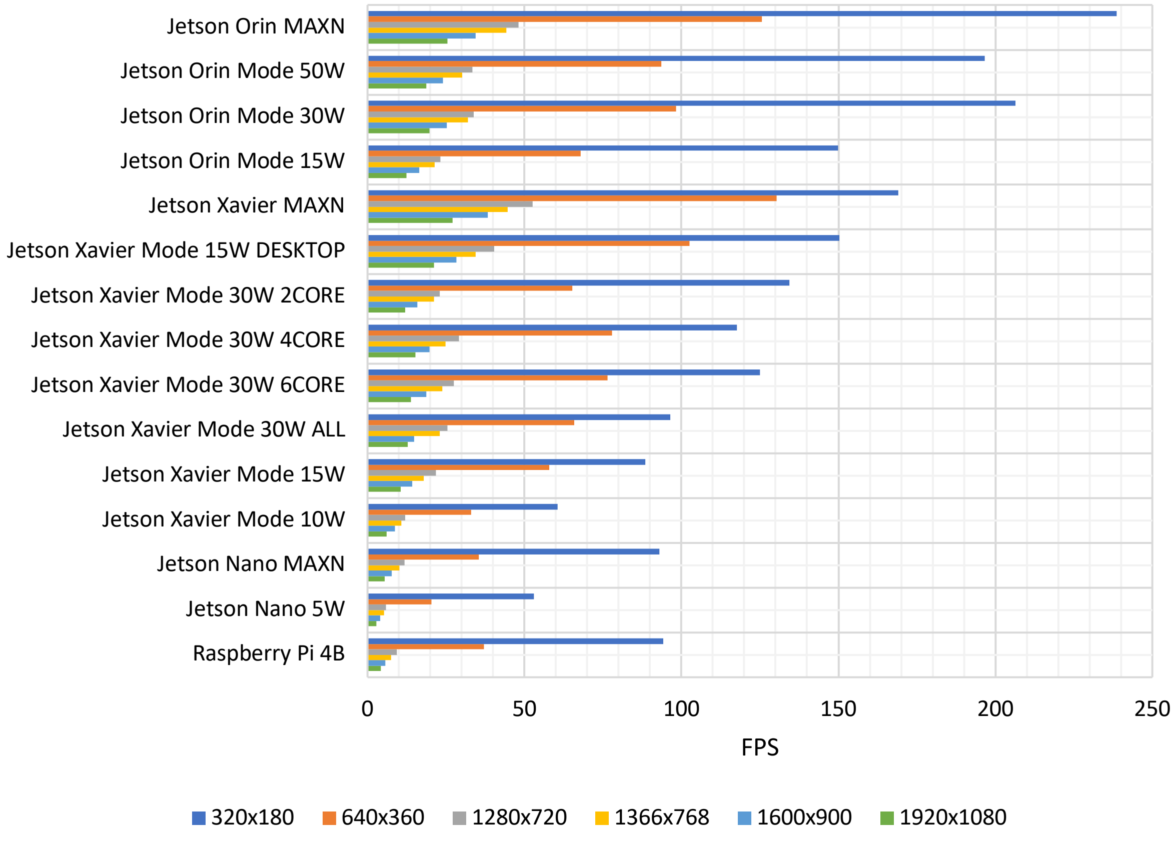

Figure 4-14 FPS of image segmentation in the HSV colour space algorithm for various power modes of tested platforms [44]

Throughout all experimentation phases, consistent software configurations were maintained, devoid of any tailored adjustments for individual hardware platforms. These tests encompassed a diverse array of power consumption modes to comprehensively assess algorithmic performance under varying operational conditions and system configurations.

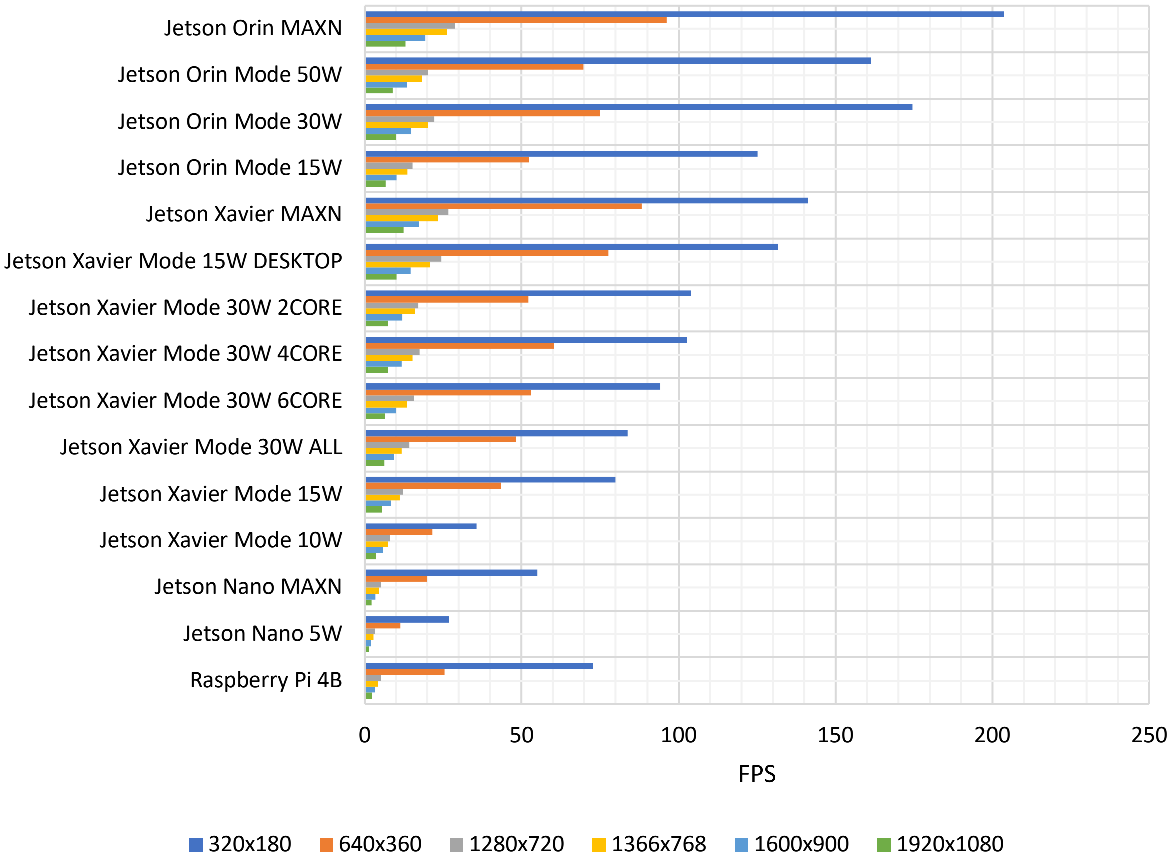

Figure 4-15 FPS of line detection using the Hough algorithm with Scharr mask filtering for various power modes of tested platforms [44]

The algorithm based on image segmentation in the HSV colour space, owing to its lower computational complexity [30], exhibits shorter processing times compared to line detection using the Hough algorithm with Scharr mask filtering. Notably, the processing time of the program increases with higher input resolutions, a relationship observed across all tested embedded devices and selected power consumption modes. For instance, the Raspberry Pi 4B microcomputer yielded nearly identical results to the NVIDIA Jetson Nano module in MAXN power mode. However, with the NVIDIA Jetson Xavier AGX, an increase in the number of processed frames per second was observed at maximum CPU processor clock speed. Table 2-5 illustrates that higher processor timings are obtained for higher power consumption modes. In the 30W mode, the maximum clock frequency changes depending on the number of processor cores used, with fewer active cores corresponding to higher frequencies. A similar pattern is evident for the NVIDIA Jetson Orin AGX, as indicated in in Table 2-6, where the processor's clock frequency also varies. Remarkably, for the most efficient units and this algorithm, such as the NVIDIA Jetson Orin AGX and NVIDIA Jetson Xavier AGX, real-time processing of video sequences at maximum resolution is achievable, with values exceeding 24 FPS.

Due to the architecture of airport line detection programs, which are typically single-threaded [30], reducing the number of active processor cores does not adversely affect the achieved results. However, it's essential to consider the computational complexity of line detection using the Hough algorithm with Scharr mask filtering, as this can impact processing time, particularly in embedded systems. Consequently, achieving performance levels of 24 frames per second (FPS) in video sequence processing was only feasible after reducing the resolution to 1366×768. Notably, with the most efficient NVIDIA Jetson Xavier MAXN modules, 24 FPS were attained, while NVIDIA Jetson Orin MAXN achieved 26 FPS.

It's crucial to acknowledge that the efficiency of line detection using the Hough algorithm with Scharr mask filtering, owing to its greater computational complexity, may result in the tested embedded devices exhibiting inferior maximum performance compared to algorithms based on image segmentation in the HSV colour space. Consequently, such approaches may not be equally suitable for real-time applications.

4.4.1. Power consumption analysis

Energy consumption was measured using the Jetson-Stats software [178], an advanced system monitoring and control package specifically designed for the NVIDIA Jetson series, including models such as the Orin, Xavier, Nano, and TX. This tool, illustrated in Figure 4-16, is essential for researchers and developers who need in-depth analysis and performance tracking of their NVIDIA Jetson boards. Key features of Jetson-Stats include:

- Hardware, Architecture, L4T, and NVIDIA Jetpack Decoding: The tool provides detailed information about the system's hardware and software configurations. This includes insights into the Linux for Tegra (L4T) operating system and NVIDIA Jetpack SDK, which are crucial for understanding the system's operational parameters and identifying opportunities for performance optimization.
- Comprehensive Monitoring: Jetson-Stats can monitor a wide array of system metrics, including CPU and GPU usage, memory consumption, engine activity, and fan speeds. This comprehensive monitoring capability ensures that users have continuous

awareness of the system's health and performance, enabling them to detect and address potential issues promptly.

- System Control: The package allows users to manage various system parameters, including the NVP model (which relates to power modes), fan speed, and jetson_clocks (a utility to maximize system performance). This control over performance and power management is particularly valuable for optimizing the balance between computational demands and energy efficiency.

Jetson-Stats serves as a vital resource, offering detailed monitoring and control features that enhance the ability to manage and optimize NVIDIA Jetson boards. By providing real-time data and control capabilities, it supports the efficient use of hardware resources, ensuring that the Jetson platforms can be used to their full potential in research and development settings.

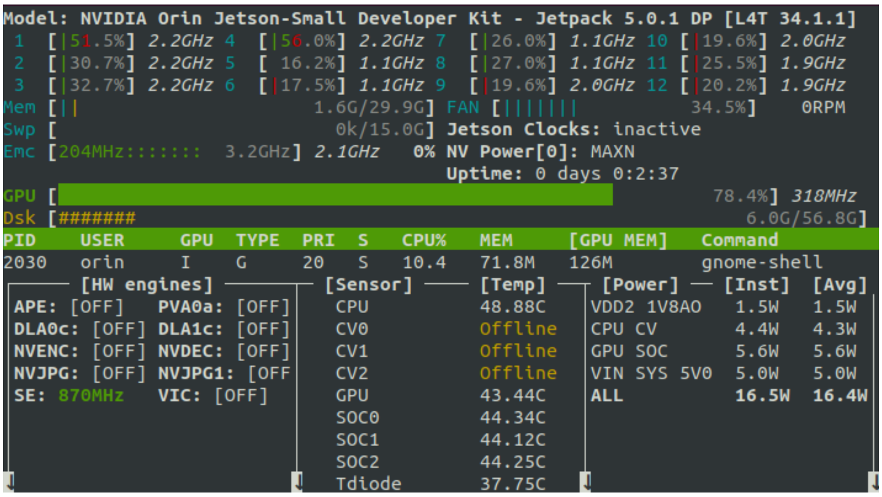

```
Model: NVIDIA Orin Jetson-Small Developer Kit - Jetpack 5.0.1 DP [L4T 34.1.1]
 1  [|51.5%] 2.2GHz 4  [|56.0%] 2.2GHz 7  [|26.0%] 1.1GHz 10 [|19.6%] 2.0GHz
 2  [|30.7%] 2.2GHz 5  [ 16.2%] 1.1GHz 8  [|27.0%] 1.1GHz 11 [|25.5%] 1.9GHz
 3  [|32.7%] 2.2GHz 6  [|17.5%] 1.1GHz 9  [|19.6%] 2.0GHz 12 [|20.2%] 1.9GHz
Mem [||                   1.6G/29.9G] FAN [|||||||        34.5%]    0RPM
Swp [                       0k/15.0G] Jetson Clocks: inactive
Emc [204MHz::::::: 3.2GHz] 2.1GHz  0% NV Power[0]: MAXN
                                      Uptime: 0 days 0:2:37
GPU [                                                78.4%] 318MHz
Dsk [#######                                              6.0G/56.8G]
PID    USER    GPU  TYPE  PRI S   CPU%   MEM    [GPU MEM]   Command
2030   orin    I    G     20  S   10.4   71.8M  126M        gnome-shell
┌───── [HW engines] ──────┬─ [Sensor] ──── [Temp] ─┬─ [Power] ─ [Inst]  [Avg]
│APE: [OFF]   PVA0a: [OFF]│  CPU          48.88C  │VDD2 1V8AO  1.5W   1.5W  │
│DLA0c: [OFF] DLA1c: [OFF]│  CV0          Offline │CPU CV      4.4W   4.3W  │
│NVENC: [OFF] NVDEC: [OFF]│  CV1          Offline │GPU SOC     5.6W   5.6W  │
│NVJPG: [OFF] NVJPG1: [OFF│  CV2          Offline │VIN SYS 5V0 5.0W   5.0W  │
│SE: 870MHz   VIC: [OFF]  │  GPU          43.44C  │ALL         16.5W  16.4W │
│                         │  SOC0         44.34C  │                         │
│                         │  SOC1         44.12C  │                         │
│                         │  SOC2         44.25C  │                         │
↓                         ↓  Tdiode       37.75C  ↓                         ↓
```

Figure 4-16 Jetson-Stats software interface running on NVIDIA Jetson Orin AGX [44]

The average power consumption measurements are presented with a precision level of 0.1 W, mirroring the accuracy of results obtained through the Jetson-stats software. In line with this precision, results obtained via hardware measurements using multimeters are also showcased with equivalent accuracy. Table 4-2 displays the outcomes of average power consumption measurements during algorithm operation across various power modes and resolutions, employing the algorithm grounded in image segmentation within the HSV colour space. Conversely, Table 4-3 delineates the results for line detection utilizing the Hough algorithm with Scharr mask filtering. Both tables encapsulate the average results derived from offline trials conducted over 10-second sequences, varying in resolution and randomly selected from the dataset. Notably, these measurements were conducted without imposing any FPS limits during the trials.

Table 4-2 Average power consumption (in Watts) for algorithm based on image segmentation in the HSV colour space using Jetson-Stats software

	320×180	640×360	1280×720	1366×768	1600×900	1920×1080
Jetson Nano 5W	2.8	3.2	3.1	3.2	3	3.2
Jetson Nano MAXN	4.8	4.9	4.8	5	5	4.8
Jetson Xavier Mode 10W	4.3	4.3	4.3	4.1	4.1	4.1
Jetson Xavier Mode 15W	4.6	4.9	4.9	4.9	5	4.9
Jetson Xavier Mode 30W ALL	5	5.5	5.4	5.4	5.4	5.4
Jetson Xavier Mode 30W 6CORE	5.4	5.5	5.6	5.7	5.8	6.1
Jetson Xavier Mode 30W 4CORE	5.5	5.9	6.2	6.2	6.5	6.5
Jetson Xavier Mode 30W 2CORE	6.8	7.1	7.3	7.3	7.3	7.4
Jetson Xavier Mode 15W DESKTOP	7.5	8.7	8.9	9.1	9.2	9.4
Jetson Xavier MAXN	10.7	13.2	13.1	13.2	13.4	13.5
Jetson Orin Mode 15W	11.3	11.4	11.5	11.5	11.5	11.7
Jetson Orin Mode 30W	12.5	13.4	13.3	13.3	13.3	13.9
Jetson Orin Mode 50W	12.1	13.1	12.5	12.5	13	13.9
Jetson Orin MAXN	15.4	17.7	16.7	16.8	16.8	16.9

Table 4-3 Average power consumption (in Watts) for line detection using Hough algorithm with Scharr mask filtering using Jetson-Stats software

	320×180	640×360	1280×720	1366×768	1600×900	1920×1080
Jetson Nano 5W	3.1	3	3	3	3	3.1
Jetson Nano MAXN	4.1	3.9	4.4	4.7	4.6	4.8
Jetson Xavier Mode 10W	4.1	4.1	4.1	4.1	4.1	4.1
Jetson Xavier Mode 15W	4.6	5.1	4.7	4.6	4.6	4.6
Jetson Xavier Mode 30W ALL	4.9	5.2	4.9	4.9	4.9	4.7
Jetson Xavier Mode 30W 6CORE	5	5.4	5.2	5.2	5.2	5.1
Jetson Xavier Mode 30W 4CORE	5.3	5.9	5.7	5.7	5.9	5.5
Jetson Xavier Mode 30W 2CORE	6.7	6.9	6.9	7.1	7.1	7.1
Jetson Xavier Mode 15W DESKTOP	7.4	8.1	8	7.9	8.2	7.9
Jetson Xavier MAXN	10.3	11.5	11.2	11.1	10.9	10.9
Jetson Orin Mode 15W	11.2	11.3	11.4	11.4	11.4	11.3
Jetson Orin Mode 30W	12.7	12.9	12.7	12.7	12.7	12.7
Jetson Orin Mode 50W	12.1	12.5	11.9	11.9	11.9	11.9
Jetson Orin MAXN	15.4	16.7	15.6	15.3	15.3	14.9

It's evident from previous sections that more advanced modules such as the NVIDIA Jetson Orin AGX operating in MAXN mode and the NVIDIA Jetson Xavier AGX in MAXN mode exhibit higher power demands, which aligns with expectations given their enhanced performance capabilities. Specifically, the FPS values obtained for these devices notably surpass those of their counterparts.

Noteworthy is the subtle variation in power consumption observed across different resolutions for individual power modes, with measured values remaining relatively consistent. This phenomenon stems from the absence of FPS limits during experimentation, where FPS values were maximized independently for each experiment.

To provide a more comprehensive assessment of power requirements, accounting for the interplay between algorithm type, resolution, and FPS values obtained, these dependencies have been meticulously considered and summarized in the subsequent sub-chapter.

As an embedded system from the Raspberry Pi family was utilized in this study, the aforementioned software solution could not be employed. Consequently, it was opted to employ standard laboratory multimeters to obtain the average energy consumption of each embedded system. It's noteworthy that the earlier Jetson-Stats software solely measures the power consumed by the microcomputer's components, disregarding the power consumption of connected accessories. To address this, measurements in the following instances include typical accessories such as a keyboard, mouse, and fan connected to the microcomputers.

Figure 4-17 presents the results of average power consumption measurements during algorithm operation across various power modes and resolutions, employing the algorithm based on image segmentation in the HSV colour space, with power meter measurements. Conversely, Figure 4-18 showcases the results for line detection using the Hough algorithm with Scharr mask filtering.

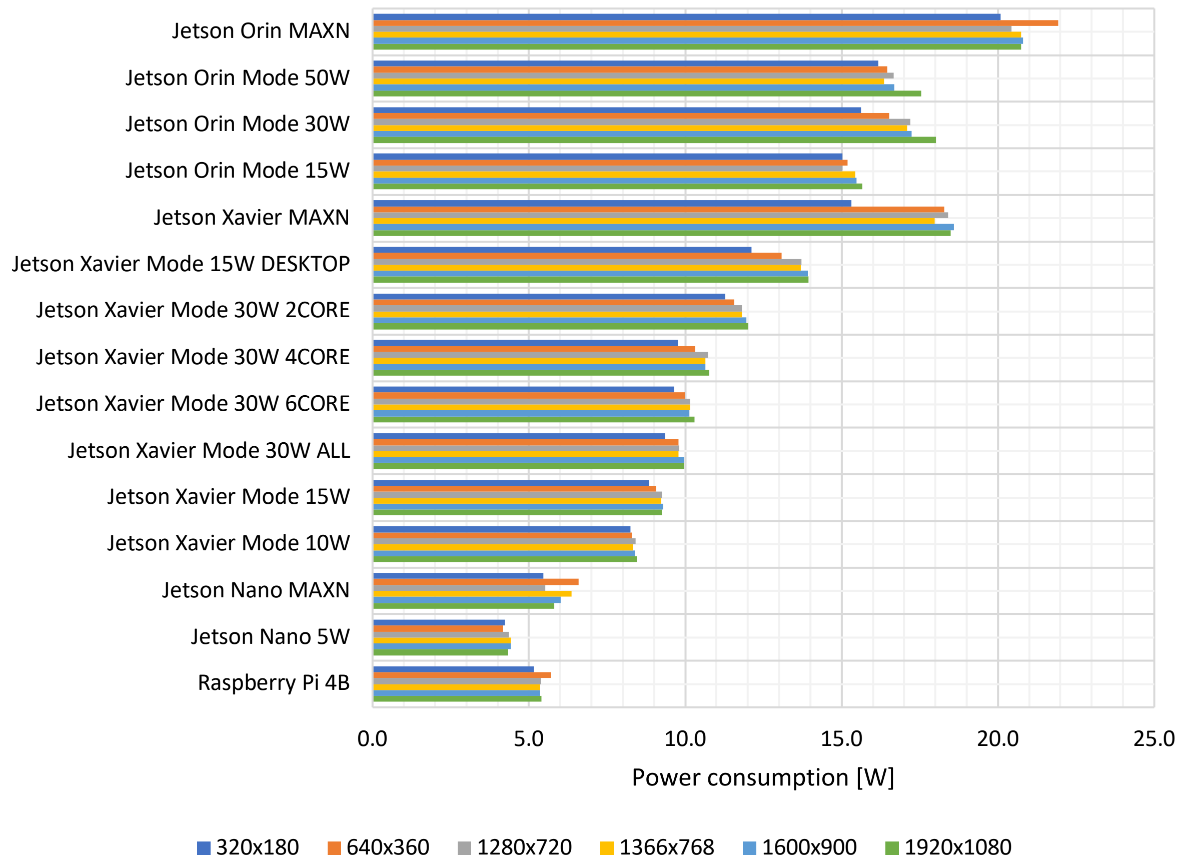

Figure 4-17 Average power consumption (in Watts) for algorithm based on image segmentation in the HSV colour space using electronic multimeter [44]

For the algorithm analysed, which relies on image segmentation in the HSV colour space, achieving the highest resolutions of 1920 × 1080 imposes a limitation on the Frames Per Second value, typically below 24 FPS. However, this FPS value is considered acceptable for airport line detection techniques, given the nature of the task and the processing requirements involved.

Two microcomputers meet these requirements with the following configurations: the NVIDIA Jetson Xavier AGX operating in MAXN mode and the NVIDIA Jetson Orin AGX also in MAXN mode. In these configurations, the average power consumption and corresponding FPS values are as follows:

- For NVIDIA Jetson Xavier AGX in MAXN mode: The average power consumption is 18.5 W, achieving a frame rate of approximately 27 FPS.
- For NVIDIA Jetson Orin AGX in MAXN mode: The average power consumption is 20.8 W, with a frame rate of approximately 25 FPS.

These results indicate that both the NVIDIA Jetson Xavier AGX and the NVIDIA Jetson Orin AGX are capable of meeting the processing requirements for airport line detection techniques at the specified resolution, while maintaining acceptable power consumption levels. The FPS values achieved by these microcomputers are within the acceptable range for effective line detection, ensuring reliable performance in real-world applications.

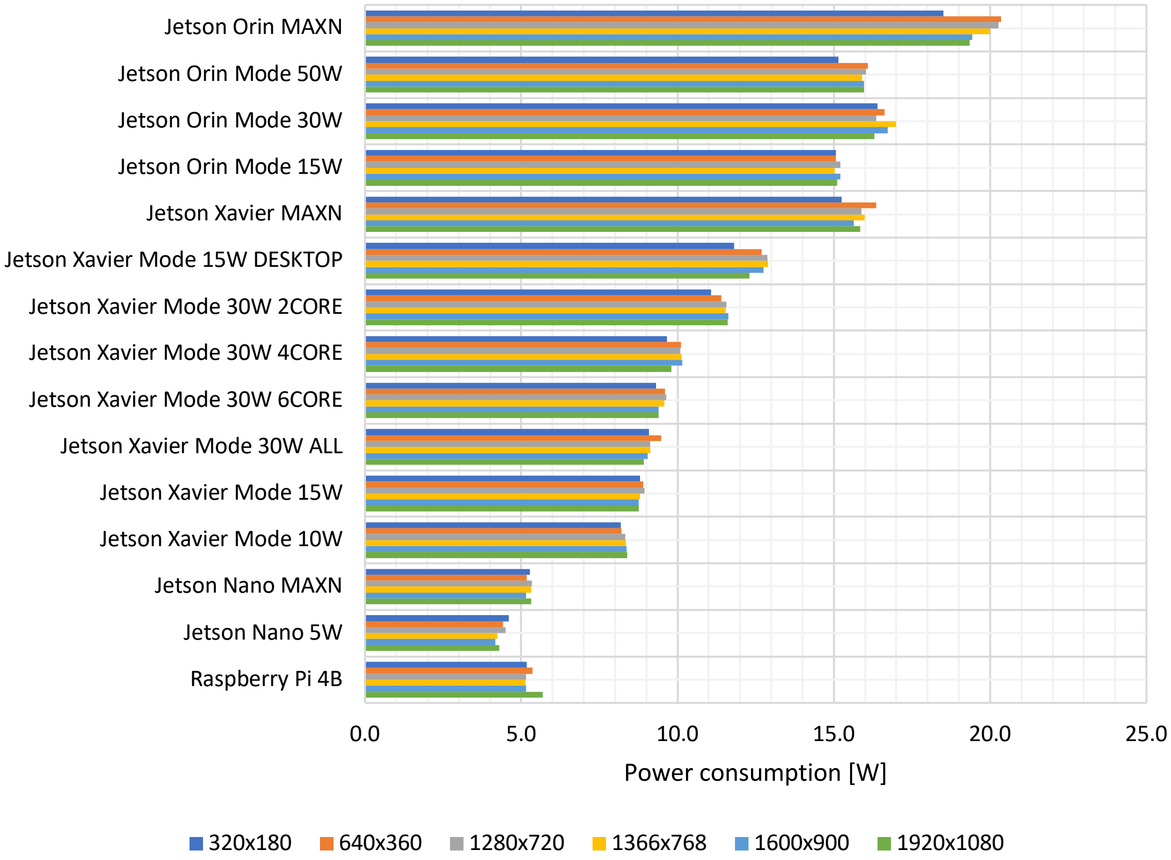

Figure 4-18 Average power consumption (in Watts) for line detection using Hough algorithm with Scharr mask filtering using electronic multimeter [44]

In the case of the second solution, which involves line detection using the Hough algorithm with Scharr mask filtering, and with the processing speed limit set at a minimum of 24 FPS, it was found that none of the microcomputers could achieve the minimum FPS value at a video resolution of 1920 × 1080. However, reducing the resolution to 1366 × 768 allowed for video sequence processing at a sufficient speed.

Two microcomputers capable of meeting these requirements are the NVIDIA Jetson Xavier AGX operating in MAXN mode and the NVIDIA Jetson Orin AGX also in MAXN mode. In these configurations, the average power consumption and corresponding FPS values are as follows:

- For NVIDIA Jetson Xavier AGX in MAXN mode: The average power consumption is 16 W, achieving a frame rate of approximately 24 FPS at a resolution of 1366 × 768.
- For NVIDIA Jetson Orin AGX in MAXN mode: The average power consumption is 20 W, with a frame rate of approximately 26 FPS at the same resolution of 1366 × 768.

These findings indicate that both the NVIDIA Jetson Xavier AGX and the NVIDIA Jetson Orin AGX can effectively process video sequences for line detection at the specified resolution while meeting the minimum FPS requirement. Despite the higher power consumption of the Jetson Orin AGX, it offers a slightly higher FPS, ensuring smooth and efficient processing of video data.

4.4.2. Single board computers energy efficiency analysis

In order to obtain a meaningful comparative value, it was necessary to find a common value for all analysed solutions. For this reason, it was decided to compare the power consumption in terms of FPS. For the FPS and power consumption values delineated in previous sections, comparative charts have been formulated to illustrate the dependency of power consumption requirements on both resolution and FPS values. Figure 4-19 illustrates the dependency of the algorithm based on image segmentation in the HSV colour space, while Figure 4-20 depicts the dependency graph for line detection utilizing the Hough algorithm with Scharr mask filtering. Lower values denote lower power requirements, with MAX modes proving optimal for faster processing speeds, expressed in FPS.

A comparative analysis of the two algorithms reveals that in the case of the algorithm based on image segmentation in the HSV colour space, it's feasible to achieve equivalent or superior FPS values with lower energy consumption. For instance, on the NVIDIA Jetson Xavier in MAXN mode, this algorithm requires 679 mJ/frame for 1920 × 1080 resolution, whereas line detection utilizing the Hough algorithm with Scharr mask filtering necessitates 680 mJ/frame for 1366 × 768 resolution.

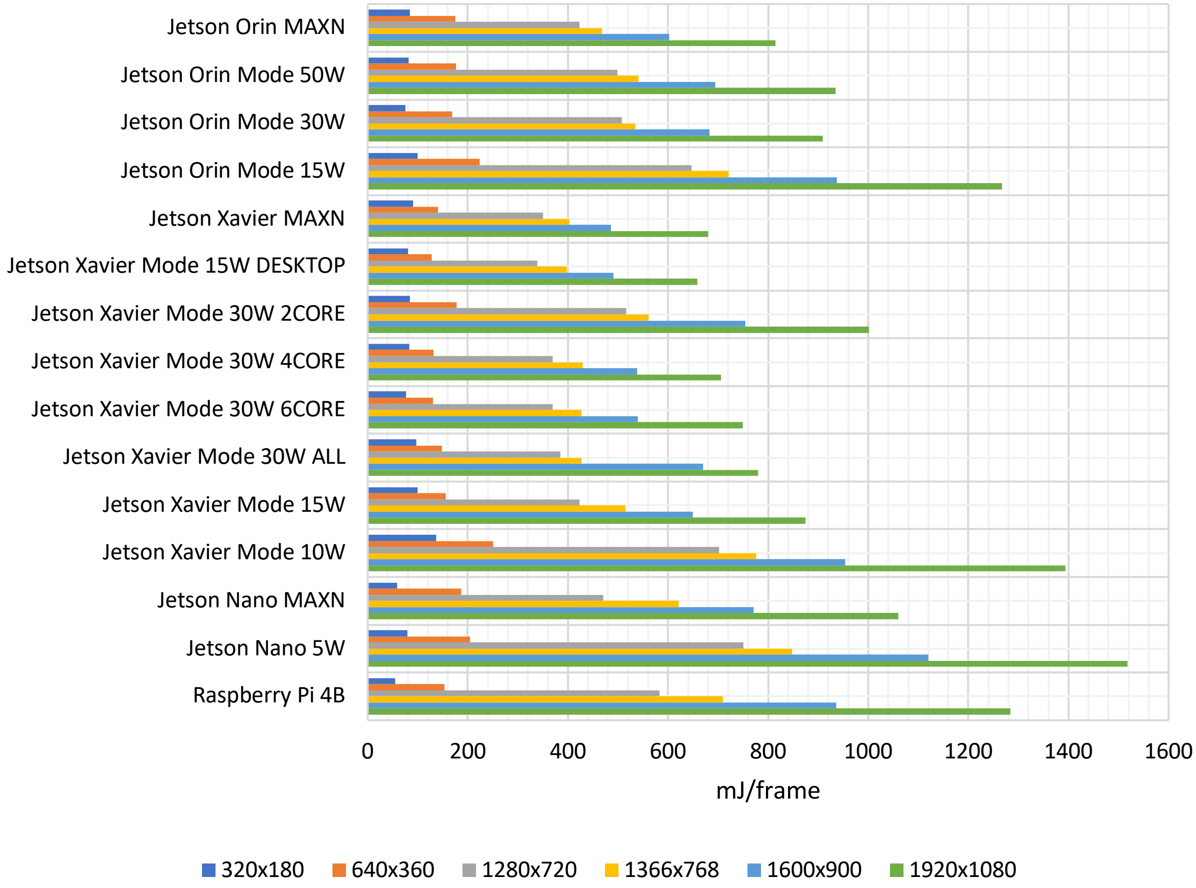

Figure 4-19 Energy efficiency analysis of algorithm based on image segmentation in the HSV colour space [44]

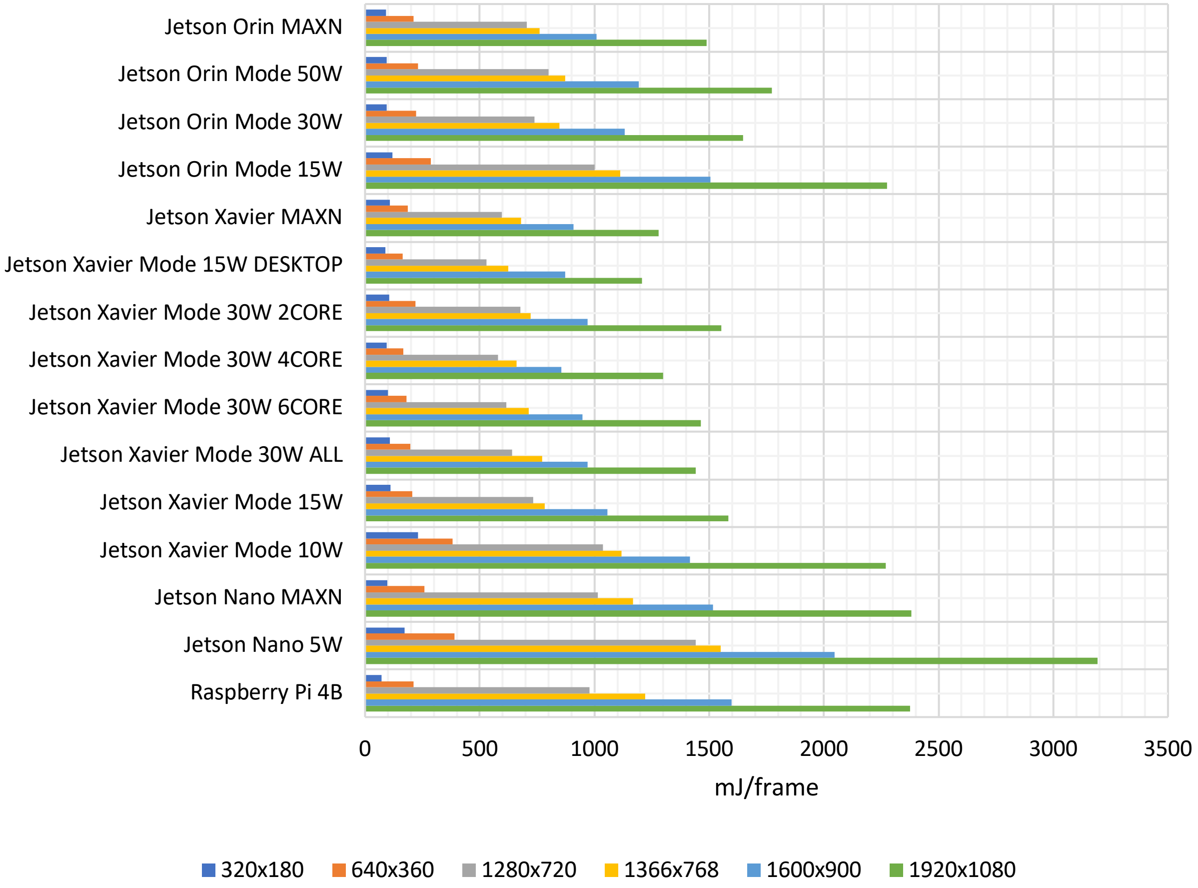

Figure 4-20 Energy efficiency analysis of line detection using Hough algorithm with Scharr mask filtering [44]

4.4.3. Energy efficiency analysis of dynamic voltage frequency switching

Another method for controlling hardware performance, similar to the power modes implemented by NVIDIA Jetson, is Dynamic Voltage and Frequency Switching (DVFS), as discussed in several studies) [179], [180], [181]. In the course of the experimentation, an additional experiment was conducted to execute image segmentation algorithms in the HSV colour space and line detection using the Hough algorithm with Scharr mask filtering, mirroring previous research methodologies. Energy consumption was monitored using multimeters and jetson-stats software. However, this time, alterations were made not only to the microcomputer's power mode but also to the DVFS policy, which includes modes such as schedutil, performance, powersave, userspace, on-demand, interactive, and conservative. The tests were conducted on the NVIDIA Jetson AGX Xavier microcomputer, given its superior performance in previous evaluations.

In terms of processing speed, the NVIDIA Jetson AGX Xavier microcomputer only met the assumptions in the MAXN mode within the DVFS policies: schedutil (27 FPS), performance (25 FPS), ondemand (27 FPS), interactive (26 FPS), conservative (27 FPS) for image segmentation in the HSV colour space at a resolution of 1920 × 1080. However, the assumptions were not fulfilled for the line detection algorithm using the Hough algorithm with Scharr mask filtering. Figure 4-21 and Figure 4-22 provide detailed results of the experiment. Notably, the MAXN and DVFS policy powersave operating modes resulted in practical incapacity to run the program, significantly extending the program's execution time and consequently increasing the energy consumption per image frame.

The experiments conducted, based on the defined assumptions and utilized algorithms, revealed that the optimal operating modes meeting the assumptions are the power mode MAXN and DVFS policy schedutil (680 mJ/frame). However, in most cases, the differences hover around 7%:

- schedutil: 27 FPS ➔ 680 mJ/frame
- performance: 25 FPS ➔ 732 mJ/frame
- ondemand: 27 FPS ➔ 697 mJ/frame
- interactive: 26 FPS ➔ 698 mJ/frame
- conservative: 27 FPS ➔ 685 mJ/frame

These findings underscore the importance of selecting appropriate power modes and DVFS policies to achieve optimal energy efficiency and processing performance for embedded systems.

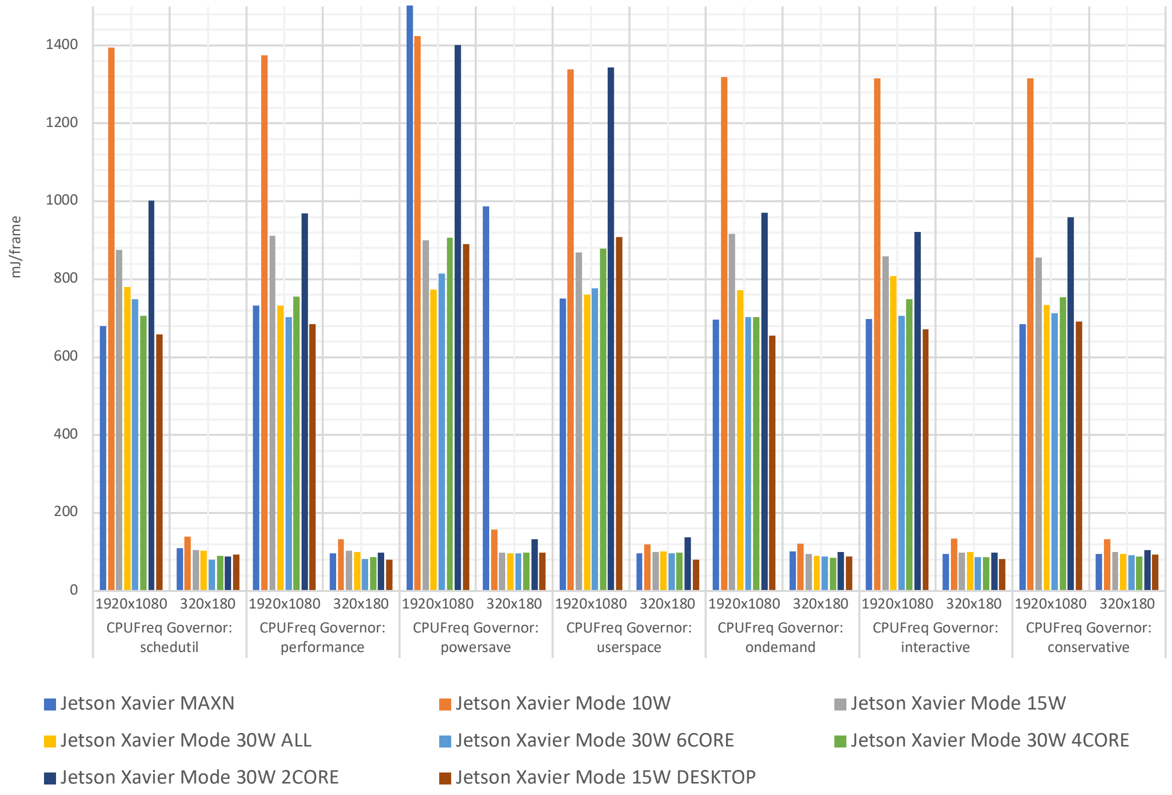

Figure 4-21 Energy efficiency analysis of algorithm based on image segmentation in the HSV colour space using different DVFS policies [44]

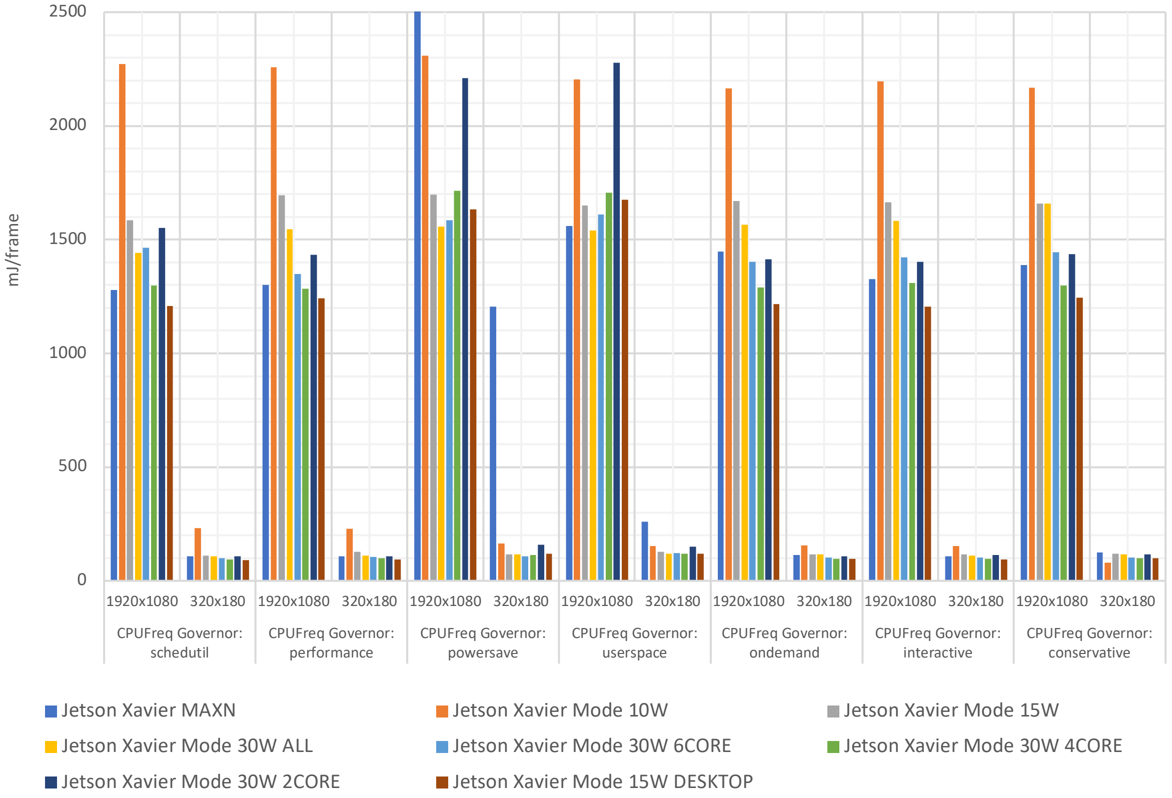

Figure 4-22 Energy efficiency analysis of line detection using Hough algorithm with Scharr mask filtering using different DVFS policies [44]

Indeed, it is noteworthy that the results obtained previously, utilizing the default DVFS policy schedutil, validate the optimization of this mode, which outperformed all other tested modes by yielding the lowest energy consumption per image frame. This underscores the significance of selecting the most efficient DVFS policy to ensure optimal energy efficiency without compromising processing performance.

Chapter

5. Quality classification of airfield ground lighting

The quality assessment of airport lamps can be carried out using stationary methods, e.g. using a goniometer, or mobile methods, such as a measurement platform for testing airport lighting [26], [27], [28], [29], [53]. For this reason, several scopes of aviation navigation lighting inspections can be distinguished. This thesis puts emphasis on the vision assessment of in-pavement airport lamps, which is based on the detection and assessment of wear (chipping) of the prism of the lamp being examined. The second type of inspection is examining the colour of a given lamp. First, to assess its type, and then to adapt the appropriate international standards, but also to assess the chromaticity of the light emitted by these lamps. Figure 5-1 shows a schematic division of the scope of research.

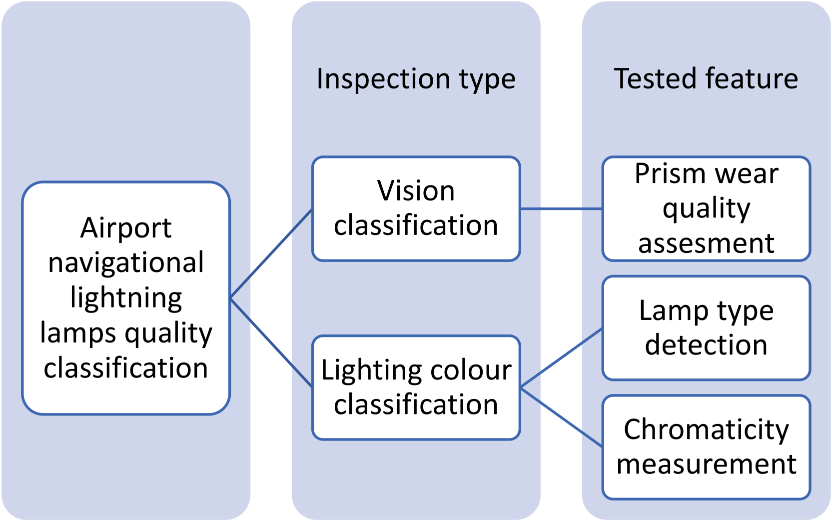

Figure 5-1 Types of airport navigational lightning lamps quality classification

5.1. Vision classification of airport navigation lighting lamps system

The quality assessment of airport lamps can be conducted through stationary methods, such as using a light goniometer, or mobile methods, which involve luminous intensity measuring platforms [28] or drones [26], [31]. The stationary approach is notably time-consuming as it necessitates the disassembly of lamps. Conversely, the utilization of measurement platforms or drones is preferred due to the need for short periods of occupation in runway areas, typically ranging from 5 to 10 minutes, to minimize disruptions to air operations.

An alternative mobile method involves the utilization of a vision system capable of analysing the mechanical wear of lamps, particularly focusing on their prisms [40]. A notable advantage of this solution, compared to luminous intensity measurement, is its ability to precisely assess the degree of degradation of the prisms' frontal plane. Additionally, the presented solution can serve as a complement to sensory luminous intensity measurement systems. Image acquisition and processing can be facilitated using embedded systems [5], [128], employing dedicated vision sensors [30], [47], [48]. As depicted in Figure 5-2, the concept of the system entails a measurement platform, towed by the airport service vehicle, housing a camera that captures images from above, facilitating vision inspection of the mechanical wear of the in-pavement navigation lamps.

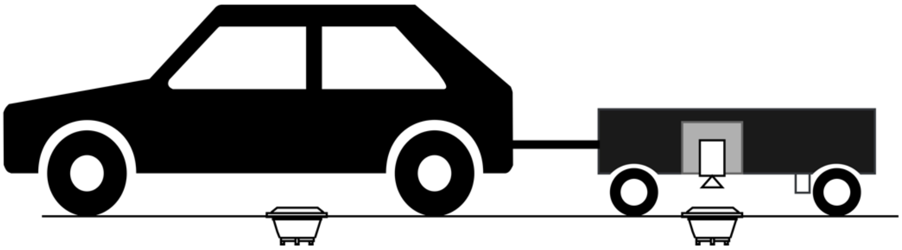

Figure 5-2 Concept of intelligent vision system for the analysis of mechanical wear of the prisms of in-pavement airport lamps

The chapter outlines the different stages involved in image processing of the integrated airport lamps. For the conclusive classification evaluation, a two-layer neural network with forward feed was employed. This neural network architecture relied on the sigmoidal function in the hidden layer and the softmax function, also known as the normalized exponential function, in the output layer. Experimental research was conducted utilizing a proprietary dataset within the MATLAB 2022a environment [105].

Figure 5-3 presents the overarching scheme of the image processing workflow. This process can be effectively segmented into two distinct stages:

- Detection of the Region of Interest (ROI): This initial stage puts emphasis on identifying the specific area within the image that requires further analysis and scrutiny. Various techniques may be employed for this purpose, including but not limited to edge detection, thresholding, or region-based segmentation methods.
- Decision-Making Process Based on a Neural Network: Following the successful detection of the ROI, the subsequent stage involves employing a neural network-based

approach for decision-making. This phase typically entails feeding the extracted features from the ROI into a trained neural network model, which then generates predictions or decisions based on the learned patterns and relationships within the data. The neural network architecture may vary depending on the specific task and objectives, ranging from convolutional neural networks (CNNs) for image classification to recurrent neural networks (RNNs) for sequential data analysis.

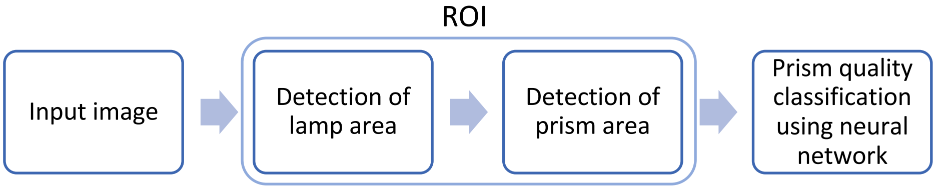

Figure 5-3 Proposed vision data processing workflow for prisms mechanical wear classification

5.1.1. Dataset of airfield ground lighting lamps

The experimental research involved the preparation of an in-pavement lamps first dataset comprising a total of 316 images [40]. In subsequent research, the dataset was expanded to 540 photos [41]. These images were carefully curated to encompass a variety of scenarios, including different weather conditions and times of the day, to ensure comprehensive testing of the algorithms under various conditions. Furthermore, efforts were made to capture images with diverse lamp positions and backgrounds, including asphalt, concrete, and a white background for lamps situated within road markings on the airfield. This diversity in image characteristics enables thorough evaluation of algorithm performance across a range of real-world situations.

The images in the dataset have a resolution of 4928 × 3264 pixels and a 24-bit colourdepth, ensuring high-quality representation of the in-pavement lamps. They are stored in JPG format, utilizing the RGB colour space to accurately capture colour information.

Figure 5-4, Figure 5-5 and Figure 5-6 provide examples of different types of in-pavement airport lamps included in the dataset. These images showcase the variability in lamp designs, orientations, and environmental contexts captured during the data collection process. Such diversity in the dataset is crucial for assessing the robustness and effectiveness of the algorithms in real-world applications, where conditions can vary significantly.

The lamps depicted in the photos exhibit variations in position and brightness, with some lamps being switched on while others are not. This diversity in the dataset is invaluable as it enables the fine-tuning of algorithms, thereby enhancing their accuracy and robustness across different conditions. For instance, runway centre line lamps function in both directions, whereas taxiway lamps typically operate in only one direction as per regulations.

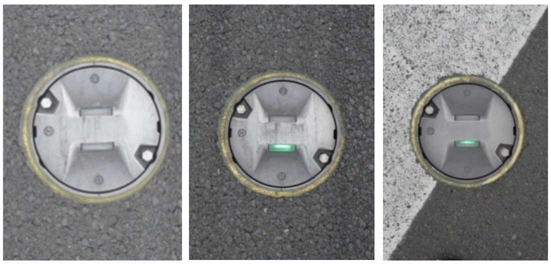

Figure 5-4 Examples of Taxiway centre line Lamp IDM5582 [40]

Figure 5-5 Examples of Runway centre line lamp IDM4582 [40]

Figure 5-6 Examples of Touchdown zone lamp IDM4671 [40]

Additionally, during the internship in Poznań–Ławica Airport, over 1000 photometric measurements of in-pavement airfield ground lighting lamps and photos were taken [43]. Photos and measurements of the lamps were taken after dismantling them from the ground surfaces and after replacing the prism and bulbs. Thanks to this, it was possible to comprehensively test the lamps and learn the consumption characteristics of navigation lighting at the airport, as well as prepare a dataset of measurements and photos. Thanks to this work it was possible to crate *PLAVS2* (Poznań Lawica Airport Video Set 2) dataset with 1004 photos of in-pavement airfield ground lighting. Table 5-1 shows number of images in dataset of each lamp type.

Table 5-1 Lamp types in the *PLAVS2* dataset

Lamp type	**Before maintenance**	**After maintenance**
RCL CC	170	170
RCL CR Crystal	77	78
RCL CR Red	77	78
TDZ	177	177
Total:	500	504
	1004	

5.1.2. Airport navigational lighting lamps and prisms detection algorithm

Figure 5-7 illustrates the process of localizing and detecting the prism. Initially, lamp localization is executed employing the circular Hough Transform, facilitating the detection of the lamp along with its precise position and orientation. Subsequently, the prism area is identified through a combination of morphological operations and high-pass filtering, employing the Sobel mask for enhanced accuracy.

The process of lamp detection and prism localization begins by loading an image from the dataset, which is then scaled to 15% of its original size. This scaling down of the image is crucial for optimizing the amount of data used during neural network training [48]. Subsequently, the image is converted to grayscale to simplify processing.

Lamp detection is carried out using the circular Hough Transform, which searches for circular shapes within the image. Specifically, the algorithm looks for circles within predefined ranges of radius values, effectively identifying potential lamp locations. The Circular Hough Transform (CHT) algorithm is chosen for its robustness against noise, occlusion, and varying illumination conditions.

Following lamp detection, the algorithm searches for smaller circles representing airport lighting mounting bolts. The pixel span for this search has been determined experimentally to optimize detection accuracy. After these operations, the input image undergoes rotation to ensure consistency in orientation across all photos. Utilizing the original image for rotation helps maintain data quality for subsequent processing steps.

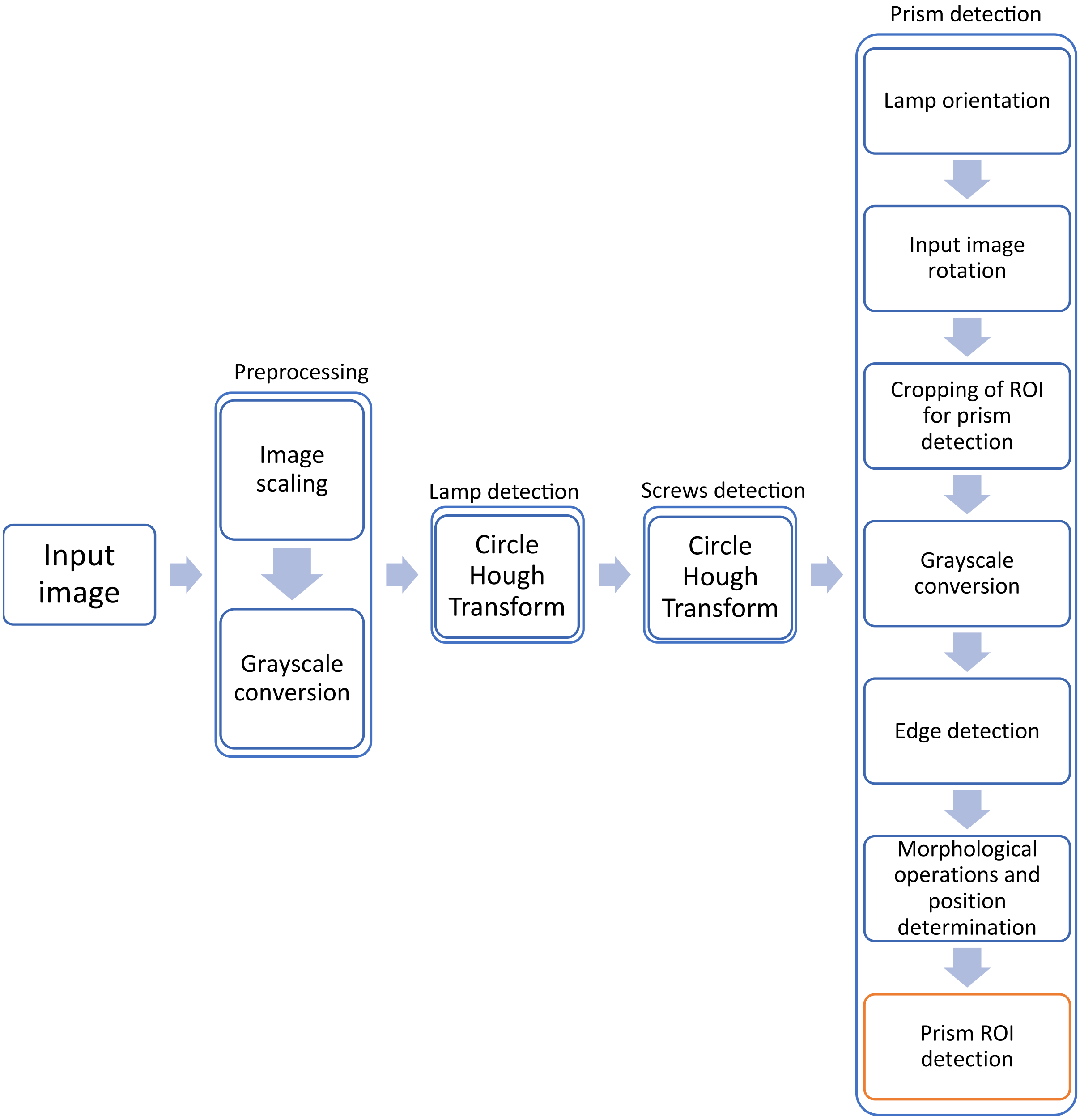

Figure 5-7 Diagram of the lamp and prism detection algorithm

Figure 5-8 illustrates the result of the lamp detection operation, with the detected lamp indicated by a blue circle. The orientation of the lamp, determined based on the positions of the mounting bolts, is depicted by green circles. This process ensures accurate localization of lamps and prisms in the images, laying the foundation for further analysis and inspection steps.

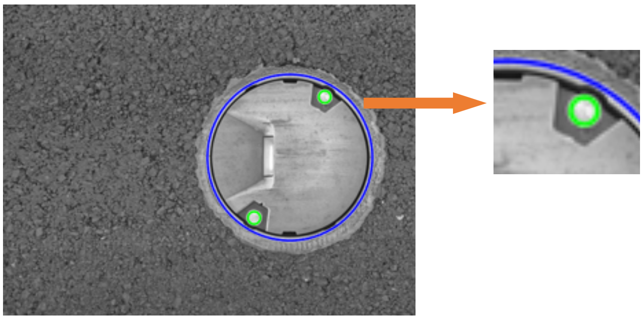

Figure 5-8 The illustration of the operation of detecting the lamp (blue circle) and its orientation (green circles) [40]

The subsequent operation involves limiting the working area by cropping to a portion of the image where the prism is located. This cropped image is then converted to grayscale, and edge detection is performed. Morphological operations and filtering using the Sobel operator are applied to determine the position of the searched prism, which also aids in reducing the Region of Interest (ROI).

The Sobel operator mask used in this process is configured to focus on finding horizontal edges, which was found to be the optimal solution for the application based on conducted experiments. This choice helps to mitigate distortions and eliminate small edges that could lead to errors in subsequent processing steps.

The Sobel mask used has the following form:

$$\text{kernel} = \begin{bmatrix} 0 & 0 & 0 \\ 1 & 1 & 1 \\ 0 & 0 & 0 \end{bmatrix} \tag{56}$$

The mask emphasizes horizontal edges, enhancing the visibility of features relevant to prism detection. Through experimentation, it was determined that this configuration effectively reduces noise and facilitates accurate prism localization.

In contrast, using a Sobel mask in diamond form resulted in an output devoid of reference points, rendering it impossible for the algorithm to determine the position of the prism accurately.

Figure 5-9 illustrates the final result of detecting the prism location on the tested in-pavement lamp. This process ensures precise localization of the prism, laying the groundwork for subsequent analysis and inspection tasks.

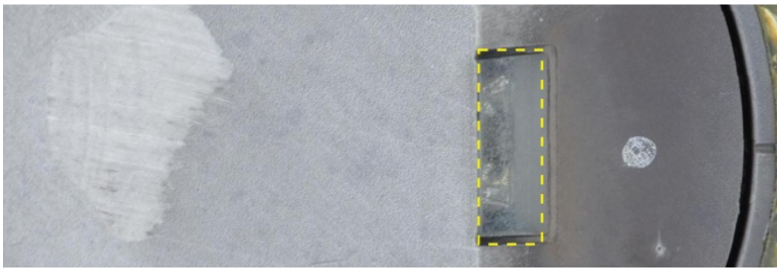

Figure 5-9 The illustration of the prism detection operation [40]

Table 5-2 summarizes the effectiveness of the various stages of the algorithm's operation.

Table 5-2 Lamp detection and orientation identification effectiveness

Type of operation	**Efficiency of identification**	
	Correct identification	**Incorrect identification**
Lamp detection	90.81%	9.09%
Lamp orientation	90.21%	9.79%

5.1.3. Datasets of airfield ground lighting prisms

Initially, the dataset was limited to 284 images due to incorrect performance in earlier stages, particularly in the detection of lamps, divided into 3 class:

- Class I - undamaged prisms (Figure 5-10)
- Class II - no longer suitable for operation (Figure 5-11)
- Class III - images when it is impossible to judge the wear of the prism (Figure 5-12).

The "Undamaged Prisms" class includes images of prisms that are in good condition, while the "Damaged Prisms" class consists of images depicting prisms that are no longer suitable for operation. The "Uncertain Prisms" class comprises images where it is difficult to assess the condition of the prism. These images often result from incorrect earlier stages of finding the location of the lamp and prism.

Figure 5-10 Examples of tarnished prisms but with no mechanical damage (Class I) [40]

Figure 5-11 Examples of damaged prisms (Class II) [40]

Figure 5-12 Examples of improper prism segmentation (Class III) [40]

Figure 5-13 provides insight into the distribution of classes in the dataset, illustrating the ratio of each class. This distribution serves as a basis for training and evaluating the performance of the neural network in classifying prism conditions based on image data.

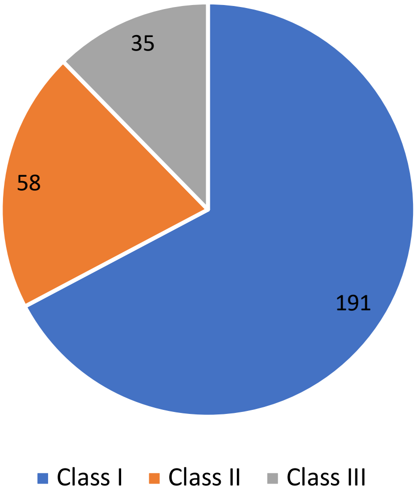

Figure 5-13 The ratio of the class distribution in the initial prisms dataset

During the training process, the samples entering the network input are randomly divided while maintaining the following proportions:

- Training: 70% of the samples, are allocated for training purposes. These images are utilized to adjust the network parameters based on its error, optimizing its performance over successive iterations.
- Validation: 15% of the samples, are designated for validation purposes. These samples are used to measure the network's generalization ability and to halt the training process when the improvement in generalization ceases. Specifically, the training process is stopped when the cross-entropy error of the validation samples begins to increase, indicating a decline in generalization performance.
- Testing: The remaining 15% of the samples, are reserved for testing purposes. Unlike the training and validation phases, this part of the process does not impact the training of the neural network. Instead, it serves as an independent indicator of the network's performance during and after training, providing valuable insights into its effectiveness in classifying prism conditions based on image data.

Following the successful experimental results, it was decided to enlarge the dataset originally built to 540 navigational lighting lamps prisms. The expanded database was also divided into 3 classes, according to the initial database. Figure 5-14 shows the ratio of the class distribution in the expanded prisms dataset.

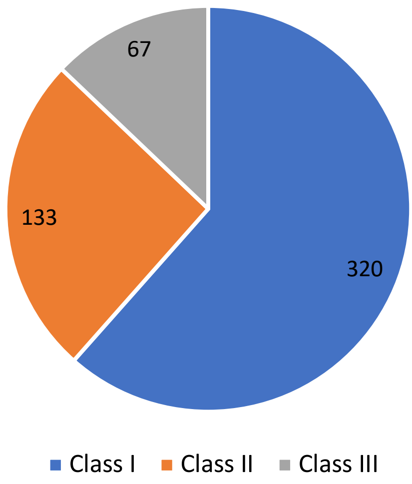

Figure 5-14 The ratio of the class distribution in the expanded prisms dataset

5.1.4. Proposed system for prism quality classification using neural networks

This experiment was conducted to test the possibility of classifying prisms based on their wear. At the beginning, the two-layer feed-forward neural network was implemented using the Open Neural Network Start app (nnstart in the MATLAB environment) demonstrates the ability to correctly classify vectors when a sufficient number of neurons are present in the hidden layer. This network architecture utilizes the sigmoidal function in the hidden layer and the softmax function (normalized exponential function) in the output layer for classification purposes. Training of the network is achieved using scaled backpropagation of the conjugate gradient.

The input to the network consists of the I matrix with dimensions of 1440000 × 284, where each sample contains 1440000 elements representing image vectors. The target matrix, denoted as T, has dimensions of 3 × 284, representing 284 samples, each with 3 elements corresponding to prism classification categories.

Training Confusion Matrix

Output Class

I	120 60.6%	15 7.6%	3 1.5%	87.0% 13.0%
II	3 1.5%	30 15.2%	2 1.0%	85.7% 14.3%
III	5 2.5%	3 1.5%	17 8.6%	68.0% 32.0%
	93.8% 6.3%	62.5% 37.5%	77.3% 22.7%	84.3% 15.7%
	I	II	III	

Target Class

Validation Confusion Matrix

Output Class

I	22 51.2%	3 7.0%	3 7.0%	78.6% 21.4%
II	8 18.6%	1 2.3%	4 9.3%	7.7% 92.3%
III	0 0.0%	1 2.3%	1 2.3%	50.0% 50.0%
	73.3% 26.7%	20.0% 80.0%	12.5% 87.5%	55.8% 44.2%
	I	II	III	

Target Class

Test Confusion Matrix

Output Class

I	29 67.4%	0 0.0%	3 7.0%	90.6% 9.4%
II	4 9.3%	5 11.6%	1 2.3%	50.0% 50.0%
III	0 0.0%	0 0.0%	1 2.3%	100% 0.0%
	87.9% 12.1%	100% 0.0%	20.0% 80.0%	81.4% 18.6%
	I	II	III	

Target Class

All Confusion Matrix

Output Class

I	171 60.2%	18 6.3%	9 3.2%	86.4% 13.6%
II	15 5.3%	36 12.7%	7 2.5%	62.1% 37.9%
III	5 1.8%	4 1.4%	19 6.7%	67.9% 32.1%
	89.5% 10.5%	62.1% 37.9%	54.3% 45.7%	79.6% 20.4%
	I	II	III	

Target Class

Figure 5-15 Confusion matrices of prism quality classification [40]

The results of the trained neural network have proven to be highly satisfactory, with an impressive accuracy rate of 81.4% achieved during the testing phase, as depicted in Figure 5-15. This level of accuracy indicates the effectiveness of the network in correctly classifying prism conditions based on the provided image data.

Such accuracy underscores the success of the network in learning and generalizing patterns from the training data to accurately classify unseen samples during testing. It demonstrates the robustness and reliability of the neural network model in effectively distinguishing between undamaged, damaged, and uncertain prisms, despite variations in image characteristics and conditions.

Due to the possibility of classifying prisms using neural networks, it was decided to conduct a second experiment using pre-trained neural network models. It was conducted using the Deep Network Designer tool within the MATLAB 2022b [109] environment and larger dataset, consisting of 540 images. This powerful tool enables the selection of pre-trained neural networks, customization of the dataset, and adjustment of network parameters to optimize results. For this research, three prominent neural network models were chosen for evaluation: GoogLeNet, VGG-19, and Resnet [182].

The workstation utilized for the experiment boasted the following specifications: an Intel Core i7-6800K CPU running at 3.40 GHz and a NVIDIA 2080 Ti graphics card. These high-performance components ensured efficient processing and computation, essential for training and evaluating neural networks with large datasets and complex architectures.

The training of the GoogLeNet network employs the stochastic gradient descent with momentum (SGDM) optimization algorithm. Setting specific parameters for the training process is facilitated by the *trainingOptions* function, encompassing various arguments governing different facets of the training regimen. These parameters encompass the optimization algorithm, learning rate, number of epochs, mini-batch size, and more.

Subsequently, the *layerGraph* serves as the foundation for constructing an empty neural network graph, which can later be furnished with layers and interconnections. Defining the initial layers of the GoogLeNet architecture is accomplished through MATLAB code, with these layers then added to the network graph via the *addLayers* function.

The foremost layer within the network, an *imageInputLayer*, stipulates the dimensions of the input images destined for processing by the network. In this context, the input images are anticipated to possess dimensions of 224 × 224 pixels and feature three colour channels (red, green, and blue).

Following this, a convolution2dLayer starts its operation, tasked with applying a series of learned filters to the input image to extract pertinent features. This layer employs a 7 × 7 filter size and generates 64 output feature maps, employing a stride of 2 pixels and padding of 3 pixels on each side to ensure congruence in size between the output feature maps and the input image. Subsequently, a *reluLayer* is applied to the convolution layer's output to introduce nonlinearity.

To downsample the preceding layer's output, reducing its spatial resolution by a factor of 2, a maxPooling2dLayer is employed. This layer adopts a 3 × 3 pooling size and a stride of 2 pixels, accompanied by padding of 1 pixel on each side to maintain parity in size between the output feature maps and the input.

The subsequent inclusion, the *crossChannelNormalizationLayer*, functions to normalize the previous layer's output across feature maps, thereby enhancing the overall generalization of the network. Utilizing a normalization window size of 5 and a scale factor of 1, this layer aids in refining the network's performance.

Moving forward, the inception module assumes prominence, serving as a fundamental building block recurrently employed throughout the GoogLeNet architecture. Comprising four parallel convolutional pathways, each characterized by distinct filter sizes, the inception module culminates in a concatenation layer merging the output of all four pathways. This framework enables the network to glean insights across multiple scales and resolutions, crucial for precise object recognition within images.

Within the inaugural inception module (inception_3a), the pathways encompass a maxPooling2dLayer followed by convolution2dLayer instances utilizing varying filter sizes: 1 × 1, 3 × 3, and 5 × 5. Each pathway yields a suite of output feature maps, subsequently amalgamated via the *depthConcatenationLayer* to yield the final output of the inception module, which then feeds into the subsequent layer of the network. Table 5-3 presents the values of Mini-branch Accuracy, Validation Accuracy, Mini-batch Loss, and Validation Loss across different epochs and iterations.

Table 5-3 Summary of parameters during GoogLeNet network training

Epoch	**Iteration**	**Mini-branch Accuracy**	**Validation Accuracy**	**Mini-batch Loss**	**Validation Loss**
1	1	31.25%	67.44%	1.638	1.8217
4	10	78.12%	74.42%	0.5817	0.6523
7	20	93.75%	81.40%	0.2075	0.4574
10	30	92.19 %	83.72%	0.1676	0.3619
14	40	98.44%	88.37%	0.0806	0.2772
17	50	98.44%	88.37%	0.0412	0.2961
17	51	100%	-	0.0430	-

The GoogLeNet model exhibited the highest accuracy in classifying the wear of the prism of the in-pavement navigation lamp, achieving an accuracy of 88.37%. The learning process and loss are visually depicted in Figure 5-16. This outcome surpassed the performance of other tested neural networks, with VGG-19 achieving an accuracy of 67.07% and ResNet reaching 75.29%. A detailed comparison of the accuracy of the neural network models used in the experiment is presented in Table 5-4.

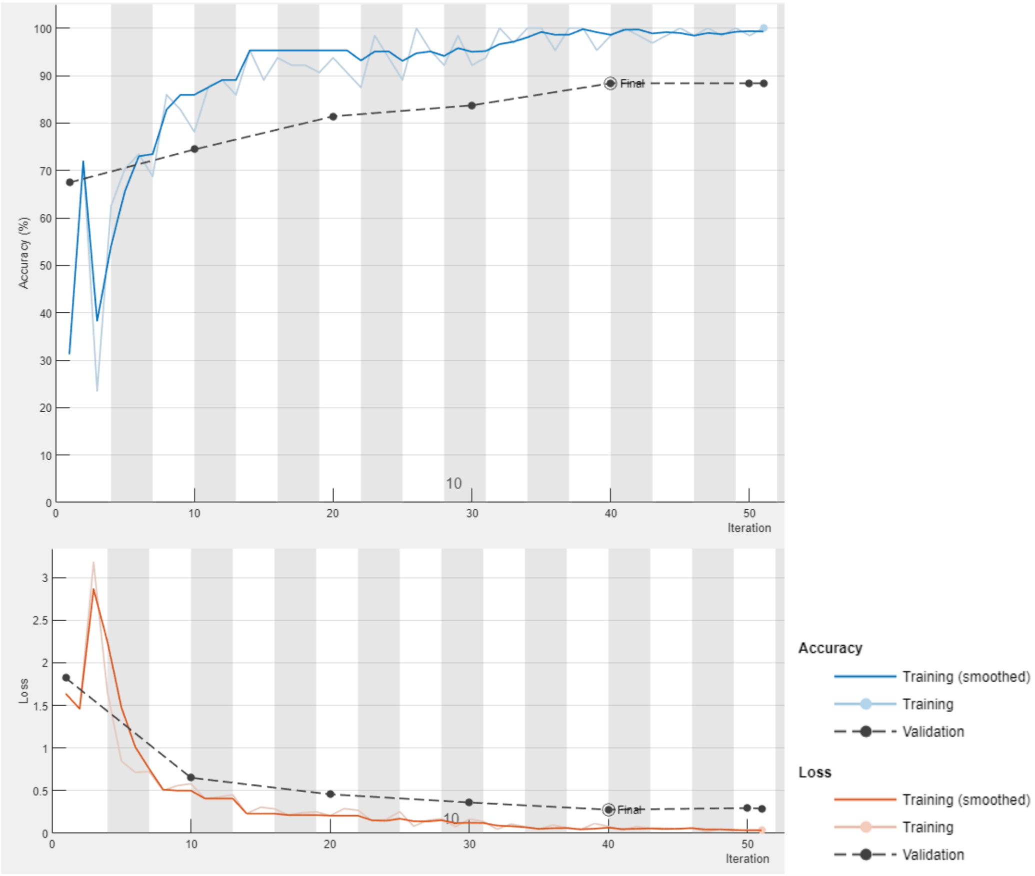

Figure 5-16 GoogLeNet expanded prisms dataset training and validation accuracy and loss graph [41]

Table 5-4 Accuracy comparison neural network models used in the experiment

Neural network model	Accuracy
GoogLeNet	88.37%
VGG-19	67.07%
Resnet	75.29%

In comparison to the previously showed system [40], which achieved an accuracy of 81.4%, it is evident that proper training and an increase in the number of images in the dataset yield significantly improved results. This observation leads to the conclusion that employing a neural network based on GoogLeNet is justified for further development and implementation in devices navigating around the airport.

5.2. Automatic classification of navigation lighting chromaticity

5.2.1. Airfield ground lighting chromaticity measurement system concept

The proposed system, in the form of a proposed measurement platform, requires recognition of the type of lamp based on the colour of the emitted light in order to select the luminosity standards of individual light points and to examine its chromaticity in order to compare it with the EASA CS-ADR-DSN standards [4]. A general block diagram outlining the individual stages of lamp measurement is depicted in Figure 5-17. During the initial stage, colour detection occurs, facilitating the identification of the tested lamp type. Subsequently, the matrix of light intensity sensors provides a result, which, based on the specific lamp type identified, is then converted according to coefficients determined in the laboratory. This process enables the accurate reading of lamp luminous intensity. The obtained results are then compared with relevant standards corresponding to the appropriate type of lighting, determining whether the lamp needs replacement or can continue to be used.

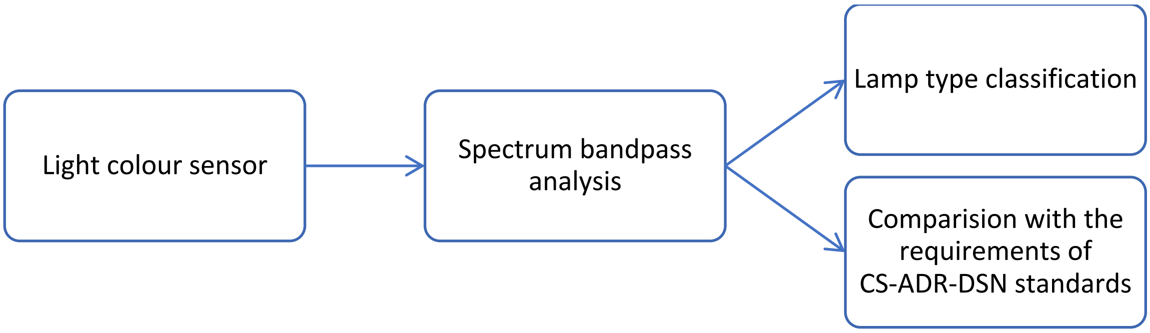

Figure 5-17 Block diagram of the light chromaticity quality assessment

5.2.2. Airport navigational lighting lamps characteristics

The testing procedure using measurement platform involves the measurement of photometric illumination intensity, radiometric irradiation intensity, and spectral radiation intensity, all quantified in absolute light units. A primary focus of the investigation was to analyse the distribution of spectral radiation intensity. Tests were conducted on five different colours of lamps installed in airport areas:

- TDZ – touchdown zone lamp (white)
- RCL_White – runway centre line lamp (white)
- RCL_Red – runway centre line lamp (red)

- TAXI_GREEN – taxiway centre line lamp (green)
- TAXI_YELLOW – taxiway centre line lamp (yellow).

As anticipated, the spectral composition of taxiway lamps exhibits a notable prevalence of green and blue light, which are hues most easily discernible by the human eye and, consequently, by sensors commonly available on the market. Conversely, other components contribute minimally to the overall spectrum, with wavelengths corresponding to warmer hues exhibiting negligible emission from these lamps (refer to Figure 5-18).

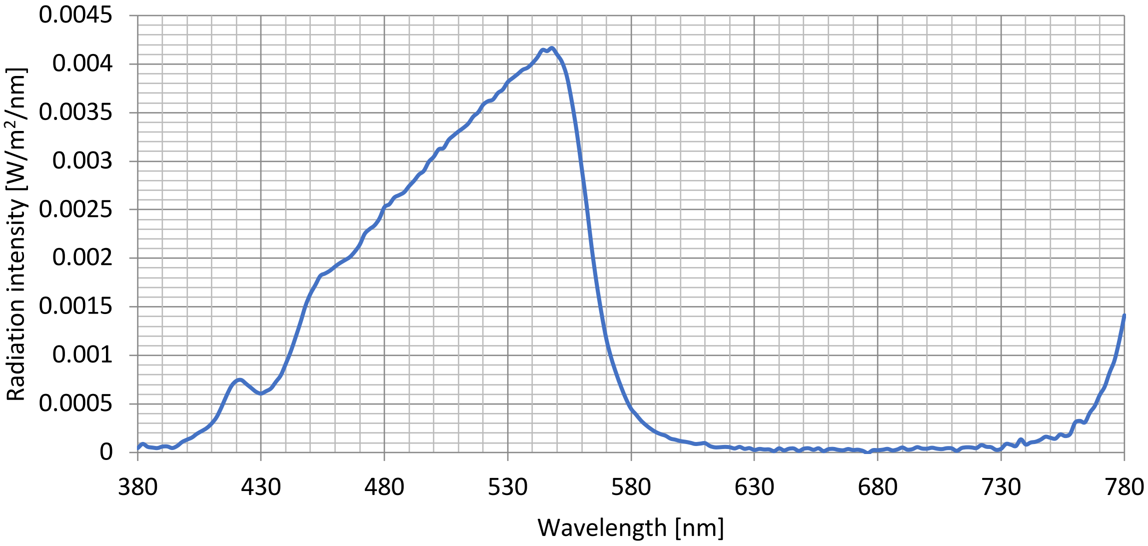

Figure 5-18 Spectral radiation intensity of the taxiway centre line lamp IDM5582 (TAXI_GREEN) [39]

The lamps illuminating the touchdown zone emit light in a warm, white colour. As a result, their spectral composition comprises a range of wavelengths across the visible light spectrum. In Figure 5-19, it is observed that the highest intensity of light is emitted by colours with longer wavelengths. This phenomenon can be attributed to the characteristics of the light source and the properties of the emitted light.

Specifically, the intensity of light emitted by a light source is influenced by both the power of the light source and the wavelength of the emitted light. In this context, the intensity can be conceptualized as the product of the power of the light source per unit area and the wavelength of the light. Since warm white light encompasses a broad spectrum of wavelengths, including those with longer wavelengths, it results in a higher overall intensity compared to light sources with narrower spectral ranges.

Therefore, the observed trend of higher intensity corresponding to longer wavelengths in the spectrum of the touchdown zone lamps can be explained by the characteristics of warm white light and its distribution across the visible spectrum.

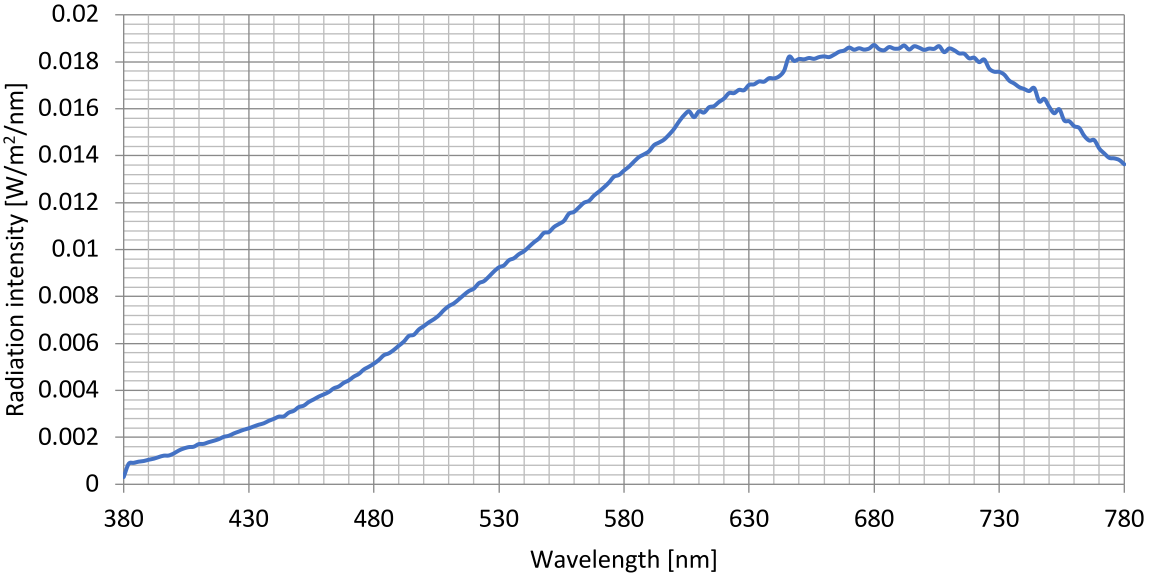

Figure 5-19 Spectral radiation intensity of the touchdown zone lamp IDM4671 (TDZ) [39]

The spectral characteristics of the red lamps marking the runway centre line primarily consist of longer wavelengths within the visible light spectrum. Notably, the wavelength of 680 nm, associated with the orange-red colour, exhibits the highest intensity. This wavelength represents a warm hue, characteristic of the red lamps used for runway centre line markings. Interestingly, these lamps emit minimal amounts of light at wavelengths corresponding to colder colours, aligning with empirical observations.

Figure 5-20 visually represents these spectral characteristics, illustrating the dominance of longer wavelengths and the absence of colder colours in the emitted light. This observation corroborates the spectral composition expected from lamps designed to emit red light.

In contrast, the spectral profile of the white-coloured lamps installed along the centre line of the runway (depicted in Figure 5-21) closely resembles that of the lamps illuminating the touchdown zone. However, there are discernible differences in the intensity values, reflecting variations in the radiation output of the respective luminaires. Despite these differences, both types of lamps exhibit a broad spectrum of wavelengths, with the white lamps emitting higher intensities due to their positioning along the central axis of the runway.

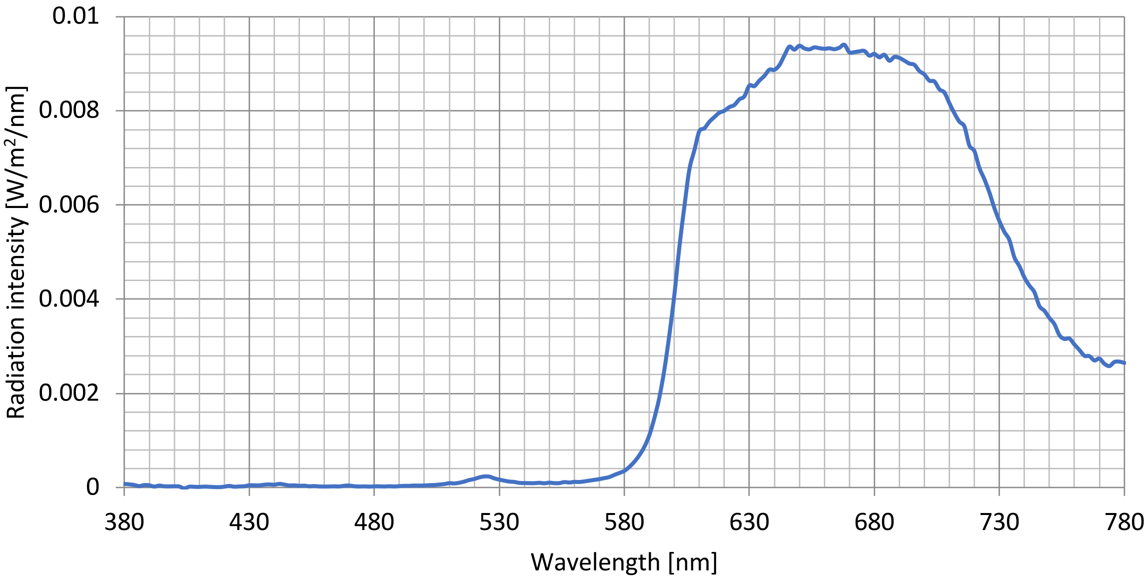

Figure 5-20 Spectral radiation intensity of the runway centre line lamp red IDM4582 (RCL_Red) [39]

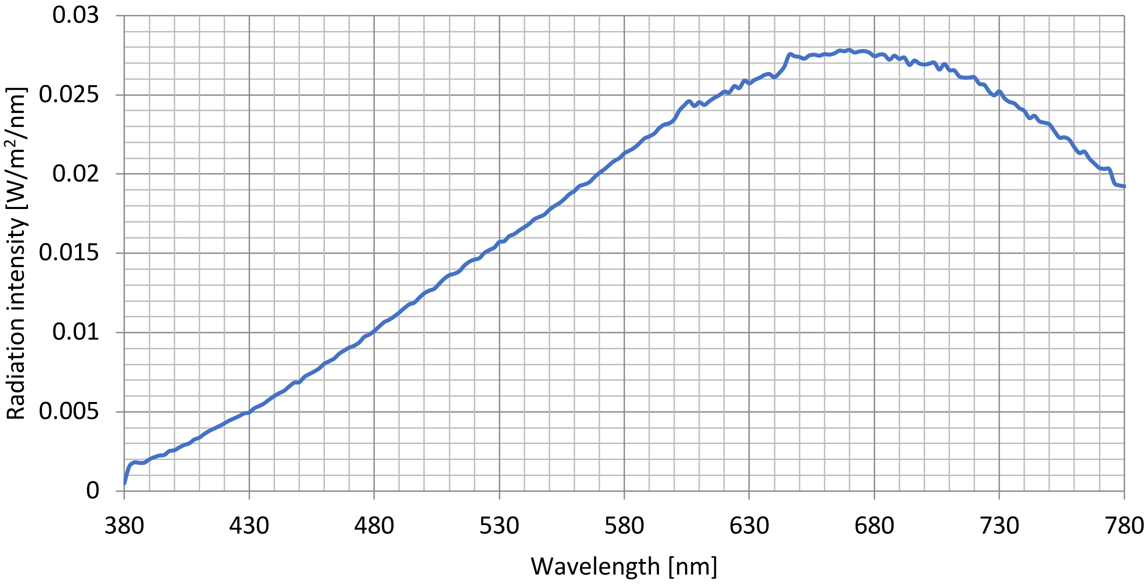

Figure 5-21 Spectral radiation intensity of the runway centre line lamp white IDM4582 (RCL_White) [39]

To assess the colour spectrum of light emitted by airport lamps, including the taxiway centre line lamp, touchdown zone lamp, and runway centre line lamps (both red and white) [28], a Gigahertz-Optik X4 Light Analyzer spectrometer was utilized [183]. The research was possible thanks to cooperation with the Department of Metrology, Electronics and Lighting Technology, Institute of Electrical Engineering and Industrial Electronics, Faculty of Automation, Robotics and Electrical Engineering, Poznań University of Technology [184].

During the examination of elevated edge lamps, particular attention was given to the approach system luminaires, exemplified by ADB Safegate UEL 1-150 – CLEAR (APP_White, Figure 5-22a) and ADB Safegate UEL 1-150 – RED (APP_Red, Figure 5-22b), are strategically positioned off the aircraft movement areas. These luminaires are categorized as unidirectional high-intensity over-ground lamps, emitting white or red light respectively, powered by a 150 W halogen bulb. According to documentation, the estimated lifespan of the light source is 1000 hours, and they are also powered by a 6.6 A current source [185]. The luminaires selected for testing were new and had not been previously utilized.

Distinct from the examination of the elevated edge lamps, the elevated luminaire identified as ADB Safegate 1-045-RED-STOPBAR – TEFT (STOP_BAR), as illustrated in Figure 5-22c. According to documentation, this luminaire is classified as a high intensity unidirectional fixture designed for use in approach, threshold, or runway end systems. It emits red light utilizing a 45 W halogen bulb and operates on a 6.6 A current source [96].


(a) (b) (c)

Figure 5-22 Elevated approach system lamps [42]: (a) White, (b) Red, and (c) Stop Bar Lamp

5.2.3. Light colour and chromaticity sensors comparison

The market offers a variety of sensors designed for colour detection, catering to different needs and applications. Some sensors are designed to detect environmental colours independently, while others utilize optional LED backlighting for enhanced performance. Among the most basic modules are the TCS34725, APDS9960, or ISL29125, which enable measurement of only the three basic RGB components. Technical documentation for these sensors indicates relatively low sensitivity for each channel.

For instance, the TCS34725 sensor module tends to lower individual RGB components when normalizing the readings for a wavelength of 755 nm (Figure 5-23). While these sensors may not offer high precision in colour measurement, they can still facilitate correct colour recognition, especially in scenarios where measurement precision is not critical. An added advantage of the TCS34725 sensor is its built-in IR filter, which helps eliminate unwanted components of infrared light [186].

The colour sensor featuring the APDS9960 is capable of measuring RGB component values and detecting gestures such as up/down and left/right. Similar to the TCS34725, the individual RGB components tend to have underestimated values compared to the standard [187]. Notably, the blue component exhibits a particularly significant difference, while the mapping of the green and red components remains relatively consistent (Figure 5-24).

On the other hand, the module equipped with the ISL29125 sensor provides the most accurate representation of the green component. However, it struggles to accurately render values in the blue light wavelength range, where the readings are notably underestimated. A similar discrepancy is observed for the third component, with the module yielding lower values for red-light wavelengths compared to the reference value (Figure 5-25).

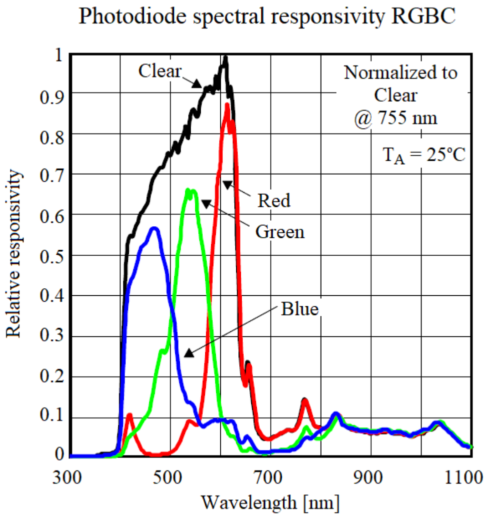

Figure 5-23 TCS34725 spectral response [186]

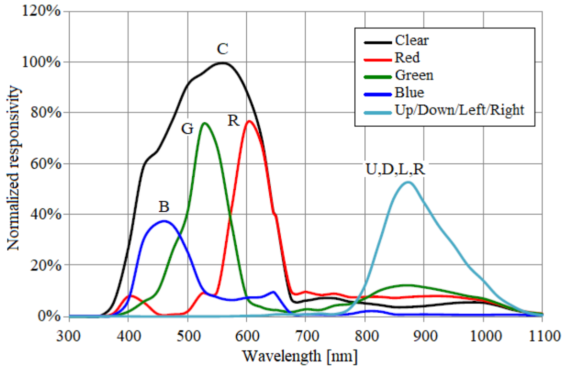

Figure 5-24 APDS9960 spectral response [187]

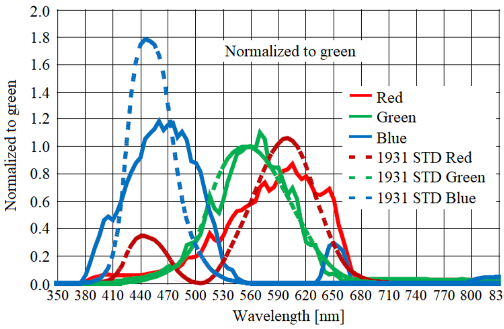

Figure 5-25 ISL29125 spectral response [188]

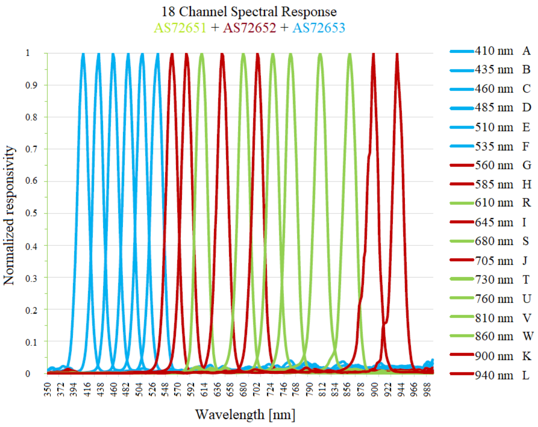

Figure 5-26 AS7265x spectral response [189]

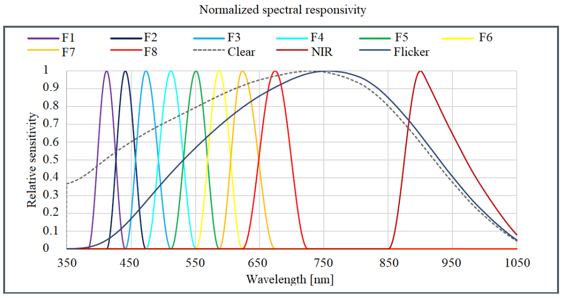

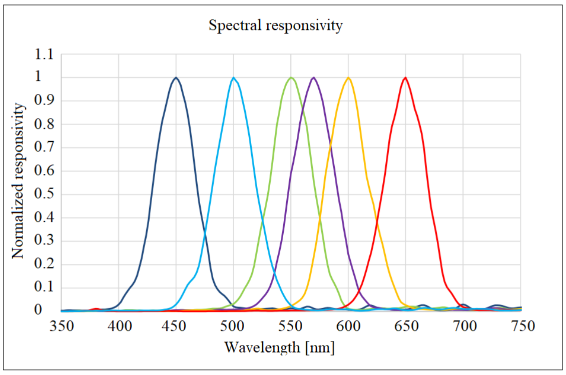

Figure 5-27 AS7341 spectral response [190]

Figure 5-28 AS7262 spectral response [191]

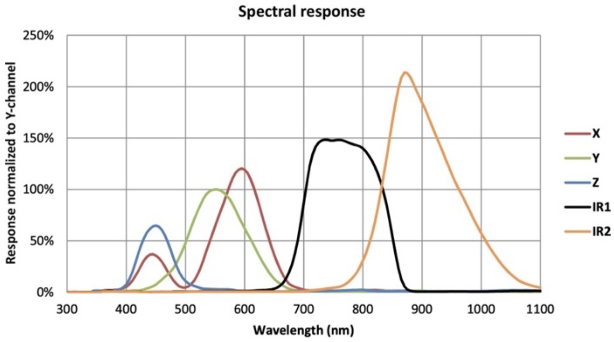

Figure 5-29 TCS3430 spectral response [192]

Despite the attractive pricing of the described modules, utilizing such sensors may not be viable for the precise task of determining airport lamp types based on the colour of emitted light. This operation demands colour measurement with greater accuracy, as each type of airport lamp adheres to specific standards governing its use. Accurate identification of a particular model is essential for selecting appropriate conversion factors for the matrix of light intensity sensors, which measure the luminous intensity of the primary beam.

An alternative group of modules falls under the category of colour sensors, specifically designed for analysing light spectra. Notably, some of these devices enable the analysis of not only visible light but also extend to cover the infrared to the beginning of the UV range. One such example is the AS7265x module, offering comprehensive functionality that spans the UV to IR spectrum. However, from the perspective of airport lamp testing, this extensive range may not be necessary and could significantly inflate device costs. The AS7265x module comprises three interconnected sensors: AS72651, AS72652, and AS72653, facilitating the examination of light wavelengths from 410 nm (UV) to 940 nm (IR) across 18 channels with a precision of ±12% [189].

The technical data provided by the manufacturer is effectively represented in the mapping charts of wavelength readings for each channel (Figure 5-26). These charts demonstrate the sensor's advanced capabilities and excellent precision. However, despite its high performance, the potential utility of the sensor in an airport lamp recognition device is limited. This limitation primarily stems from the module's high price, which may not justify its full utilization.

In practical terms, simpler modules that offer examination of the visible light range may suffice for the purposes of airport lamp recognition. While the advanced features of the AS7262 sensor are commendable, their added complexity and cost may outweigh their benefits in certain applications, such as airport lighting systems.

Sensors such as the AS7341 and AS7262 can be distinguished based on their specific modules. The primary difference between them lies in the number of visible channels they possess. The AS7341 boasts 11 channels, whereas the AS7262 is equipped with only 6 channels [190], [191]. Both sensors demonstrate excellent performance in representing reading values for individual wavelengths.

The module utilized in the device features the AS7341 sensor. In addition to detecting visible light components, this sensor also facilitates the identification of the NIR (near-infrared) range [190]. Figure 5-27 illustrates the sensitivity and precision of all channels relative to the reference waveform, indicating exemplary performance across the board. Upon comparing technical documentation with results obtained from research utilizing a professional spectrometer, it was determined that employing a module with a smaller number of channels, such as the AS7262, would suffice for the intended task.

Consequently, the device module responsible for detecting specific lamp types was constructed using the AS7262 visible light spectrum sensor [191]. Tests conducted on both stationary and moving sensors revealed variations in the values of individual colour components. Based on these findings, the lamps slated for inspection were accurately classified, and software was developed to select coefficients for the results obtained from the light intensity sensors.

The module tailored for examining the visible light spectrum (Figure 5-28) is capable of detecting wavelengths at key intervals, namely 450, 500, 550, 570, 600, and 650 nm, with a corridor width of 40 nm and a half-maximum detection width. This approach facilitates the easy differentiation of colours emitted by the tested lamps, aligning with the design assumptions. Communication between the sensor and the microprocessor occurs via either the I2C or UART interface. In this instance, the I2C interface is utilized, which is the default choice made by the device manufacturer. Data transmission is carried out digitally, employing a 16-bit format. It's worth noting that all module signals require a voltage supply of 3.3 V [191].

The TCS3430 sensor is a highly sophisticated device employed in various colour sensing and ambient light sensing applications. It operates within the visible light spectrum, covering wavelengths from 380 nm to 780 nm, and boasts exceptional sensitivity to light, enabling it to detect even minute variations in the spectral output of different light sources. This sensor utilizes a combination of photodiodes and an on-chip filter to accurately measure light intensity across different wavelengths. Thanks to its dynamic range, the TCS3430 is well-suited for a wide array of lighting conditions. The integrated filter ensures precise light intensity measurements while also providing significant noise reduction, enhancing the accuracy of the readings [192].

Designed to be compact and energy-efficient, the TCS3430 consumes just 0.45 mW during full operation and is housed in a small surface-mount package, facilitating easy integration into various sensing and control systems. It is capable of operating within a broad temperature range, from −40 °C to 105 °C, making it suitable for demanding environments. One of the standout features of the TCS3430 is its ability to compensate for the effects of temperature and aging on the photodiodes. This capability ensures that the sensor maintains accuracy and reliability across a wide range of environmental conditions, which is crucial for use in harsh industrial or outdoor settings [192].

Additionally, the TCS3430 sensor can adjust the intensity of lighting based on ambient light levels, making it an invaluable tool for reducing energy consumption and light pollution in indoor lighting applications. By measuring ambient light levels and adjusting the lighting accordingly, the sensor contributes to more efficient and environmentally friendly lighting systems. Table 5-5 provides a detailed overview of the electrical and optical parameters of the TCS3430 sensor [192].

In the context of airport navigation lighting, the TCS3430 plays a critical role in ensuring optimal performance and adherence to safety and visibility standards. It achieves this by measuring the spectral output of various light sources used in the navigation lighting system. Figure 5-29 depicts its spectral response, which includes five channels: X, Y, Z, IR1 (Far Red LED), and IR2 (IR LED). By combining readings from these channels, the TCS3430 can accurately determine the colour of the light. The spectral response of each photodiode in the TCS3430 is meticulously designed to align with the human eye's response to different colours, ensuring precise colour detection [87].

Table 5-5 Electrical and optical parameters of the TCS3430 sensor [192]

Parameter	**Min.**	**Max.**	**Units**
Supply voltage	−0.3	2.2	V
Digital I/O terminal voltage	−0.3	3.6	V
Output terminal current	−1	20	mA
Channel X (Warm White LED)	58	90	counts/(µW/cm^2)
Channel Y (Warm White LED)	56	70	counts/(µW/cm^2)
Channel Z (Warm White LED)	6.5	14	counts/(µW/cm^2)
Far Red LED	90	180	counts/(µW/cm^2)
IR LED	90	230	counts/(µW/cm^2)

The sensor provides colour information in the form of XYZ coordinates, which represent the tristimulus values of the light. These coordinates describe the relative contributions of three primary colours: red, green, and blue, based on tristimulus theory. According to this theory, any colour can be represented as a mixture of these three primary colours. However, to plot these colours on a chromaticity chart, it is necessary to convert the XYZ coordinates into x, y coordinates within the CIE 1931 colour space.

Table 5-6 shows a comparison of selected light spectrum and chromaticity sensors, highlighting the result representation and measurement range of each of the analysed sensors.

Table 5-6 Comparison of selected spectrum and chromaticity sensors

Sensor	Measurement range	Measurement speed	Result representation (Colour space)
TCS34725	380 - 780 nm	Integration time from 2.4 ms to 614 ms	RGB
APDS9960	400 - 700 nm	Integration time from 2.78 ms	RGB
ISL29125	410 - 700 nm	Integration time from 1 ms to 360 ms	RGB
AS7265x	410 - 940 nm	Measurement time starting from 5 ms	18-channel multispectral
AS7341	350 - 1000 nm	Integration time from 2.78 ms to 7.14 s	11-channel multispectral
AS7262	450 - 670 nm	Integration time from 5 ms to 255 ms	6-channel multispectral
TCS3430	300 - 1000 nm	Integration time from 2.78 ms to 700 ms	XYZ (CIE 1931 colour space)

5.2.4. Analysis of spectrum sensors for detecting type of airport lamps

As mentioned previously, in order to properly classify the type of lamp based on the colour of the emitted light, it was necessary to develop a method to distinguish each type. In the research conducted on the selected visible light spectrum sensor AS7262, numerous experiments and measurements were performed utilizing original airport lamps. These luminaires, integrated into the surface of the runway and taxiways, underwent not only direct measurements but also testing with a built-in measuring matrix enclosed in acrylic glass cover. This cover is essential for the measurement method employed. The matrix is affixed to a specialized frame beneath the chassis, positioned in proximity to the surface. Given the heightened risk of damage to the matrix, including the sensors, additional protection measures were implemented.

The lamps of interest were subjected to laboratory testing under controlled conditions, with a consistent distance of approximately 1 meter between the light source and the sensor. Three distinct types of brand-new lamps were utilized for lighting testing: runway centre line white (RCW), runway centre line red (RCR), and taxiway centre line (TC). Each lamp type underwent multiple series of measurements, and the average results are summarized in Table 5-7.

Table 5-7 Spectrum results of the embedded airport lamps examination [in counts/(μW/cm^2)]

	Channel	RCW	RCR	TC
Without cover	**V**	61259.47	16596.37	42350.37
	B	65474.53	11769.84	63098.99
	G	57115.52	5666.82	52538.19
	Y	48994.17	28503.14	34594.12
	O	51246.94	51246.94	4319.873
	R	45703.38	45703.38	2086.367
With cover	**V**	61259.47	15113.16	38246.94
	B	65474.53	11228.07	60962.59
	G	57115.52	5701.4	49748.65
	Y	48994.17	27103.2	31231.9
	O	51246.94	51246.94	3978.233
	R	45703.38	45703.38	1896.83

Based on the collected data (Figure 5-30), the individual VBGYOR components (Table 5-7) exhibit graphs that closely resemble those of spectral radiation intensity. The characteristic shape of the graphs for each lamp type has been preserved, facilitating the identification of specific luminaires based on the spectrum of emitted light beams.

The white-coloured lamp of the runway centre line predominantly emits blue and purple hues, while the red lamp is characterized by dominant orange, red, and yellow components. Notably, the second type of runway centre line luminaire demonstrates significantly lower readings in the violet, blue, and green channels. Conversely, the light emitted by the taxiway centre line lamp is primarily composed of blue and green components, with moderate readings in the violet and yellow channels, and minimal values for orange and red.

Furthermore, the influence of using an acrylic glass cover on the AS7262 module on the visible light spectrum graphs for each lamp type was investigated (Figure 5-31). It was observed that, for white-coloured runway centre line lamps, there was no discernible impact of the acrylic glass cover on the readings for individual channels.

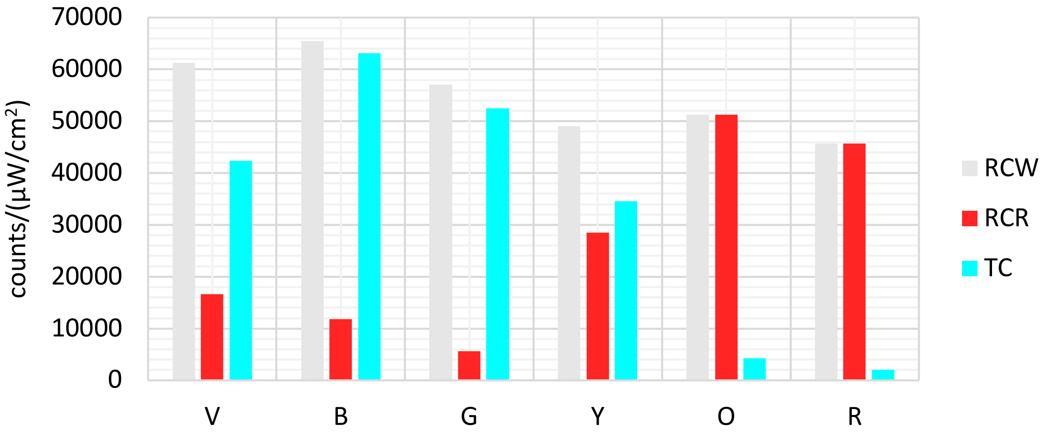

Figure 5-30 Average visible light spectrum of in-pavement airport lamps without the acrylic glass cover on the AS7262 module [39]

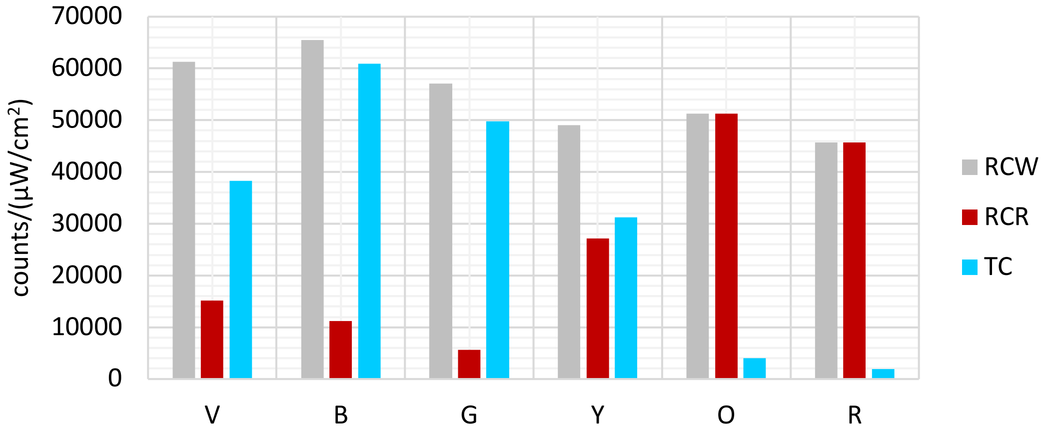

Figure 5-31 Average visible light spectrum of in-pavement airport lamps with the acrylic glass cover on the AS7262 module [39]

However, for the second type of runway centre line lamps emitting red light, slight differences in luminous intensity values were observed, particularly for the channels responsible for violet and yellow components. The obtained results were lower than in the test without cover. With the luminaire of the taxiway centre line, the effect of the acrylic glass cover is noticeable for each channel, causing a slight decrease in the reading value for each channel.

$$\mathrm{d}(\mathrm{LT}_1, \mathrm{LT}_2) = \sqrt{\sum_{\mathrm{channel=V}}^{\mathrm{channel=R}} \left(\mathrm{LT}_{1_{\mathrm{channel}}} - \mathrm{LT}_{2_{\mathrm{channel}}}\right)^2} \tag{57}$$

$$\mathrm{d}(\mathrm{LT}_1, \mathrm{LT}_2) = \sqrt{\sum_{\mathrm{channel=R}}^{\mathrm{channel=B}} \left(\mathrm{LT}_{1_{\mathrm{channel}}} - \mathrm{LT}_{2_{\mathrm{channel}}}\right)^2} \tag{58}$$

To quantitatively visualize the distinctions among various types of the tested airport lamps, Euclidean distances were computed using two distinct equations. For 6-channel sensors, the Euclidean distance d was calculated according to equation (57), while for RGB sensors, the calculation followed Equation (58), where LT represents the lamp type. The resulting Euclidean distances are presented in Table 5-8. These calculations enabled a quantitative assessment of the dissimilarities between the spectral characteristics of the different airport lamp types, facilitating a comprehensive understanding of their distinctive features.

Table 5-8 Results of calculated Euclidean distance of different types of the embedded airport lamps [in count/(μW/cm^2)]

Euclidean distance between airport lamps spectrum			
6-channels (VBGYOR)			
	RCW	**RCR**	**TC**
RCW	0	89139.43	68528.13
RCR	89139.43	0	98166.03
TC	68528.13	98166.03	0
3-channels (RGB)			
	RCW	**RCR**	**TC**
RCW	0	74371.79	43920.83
RCR	74371.79	0	82061.26
TC	43920.83	82061.26	0

The examination of the compiled results reveals the feasibility of programmatically distinguishing between individual types of airport lamps, leveraging the analysis of data retrieved from the AS7262 spectrum sensor. Notably, Euclidean distance values obtained for a greater number of channels are elevated, indicating that employing more sophisticated sensors, such as those capable of capturing multiple channels, enhances the confidence in decision-making processes.

The positional representation of each lamp type within the RGB colour space for the 3-channel sensor is depicted in Figure 5-32. This visualization offers a clear insight into the distribution of lamp types based on their RGB colour readings, facilitating a deeper understanding of their spectral characteristics and aiding in the development of robust classification algorithms.

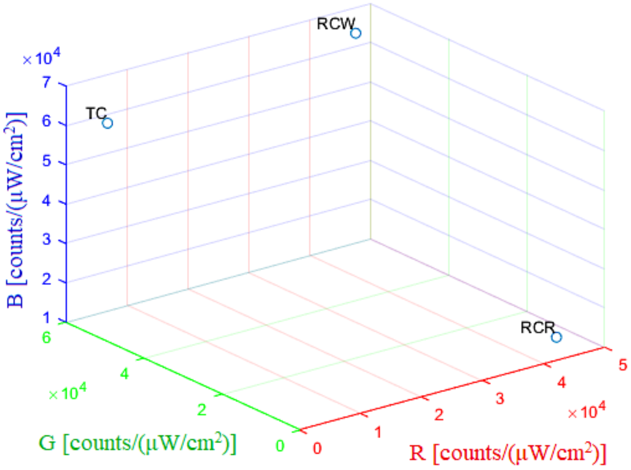

Figure 5-32 RCW, RCR, and TC airport lamps in RGB colour space [39]

The comparison of the visible light spectrum emitted by individual luminaires reveals both similarities and differences across various planes. However, it's notable that while such a characteristic can be effectively visualized for RGB sensors due to their three-dimensional colour space representation, the same cannot be easily achieved for 6-channel sensors. This limitation arises from the higher dimensionality of the data, making it challenging to visualize the similarities and differences in a comprehensible manner. Despite this challenge, the analysis of the data from 6-channel sensors still provides valuable insights into the spectral characteristics of the luminaires, albeit through alternative means such as statistical analysis or machine learning techniques.

The methodology employed for testing the efficiency of the second type of lamps in elevated luminaires differs significantly from the approach used for the edge lamps. In this scenario, the test device is an independent tool in the form of a tube terminated with a measuring module, not mounted on a vehicle. During inspection, the operator manually attaches it to the original lamp holders, utilizing a structure that impedes direct access to the sensors without prior disassembly. Consequently, additional protection of the measurement modules is unnecessary. As a result, the spectrum study for these lamps was restricted to readings obtained when the beam directly illuminated the sensor.

The emitted light beam spectrum of a brand-new lamp from the white-coloured approach system was subjected to testing, involving multiple series of measurements. The averaged measurement results derived from these tests are meticulously compiled and presented in Table 5-9.

Table 5-9 Spectrum results of the approach system lamp (white) examination [in counts/(µW/cm^2)]

Approach system lamp (white)					
Channel	**Distance from lamp [m]**				
	0.5	**0.75**	**1**	**1.25**	**1.5**
V	30285.84	30285.72	30285.88	30285.91	20518.76
B	34167.91	34166.84	34165.87	34169.84	25872.91
G	27988.54	26220.12	24041.31	22989.64	6324.16
Y	24041.03	24039.81	24041.18	20357.57	15134.46
O	24898.79	24898.74	24899.81	22988.64	24853.31
R	23949.38	23948.46	23950.31	23947.47	23948.16

The findings gathered from the experimentation indicate a notable trend wherein the reading value decreases as the distance between the sensor and the light source increases, particularly evident for distances exceeding 1.25 meters. Notably, measurements conducted within the range of 0 to 100 centimetres exhibit repeatability, whereas measurements taken at distances of 125 centimetres and 150 centimetres manifest a decline in recorded data, suggesting a potential limitation in measurement accuracy at greater distances.

An analysis of the visible light spectrum emitted by the approach system lamps, characterized by a white beam, reveals predominant colours in the blue and purple regions. As depicted in Figure 5-33, these hues dominate the spectral composition of the emitted light. Given that white light is a composite of all spectral components, all channels register a discernible signal, underscoring the comprehensive nature of the recorded data.

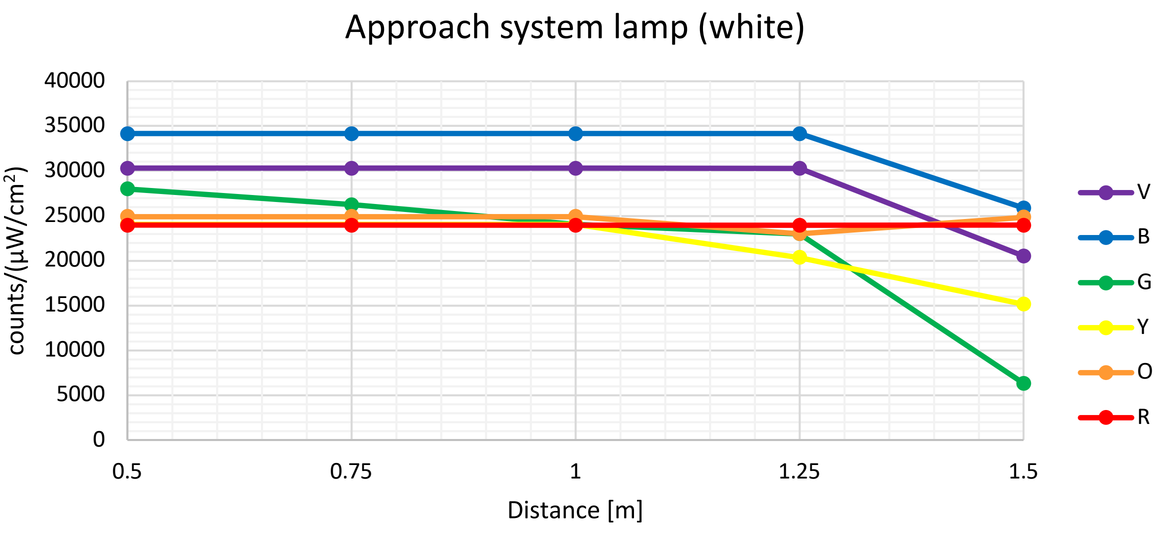

Figure 5-33 Visible light spectrum of the approach system lamps (white) [39]

As in the previous case, the investigation encompassed also an examination of the spectral characteristics of a newly installed red approach lamp. Multiple rounds of measurements were conducted to ensure thorough data collection, resulting in averaged measurement outcomes that have been methodically compiled and are presented in Table 5-10.

Table 5-10 Spectrum results of the approach system lamp (red) examination [in counts/(µW/cm^2)]

Approach system lamp (red)					
Channel	**Distance from lamp [m]**				
	0.5	**0.75**	**1**	**1.25**	**1.5**
V	30285.84	30285.72	14668.18	8113.64	6547.41
B	33532.45	10767.21	13588.13	9492.25	7122.26
G	27996.43	26221.31	15389.41	8597.91	6322.05
Y	24038.98	24038.98	24039.11	20359.15	15134.99
O	24899.78	24899.77	24898.94	22984.92	24851.86
R	23951.41	23951.43	23950.94	23950.94	23950.41

In a similar fashion to previous observations, an evident decrease in readings for certain individual channels was noted as the distance between the spectrum sensor and the light source increased. This trend was particularly pronounced beyond a distance of approximately 75 cm, indicating a diminishing intensity of light as the distance between the sensor and the source widened. Such findings underscore the importance of considering distance as a critical factor influencing the accuracy and reliability of light intensity measurements.

Upon closer examination of the visible light spectrum emitted by the approach system lamp, it was observed that the red component predominated, with blue comprising the smallest portion of the overall spectral composition. This spectral profile, illustrated in Figure 5-34, highlights the dominance of red wavelengths in the emitted light beam, underscoring the lamp's specific emission characteristics.

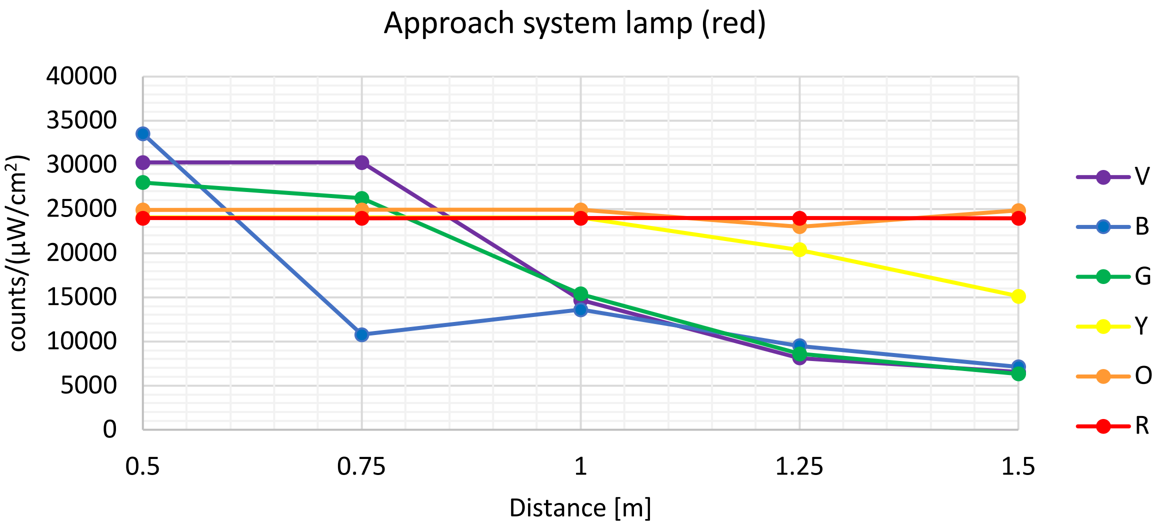

Figure 5-34 Visible light spectrum of the approach system lamps (red) [39]

The emitted light beam spectrum of a brand-new runway end lamp was subjected to rigorous testing, with multiple series of measurements conducted to ensure robust and comprehensive data collection. The averaged measurement results derived from these meticulous measurements are meticulously compiled and presented in Table 5-11.

Table 5-11 Spectrum results of the runway end lamp examination [in counts/(µW/cm^2)]

Runway end lamp					
Channel	**Distance from lamp [m]**				
	0.5	**0.75**	**1**	**1.25**	**1.5**
V	2262.99	1907.87	1347.51	774.71	606.81
B	392.13	1024.31	325.84	673.14	387.62
G	4827.02	1682.15	1062.01	699.79	498.02
Y	5395.98	3504.98	1949.52	1636.88	1101.84
O	24203.85	10956.67	7504.14	4126.21	3292.67
R	26148.37	13943.97	5178.99	5932.31	5080.03

The study investigating the distance effect between the spectrum sensor and the light source, specifically focusing on a particular lamp, revealed a notable trend: as the distance between the sensor and the light source increased, the recorded readings exhibited a corresponding decrease. Unlike other luminaires where a distinct limit distance can often be discerned, beyond which measurements stabilize, the data from this lamp displayed a continuous decrease in readings with increasing distance. This characteristic behaviour is represented by a curve reminiscent of a hyperbola, indicating a non-linear relationship between distance and recorded values.

Further analysis delved into the spectral composition of the light emitted by the runway end lamp and stop bar, revealing predominant wavelengths in the orange and red regions of the spectrum. These wavelengths constituted the majority of the emitted light beam, while other spectral components made up only a minimal fraction of the total output. This spectral profile underscores the lamp's specific emission characteristics, which may have implications for its visibility and effectiveness in various operational conditions.

Figure 5-35 visually depicts the spectral composition of the emitted light beam, highlighting the dominance of orange and red wavelengths. The graphical representation provides a clear illustration of the relative intensities of different spectral components, offering valuable insights into the spectral characteristics of the lamp's emitted light.

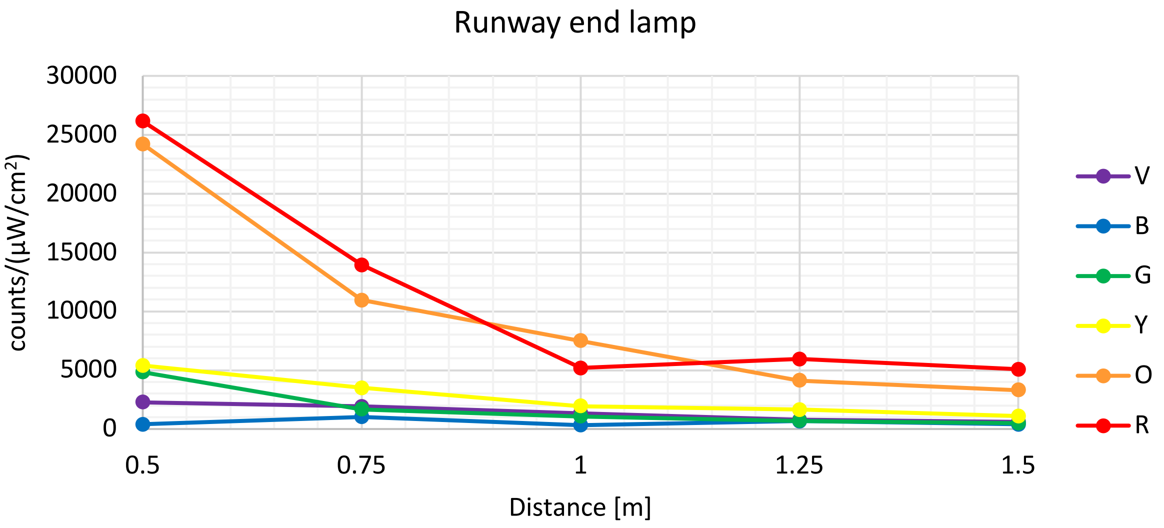

Figure 5-35 Visible light spectrum of the runway end lamp [39]

Sensors integrated into the rear matrix of the measurement platform primarily include BH1750 modules, which are responsible for measuring light intensity. Furthermore, to enable the automatic identification of lamp types, the AS7262 visible light spectrum sensor has been incorporated into the system. This sensor operates by recognizing the colour of the light beam, utilizing the values of its individual spectral components [28].

5.2.5. Proposed system for automatic chromaticity measurement of airport navigation lighting

As part of this research, extensive testing was conducted using the TCS3430 sensor alongside in-pavement airport navigation lamps. Specifically, ten series of measurements were performed, with each series comprising 1000 individual measurements taken at varying distances from the light source. These measurements were carried out in strict accordance with the guidelines set by international regulatory bodies such as the European Union Aviation Safety Agency (EASA) and the International Civil Aviation Organization (ICAO). The tests were conducted at the maximum power output of the respective light points, utilizing halogen bulbs rated at either 48 W or 40 W with a current of 6.6 A [193], [194].

To ensure the reliability and accuracy of the data, statistical parameters such as the standard deviation and median were computed for the measurements. The electrical and optical parameters of the in-pavement aeronautical ground lights are detailed in Table 5-12. The analysis of the results shows a minimal dispersion in the data across different distances from the light source. This minimal scatter indicates that the measurements were executed correctly, taking into account the geometric relationships as defined by the relevant standards, including the angular alignment with respect to the main beam of the emitted light. The sensor used in this study ensures high repeatability of the measurements [25].

Table 5-12 Electrical and optical parameters of in-pavement aeronautical ground lights [193], [194]

Lamp type	Power of the light source [W]	Colour	Average intensity [cd]	Horizontal distribution [degrees]	Vertical distribution [degrees]
TDZ	48	White	5800	−12 to +12	0 to 16
RCL_White	48	White	5800	−12 to +12	0 to 16
RCL_Red	48	Red	870	−12 to +12	0 to 16
TAXI_GREEN	40	Green	442	−18 to +18	0 to 12
TAXI_YELLOW	40	Yellow	663	−18 to +18	0 to 12

Furthermore, the mean values derived from these measurements are summarized in Table 5-13. It is evident from the data that the measured values exhibit a strong dependence on the distance between the light source and the sensor. Despite this dependency, the TCS3430 sensor's measurement range effectively encompasses all the distances that were investigated. Additionally, it is noteworthy that the standard deviation values for these measurements are consistently low, underscoring the precision and reliability of the testing process across all examined distances.

Table 5-13 Data from the TCS3430 sensor of the tested in-pavement aeronautical ground lights (XYZ coordinates)

Lamp type		**Distance from lamp [m]**																	
		0.5			**1.0**			**1.5**			**2.0**			**2.5**			**3.0**		
		Mean	**Standard deviation**	**Median**	**Mean**	**Standard deviation**	**Median**	**Mean**	**Standard deviation**	**Median**	**Mean**	**Standard deviation**	**Median**	**Mean**	**Standard deviation**	**Median**	**Mean**	**Standard deviation**	**Median**
TAXI_YELLOW	X	3473	1	3473	850	0	850	380	0	380	222	0	222	140	0	140	98	0	98
	Y	2787	1	2787	690	0	690	296	0	296	173	0	173	110	1	110	75	0	75
	Z	145	0	145	35	0	35	15	0	15	9	0	9	6	0	6	4	0	4
TAXI_GREEN	X	525	1	525	182	1	182	75	0	75	45	0	45	28	0	28	22	0	22
	Y	1127	2	1127	375	1	375	161	0	161	98	0	98	60	0	60	46	0	46
	Z	396	1	396	131	1	131	62	0	62	38	0	38	23	0	23	17	0	17
TDZ	X	27826	7	27824	10687	2	10687	4173	1	4173	2346	0	2346	1261	1	1261	772	0	772
	Y	25063	6	25062	9590	2	9590	3808	1	3808	2139	0	2139	1150	0	1150	693	0	693
	Z	5323	1	5323	217	1	2127	831	0	831	472	0	472	195	0	195	82	0	82
RCL_White	X	36100	20	36099	10261	3	10261	4445	1	4445	2534	2	2535	1439	2	1439	982	2	982
	Y	31755	17	31753	8997	3	8997	4021	1	4021	2225	2	2225	1292	1	1292	882	1	882
	Z	6923	3	6922	1966	1	1966	871	0	871	481	0	481	283	0	283	192	0	192
RCL_Red	X	15358	3	15359	4705	1	4705	2244	1	2244	1466	0	1466	857	0	857	427	0	427
	Y	8130	2	8130	2465	1	2466	1167	0	1167	803	0	803	453	0	453	227	0	227
	Z	447	0	447	136	0	136	65	0	65	43	0	43	24	0	24	12	0	12

The data collected from the TCS3430 sensor, originally in the form of XYZ values, were normalized and transformed to coordinates compatible with the CIE 1931 colour space, represented as x, y coordinates. This conversion, shown in Table 5-14, standardizes the values, making them independent of the measurement distance. As a result, the values in the respective rows are now consistent and comparable, regardless of the distance from which the measurements were taken.

Table 5-14 Normalised TCS3430 sensor data from in-pavement navigation lighting converted to CIE 1931 x, y coordinates

Lamp type		**0.5 [m]**	**1.0 [m]**	**1.5 [m]**	**2.0 [m]**	**2.5 [m]**	**3.0 [m]**
TAXI YELLOW	x	0.54	0.54	0.55	0.55	0.55	0.55
	y	0.44	0.44	0.43	0.43	0.43	0.42
TAXI GREEN	x	0.26	0.26	0.25	0.25	0.25	0.26
	y	0.55	0.54	0.54	0.54	0.54	0.54
TDZ	x	0.48	0.48	0.47	0.47	0.48	0.50
	y	0.43	0.43	0.43	0.43	0.44	0.45
RCL White	x	0.48	0.48	0.48	0.48	0.48	0.48
	y	0.42	0.42	0.43	0.42	0.44	0.43
RCL Red	x	0.64	0.64	0.65	0.63	0.64	0.64
	y	0.34	0.34	0.34	0.35	0.34	0.34

Figure 5-36 presents a point with specific measurements marked, demonstrating the data in an illustrative manner. The graph features five distinct lamps, which enables a clear differentiation between the lamp types and an easy verification of the accuracy of the reproduced colours. This graphical representation facilitates a straightforward assessment of whether the colours produced by the lamps conform to expected standards. Notably, all the in-pavement lamps tested adhere to the standards specified in international regulations.

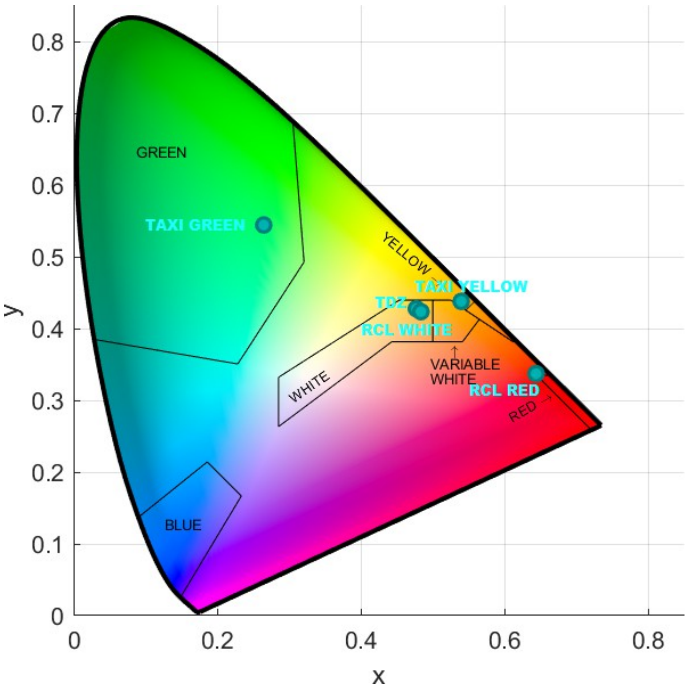

Figure 5-36 Chromaticity chart of in-pavement airport navigation lighting system [42]

In Figure 5-37, the relationship between the x, y coordinates values within the CIE 1931 colour space and the distance from the light source is depicted. For the in-pavement lamps, the maximum sensor values were not exceeded, which implies that measurements can be accurately taken from a distance of 0.5 meters. The observed waveforms are linear, suggesting that the measurement system is robust against environmental variations. This linearity confirms that the measurements can be reliably performed regardless of the distance from the lamp under test.

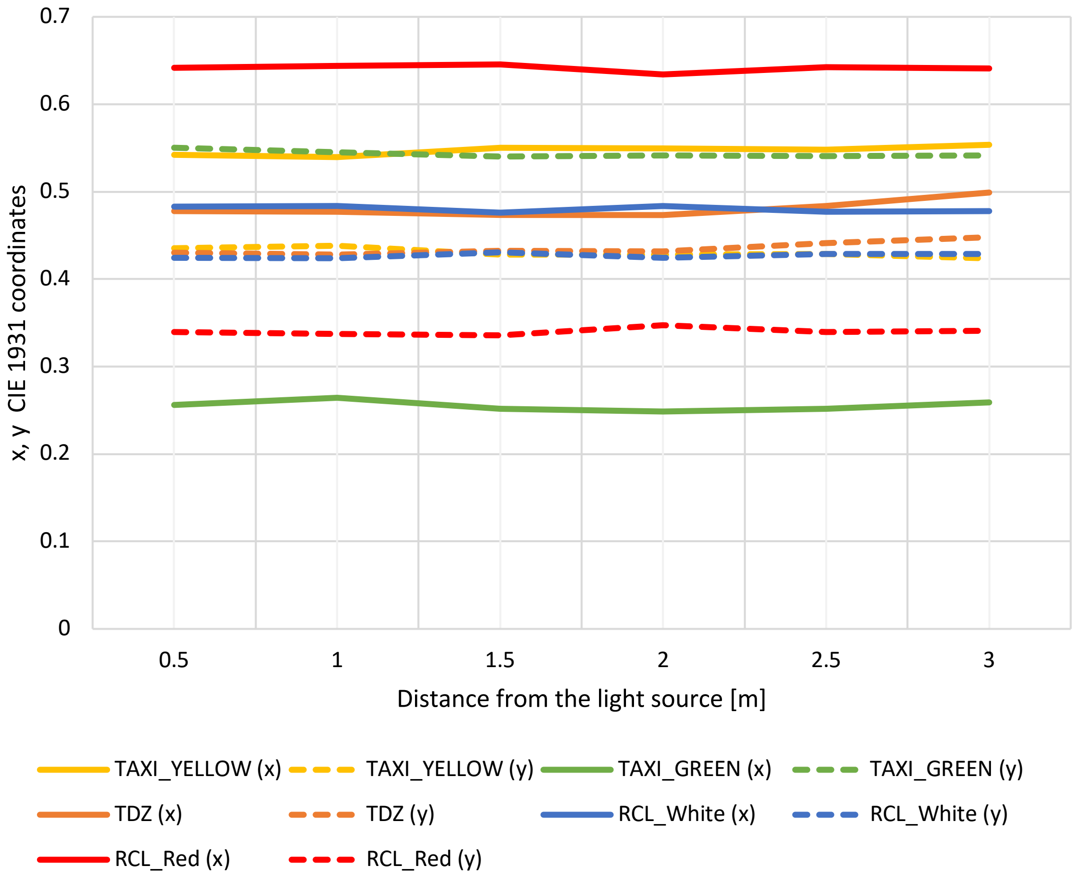

Figure 5-37 Graph of the CIE 1931 x, y coordinates of the tested in-pavement lamps as a function of the distance from the light source [42]

As part of the study, tests were conducted on elevated airport navigation lighting using the TCS3430 colour sensor. Ten series of measurements were taken, with each series comprising 1000 measurements at distances of 0.5 meters, 1.0 meters, 1.5 meters, 2.0 meters, 2.5 meters, and 3.0 meters from the tested light source. These measurements were performed with the light sources operating at their maximum power (current 6.6 A). It is important to note that the stop bar lamp uses a lower power bulb (45 W) compared to the approach lamps, which use higher power bulbs (150 W) [195]. The type of light source significantly influences the intensity of the emitted main beam.

Table 5-15 provides the electrical and optical parameters of elevated aeronautical ground lights. Similar to the in-pavement lamps, the standard deviation and median values indicated high repeatability and accuracy of the sensor used. The data dispersion was minimal, representing only a fraction of the values obtained across the entire measurement series. The average values from these measurements are presented in Table 5-16. Accurate measurements are feasible from a distance of 0.5 meters for the STOP_BAR lamp, 1 meter for the APP_Red lamp, and 1.5 meters for the APP_White lamp. Although the standard deviation is slightly higher than that observed in in-pavement aeronautical ground lights, it remains within 2% of the mean value, ensuring reliable measurement results.

Table 5-15 Electrical and optical parameters of elevated aeronautical ground lights [195]

Lamp type	The power of the light source [W]	Colour	Average intensity [cd]	Horizontal distribution [degrees]	Vertical distribution [degrees]
APP_White	150	White	22 108	-10 to +10	2 to 13
APP_ Red	150	Red	6 921	-5 to +9	3 to 13
STOP_BAR	45	Red	309	-10 to +10	1 to 8

In a similar manner to previous experiments, the data obtained from the TCS3430 sensor, presented in the form of XYZ coordinates, underwent normalization and subsequent transformation to the CIE 1931 colour space, resulting in x, y coordinates. Table 5-17 provides the coordinates post-conversion.

Consistent with earlier observations (refer to Table 5-16), it was noted that sensor saturation occurred at a distance of 0.5 m for APP_Red and at distances of 0.5 m and 1 m for APP_White. Consequently, these particular results are deemed unsuitable for further analysis and consideration due to their overrange nature.

Table 5-16 Data from the TCS3430 sensor of tested elevated aeronautical ground lights (XYZ coordinates)

Lamp type		0.5 [m]			1.0 [m]			1.5 [m]			2.0 [m]			2.5 [m]			3.0 [m]		
		Mean	**Standard deviation**	**Median**	**Mean**	**Standard deviation**	**Median**	**Mean**	**Standard deviation**	**Median**	**Mean**	**Standard deviation**	**Median**	**Mean**	**Standard deviation**	**Median**	**Mean**	**Standard deviation**	**Median**
APP_White	X	36805	284	36863	36863	0	36863	18551	81	18528	9415	116	9405	5220	68	5221	3701	31	3698
	Y	35058	2055	35628	36697	609	36863	15789	63	15776	7998	81	7998	4456	57	4449	3166	22	3159
	Z	10167	1698	9787	10271	266	10320	4241	16	4236	2130	29	2128	1180	14	1181	835	7	834
APP_Red	X	36863	0	36863	15695	139	15681	6849	61	6837	3381	43	3357	2044	31	2059	1486	18	1491
	Y	36863	0	36863	8660	82	8630	3767	25	3770	1799	30	1785	1088	22	1098	798	16	806
	Z	36863	0	36863	1338	12	1334	560	5	559	280	3	280	165	1	166	120	2	121
STOP_BAR	X	2688	34	2679	822	4	822	408	5	405	240	1	240	154	1	154	111	0	111
	Y	1381	20	1377	429	2	429	208	4	206	120	1	120	79	0	79	58	0	58
	Z	251	3	251	77	0	77	38	0	38	22	0	22	14	0	14	10	0	10

Table 5-17 Normalised TCS3430 sensor data from elevated navigation lighting converted to CIE 1931 x, y coordinates

Lamp type		**Distance from lamp [m]**					
		0.5	**1.0**	**1.5**	**2.0**	**2.5**	**3.0**
APP_ Red	x	0.33	0.61	0.61	0.62	0.62	0.62
	y	0.33	0.34	0.34	0.33	0.33	0.33
APP_White	x	0.45	0.44	0.48	0.48	0.48	0.48
	y	0.43	0.44	0.41	0.41	0.41	0.41
TDZ	x	0.62	0.62	0.62	0.63	0.62	0.62
	y	0.32	0.32	0.32	0.31	0.32	0.32

Figure 5-38 provides a visual representation of the measured data, with a specific point marked for illustrative purposes, showcasing measurements from three different lamps in a single graph. This graphical visualization facilitates the easy distinction between lamp types and enables the verification of colour reproduction accuracy.

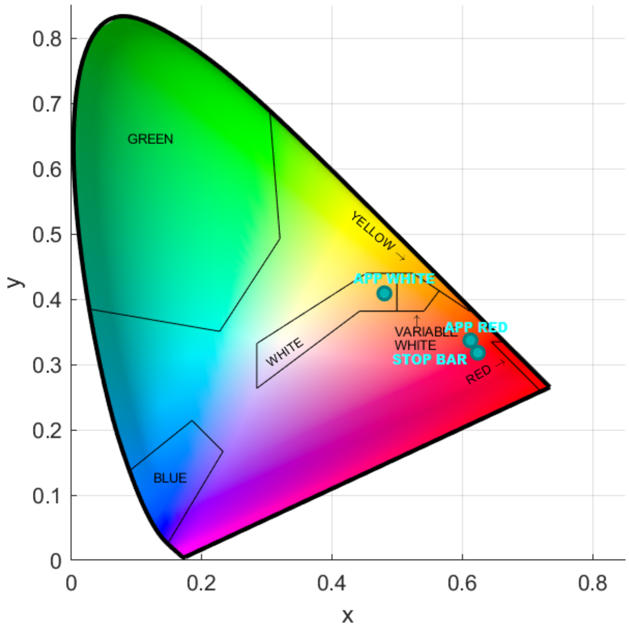

Figure 5-38 Chromaticity chart of the elevated airport navigation lighting system [42]

Upon closer inspection, it becomes evident that the Stop Bar and APP_Red lamps (previously utilized lamps) no longer conform to the standards regarding the chromaticity of the emitted light beam. Several factors could contribute to this deviation, including the wear and tear of the halogen bulb light source and the lampshade, which also acts as a colour filter. Exposure to various weather conditions can lead to the degradation of the lampshade's structure and physical properties, resulting in issues such as discolouration, cracks, matting, and fading.

Consequently, regular and dependable verification of the chromaticity of the lamps becomes imperative to facilitate timely maintenance and replacement processes. By ensuring the adherence to established standards, potential safety hazards and operational disruptions can be mitigated effectively within airport environments.

As previously mentioned, approach lamps are equipped with significantly more powerful light sources. Figure 5-39 illustrates the relationship between the x, y coordinates in the CIE 1931 space and the distance to the tested lamp. Notably, during the measurements for APP_Red at a distance of 0.5 m and APP_White at distances of 0.5 m and 1.0 m, the values of individual components exceeded the sensor's saturation threshold. Consequently, the results obtained at these points are deemed unreliable after conversion.

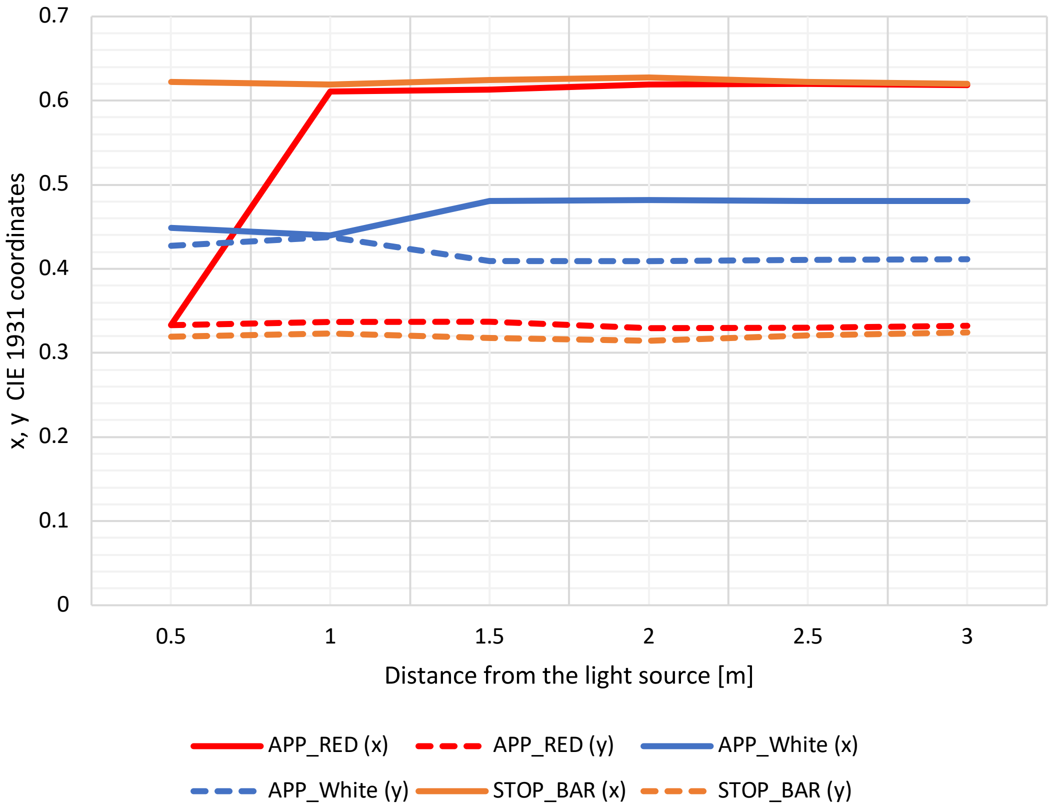

Figure 5-39 Graph of the CIE 1931 x, y coordinates of the tested elevated lamps as a function of the distance from the light source [42]

It has been conclusively determined that the minimum measurement distance for the approach lamps should be set at 1.5 m to ensure accurate and reliable data collection. This adjustment ensures that the measurements remain within the sensor's operational range, thereby enhancing the credibility and validity of the obtained results.

As part of this research [42], a software application was developed to automate data conversion, plot measured points, and compare these results against the relevant aviation standards. The software allows users to input data obtained from the sensor in the form of XYZ coordinates. After entering the data, the user selects the colour standard that the tested lamp should conform to. The system then determines whether the standard has been met and generates a chromaticity graph to visualize the data. This graph includes a point provided by the user and visualizes whether the lamp meets the specified colour standards. The chromaticity chart incorporates the standards for individual colours as defined by the equations in the EASA document [4].

It was chosen to create the chromaticity plot using the 2-degree x, y chromaticity coordinates from the CIE 1931 colour space, based on data provided by the Colour & Vision Research Institute of Ophthalmology at University College London [196]. This approach ensures the highest accuracy in generating the chromaticity diagram, capturing every nanometre of the visible light spectrum within the range of 360 to 830 nm. Figure 5-40 showcases the user interface, displaying the visual representation of the measurements obtained through the system.

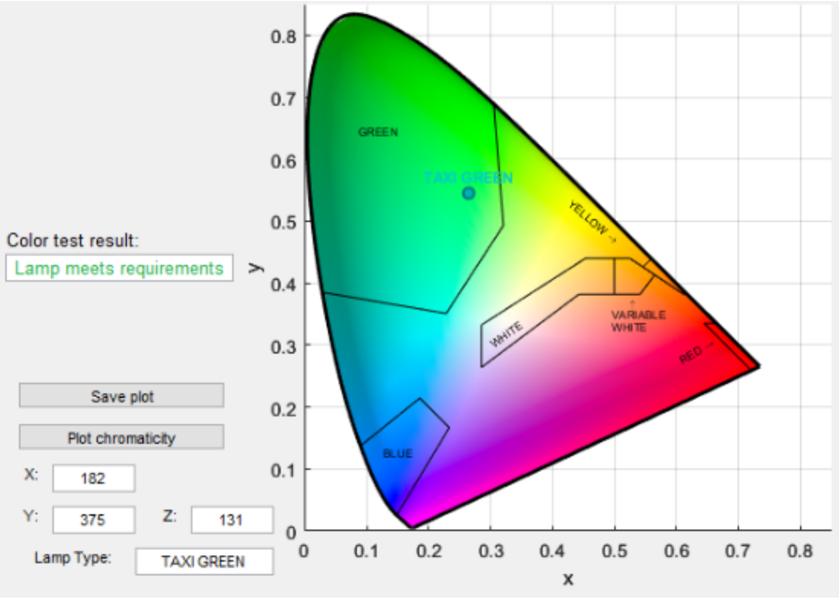

Color test result: Lamp meets requirements

X: 182

Y: 375

Z: 131

Lamp Type: TAXI GREEN

Figure 5-40 Proposed graphical user interface of the prepared software for colour classification [42]

The system not only enhances the efficiency of the measurement process but also ensures precision by automating the comparison against stringent aviation standards. This tool is particularly valuable for professionals in the field, enabling them to quickly and accurately verify whether the tested lamps meet the required specifications, thereby ensuring compliance with international aviation safety regulations.

Chapter

6. Conclusions

The doctoral dissertation addresses European Union Aviation Safety Agency (EASA) recommendations, concerning the implementation of AI to support safety inspections in aerodromes. It is rooted in international standards for aviation regulations, reliability levels, and recommendations from EASA, the International Civil Aviation Organization (ICAO), and the Federal Aviation Administration (FAA). The developed systems contribute significantly to the continuous improvement of airport safety. The research benefited from effective scientific collaboration between specialists from the Department of Electronic Systems and Signal Processing at Poznań University of Technology and Poznań–Ławica Airport.

In examining the detection of Foreign Object Debris, the author justified the importance of this issue by analysing available databases, such as the FOD-A dataset, and constructing a proprietary *PUT dataset* comprising 1480 images of FOD objects based on real images from Poznań–Ławica Airport, built in accordance with the FAA recommendations. The study compared traditional image processing methods (e.g., k-means) with advanced neural network models such as GoogLeNet and YOLOv5. A co-evolutionary neural network model based on GoogLeNet achieved 95.73% accuracy in object detection and classification, while a significantly expanded dataset of over 19000 images from FOD-A, used to train the YOLOv5 network, reached an accuracy of up to 99%, which is the highest result among the analysed literature and FOD-A database, which achieved an efficiency of maximum 95.73% on this dataset. Additionally, the YOLOv5 model trained on the *PUT dataset* achieved an accuracy of 99.3%.

For the detection of aerodrome horizontal markings, the dissertation introduced the *PLAVS1* (*Poznań Lawica Airport Video Set 1*) dataset, comprising over 303 minutes of recordings (over 98 GB) showing runways, taxiways, and aprons under various meteorological conditions and times of day. The proposed algorithm for detecting lines developed a line detection algorithm based on colour space conversion to HSV and colour filtering, achieving nearly 99.9% accuracy. Additional advantage of this algorithm is independence from the analysed input resolutions. The second algorithm achieved values close to 98%, but there was also a visible dependence on the input image size and also in certain cases its efficiency was lower by 34% than the proposed solution.

The evaluation and selection of Single Board Computers (SBCs) is a complex task, involving multiple considerations detailed in this dissertation. The energy aspects, particularly relevant for mobile devices, are addressed by manufacturers who offer various power modes in their experimental modules. However, there is a scarcity of comprehensive publications assessing the use of these features. The algorithms examined exhibit typical challenges in video sequence processing. Therefore, the estimates provided in this dissertation serve as valuable guidelines for designers of intelligent embedded systems for video processing. It is important to note that to accurately determine energy requirements, individual algorithm tests are necessary.

The performance of the proposed algorithms was evaluated on selected SBCs for experimental tests. The Raspberry Pi 4B modules are adequate for applications where high resolution is not critical. Experimental results demonstrated that these modules could handle standard 30 FPS video processing at a maximum resolution of 640 × 360. The primary benefits of using Raspberry Pi 4B modules include their low cost and relatively low energy consumption per processed video frame. These devices can operate with passive cooling, eliminating the need for an additional fan, which would otherwise consume an extra 0.5 W.

Processing efficiency is also related to energy aspects, and modules can work in different modes. NVIDIA Jetson family solutions have been tested. The most efficient units, such as the NVIDIA Jetson Xavier AGX and NVIDIA Jetson Orin AGX, are the only ones that meet the FPS requirements for video sequence processing. Despite being the latest model, the NVIDIA Jetson Orin AGX did not outperform the NVIDIA Jetson Xavier AGX in most tests conducted. The Xavier AGX achieved superior results in FPS values and power efficiency per processed frame, especially under the default schedutil Dynamic Voltage and Frequency Scaling (DVFS) policy.

The author introduced an intelligent vision system and conducted experiments for the quality classification of prisms in in-pavement airport lamps. This assessment utilized a proprietary *PLAVS2 (Poznań Lawica Airport Video Set 2) dataset*, developed in collaboration with Poznań–Ławica Airport, comprising 1004 images of lamps. The experiments were conducted using the standard Open Neural Network Start application within the MATLAB environment and Google Colab. Due to the unique characteristics of airport lamps, it was crucial to appropriately select parameters for image processing algorithms and the neural network's functionality. Enhancing the efficiency of Region of Interest (ROI) detection could be achieved through optimized lighting systems during image capture, a focus of ongoing research. The implemented GoogLeNet neural network model achieved an accuracy of 88.37%

in the classification process. This accuracy can be improved by expanding the dataset and ensuring a balanced number of images in each class.

To select appropriate cameras for SBCs, extensive testing of various video cameras was conducted, with the results analysed according to the ISO 12233 standard test chart. The tests indicated that the Raspberry Pi Camera HD v2 and the IMX477 camera with a 6mm CS-Mount lens produced the best image detail. Additionally, the IMX477 camera offers significant advantages due to its construction and compatibility with standard mount lenses. This feature greatly enhances its adaptability for use in measurement platforms for quality testing at airports and for assessing mechanical damage to airport lamps.

The author investigated the feasibility of utilizing a light spectrum sensor for detecting the colour of airport lamps, focusing specifically on the AS7262 sensor. The detailed examination revealed that, for in-pavement airport lamps, measurement repeatability is maintained even with the use of an acrylic glass cover. However, for elevated lamps, the measurement variability is noticeable due to the changes in the distance between the sensor and the light source. The research indicated a dependency on this distance, with red and orange components primarily requiring adjustments as the distance increases. These corrections can be addressed programmatically, but proper calibration is essential to ensure accuracy.

The investigation into the utilization of the TCS3430 sensor for the chromaticity assessment of airport navigation lighting, along with the development of software for automatic conversion and visualization of the obtained measurements, facilitated the creation of a system for evaluating the chromaticity of navigation lighting. This system enables users to verify compliance with chromaticity standards for specific types of tested navigation lamps. Experiments were conducted on seven types of lamps installed at Poznań–Ławica Airport, examining the impact of measurement distance from the light source. It was determined that measurements for in-pavement airport navigation lamps can be performed from a minimum distance of 1 meter, while for elevated lamps, a minimum distance of 1.5 meters is required. A key advantage of the TCS3430 sensor is its capability to provide CIE 1931 colour coordinates in accordance with EASA standards. However, a limitation of the TCS3430 sensor is its insufficient range of results for each type of lamp at the same distance, leading to the recommendation that in-pavement aeronautical ground lighting be tested at a distance of 1 meter and elevated aeronautical ground lighting at a distance of 1.5 meters.

Experiments related to the inspection of chromaticity of airport navigation lighting can also be combined and performed simultaneously, during a single measurement. On the one hand, the lamp is categorized according to the colour of the emitted light, which determines the light intensity levels that a given lamp must meet, according to EASA standards, and on the other hand, it is possible to perform a light chromaticity test and check whether it is within the EASA standard for light colour in CIE 1931 colour space.

An important advantage of the proposed solutions is also the universality of the systems and the possibility of performing many inspections using one vehicle and one camera. For example, it is possible to detect horizontal markings in airports while simultaneously detecting FOD objects. Such a solution significantly shortens the time of occupation of the runway and taxiways, which in turn is economically beneficial for the airport. Moreover, the proposed solutions are not designed for a specific type of vehicle, thanks to which it is possible to easily dismantle the camera and the data processing system, and then install it in another vehicle, for example for the time of repair or other unforeseen events.

In conclusion, the author has advanced solutions for vision inspection leveraging artificial intelligence to enhance aerodrome safety. Consequently, the scientific objectives of this Ph.D. dissertation have been successfully achieved. The scientific thesis — *Proposed vision preprocessing methods, together with neural network solutions within the domain of embedded systems, substantially improve and facilitate the automated inspection process at the airports* — has been validated. The developed systems demonstrate applicability across various airport service vehicles and measuring platforms, thereby supporting the inspection and safety management of airport operations.

Bibliography

[1] European Union Aviation Safety Agency. and European Environment Agency., *European aviation environmental report 2022.* LU: Publications Office, 2023. Accessed: Aug. 12, 2024. [Online]. Available: https://data.europa.eu/doi/10.2822/04357

[2] “PROGNOZA RUCHU LOTNICZEGO 2022-2040,” Urząd Lotnictwa Cywilnego, Sep. 11, 2023. Accessed: Apr. 15, 2024. [Online]. Available: https://www.ulc.gov.pl/_download/personel_lotniczy/dla-egzaminatora/Prezentacja_-_Prognoza_ruchu_lotniczego_dla_Polski_na_lata_2022-2040.r.pdf

[3] INTERNATIONAL CIVIL AVIATION ORGANIZATION, *AERODROMES: aerodromes design and operations*. ICAO, 2018. [Online]. Available: https://www.iacm.gov.mz/app/uploads/2018/12/an_14_v1_Aerodromes_8ed._2018_rev.14_01.07.18.pdf

[4] European Union Aviation Safety Agency, “Certification Specifications and Guidance Material for Aerodrome Design (CS-ADR-DSN).” Mar. 29, 2022. Accessed: Jun. 30, 2022. [Online]. Available: https://www.easa.europa.eu/en/downloads/136283/en

[5] K. Podbucki, J. Suder, T. Marciniak, and A. Dabrowski, “CCTV based system for detection of anti-virus masks,” in *2020 Signal Processing: Algorithms, Architectures, Arrangements, and Applications (SPA)*, Poznan, Poland: IEEE, Sep. 2020, pp. 87–91. doi: 10.23919/SPA50552.2020.9241303.

[6] J. Suder, T. Marciniak, K. Podbucki, and A. Dabrowski, “Real-time density maps generation of moving objects using embedded systems,” in *2022 International Symposium ELMAR*, Zadar, Croatia: IEEE, Sep. 2022, pp. 179–184. doi: 10.1109/ELMAR55880.2022.9899807.

[7] *Safety management*, Second edition. Montreal, Quebec: International Civil Aviation Organization, 2016.

[8] E. Batuwangala, J. Silva, and G. Wild, “The Regulatory Framework for Safety Management Systems in Airworthiness Organisations,” *Aerospace*, vol. 5, no. 4, p. 117, Nov. 2018, doi: 10.3390/aerospace5040117.

[9] “Doc 9859 - Safety Management Manual, Fourth Edition.” International Civil Aviation Organization, 2018. [Online]. Available: https://skybrary.aero/sites/default/files/bookshelf/5863.pdf

[10] D. A. Ludwig, *Safety management systems for airports. volume 1: Overview*. in ACRP report, no. 1. Washington, D.C: Transportation Research Board, 2007.

[11] “Regulation (EU) 2018/1139 of the European Parliament and of the Council.” European Union Aviation Safety Agency. [Online]. Available: https://www.easa.europa.eu/en/document-library/easy-access-rules/easy-access-rules-basic-regulation-regulation-eu-20181139

[12] “AC 150/5200-37A - Safety Management Systems for Airports.” Federal Aviation Administration, 2023. Accessed: Jul. 12, 2024. [Online]. Available: https://www.faa.gov/documentLibrary/media/Advisory_Circular/150_5200_37A_Part_139_SMS.pdf

[13] “EASA Artificial Intelligence Roadmap 2.0.” uropean Union Aviation Safety Agency, May 10, 2023. Accessed: Jun. 10, 2024. [Online]. Available: https://www.easa.europa.eu/en/downloads/137919/en

[14] “EASA Artificial Intelligence Concept Paper Issue 2 Guidance for Level 1 & 2 machine-learning applications.” European Union Aviation Safety Agency, Mar. 06, 2024. [Online]. Available: https://www.easa.europa.eu/en/downloads/139504/en

[15] “AC 150/5210-24 - Airport Foreign Object Debris (FOD) Management.” Federal Aviation Administration, Sep. 30, 2010. [Online]. Available: https://www.faa.gov/documentLibrary/media/Advisory_Circular/AC_150_5210-24.pdf

[16] “Air France Flight 4590 FOD Explained,” FODprevention. Accessed: Apr. 19, 2024. [Online]. Available: https://fodprevention.com/air-france-flight-4590-fod-explained/

[17] “Foreign Object Debris.” [Online]. Available: https : / / www . boeing . com / commercial / aeromagazine/aero_01/textonly/s01txt.html

[18] J. J. Ruschau, T. Nicholas, and S. R. Thompson, “Influence of foreign object damage (FOD) on the fatigue life of simulated Ti-6Al-4V airfoils,” *Int. J. Impact Eng.*, vol. 25, no. 3, pp. 233–250, Mar. 2001, doi: 10.1016/S0734-743X(00)00044-0.

[19] “Concorde Crashes, Killing Total of 113 And Putting Jets’ Future in Question,” The Wall Street Journal. [Online]. Available: https://www.wsj.com/articles/SB964574859870269692

[20] “Airport Foreign Object Debris (FOD) Detection Equipment - 150/5220-24.” Federal Aviation Administration, Sep. 30, 2009. [Online]. Available: https://www.faa.gov/documentLibrary/media/Advisory_Circular/AC_150_5220-24.pdf

[21] "Bureau of Aircraft Accidents Archives, ACCIDENTS PICTURES." Accessed: Jun. 20, 2024. [Online]. Available: https://www.baaa-acro.com/crash-pictures

[22] "Information Paper on French Study on Automatic FOD Detection Systems – Workshop EUROCONTROL, 9-10 June 2008."

[23] "Examples of FOD items in ramstein air base," U.S. Air Force graphic/Senior Airman Damon Kasberg. Accessed: Apr. 12, 2024. [Online]. Available: https://www.ramstein.af.mil/News/Art/igphoto/2001490818/

[24] T. Novak, J. Dudek, V. Kolar, K. Sokansky, and R. Baleja, "Solution of problems with short lifetime of airfield halogen lamps," in *2017 18th International Scientific Conference on Electric Power Engineering (EPE)*, Kouty nad Desnou, Czech Republic: IEEE, May 2017, pp. 1–5. doi: 10.1109/EPE.2017.7967298.

[25] S. Raggiunto, A. Belli, L. Palma, P. Ceregioli, M. Gattari, and P. Pierleoni, "An Efficient Method for LED Light Sources Characterization," *Electronics*, vol. 8, no. 10, p. 1089, Sep. 2019, doi: 10.3390/electronics8101089.

[26] D. S. D. Sitompul, F. E. Surya, F. P. Suhandi, and H. Zakaria, "Runway Edge Light Photometry System by Using Drone-Mounted Instrument," in *2019 International Symposium on Electronics and Smart Devices (ISESD)*, Badung-Bali, Indonesia: IEEE, Oct. 2019, pp. 1–5. doi: 10.1109/ISESD.2019.8909498.

[27] D. S. D. Sitompul, F. E. Surya, F. P. Suhandi, and H. Zakaria, "Runway Edge Light Photometry by Vertical Scanning Method Using Drone Mounted Photodiode Array," in *2019 International Conference on Electrical Engineering and Informatics (ICEEI)*, Bandung, Indonesia: IEEE, Jul. 2019, pp. 301–305. doi: 10.1109/ICEEI47359.2019.8988830.

[28] J. Suder, P. Maciejewski, K. Podbucki, T. Marciniak, and A. Dąbrowski, "Measuring Platform for Quality Testing of Airport Lamps," *Pomiary Autom. Robot.*, vol. 23, no. 2, pp. 5–13, Jun. 2019, doi: 10.14313/PAR_232/5.

[29] K. Podbucki, J. Suder, T. Marciniak, and A. Dąbrowski, "Electronic measuring matrix for testing airport lamps," *Przegląd Elektrotechniczny*, vol. 97, no. 2, pp. 49–53, Feb. 2021, doi: 10.15199/48.2021.02.12.

[30] J. Suder, K. Podbucki, T. Marciniak, and A. Dąbrowski, "Low Complexity Lane Detection Methods for Light Photometry System," *Electronics*, vol. 10, no. 14, 2021, doi: 10.3390/electronics10141665.

[31] D. S. D. Sitompul, F. E. Surya, F. P. Suhandi, and H. Zakaria, "Horizontal Scanning Method by Drone Mounted Photodiode Array for Runway Edge Light Photometry," in *2019 International Seminar on Intelligent Technology and Its Applications (ISITIA)*, Surabaya, Indonesia: IEEE, Aug. 2019, pp. 41–45. doi: 10.1109/ISITIA.2019.8937211.

[32] P. Croucher, *EASA Professional Pilot Studies*. Glasstree, 2016.

[33] F. Jentsch, "The Effects of Taxiway Light Geometry, Color, and Location on Position Determination by Pilots," *Proc. Hum. Factors Ergon. Soc. Annu. Meet.*, vol. 38, no. 1, pp. 76–80, Oct. 1994, doi: 10.1177/154193129403800114.

[34] Y. Lai, Y. Liu, and D. Ma, "Automatically melting snow on airport cement concrete pavement with carbon fiber grille," *Cold Reg. Sci. Technol.*, vol. 103, pp. 57–62, Jul. 2014, doi: 10.1016/j.coldregions.2014.03.008.

[35] United States. Federal Aviation Administration, "Measurement, Construction, and Maintenance of Skid-Resistant Airport Pavement Surfaces," 1997, doi: 10.21949/1402821.

[36] INTERNATIONAL CIVIL AVIATION ORGANIZATION, "Aerodrome Design Manual Fifth Edition, Part 4 — Visual Aids." 2021. [Online]. Available: http://icscc.org.cn/upload/file/20220712/20220712090914_13813.pdf

[37] J. Suder and T. Marciniak, "Foreign Object Debris detection system using GoogLeNet," *Przegląd Elektrotechniczny*, vol. 99, no. 11, pp. 251–254, Nov. 2023, doi: 10.15199/48.2023.11.47.

[38] J. Suder and T. Marciniak, "Foreign Object Debris detection at aerodromes using YOLOv5," in *2024 Signal Processing: Algorithms, Architectures, Arrangements, and Applications (SPA)*, Poznan, Poland: IEEE, Sep. 2024, pp. 66–71. doi: 10.23919/SPA61993.2024.10715612.

[39] J. Suder, K. Podbucki, T. Marciniak, and A. Dąbrowski, "Spectrum sensors for detecting type of airport lamps in a light photometry system," *Opto-Electron. Rev.*, vol. 29, no. 4, pp. 133–140, 2021, doi: 10.24425/OPELRE.2021.139383.

[40] J. Suder, K. Podbucki, T. Marciniak, and A. Dąbrowski, "Intelligent vision system for quality classification of airport lamp prisms," in *2022 Signal Processing: Algorithms, Architectures, Arrangements, and Applications (SPA)*, 2022, pp. 151–154. doi: 10.23919/SPA53010.2022.9927908.

[41] J. Suder and T. Marciniak, "Fast Prototyping of In-Pavement Airport Navigation Lamp Prism Classification," in *2023 Signal Processing: Algorithms, Architectures, Arrangements, and Applications (SPA)*, Poznan, Poland: IEEE, Sep. 2023, pp. 95–99. doi: 10.23919/SPA59660.2023.10274434.

[42] J. Suder, K. Podbucki, and T. Marciniak, "Chromaticity measurement of airport navigation lighting using integrated colour sensor," *Opto-Electronics Review*, vol. 31, no. 4. Polish Academy of Sciences (under the

auspices of the Committee on Electronics and Telecommunication) and Association of Polish Electrical Engineers in cooperation with Military University of Technology, p. e147040, 2023. doi: 10.24425/opelre.2023.147040.

[43] J. Suder, K. Podbucki, and T. Marciniak, “Raport z pomiarów fotometrycznych zagłębionych lamp oświetlenia nawigacyjnego drogi startowej Portu Lotniczego Poznań – Ławica,” Politechnika Poznańska, Poznan, Poland, r3335_2022, Aug. 2022. [Online]. Available: https://sin.put.poznan.pl/reports/details/r3335_2022

[44] J. Suder, K. Podbucki, and T. Marciniak, “Power Requirements Evaluation of Embedded Devices for Real-Time Video Line Detection,” *Energies*, vol. 16, no. 18, p. 6677, Sep. 2023, doi: 10.3390/en16186677.

[45] A. Dąbrowski, T. Marciniak, K. Podbucki, and J. Suder, “Method for measuring the quality of operation of airport lamps and a measuring set for testing the quality of operation of recessed airport lamps,” P.442569

[46] J. Suder, “Parameters evaluation of cameras in embedded systems,” *Przegląd Elektrotechniczny*, vol. 98, no. 9, pp. 218–221, Sep. 2022, doi: 10.15199/48.2022.09.50.

[47] J. Suder, “Possibilities of processing video sequences in embedded systems,” *Przegląd Elektrotechniczny*, vol. 98, no. 1, pp. 190–193, Jan. 2022, doi: 10.15199/48.2022.01.41.

[48] K. Podbucki, J. Suder, T. Marciniak, and A. Dabrowski, “Evaluation of Embedded Devices for Real- Time Video Lane Detection,” in *2022 29th International Conference on Mixed Design of Integrated Circuits and System (MIXDES)*, Wrocław, Poland: IEEE, Jun. 2022, pp. 187–191. doi: 10.23919/MIXDES55591.2022.9838167.

[49] T. Marciniak, K. Podbucki, J. Suder, and A. Dąbrowski, “Analysis of Digital Filtering with the Use of STM32 Family Microcontrollers,” in *Advanced, Contemporary Control*, vol. 1196, A. Bartoszewicz, J. Kabziński, and J. Kacprzyk, Eds., in Advances in Intelligent Systems and Computing, vol. 1196. , Cham: Springer International Publishing, 2020, pp. 287–295. doi: 10.1007/978-3-030-50936-1_25.

[50] T. Marciniak, K. Podbucki, and J. Suder, “Application of the Nucleo STM32 module in teaching microprocessor techniques in automatic control,” *Przegląd Elektrotechniczny*, vol. 98, no. 10, pp. 247–250, Oct. 2022, doi: 10.15199/48.2022.10.55.

[51] K. Podbucki, J. Suder, T. Marciniak, W. Mańczak, and A. Dąbrowski, “Microprocessor-based photometric light intensity sensor for airport lamps quality testing,” *Opto-Electronics Review*, vol. 30, no. 4. Polish Academy of Sciences and Association of Polish Electrical Engineers in cooperation with Military University of Technology, p. e143396, 2022. doi: 10.24425/opelre.2022.143396.

[52] K. Podbucki, J. Suder, T. Marciniak, and A. Dąrowski, “Influence of power supply on airport navigation lamps photometric test accuracy,” in *2023 Signal Processing: Algorithms, Architectures, Arrangements, and Applications (SPA)*, Poznan, Poland: IEEE, Sep. 2023, pp. 183–188. doi: 10.23919/SPA59660.2023.10274440.

[53] K. Podbucki, T. Marciniak, and J. Suder, “Laboratory Assessment of In-Pavement Airport Lamp’s Luminous Intensity Distribution,” *Appl. Sci.*, vol. 13, no. 24, p. 13242, Dec. 2023, doi: 10.3390/app132413242.

[54] “Bezzałogowa, autonomiczna platforma pomiarowa do badania nośności naturalnych nawierzchni lotniskowych w sposób ciągły,” Dobrowolski Sp. z o.o., Instytut Techniczny Wojsk Lotniczych, POIR.01.01.01-00-0919/19-00.

[55] A. Elrayes, M. H. Ali, A. Zakaria, and M. H. Ismail, “Smart airport foreign object debris detection rover using LiDAR technology,” *Internet Things*, vol. 5, pp. 1–11, Mar. 2019, doi: 10.1016/j.iot.2018.11.001.

[56] A. Rowicki, A. Kawalec, K. Krenc, and M. Walenczykowska, “Bird Collision Prevention Systems in Passenger Aviation,” *Probl. Mechatron. Armament Aviat. Saf. Eng.*, vol. 14, no. 4, pp. 103–122, Dec. 2023, doi: 10.5604/01.3001.0054.1660.

[57] G. F. Et.al, “Review on Foreign Object Debris Detection Technologies and Advancement for Airport Safety and Surveillance,” *Turk. J. Comput. Math. Educ. TURCOMAT*, vol. 12, no. 3, pp. 1431–1436, Apr. 2021, doi: 10.17762/turcomat.v12i3.940.

[58] Xu Qunyu, Ning Huansheng, and Chen Weishi, “Video-based Foreign Object Debris detection,” in *2009 IEEE International Workshop on Imaging Systems and Techniques*, Shenzhen, China: IEEE, May 2009, pp. 119–122. doi: 10.1109/IST.2009.5071615.

[59] E. Papadopoulos and F. Gonzalez, “UAV and AI Application for Runway Foreign Object Debris (FOD) Detection,” in *2021 IEEE Aerospace Conference (50100)*, Big Sky, MT, USA: IEEE, Mar. 2021, pp. 1–8. doi: 10.1109/AERO50100.2021.9438489.

[60] P. Li and H. Li, “Research on FOD Detection for Airport Runway based on YOLOv3,” in *2020 39th Chinese Control Conference (CCC)*, Shenyang, China: IEEE, Jul. 2020, pp. 7096–7099. doi: 10.23919/CCC50068.2020.9188724.

[61] Y. Jing, H. Zheng, C. Lin, W. Zheng, K. Dong, and X. Li, “Foreign Object Debris Detection for Optical Imaging

Sensors Based on Random Forest," *Sensors*, vol. 22, no. 7, p. 2463, Mar. 2022, doi: 10.3390/s22072463.

[62] T. Munyer, D. Brinkman, C. Huang, and X. Zhong, "Integrative Use of Computer Vision and Unmanned Aircraft Technologies in Public Inspection: Foreign Object Debris Image Collection," in *DG.O2021: The 22nd Annual International Conference on Digital Government Research*, Omaha NE USA: ACM, Jun. 2021, pp. 437–443. doi: 10.1145/3463677.3463743.

[63] V. Malligere Shivanna and J.-I. Guo, "Object Detection, Recognition, and Tracking Algorithms for ADASs—A Study on Recent Trends," *Sensors*, vol. 24, no. 1, p. 249, Dec. 2023, doi: 10.3390/s24010249.

[64] S. Lu, Z. Luo, F. Gao, M. Liu, K. Chang, and C. Piao, "A Fast and Robust Lane Detection Method Based on Semantic Segmentation and Optical Flow Estimation," *Sensors*, vol. 21, no. 2, p. 400, Jan. 2021, doi: 10.3390/s21020400.

[65] W. Liu, F. Yan, J. Zhang, and T. Deng, "A Robust Lane Detection Model Using Vertical Spatial Features and Contextual Driving Information," *Sensors*, vol. 21, no. 3, p. 708, Jan. 2021, doi: 10.3390/s21030708.

[66] K. Rebai, N. Achour, and O. Azouaoui, "Road intersection detection and classification using hierarchical SVM classifier," *Adv. Robot.*, vol. 28, no. 14, pp. 929–941, Jul. 2014, doi: 10.1080/01691864.2014.902327.

[67] L. Cao, Z. Chen, L. Yan, Q. Qin, and R. Zhang, "A proposed vision and vehicle-to-infrastructure communication-based vehicle positioning approach," *J. Intell. Transp. Syst.*, vol. 21, no. 2, pp. 123–135, Mar. 2017, doi: 10.1080/15472450.2016.1247704.

[68] V. Popescu, S. Nedevschi, R. Danescu, and T. Marita, "A Lane Assessment Method Using Visual Information Based on a Dynamic Bayesian Network," *J. Intell. Transp. Syst.*, vol. 19, no. 3, pp. 225–239, Jul. 2015, doi: 10.1080/15472450.2013.856724.

[69] E. Jang, J. Suhr, and H. Jung, "Lane Endpoint Detection and Position Accuracy Evaluation for Sensor Fusion-Based Vehicle Localization on Highways," *Sensors*, vol. 18, no. 12, p. 4389, Dec. 2018, doi: 10.3390/s18124389.

[70] H. Vokhidov, H. Hong, J. Kang, T. Hoang, and K. Park, "Recognition of Damaged Arrow-Road Markings by Visible Light Camera Sensor Based on Convolutional Neural Network," *Sensors*, vol. 16, no. 12, p. 2160, Dec. 2016, doi: 10.3390/s16122160.

[71] J. Kim, "Efficient Vanishing Point Detection for Driving Assistance Based on Visual Saliency Map and Image Segmentation from a Vehicle Black-Box Camera," *Symmetry*, vol. 11, no. 12, p. 1492, Dec. 2019, doi: 10.3390/sym11121492.

[72] K.-H. Choi *et al.*, "Methods to Detect Road Features for Video-Based In-Vehicle Navigation Systems," *J. Intell. Transp. Syst.*, vol. 14, no. 1, pp. 13–26, Feb. 2010, doi: 10.1080/15472450903386005.

[73] M. Haris and A. Glowacz, "Lane Line Detection Based on Object Feature Distillation," *Electronics*, vol. 10, no. 9, p. 1102, May 2021, doi: 10.3390/electronics10091102.

[74] Y. Tian *et al.*, "Lane marking detection via deep convolutional neural network," *Neurocomputing*, vol. 280, pp. 46–55, Mar. 2018, doi: 10.1016/j.neucom.2017.09.098.

[75] H. Kim, S. Kwon, and S. Kim, "Hyperspectral Image-Based Night-Time Vehicle Light Detection Using Spectral Normalization and Distance Mapper for Intelligent Headlight Control," *Sensors*, vol. 16, no. 7, p. 1058, Jul. 2016, doi: 10.3390/s16071058.

[76] K. Choi, H. Jung, and J. Suhr, "Automatic Calibration of an Around View Monitor System Exploiting Lane Markings," *Sensors*, vol. 18, no. 9, p. 2956, Sep. 2018, doi: 10.3390/s18092956.

[77] P. R. Palafox, J. Betz, F. Nobis, K. Riedl, and M. Lienkamp, "SemanticDepth: Fusing Semantic Segmentation and Monocular Depth Estimation for Enabling Autonomous Driving in Roads without Lane Lines," *Sensors*, vol. 19, no. 14, p. 3224, Jul. 2019, doi: 10.3390/s19143224.

[78] D. Wolters and R. Koch, "Precise and Robust Line Detection for Highly Distorted and Noisy Images," in *Pattern Recognition*, vol. 9796, B. Rosenhahn and B. Andres, Eds., in Lecture Notes in Computer Science, vol. 9796. , Cham: Springer International Publishing, 2016, pp. 3–13. doi: 10.1007/978-3-319-45886-1_1.

[79] G. H. Bae and S. B. Lee, "A Study on the Evaluation Method of Highway Driving Assist System Using Monocular Camera," *Appl. Sci.*, vol. 10, no. 18, p. 6443, Sep. 2020, doi: 10.3390/app10186443.

[80] D. Gruyer, R. Belaroussi, and M. Revilloud, "Accurate lateral positioning from map data and road marking detection," *Expert Syst. Appl.*, vol. 43, pp. 1–8, Jan. 2016, doi: 10.1016/j.eswa.2015.08.015.

[81] W.-W. Hu, X.-H. Ge, and W.-R. Ye, "Summarization of Airport Runway Lights Cleaning Methods," in *Proceedings of the 3rd 2017 International Conference on Sustainable Development (ICSD 2017)*, Tianjin, China: Atlantis Press, 2017. doi: 10.2991/icsd-17.2017.17.

[82] J. Burns *et al.*, *LED Airfield Lighting System Operation and Maintenance*. Washington, D.C.: Transportation Research Board, 2015, p. 22076. doi: 10.17226/22076.

[83] T. J. Squire, M. Rodriguez-Carmona, A. D. B. Evans, and J. L. Barbur, "Color vision tests for aviation: comparison of the anomaloscope and three lantern types," *Aviat. Space Environ. Med.*, vol. 76, no. 5, pp.

421–429, May 2005.

[84] K. Tangri, “Meeting the challenge: Runway lighting serviceability.” Accessed: Feb. 02, 2023. [Online]. Available: https://www.internationalairportreview.com/article/76356/challenge-runway-lighting/

[85] J. D. Bullough, “Human Factors Impacts of Light-Emitting Diode Airfield Lighting,” *Transp. Res. Rec. J. Transp. Res. Board*, vol. 2626, no. 1, pp. 51–57, Jan. 2017, doi: 10.3141/2626-07.

[86] P. Szpakowski, “Lotnicza choinka - czyli o świetlnych pomocach nawigacyjnych i ich kontroli,” *Safe Sky Biul. Bezpieczeństwa Pol. Agencji Żegl. Powietrznej*, no. 4, pp. 4–13, 2020.

[87] W. Żagan, *Podstawy techniki świetlnej*, Wydanie 3. Warszawa: Oficyna Wydawnicza Politechniki Warszawskiej, 2022.

[88] W. R. McCluney, *Introduction to radiometry and photometry*. Boston London: Artech House, 1994.

[89] W. D. Wright, “A re-determination of the trichromatic coefficients of the spectral colours,” *Trans. Opt. Soc.*, vol. 30, no. 4, pp. 141–164, Mar. 1929, doi: 10.1088/1475-4878/30/4/301.

[90] CIE TC 1-36, *CIE 170-1:2006 Fundamental chromaticity diagram with physiological axes - Part 1*. doi: 10.25039/TR.170-1.2006.

[91] A. Materka and P. Strumiłło, “Wstęp do komputerowej analizy obrazów,” *Politech. Łódz.*, 2009.

[92] J. Guild, “The colorimetric properties of the spectrum,” *Philos. Trans. R. Soc. Lond. Ser. Contain. Pap. Math. Phys. Character*, vol. 230, no. 681–693, pp. 149–187, Sep. 1931, doi: 10.1098/rsta.1932.0005.

[93] A. Dąbrowski, “Inteligentne systemy wizyjne, Fotometria i kolorymetria,” Poznan, Poland, Mar. 16, 2021.

[94] T. Smith and J. Guild, “The C.I.E. colorimetric standards and their use,” *Trans. Opt. Soc.*, vol. 33, no. 3, pp. 73–134, Jan. 1931, doi: 10.1088/1475-4878/33/3/301.

[95] K. McMenemy and J. Niblock, “Classification of luminaire color using CCDs,” presented at the Electronic Imaging 2006, M. M. Blouke, Ed., San Jose, CA, Feb. 2006, p. 60680M. doi: 10.1117/12.643034.

[96] P. Ptak, K. Górecki, and M. Gensikowski, “Comparison of dynamic properties of the selected photometric sensors,” *Przegląd Elektrotechniczny*, vol. 96, no. 12, pp. 112–116, Dec. 2020, doi: 10.15199/48.2020.12.21.

[97] “PAC^2 V5 Photometric Airfield Calibration.” Accessed: May 17, 2024. [Online]. Available: https://www.fbtechnology.com/our-products-agl-photometric-maintenance/airfield-lighting-photometric-measurement/

[98] “DALMAS AFL Analysis.” Accessed: May 17, 2024. [Online]. Available: https://www.dewitec.de/en/airport-technology/dalmas-afl-analysis

[99] M. Royer *et al.*, “Improved Method for Evaluating and Specifying the Chromaticity of Light Sources,” *LEUKOS*, vol. 19, no. 1, pp. 35–52, Jan. 2023, doi: 10.1080/15502724.2022.2029710.

[100] J. Agudo, P. Pardo, H. Sánchez, Á. Pérez, and M. Suero, “A Low-Cost Real Color Picker Based on Arduino,” *Sensors*, vol. 14, no. 7, pp. 11943–11956, Jul. 2014, doi: 10.3390/s140711943.

[101] K. Choi, J. Lee, and H.-J. Suk, “Context-based presets for lighting setup in residential space,” *Appl. Ergon.*, vol. 52, pp. 222–231, Jan. 2016, doi: 10.1016/j.apergo.2015.07.023.

[102] S. Balkan and T. Kholod, “Video Analytics in Market Research,” *Inf. Syst. Manag.*, vol. 32, no. 3, pp. 192–199, Jul. 2015, doi: 10.1080/10580530.2015.1044337.

[103] “Image Processing in OpenCV,” OpenCV Open Source Computer Vision. Accessed: Jun. 07, 2024. [Online]. Available: https://docs.opencv.org/4.x/d2/d96/tutorial_py_table_of_contents_imgproc.html

[104] “OpenCV - About.” Accessed: Jun. 07, 2024. [Online]. Available: https://opencv.org/about/

[105] “MATLAB The Language of Technical Computing.” Accessed: May 17, 2024. [Online]. Available: https://www.mathworks.com/help/matlab/index.html?s_tid=hc_panel

[106] S. Osowski and R. Szmurło, Eds., *Matematyczne modele uczenia maszynowego w językach MATLAB i PYTHON*, Wydanie 1. Warszawa: Oficyna Wydawnicza Politechniki Warszawskiej, 2023.

[107] TensorFlow Developers, *TensorFlow*. (Mar. 08, 2024). doi: 10.5281/ZENODO.4724125.

[108] A. Géron and K. Sawka, *Uczenie maszynowe z użyciem Scikit-Learn i TensorFlow*, Wydanie II, Aktualizacja do modułu TensorFlow 2. Gliwice: Helion, 2020.

[109] “MATLAB Deep Network Designer.” [Online]. Available: https://www.mathworks.com/help/deeplearning/ref/deepnetworkdesigner-app.html

[110] R. C. Gonzalez and R. E. Woods, *Digital image processing*, Fourth edition, Global edition. New York, NY: Pearson, 2018.

[111] R. Tadeusiewicz and P. Korohoda, *Komputerowa analiza i przetwarzanie obrazów*. in Społeczeństwo Globalnej Informacji. Kraków: Wydaw. Fundacji Postępu Telekomunikacji, 1997.

[112] A. Dziech, “New Orthogonal Transforms for Signal and Image Processing,” *Appl. Sci.*, vol. 11, no. 16, p. 7433, Aug. 2021, doi: 10.3390/app11167433.

[113] R. Szeliski, *Computer vision: algorithms and applications*, Second edition. in Texts in computer science.

Cham: Springer, 2022.

[114] J. C. Russ, *The image processing handbook*, 3rd ed. Boca Raton, FL: CRC Press, 1998.

[115] D. Itô, Ed., *Robot vision: strategies, algorithms and motion planning*. New York: Nova Science Publishers, Inc, 2009.

[116] V. Chernov, J. Alander, and V. Bochko, “Integer-based accurate conversion between RGB and HSV color spaces,” *Comput. Electr. Eng.*, vol. 46, pp. 328–337, Aug. 2015, doi: 10.1016/j.compeleceng.2015.08.005.

[117] A. Dąbrowski, “Przetwarzanie sygnałów i informacji, Ludzki system wizyjny,” Poznan, Poland, May 10, 2018.

[118] W. Burger and M. J. Burge, *Principles of Digital Image Processing: Advanced Methods*. in Undergraduate Topics in Computer Science. London: Springer London, 2013. doi: 10.1007/978-1-84882-919-0.

[119] P. Skulimowski, M. Owczarek, and P. Strumillo, “Door detection in images of 3D scenes in an electronic travel aid for the blind,” in *Proceedings of the 10th International Symposium on Image and Signal Processing and Analysis*, Ljubljana, Slovenia: IEEE, Sep. 2017, pp. 189–194. doi: 10.1109/ISPA.2017.8073593.

[120] W. Żorski, *Metody segmentacji obrazów oparte na transformacie Hougha*. Warszawa: Instytut Automatyki i Robotyki. Wojskowa Akademia Techniczna, 2000.

[121] D. J. C. MacKay, *Information theory, inference, and learning algorithms*, 22nd printing. Cambridge: Cambridge University Press, 2019.

[122] S. Cygert and A. Czyżewski, “Robust Object Detection with Multi-input Multi-output Faster R-CNN,” in *Image Analysis and Processing – ICIAP 2022*, vol. 13231, S. Sclaroff, C. Distante, M. Leo, G. M. Farinella, and F. Tombari, Eds., in Lecture Notes in Computer Science, vol. 13231. , Cham: Springer International Publishing, 2022, pp. 572–583. doi: 10.1007/978-3-031-06427-2_48.

[123] D. Grabowski and A. Czyżewski, “System for monitoring road slippery based on CCTV cameras and convolutional neural networks,” *J. Intell. Inf. Syst.*, vol. 55, no. 3, pp. 521–534, Dec. 2020, doi: 10.1007/s10844-020-00618-5.

[124] R. Tadeusiewicz and M. Szaleniec, *Leksykon sieci neuronowych*. Projekt Nauka. Fundacja na rzecz promocji nauki polskiej. [Online]. Available: https://books.google.pl/books?id=LX4_CgAAQBAJ

[125] A. Géron, *Hands-on machine learning with Scikit-Learn and TensorFlow: concepts, tools, and techniques to build intelligent systems*, First edition. Beijing ; Boston: O’Reilly Media, 2017.

[126] J. Zhou *et al.*, “Graph neural networks: A review of methods and applications,” *AI Open*, vol. 1, pp. 57–81, 2020, doi: 10.1016/j.aiopen.2021.01.001.

[127] N. M. Arshad and N. A. Razak, “Vision-based detection technique for effective line-tracking autonomus vehicle,” in *2012 IEEE 8th International Colloquium on Signal Processing and its Applications*, Malacca, Malaysia: IEEE, Mar. 2012, pp. 441–445. doi: 10.1109/CSPA.2012.6194765.

[128] B. Barua, C. Gomes, S. Baghe, and J. Sisodia, “A Self-Driving Car Implementation using Computer Vision for Detection and Navigation,” in *2019 International Conference on Intelligent Computing and Control Systems (ICCS)*, Madurai, India: IEEE, May 2019, pp. 271–274. doi: 10.1109/ICCS45141.2019.9065627.

[129] W. Vijitkunsawat and P. Chantngarm, “Comparison of Machine Learning Algorithm’s on Self-Driving Car Navigation using Nvidia Jetson Nano,” in *2020 17th International Conference on Electrical Engineering/Electronics, Computer, Telecommunications and Information Technology (ECTI-CON)*, Phuket, Thailand: IEEE, Jun. 2020, pp. 201–204. doi: 10.1109/ECTI-CON49241.2020.9158311.

[130] A. K. Jain, “Working model of Self-driving car using Convolutional Neural Network, Raspberry Pi and Arduino,” in *2018 Second International Conference on Electronics, Communication and Aerospace Technology (ICECA)*, Coimbatore: IEEE, Mar. 2018, pp. 1630–1635. doi: 10.1109/ICECA.2018.8474620.

[131] E. Civik and U. Yuzgec, “Real-time driver fatigue detection system with deep learning on a low-cost embedded system,” *Microprocess. Microsyst.*, vol. 99, p. 104851, Jun. 2023, doi: 10.1016/j.micpro.2023.104851.

[132] “Raspberry Pi 4 model B DATASHEET.” Accessed: Jul. 01, 2021. [Online]. Available: https://datasheets.raspberrypi.com/rpi4/raspberry-pi-4-datasheet.pdf

[133] “Raspberry Pi 4, 3A+, Zero W - specs, benchmarks & thermal tests.” Accessed: Jun. 10, 2023. [Online]. Available: https://magpi.raspberrypi.com/articles/raspberry-pi-specs-benchmarks

[134] “Google Coral Dev Board datasheet.” [Online]. Available: https://coral.ai/docs/dev-board/datasheet/#features

[135] “NVIDIA Jetson Nano System-on-Module Data Sheet.” [Online]. Available: https://developer.download.nvidia.com/assets/embedded/secure/jetson/Nano/docs/Jetson-Nano-System-On-Module-Data-Sheet-DA-09366-001_v1.2.pdf?Mgs-un9R9CFO_vXNewDtvktlcmv-X6Jh64TnsOSvB1n_NQ3QCAcO_iXfOsIYLr-P4_zE3Twd-

VFAQ2DQwrJAAYZEUzIA5a1202wwLMiFUBpF985SiNkOscC3c7BpkNDT6ww2RUAyZCt6D3Hr2DNdjnmz7J4V3ebadjF-4e2QPhVCozg1VL4bWxnl7yR42LgrrSmZpjoBBcmePMqZj1T63YiRRqY=&t=eyJscyI6ImdzZW8iLCJsc2QiOiJodHRwczovL3d3dy5nb29nbGUuY29tLyJ9

[136] A. A. Suzen, B. Duman, and B. Sen, “Benchmark Analysis of Jetson TX2, Jetson Nano and Raspberry PI using Deep-CNN,” in *2020 International Congress on Human-Computer Interaction, Optimization and Robotic Applications (HORA)*, Ankara, Turkey: IEEE, Jun. 2020, pp. 1–5. doi: 10.1109/HORA49412.2020.9152915.

[137] “NVIDIA CORPORATION, NVIDIA Jetson Linux Developer Guide 32.7.1 Release.” Accessed: Jun. 05, 2023. [Online]. Available: https://docs.nvidia.com/jetson/l4t/index.html#page/Tegra%20Linux%20Driver%20Package%20Development%20Guide/power_management_nano.html

[138] “Jetson Xavier NX Series and Jetson AGX Xavier Series.” Accessed: Jul. 17, 2024. [Online]. Available: https://docs.nvidia.com/jetson/archives/r35.1/DeveloperGuide/text/SD/PlatformPowerAndPerformance/JetsonXavierNxSeriesAndJetsonAgxXavierSeries.html

[139] “Jetson Orin NX Series and Jetson AGX Orin Series.” [Online]. Available: https://docs.nvidia.com/jetson/archives/r35.1/DeveloperGuide/text/SD/PlatformPowerAndPerformance/JetsonOrinNxSeriesAndJetsonAgxOrinSeries.html

[140] “OpenBenchmarking.org.” Accessed: Jul. 16, 2024. [Online]. Available: https://openbenchmarking.org

[141] “Revolution Pi.” Accessed: Jul. 10, 2023. [Online]. Available: https://revolutionpi.com/revolution-pi-series

[142] “CPU Benchmarks, PassMark® Software.” Accessed: Jul. 10, 2023. [Online]. Available: https://www.cpubenchmark.net/cpu.php?cpu=BCM2711&id=4297

[143] “Jetson Benchmarks, Nvidia Developer.” Accessed: Jul. 05, 2023. [Online]. Available: https://developer.nvidia.com/embedded/jetson-benchmarks

[144] M. Yildirim, O. Karaduman, and H. Kurum, “Real-Time Image and Video Processing Applications Using Raspberry Pi,” in *2022 IEEE 1st Industrial Electronics Society Annual On-Line Conference (ONCON)*, kharagpur, India: IEEE, Dec. 2022, pp. 1–6. doi: 10.1109/ONCON56984.2022.10127034.

[145] S. J. Lee, “Challenges of Real-time Processing with Embedded Vision for IoT Applications,” in *2022 International Conference on Electrical, Computer, Communications and Mechatronics Engineering (ICECCME)*, Maldives, Maldives: IEEE, Nov. 2022, pp. 1–6. doi: 10.1109/ICECCME55909.2022.9988338.

[146] A. Annusewicz and J. Zwierzchowski, “Marker Detection Algorithm for the Navigation of a Mobile Robot,” in *2020 27th International Conference on Mixed Design of Integrated Circuits and System (MIXDES)*, Lodz, Poland: IEEE, Jun. 2020, pp. 223–226. doi: 10.23919/MIXDES49814.2020.9155658.

[147] M. Barnell, C. Raymond, S. Smiley, D. Isereau, and D. Brown, “Ultra Low-Power Deep Learning Applications at the Edge with Jetson Orin AGX Hardware,” in *2022 IEEE High Performance Extreme Computing Conference (HPEC)*, Waltham, MA, USA: IEEE, Sep. 2022, pp. 1–4. doi: 10.1109/HPEC55821.2022.9926369.

[148] Y. Kortli, S. Gabsi, L. F. C. L. Y. Voon, M. Jridi, M. Merzougui, and M. Atri, “Deep embedded hybrid CNN–LSTM network for lane detection on NVIDIA Jetson Xavier NX,” *Knowl.-Based Syst.*, vol. 240, p. 107941, Mar. 2022, doi: 10.1016/j.knosys.2021.107941.

[149] C. Choe, M. Choe, and S. Jung, “Run Your 3D Object Detector on NVIDIA Jetson Platforms:A Benchmark Analysis,” *Sensors*, vol. 23, no. 8, p. 4005, Apr. 2023, doi: 10.3390/s23084005.

[150] P. Warden and D. Situnayake, *TinyML: machine learning with Tensorflow Lite on Arduino, and ultra-low power micro-controllers*, First edition. Beijing: O’Reilly, 2020.

[151] P. Kumar, “MIPI camera vs USB camera – a detailed comparison,” Camera blog. Accessed: May 17, 2024. [Online]. Available: https://www.e-consystems.com/blog/camera/technology-thursday/mipi-camera-vs-usb-camera-a-detailed-comparison/

[152] “Photography — Electronic still picture imaging — Resolution and spatial frequency responses (ISO Standard No. 12233:2017).” International Organization for Standardization, 2017.

[153] “IMX219 Camera Module, 160 degree FoV.” Accessed: May 17, 2024. [Online]. Available: https://www.waveshare.com/imx219-d160.htm

[154] “Raspberry Pi Camera: Comparison of High Quality Camera with Camera Module V2.” Accessed: May 17, 2024. [Online]. Available: https://www.seeedstudio.com/blog/2020/05/14/raspberry-pi-camera-comparison-of-high-quality-camera-with-camera-module-v2/

[155] “C922 Pro Stream Webcam Technical Specifications.” Accessed: May 17, 2024. [Online]. Available: https://support.logi.com/hc/en-us/articles/360023462473-C922-Pro-Stream-Webcam-Technical-Specifications

[156] P. Drap and J. Lefèvre, “An Exact Formula for Calculating Inverse Radial Lens Distortions,” *Sensors*, vol. 16, no. 6, p. 807, Jun. 2016, doi: 10.3390/s16060807.

[157] A. Stanisz, *Modele regresji logistycznej: zastosowanie w medycynie, naukach przyrodniczych i społecznych*. Kraków: Wydawnictwo StatSoft Polska, 2016.

[158] T. Fawcett, "An introduction to ROC analysis," *Pattern Recognit. Lett.*, vol. 27, no. 8, pp. 861–874, Jun. 2006, doi: 10.1016/j.patrec.2005.10.010.

[159] C. D. Manning, P. Raghavan, and H. Schütze, *Introduction to information retrieval*. New York: Cambridge University Press, 2008.

[160] T. Munyer, P.-C. Huang, C. Huang, and X. Zhong, "FOD-A: A Dataset for Foreign Object Debris in Airports," 2021, doi: 10.48550/ARXIV.2110.03072.

[161] W. Leśna and Ł. Kozak, "Foreign Object Debris (FOD) dataset." [Online]. Available: https://www.kaggle.com/datasets/lukaszkozak/foreign-object-debris-fod-dataset?resource=download

[162] W. Leśna and Ł. Kozak, "Automatic visual detection of FOD on airport surfaces," Master thesis, supervisor: Tomasz Marciniak, Poznan University of Technology, Poznan, Poland, 2023.

[163] B. Dwyer, J. Nelson, and T. Hansen, *Roboflow*. (2024). [Online]. Available: https://roboflow.com/

[164] I. Elmanaa, M. A. Sabri, Y. Abouch, and A. Aarab, "Efficient Roundabout Supervision: Real-Time Vehicle Detection and Tracking on Nvidia Jetson Nano," *Appl. Sci.*, vol. 13, no. 13, p. 7416, Jun. 2023, doi: 10.3390/app13137416.

[165] B. Jabłoński *et al.*, "Evaluation of NVIDIA Xavier NX Platform for Real-Time Image Processing for Plasma Diagnostics," *Energies*, vol. 15, no. 6, p. 2088, Mar. 2022, doi: 10.3390/en15062088.

[166] B. Jabłoński, D. Makowski, and P. Perek, "Implementation of Thermal Event Image Processing Algorithms on NVIDIA Tegra Jetson TX2 Embedded System-on-a-Chip," *Energies*, vol. 14, no. 15, p. 4416, Jul. 2021, doi: 10.3390/en14154416.

[167] "GoPro, GoPro Hero+ LCD User Manual." Accessed: Jun. 05, 2023. [Online]. Available: https://gopro.com/content/dam/help/heroplus-lcd/manuals/UM_HEROPlusLCD_ENG_REVB_WEB.pdf

[168] M. S. Park, A. Brock, V. Mortimer, P. Taussky, W. T. Couldwell, and E. Quigley, "GoPro Hero Cameras for Creation of a Three-Dimensional, Educational, Neurointerventional Video," *J. Digit. Imaging*, vol. 30, no. 5, pp. 561–565, Oct. 2017, doi: 10.1007/s10278-017-9948-7.

[169] A. Roy and N. Biswas, "GoPro: a Low Complexity Task Allocation Algorithm for a Mobile Edge Computing System," in *2022 National Conference on Communications (NCC)*, Mumbai, India: IEEE, May 2022, pp. 413–418. doi: 10.1109/NCC55593.2022.9806731.

[170] L. Gang, M. Zhang, L. Zhang, and J. Hu, "Automatic road marking recognition for intelligent vehicle systems application," *Adv. Mech. Eng.*, vol. 9, no. 5, p. 168781401770626, May 2017, doi: 10.1177/1687814017706267.

[171] H. Wang, "Airport Signs and Markings Recognition for Enhanced Runway Incursion Avoidance," 2015. [Online]. Available: https://api.semanticscholar.org/CorpusID:8371376

[172] Y. Wang, D. Shen, and E. K. Teoh, "Lane detection using spline model," *Pattern Recognit. Lett.*, vol. 21, no. 8, pp. 677–689, Jul. 2000, doi: 10.1016/S0167-8655(00)00021-0.

[173] Q. Chen and H. Wang, "A Real-time Lane Detection Algorithm Based on a Hyperbola-Pair Model," in *2006 IEEE Intelligent Vehicles Symposium*, Meguro-Ku, Japan: IEEE, 2006, pp. 510–515. doi: 10.1109/IVS.2006.1689679.

[174] M. Bertozzi and A. Broggi, "GOLD: a parallel real-time stereo vision system for generic obstacle and lane detection," *IEEE Trans. Image Process.*, vol. 7, no. 1, pp. 62–81, Jan. 1998, doi: 10.1109/83.650851.

[175] Abdulhakam. AM. Assidiq, O. O. Khalifa, Md. R. Islam, and S. Khan, "Real time lane detection for autonomous vehicles," in *2008 International Conference on Computer and Communication Engineering*, Kuala Lumpur, Malaysia: IEEE, May 2008, pp. 82–88. doi: 10.1109/ICCCE.2008.4580573.

[176] T.-H. Kwon, J.-E. Kim, Y.-H. Kim, and K.-D. Kim, "Color-Independent Visible Light Communications Based on Color Space: State of the Art and Potentials," *Electronics*, vol. 7, no. 9, p. 190, Sep. 2018, doi: 10.3390/electronics7090190.

[177] D. Tian, "DeepPiCar — Part 4: Autonomous Lane Navigation via OpenCV." Accessed: Nov. 03, 2020. [Online]. Available: https://towardsdatascience.com/deeppicar-part-4-lane-following-via-opencv-737dd9e47c96

[178] "Simple package for monitoring and control your NVIDIA Jetson [Orin, Xavier, Nano, TX] series." Accessed: May 05, 2023. [Online]. Available: https://github.com/rbonghi/jetson_stats

[179] Y.-L. Chen, M.-F. Chang, C.-W. Yu, X.-Z. Chen, and W.-Y. Liang, "Learning-Directed Dynamic Voltage and Frequency Scaling Scheme with Adjustable Performance for Single-Core and Multi-Core Embedded and Mobile Systems," *Sensors*, vol. 18, no. 9, p. 3068, Sep. 2018, doi: 10.3390/s18093068.

[180] D.-K. Kang, K.-B. Lee, and Y.-C. Kim, "Cost Efficient GPU Cluster Management for Training and Inference of Deep Learning," *Energies*, vol. 15, no. 2, p. 474, Jan. 2022, doi: 10.3390/en15020474.

[181] S. Khriji, R. Chéour, and O. Kanoun, “Dynamic Voltage and Frequency Scaling and Duty-Cycling for Ultra Low-Power Wireless Sensor Nodes,” *Electronics*, vol. 11, no. 24, p. 4071, Dec. 2022, doi: 10.3390/electronics11244071.

[182] “GoogLeNet.” [Online]. Available: https://www.mathworks.com/help/deeplearning/ref/googlenet.html

[183] “Gigahertz-Optik GmbH, X4 Light Analyzer Datasheet.” [Online]. Available: http://www.industrycortex.com/datasheets/profile/506792174

[184] M. Zalesińska, “Ekspertyza fotometryczna czujników BH 1750,” Jan. 2023. [Online]. Available: https://sin.put.poznan.pl/reports/details/r3578_2023

[185] “ADB Safe gate, High Intensity Unidirectional Elevated Light for Approach, Threshold and Runway End and for Sequenced Flashing Lights (SFLS) Runway Threshold Identification (RTILS) Systems, User Manual, UM-4020/AM02-630e, Rev. 2.0.” [Online]. Available: https://adbsafegate.com/documents/2326/en/manual-uel

[186] “Texas Advanced Optoelectronic Solutions Inc., TCS3472 Colour light-to-digital converter with IR filter, TAOS135,” 2012, [Online]. Available: http://www.datenblatt-pdf.com/pinout/911411/TCS3472-

[187] “Avago Technologies, APDS-9960 Digital Proximity, Ambient Light, RGB and Gesture Sensor, Data Sheet, AV02-4191EN.” [Online]. Available: https://content.arduino.cc/assets/Nano_BLE_Sense_av02-4191en_ds_apds-9960.pdf

[188] “Intersil, Digital Red, Green and Blue Colour Light Sensor with IRBlocking Filter ISL29125, FN8424.2.” [Online]. Available: https://cdn.sparkfun.com/datasheets/Sensors/LightImaging/isl29125.pdf

[189] “AMS, AS7265x Smart 18-Channel VIS to NIR Spectral_ID 3- Sensor Chipset with Electronic Shutter, Datasheet [v1-04].” [Online]. Available: https://datasheetspdf.com/pdf/1315799/ams/AS72651/1

[190] “AMS, AS7341 11-Channel Multi-Spectral Digital Sensor, Datasheet DS000504 [v3-00].” [Online]. Available: https://datasheetspdf.com/pdf/1402690/ams/AS7341/1

[191] “AMS, AS7262 6-Channel Visible Spectral_ID Device with Electronic Shutter and Smart Interface, Datasheet [v1-01].” [Online]. Available: https://ams.com/documents/20143/36005/AS7262_DS000486_2-00.pdf

[192] “TCS3430 Datasheet v3-00.” Accessed: Apr. 05, 2023. [Online]. Available: https://ams.com/documents/20143/9310857/TCS3430_DS000464_7-00.pdf

[193] “Taxiway centre line light IDM 5582 Data sheet.” Accessed: Aug. 01, 2023. [Online]. Available: https://asset-prod1a-euw.productmarketingcloud.com/api/assetstorage/3813_cd74f072-b40b-4f34-bdd9-0e71e89e8451

[194] “Airfield Lighting Manual 8" Inset Lights - IDM 4671, IDM 4581, IDM 4582.” Accessed: Aug. 01, 2023. [Online]. Available: https://asset-prod1a-euw.productmarketingcloud.com/api/assetstorage/3813_cd74f072-b40b-4f34-bdd9-0e71e89e8451

[195] “ADB SAFEGATE UEL - Approach Centerline and Crossbar, Elevated, Halogen.” [Online]. Available: https://adbsafegate.com/products/airfield/approach-lighting/uel-approach-centerline-and-crossbar-elevated-halogen/?fbclid=IwAR3fZ69YNa8WDECDSqMRMAQW0fKPEdPm3qjz4s1ixjadCk6kYCx_YB9eXqI

[196] “CIE 1931 2-deg xyz chromaticity coordinates.” The Colour & Vision Research laboratory, University College London.

List of Figures

List of Tables